From Oscillating Flat Plate to Maneuvering Bat Flight – Role of Kinematics, Aerodynamics, and Inertia

Aevelina Rahman

Dissertation submitted to the faculty of the
Virginia Polytechnic Institute and State University
in partial fulfillment of the requirements for the degree of

Doctor of Philosophy
in
Mechanical Engineering

Danesh K. Tafti
Mayuresh J. Patil
Mark R. Paul
Rui Qiao
Kevin G. Wang

December 16, 2021

Blacksburg, Virginia

Keywords: Plunging flat plate, vortex dynamics, thrust coefficient, maneuvering bat flight, kinematics and aerodynamics, motion dynamics, wing inertia

From Oscillating Flat Plate to Maneuvering Bat Flight – Role of Kinematics, Aerodynamics, and Inertia

Aevelina Rahman

ABSTRACT

With the aim to understand the synergistic roles played by kinematics, aerodynamics, and inertia in flapping wing maneuvers, this thesis first investigates the plunging motion of a simple flat plate as it is a fundamental motion in the kinematics of many flying animals. A wide range of frequency (k) and amplitude (h) is investigated to account for a robust kinematic characterization in the form of plunge velocity (kh). Leading Edge Vortices (LEVs) are found to be responsible for producing thrust while Trailing Edge Vortices (TEVs) produce drag. The vortex dynamics becomes nonlinear for higher *kh* and three main vortex-vortex interactions (VVI) are identified in the flow-field. To estimate the sole effect of LEVs on thrust coefficient, TEVs are eliminated by introducing a splitter plate. This resulted in reduced non-linearity in VVI and facilitated a parametrization of aerodynamic thrust coefficient with key kinematic features, frequency (k) and amplitude (h) [$C_T = A.k^{1.4}h - B$ where A and B are constants].

This is followed by investigating the more direct problem of bio-inspired MAV research – the interplay of kinematics, aerodynamics, and inertia on maneuvering bat flights. At first, an ascending right turn of a *H. pratti* bat is investigated to elucidate on the kinematic features and aerodynamic mechanisms used to effectuate the maneuver. Deceleration in flight speed, an increase in flapping frequency, shortening of the upstroke, and thrust generation at the end of the upstroke is observed during this maneuver. The turn is initiated by the synergisytic implementation of roll and yaw rotation where the turning moments are generated by drawing the inside wing closer to the body, by introducing phase lags in force generation between the two wings and by redirecting force production to the outer part of the wing outside of the turn. Upon comparison with a similar maneuver by a *H. armiger* bat, some commonalities as well as differences were observed. This analysis was followed by a comparative study among different maneuvering flights (a straight flight, two ascending right turns, and a U-turn) in order to establish the complete motion dynamics of a maneuver in action. The individual effects of aerodynamics and wing inertia for maneuvering flights of a *H. armiger* and *H. pratti* are investigated. It is found that for both, translation and rotation the overall trajectory trend is mostly driven by the aerodynamic forces and moments, whereas inertial effects drive the intricate intra-cycle fluctuations as well as the vertical velocity and altitude gain during ascent. Additionally, inertial moments play a dominant role for effecting yaw rotations where the importance of the Coriolis and centrifugal moments increase with increasing acuteness of the maneuver, with the largest effect of centrifugal moments being evidenced in the U-turn.

From Oscillating Flat Plate to Maneuvering Bat Flight – Role of Kinematics, Aerodynamics, and Inertia

Aevelina Rahman

GENERAL AUDIENCE ABSTRACT

The study of flapping wing is of paramount interest in the field of small aerial and aquatic vehicle propulsion. The intricate mechanisms acting behind a flapping wing maneuver can be explained by the synergistic roles played by 3 main components; details of the wing motion or the kinematics, how the air reacts to the wing motion or the aerodynamics, and the effort or force required to move the wings or wing inertia. This dissertation systematically reports the contribution of these components to a flapping flight maneuver. At first, the plunging motion of a simple flat plate is investigated as it is a fundamental motion in the flapping flight of many flying animals. A wide range of frequency and amplitude is investigated and their effect is characterized by a single parameter called "plunge velocity". It is found that, the resultant flow field becomes disorderly for higher plunge velocities which can be characterized by three different types of vortex interactions. The observed results facilitated a robust parametrization of aerodynamic thrust production with key kinematic features, frequency and amplitude.

After this, the dissertation focuses on the bio-inspiration aspect of flapping flight by investigating the interplay of kinematics, aerodynamics, and inertia of maneuvering bat flights. At first, an ascending right turn of one species (*H. pratti)* is investigated to elucidate on the kinematic features and aerodynamic mechanisms used to effectuate the maneuver. Some characteristic features observed are – lowering of flight speed, increase in flapping rate, shortening of upstrokes, and generation of a forward force at the end of the upstroke. It is observed, that the bat turns by using synergistic body rotations in multiple directions which are effected by various techniques such as - drawing the wing inside the turn closer to the body, and changing the timing and location of the forces produced between the two wings. Upon comparison with a similar maneuver by a *H. armiger* bat, some commonalities as well as differences were observed in the maneuver mechanisms. This analysis was followed by a comparative study among different maneuvering flights (a straight flight, two ascending right turns, and a U-turn) to establish the complete motion dynamics of a maneuver. The individual contributions of aerodynamics and wing inertia for maneuvering flights of a *H. armiger* and *H. pratti* are investigated. It is found that for both, translation and rotation the overall trajectory is mostly influenced by the aerodynamic forces and moments, whereas inertial effects are responsible for trajectory fluctuations during a flapping cycle as well contributing to altitude gain during ascent for the *H. armiger* bat.

ACKNOWLEDGMENTS

To start, I would like to thank Almighty ALLAH for giving me the strength, knowledge, ability, endurance, and opportunity to complete this research satisfactorily. Next, I would take the opportunity to thank my parents and brother for their continual support. I could not have succeeded without their constant encouragement and guidance throughout the years. Also a special gratitude to my husband Ashrarul Haq Sifat for his endless support both academically and mentally. I thank my advisor, Dr. Danesh Tafti, who provided me the opportunity to work on this exciting project of flapping flight. I am very grateful for the continual guidance, resources, and advice provided by him. Particular thanks to Dr. Rolf Mueller for providing the experimental facilities for bat flight measurements. Thanks as well to Dr. Mayuresh Patil, Dr. Mark R. Paul, Dr. Rui Qiao and Dr. Kevin Wang for lending their time and wisdom to my research. I thank the Advanced Research Computing at Virginia Tech for the computational resources and technical support provided. Thanks to my lab mates in HPCFD lab who helped me with their valuable feedback and suggestions. Finally, I would like to thank Virginia Tech, Mechanical Engineering Department and all the students who came before me for providing this opportunity to work on this amazing and impactful project.

TABLE OF CONTENTS

Chapter 1: Introduction

Unmanned vehicle research is rapidly gaining interest with its increasing prospect in pervasive air and water applications like environmental monitoring, homeland security, military purposes, seabed oil and gas explorations, scientific deep ocean surveys and ecological studies. Low Reynolds number (Re) is a prominent feature of micro-air vehicles (MAV) flight, which gives rise to unfavorable aerodynamic conditions to support controlled flight. Fixed-wing airfoil performance deteriorates significantly as lower lift coefficient results in lower loading capability while higher drag coefficient results in high power input. However, numerous flyers in nature like small birds and insects overcome the deteriorating aerodynamic performance under steady flow conditions at low Re and retain efficient performance and maneuverability by employing unsteady mechanisms via flapping and flexible wings. Therefore, bio-inspiration is a fundamental propulsion option for MAVs and a number of studies are found in the literature featuring design and construction of various bio-mimetic devices.

Most biological propulsors (birds, bats, insects, fishes etc.) use the flapping motion to generate both thrust and lift. Thus, understanding the unsteady aerodynamic forces associated with this motion is crucial. While pitching-plunging airfoils have been studied extensively in the literature in an effort to unfold working mechanisms of flapping flight, there are relatively fewer studies on pure plunging motion. Pure oscillation or plunging is one of the principal motions which comprise the kinematics used by many flying and swimming organism for locomotion. The complex phenomena of animal propulsion can be effectively expressed by oscillatory motion of a thin plate or an airfoil like appendage. Thus, plunging bodies have been studied in the literature in relation to low Reynolds number (Re) flapping flight with a view to shed light on the unsteady flow phenomena of flapping flight. Researchers have examined various kinematic parameters

influencing the unsteady aerodynamics and identified reduced frequency (k, Eq. 1) and plunge amplitude (h, Eq. 2) as two of the most important parameters for thrust generation.

$$k = \frac{\pi f^* c^*}{U_\infty^*} \tag{1}$$

$$h = \frac{a^*}{c^*} \tag{2}$$

where, $f^* =$ Frequency of oscillation (Hz), $U_\infty^* =$ Free-stream velocity ($\frac{m}{s}$), $a^* =$ Amplitude (Half-cycle) of oscillation (m) and $c^* =$ Chord length (m).

A key factor in almost all previous research regarding plunging motion is that, the plunge amplitude (h, Eq. 2) studied was in a significantly smaller working range which is applicable for insect like flyers but fails to cover bird, bat, or fish like propulsors. To successfully analyze these unexplored regions and aid in the development of associated instrumentation, a predictive guide is extremely helpful to decide upon an optimum kinematic combination i.e. what combination of frequency and amplitude shall result in targeted force parameters like thrust coefficient. As the literature is not very abundant on the effect of pure plunge motion of a flat plate at a very low Reynolds number (less than 10^3), the initial aim of this research is to unfold the aerodynamic mechanisms behind thrust production and parameterize it with key kinematic variables of plunging.

After completion of the elemental project on varying the kinematics of a plunging flat plate and its effect on the aerodynamics, the research switched gears to a more direct problem of bio-inspired MAV research. As Micro Air Vehicles (MAVs) have the potential to revolutionize our capabilities of sensing and collecting information, this technology is leading to smaller and more maneuverable unmanned platforms expanding the envelope of operations into more challenging and complicated environments. The second and final part of this thesis will discuss a research problem with a view

to unfold some fundamental techniques applicable to efficient maneuver of MAVs. It is done by a rigorous investigation of the kinematics, aerodynamics, and inertia of a maneuvering bat flight. Among the numerous flying species of nature, bats exhibit excellent agility at maneuvering. Their elevated agility can be linked to their highly articulated skeletal structures and pliant wing membrane that provides flexibility and control over aerodynamic force generation. They are very agile in air which is one of the most important survival element for most flying species as it is critical for capturing prey or avoiding predators. Different species of bats adapt maneuverability for differing motivations; either to prey on flying insects or to navigate through winding cave passages or dense forests. This natural maneuverability allows bats to initiate a turn in a very short period of time, to execute a turn within a tight radius or to re-direct its trajectory practically within a wing beat cycle. Although these flight traits are consequential and highly desirable in today's micro air vehicles (MAVs), the majority of the bioinspired MAV research has been studying birds and insects extensively. Equivalent studies for bat flights compared to insects are scarce mainly because of the challenges associated with capturing the complex wing articulation during flight. However, with recent advances in motion capturing technology, bats provide a compelling model for highly maneuverable MAV designs.

The research in this thesis aims to establish robust explanations and highlight recurring techniques that bats use to perform a certain maneuver. Combined kinematic and aerodynamic studies on maneuvering bat flights are scarce in the literature and provide a much needed gateway for a deeper characterization of the relationship between wing motions and the ensuing aerodynamics. In most of the previous studies with detailed aerodynamics, may that be of a straight flight or a maneuvering one, bats from a fixed species are usually used giving singular speciological inference to the kinematic and aerodynamic results. In search of robust maneuvering techniques

indifferent to species, the study focuses on a right ascending turn of a Pratt's Roundleaf bat (*H. pratti*) and compares the kinematic and aerodynamic features with a previous study of the same maneuver by a different species of bat (*H. armiger*). Being individual living animals, bats might exhibit certain individual flight traits to effect a certain maneuver. Comparing two similar maneuvering flights coming from two morphologically comparable but different species of bats allows for identifying these individual traits from the general features.

After establishing an understanding of the maneuver mechanics of two different bat species by relating the wing kinematics to the resulting aerodynamics, the research focuses on developing the complete motion dynamics of maneuvering bats by including the wing inertial effects. As bat wings entail considerable mass (~20-30% of the total) and undergo dramatic accelerations while effectuating complex maneuvers, the inertial forces resulting from the wing deformations are deemed to be substantial. Thus, the measured wing kinematics is utilized along with the detailed mass distribution to account for the inertial consequences in the complete motion dynamics. Finally, the ultimate goal of this research can be stated as: to investigate the synergistic effects of the wing kinematics, the resulting aerodynamics, and inertial consequences on the complete motion dynamics active in flapping maneuvers.

1. LIST OF PUBLICATIONS

The publications that came out from this research are listed below-

- Rahman, A., Tafti, D. K. *The role of vortex-vortex interactions in thrust production for a plunging flat plate.* Published in the Journal of Fluids and Structures, Vol. 96, July 2020
- Rahman, A., Tafti, D. K. *Characterization of heat transfer enhancement for an oscillating flat plate-fin.* Published in the International Journal of Heat and Mass

Transfer, Vol. 147, Feb. 2020 [Used for taking MS degree along the way, hence not included in this report]

- Rahman, A., Tafti, D. K. *Effect of Leading Edge Vortices (LEVs) on Thrust Coefficient of a Plunging Flat Plate*. Published in the Proceedings of the ASME 2020 Fluids Engineering Division Summer Meeting, July 12-16, 2020
- Rahman, A., Tafti, D. K. *Turning-Ascending Flight of a H. pratti Bat.* Manuscript submitted to Royal Society Open Science, Nov. 2021.
- Rahman, A., Tafti, D. K. *Effect of Wing Inertia and Aerodynamics on Maneuvering Bat Flights.* Manuscript awaiting journal submission

2. BRIEF DESCRIPTION OF FOLLOWING CHAPTERS

The following chapters of the thesis are organized as follows -

Chapter 2 studies the unsteady vortex dynamics of a pure plunge motion as it is a fundamental component of the complex flapping phenomena observed in efficient biological flyers. Applying the motion on a flat plate is beneficial in understanding the fundamental effects and explaining the basic phenomena regarding the motion itself. This paper addresses the limitation of most past investigations which only studied a limited range of plunge velocities and plunge amplitudes. Although a number of previous studies mentioned optimum frequency range for efficiency maximization, they did not relate the vortex dynamics with thrust generation. Thus, to have a comprehensive and robust understanding of the factors governing thrust generation from a plunging body, the current study analyzes a plunging flat plate at a low Reynolds number (Re = 100). The study covers a broad range of reduced frequencies $0.25 \leq k \leq 16$ and plunge amplitudes

$0.03125 \leq h \leq 8$ to give a plunge velocitiy range of $0.25 \leq kh \leq 4$. The study investigates thrust generation and its dependence on reduced frequency (k) and plunge amplitude (h) and characterizes the dynamics of plunge induced vorticity by identifying three major mechanisms of vortex-vortex interactions. It is shown that, in general LEVs have a positive impact on thrust production. Moreover, the detrimental dynamics of plunge induced vortex-vortex interactions involving TEVs at high amplitude and frequency is identified. Finally, a detailed analysis of the wake is provided in relation with different plunge attributes.

Chapter 3 addresses the gap in the literature of studies focused on separating the effect of Trailing Edge Vortices (TEVs) and Leading Edge Vortices (LEVs). Some previous studies identified reduced frequency (*k)* to be the primary factor governing the vortex topology while others mentioned a combined frequency amplitude parameter called plunge velocity (*kh)* to be the main driver. However, none of those studies explained the synergy between the two key parameters (*k* and *h)* and directly related the vortex dynamics with them. This paper investigates the individual effect of LEVs and TEVs on thrust production in the same range of reduced frequencies $0.25 \leq k \leq 16$ and plunge amplitudes $0.03125 \leq h \leq 8$ as Chapter 2. To investigate the sole effect of LEVs on thrust production, TEVs are eliminated through numerical experiments. It is shown that in the absence of TEVs, the vortex-vortex interactions detrimental to thrust production diminishes. Thus, thrust increases monotonically facilitating a representative parametrization of thrust coefficient with plunging frequency (k) and amplitude (h). This also establishes a novel mechanism for thrust enhancement over a range of scales.

Chapter 4 investigates the kinematics and aerodynamics of a maneuvering bat with a view to establish the generic and specific traits associated with a turning ascending flight. There have been a number of bat flight researches that focused on different aspects of straight flight such as wing and bone structure, flight efficiency and performance, complexity in wing kinematics-aerodynamics and so on. While these studies have provided tremendous insight into wing structure and articulation, study of maneuvering flight requires additional focus on supplementary elements in wing articulation and aerodynamic force generation during flight time. Thus, the inherent challenges in studying the intricate features and techniques of maneuvering bat flight predominantly includes capturing the flight kinematics and aerodynamics in detail and interconnecting them. The current study tackles the above mentioned challenge by using measured wing kinematic data via a 3D motion capture system as input boundary conditions to run detailed aerodynamic simulations. An elementary interest of this paper is to establish robust explanations and highlight certain techniques that bats use to perform a certain maneuver. It is done by comparing two similar maneuvering flights coming from two morphologically comparable but different species of bats and focusing on differentiating the traits that are general to bat flight and the ones that are specific to the individual bats.

Chapter 5 aims to investigate the complete motion dynamics encompassing both translation and rotation associated with maneuvering bat flights by considering the kinematic, aerodynamic and inertial consequences. Of primary interest is to identify the individual roles of inertial versus aerodynamic forces and moments in effecting bat flight trajectories. This is done by analyzing multiple bat flights featuring a straight-descending flight path, two ascending right turns or sweeping turns, and a 180° U-turn. The flights performed by two different but morphologically

similar bats coming from two different species, namely *H. armiger* and *H. pratti* provides effective ground for detailed comparisons on the individual effects of flight aerodynamics and wing inertia.

Chapter 6 provides the main concluding remarks of the research conducted in this thesis and indicates scope for future work. A detailed literature review is included in the introductions of each individual chapters (2 – 5) presented in already published (chapter 2 and 3) or awaiting publication (chapter 4 and 5) paper format.

Chapter 2: The Role of Vortex-Vortex Interactions in Thrust Production for a Plunging Flat plate

Aevelina Rahman
Danesh Tafti[1]
Department of Mechanical Engineering, Virginia Tech, Blacksburg, VA 24061.

ABSTRACT

Oscillating plunging motion is one of the fundamental motions which comprise the kinematics used by many flying and swimming organism for locomotion. It is characterized by the frequency and amplitude of oscillation. Past studies have investigated this motion for relatively small amplitudes. In this paper we investigate reduced frequencies $0.25 \leq k \leq 16$ and plunge amplitudes $0.03125 \leq h \leq 8$ to give plunge velocities ranging from $0.25 \leq kh \leq 4$ at Re=100. It is found that unlike previous investigations for small plunge amplitudes, thrust does not increase monotonically with *kh* but reaches a maximum and then decreases reverting back to drag for high *h* values. It is shown that Leading Edge Vortices (LEVs) are responsible for the production of thrust whereas Trailing Edge Vortices (TEVs) induce drag on the plate. In the regime of increasing thrust with *kh*, the LEVs and TEVs are not strong enough to influence each other's trajectory and vortex-vortex interactions are minimal. As *kh* increases to higher values, LEVs and TEVs gain in size and strength such that vortex induced velocities dominate the flow resulting in strong vortex-vortex interactions. Three main mechanisms of vortex-vortex interactions are identified, which either result in LEVs induced away from the plate or TEVs being induced near the plate. The net effect of these interactions result in reducing the residence time of the LEVs near the plate and decreasing thrust production. Finally, a detailed analysis of the wake is provided for the plunging plate. The

[1] Corresponding author: 213E Goodwin Hall, 635 Prices Fork Road, Blacksburg, VA 24061; Tel: +1 (540) 231-9975; email: dtafti@exchange.vt.edu

inter-vortex distance in the wake is found to correlate directly with plunge amplitude and inversely with frequency. On the other hand, vortex strength is found to be a strong function of reduced frequency *(k)* where the functional relationship is near linear for different plunge velocities *(kh)*.

Keywords: Plunging flat plate, low Reynolds number, thrust coefficient, vortex dynamics

Declarations of interest: none

1. INTRODUCTION

Oscillating or plunging bodies have been extensively studied in the literature in relation to low Reynolds number (*Re*) flapping flight. Low *Re* gives rise to unfavorable aerodynamic conditions for conventional fixed wing flight [1]. The coefficient of lift is significantly reduced with an increase in drag resulting in lower load carrying capacity and higher power input. However, numerous flyers in nature like small birds and insects overcome the deteriorating aerodynamic performance under steady flow conditions at low Re and retain efficient performance and maneuverability by employing unsteady mechanisms via flapping their wings [1,2].Thus, studying the aerodynamic features of biological flyers has been a useful guide for low *Re* flight research. For biological flyers, the flapping frequency ranges from 10 to 600 Hz, and the wing length varies from 0.3 to 600 mm yielding a Reynolds number in the order of 10^1 to10^4 [3]. Most biological propulsors (birds, bats, insects, fishes etc.) use the flapping motion to generate both thrust and lift. The complex phenomena of animal propulsion can be significantly depicted by oscillatory motion of a thin plate or an airfoil like appendage. Thus study of plunging or oscillatory motion has been done to understand the unsteady aerodynamic forces associated with flapping motion.

Theoretical analyses and experimental studies show that oscillating airfoils generate thrust at certain combinations of oscillation frequency and amplitude. Thrust producing capabilities of an oscillating airfoil was first described in the literature in the early twentieth century. Knoller [4] and Betz [5] independently stated that an effective angle of attack is produced by the plunging motion which results in a component of the normal force in the forward direction. The first experimental observation of this effect was done by Katzmayr [6]. Theoretical explanations and simple calculations for Katzmayr's results was provided by Ober [7]. Later, Garrick [8] provided theoretical formulas for the propelling (thrust) or drag force experienced by a plunging and pitching airfoil in an ideal fluid.

In an effort to shed light on the unsteady flow phenomena, researchers have extensively studied the wake structure of an oscillating foil, the dynamic stall phenomena associated with the motion, and the application of this motion in various forms of flow control and practical implementations. Katz and Weihs [9] exhibited the rollup of the wake of an oscillating airfoil in heaving motion. They examined the parameters influencing the rollup and the frequency ranges for which such instabilities occurred and identified reduced frequency (k, Eq. 1), to be an important parameter for thrust generation.

$$k = \frac{\pi f^* c^*}{U_\infty^*} \tag{1}$$

$$h = \frac{a^*}{c^*} \tag{2}$$

where,

$f^* =$ Frequency of oscillation (Hz)

$U_\infty^* =$ Free-stream velocity ($\frac{m}{s}$)

$a^* =$ Amplitude (Half-cycle) of oscillation (m)

$c^* =$ Chord length (m)

While pitching-plunging airfoils have been studied extensively in the literature [10–16] there are relatively fewer studies on pure plunging motion. Young and Lai. [17] numerically studied a plunging airfoil to show the effect of reduced frequency on thrust and propulsive parameters. They characterized the wake structures responsible for producing the aerodynamic forces from a plunging airfoil for a wide range of reduced frequencies. Heathcote et al. [18] presented experimental results showing an increasing trend for thrust coefficient while a decreasing one for propulsive efficiency with increasing reduced frequencies. Cleaver et al. [19] experimentally studied the effect of geometry on small amplitude plunging motion and showed that as oscillation frequency increased, drag decreased due to the leading-edge vortices shedding and convecting over the suction surface of the airfoil [20]. Freymuth [21], Lai and Platzer [22] and Jones et al. [23] have shown that the wakes of plunging airfoils can be characterized as drag-producing, neutral, or thrust-producing depending on plunge frequency and amplitude. Gopalkrishnan and Tafti [24] used the same computational software as the current study to investigate the effect of varying reduced frequencies on thrust coefficient and propulsive efficiency at Re=20,000. Visbal [25] investigated the unsteady flow field encountered by an airfoil plunging with prescribed angle of attacks at a relatively broad Re range (10^3 to $6x10^4$). The numerical study of a heaving airfoil by Martín-Alcántara et al. [26] showed that the maximum thrust efficiency is reached for an optimum combination of plunge frequency and amplitude.

A key factor is that in almost all previous research the plunge amplitude (h, Eq. 2) was in a significantly smaller working range which is applicable for insect like flyers but fails to cover bird, bat, or fish like propulsors. Previous studies on pure plunge motion are tabulated categorically in

Table 1. Studies containing a plunge velocity and amplitude value comparable to the current study are highlighted in bold. As evident from Table 1, the literature is not very abundant on the effect of pure plunge motion of a flat plate at a very low Reynolds number (less than 10^3).

Table 1: Chronological summary of previous studies with pure plunging motion

Author, Year	**Paper title**	**Study type**	**Geometry**	Re	k	h	kh
Katz, J. & Weihs, D.[9], (1978)	Behavior of vortex wakes from oscillating airfoils.	Comp.	Thin airfoil	inviscid	8.52, 2.15, 0.65	0.019, 0.076, **0.259**	0.162, 0.163, 0.168
Freymuth, P.[21], 1988	Propulsive Vortical Signature of Plunging and Pitching Airfoils.	Exp.	NACA 0015	5200	2.7	0.2	**0.54**
Jones, K. D., Dohring, C. M. & Platzer, M. F.[23], (1998)	Experimental and Computational Investigation of the Knoller-Betz Effect	Exp. + Comp.	NACA 0012	50000	1.5 - 13.05	0.04 - 0.12	**0.3-1.188**
Tuncer, I., Lai, J. & Platzer, M.[11], (1998)	A computational study of flow entrainment over a stationary/flapping airfoil combination in tandem.	Comp.	NACA 0012 Tandem combination	30000	0.375 - 5	0.01-0.03	0.004-0.15
Lai, J. C. S. & Platzer, M. F.[22], (1999)	Jet Characteristics of a plunging airfoil	Exp.	NACA 0012	21000	2.97-130	0.0125 -**0.6**	0.09-**4.65**
Lai, J. C. S. & Platzer, M. F.[27] (2001)	Characteristics of a Plunging Airfoil at Zero Freestream Velocity	Exp.	NACA 0012	No Free-stream	0-15.25	0.025 - 0.25	0-0.785
Lai, J. C. S., Yue, J. &	Control of backward-facing step flow using a flapping foil	Exp.	NACA 0012	12700	0.491 - 1.964	0.04 - **0.494**	0.039-**0.97**

Platzer, M. F.[10], (2002)			Backward facing step				
Lewin, G. C. & Haj-Hariri, H. [28], (2003)	Modelling thrust generation of a two-dimensional heaving airfoil in a viscous flow	Comp.	Airfoil	500	1 - 5	0.08 – **0.75**	0.4 – 0.75
Young, J. & S. Lai, J. C.[17], (2004)	Oscillation Frequency and Amplitude Effects on the Wake of a Plunging Airfoil.	Comp.	NACA 0012	20000	2 - 8	0.0063 -0.075	0.05-0.3
Heathcote, S., Wang, Z. & Gursul, I.[18], (2008)	Effect of spanwise flexibility on flapping wing propulsion.	Exp.	NACA 0012	10000, 20000, 30000	0 - 7	0.175	0-**1.225**
Visbal, M. R.[25], (2009)	High-fidelity simulation of transitional flows past a plunging airfoil.	Comp.	SD7003 airfoil	1000-60000	3.93 10 10	0.05 0.005 0.04	0.197 0.05 **0.4**
Cleaver, D. J., Wang, Z., Gursul, I. & Visbal, M. R.[20], (2011)	Lift enhancement by means of small-amplitude airfoil oscillations at low Reynolds numbers.	Exp.	NACA 0012	10000	0 - 9.42	0.025-0.2	0-**1.884**
Cleaver, D. J., Wang, Z. & Gursul, I.[19], (2013)	Investigation of High-Lift Mechanisms for a Flat-Plate Airfoil Undergoing Small-Amplitude Plunging Oscillations.	Exp.	**Flat plate**, NACA 0012	10000	0 - 9.42	0.025-0.2	0-**1.884**
Martin-Alcantara, A., Fernandez-Feria, R. & Sanmiguel-Rojas, E.[26], (2015)	Vortex flow structures and interactions for the optimum thrust efficiency of a heaving airfoil at different mean angles of attack.	Comp.	elliptic airfoil	500	1.26-6.28	0.133-**0.6**	0.168-**0.691**

Pure plunge motion is a fundamental component of the complex flapping phenomena observed in efficient biological flyers. Applying the motion on a flat plate is beneficial in understanding the fundamental effects and explaining the basic phenomena regarding the motion itself. Additionally, as summarized in Table 1, in past investigations of plunging motion only a limited range of plunge velocities and plunge amplitudes have been investigated in the literature. Accordingly, Lewin et al. [28] explained the vortex dynamics at various combinations of frequency and amplitude for a plunging airfoil at Re = 500. Although they mention the efficiency being optimum for specific frequency, they did not relate the vortex dynamics with thrust generation. Moreover, their study too was only valid for a narrow frequency and amplitude range and identified k to be the primary factor governing the vortex topology with kh being the secondary factor. On the other hand, Lai and Platzer [22] found kh to be the defining parameter in thrust generation for a similar frequency range but a broader amplitude range than Lewin et al. Thus, to have a comprehensive and robust understanding of the factors governing thrust generation from a plunging body, the current study concentrates on the plunging motion of a flat plate at a low Reynolds number (Re = 100). The study covers a broader range of reduced frequencies $0.25 \leq k \leq 16$ and plunge amplitudes $0.03125 \leq h \leq 8$ to give plunge velocities ranging from $0.25 \leq kh \leq 4$. The study investigates thrust generation and its dependence on reduced frequency (k) and plunge amplitude (h). We characterize the dynamics of plunge induced vorticity at the plate by identifying three major mechanisms of vortex-vortex interactions. Finally, a detailed analysis of the wake is provided for the plunging plate where wake characteristics defined by inter-vortex distance and vortex strength is parameterized with different plunge attributes.

2. GOVERNING EQUATIONS AND METHODOLOGY

Space, mass and momentum conservation laws together make up the governing equations for an unsteady incompressible viscous flow in a moving grid coordinate system. The governing equations are solved in a two-dimensional framework with the assumption of constant properties. Non-dimensionalization is done using a suitable reference length scale and velocity scale. The conservative non-dimensional form of the governing equations are written as follows:

Space Conservation Law (SCL):

$$\frac{\partial}{\partial t}(\forall) - \frac{\partial}{\partial x_j}\left(\forall u_j^g\right) = 0 \tag{3}$$

Mass Conservation Law:

$$\frac{\partial}{\partial x_j}\left(\forall u_j\right) = 0 \tag{4}$$

Momentum Conservation Law:

$$\frac{\partial}{\partial t}(u_i) + \frac{\partial}{\partial x_j}\left(\left[u_j - u_j^g\right]u_i\right) = -\frac{\partial}{\partial x_i}(p) + \frac{\partial}{\partial x_j}\left(\left(\frac{1}{Re}\right)\frac{\partial u_i}{\partial x_j}\right) \tag{5}$$

where,

$\forall$ = cell volume

u_i = Cartesian velocity vector

u_j^g = Grid Cartesian velocity and

p = Pressure.

For non-dimensionalization the reference length and velocity scale are taken to be the chord length (c^*) and inflow velocity (U_∞^*) respectively. Time is non-dimensionalized by $\frac{c^*}{U_\infty^*}$ and forces

by $\rho^* U^{*2}_{\infty} c^*$. In this paper, the entries with asterisks (*) depict dimensional values. The Reynolds number is given by $Re = \frac{U^*_{\infty} c^*}{\nu^*}$,

where,

$U^*_{\infty} =$ Inflow velocity in $\mathrm{m/s}$

c^* = Chord length in m = Chord area for 2D

$\rho^* =$ Fluid density in $\mathrm{kg/m^3}$

$\nu^* =$ Kinematic viscosity in $\mathrm{m^2/s}$

For this study, *Re* = 100.

An in-house body-fitted multi-block incompressible Navier-Stokes Arbitrary Lagrangian Eulerian (ALE) solver, GenIDLEST [29,30] is used for the solution of Eqns. (3 - 5). The grid movement is decoupled from the implementation of fluid conservation laws in the solution algorithm. At the start of a time step the nodes on the boundaries that are to move get displaced according to the prescribed motion and the velocity boundary conditions are formulated based on that displacement. This is followed by a rezoning phase during which the movement of the boundary is transmitted to the interior of the domain to obtain the volume grid motion. The boundary motion is first transmitted to the block corners by a series of springs attached to block boundary edges. The corner displacement of each block is then used to get the new nodal distribution in each block edge, face, and volumes, respectively, by using a modified transfinite interpolation (TFI) procedure. The SCL condition (Eqn. 3) is satisfied to get the new grid metrics and the flux due to grid movement. The mass and momentum conservation laws given by (Eq. 4-5) are advanced in time by using a fractional-step method to complete the time step.

To discretize the governing equations (Eqns. 3-5) a conservative finite-volume discretization is used on a non-staggered orthogonal grid. Both the convection and diffusion terms in the

momentum equation are discretized using a second-order central difference scheme. Velocities and pressure are calculated and stored at the computational cell center with fluxes stored at the cell faces. Two steps are used to carry out the time integration, a predictor step and a corrector step. In the predictor step an intermediate velocity field is calculated while in the corrector step the intermediate velocity field is updated by solving a pressure equation and satisfying discrete continuity to obtain the velocity at the new time step. The corrector step is advanced in time by using an implicit Crank-Nicolson scheme for the diffusion terms and an explicit second-order Adams-Bashforth scheme for the convection terms. A pre-conditioned BiCGSTAB method is used to solve for the resulting linear systems for momentum and pressure. Convergence is achieved when the L_1 residual norms are less than 1×10^{-7}.

3. COMPUTATIONAL GEOMETRY AND PARAMETRIC RANGE

The two dimensional (2D) computational domain extends up to 30 chord lengths upstream and 130 chord lengths downstream of the flat plate of unit chord length. Both the top and bottom boundaries are located at 30 chord lengths distance from the flat plate. In effect, the domain is 160 times larger than the flat plate length in the stream wise direction and 60 times larger in the normal direction to ascertain that the boundaries do not have any effect on the flow generated by the plunging plate. The plunging plate is initially located at $y = 0$ between $x = 0$ and 1. In theory, the plate has zero thickness as the boundary conditions are directly applied to the plate location of $y = 0$. A total of 2,173,600 computational cells are used to discretize the domain. Figure 1 shows the variation of the grid spacing with relative position in the domain. The grid has uniform spacing in the stream wise direction from 2 plate lengths upstream to 5 plate lengths downstream. In the normal direction the uniformly spaced region starts from 1.8 plate lengths below the initial position

of the plate and extends up to 1.8 plate lengths above the plate. Also, the grid is finest in the region surrounding the plate to accurately resolve the vortices created by the plunging motion. Beyond this uniformly spaced region, the grid is coarsened gradually to balance computational cost. This fine region oscillates with the plate as a moving grid method is implemented ensuring that the vortices created in the vicinity of the plate are resolved with high precision. In the fine grid region near the plate, the grid spacing is such that there are approximately 150 cells in one boundary layer thickness approximated by the Blasius solution at $x = 0.5$.

Figure 2 shows the z-vorticity (ω) of a flow field containing some of the most energetic vortex structures ($k = 12;\ kh = 4$). As shown in Figure 2, the vortex structures are contained well within the domain and resides significantly far away from all the four boundaries. This ascertains that the boundary conditions do not influence the evolution of these vortex structures near the plate. Also, when zoomed in very close to the plate (2^{nd} inset of Figure 2), sufficient number of grid cells are present in each vortex core.

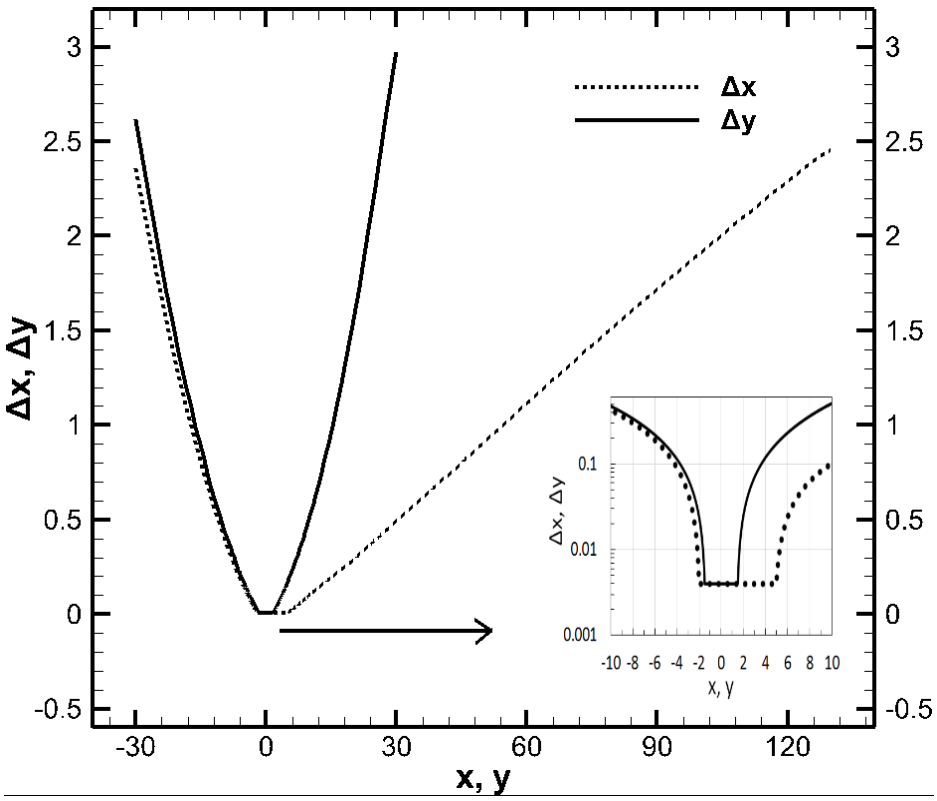

Figure 1: Grid spacing in both stream wise (x) and normal (y) direction. Inset shows uniform grid spacing along the plate in both stream wise and normal direction.

The upstream boundary of the domain ($x = -30$) is set at a unit non-dimensional inlet velocity. Outflow zero gradient conditions ($\frac{d\phi}{dx} = 0;\ \phi = u, v, P$) are applied at the downstream boundary ($x = 130$). Boundary conditions ($\frac{d\phi}{dy} = 0, \phi = u, p\ \&\ v = 0$) are applied at the top and bottom y-directional boundaries of the domain ($y = \pm 30$). The oscillating flat plate is treated as a no-slip, no-penetration wall ($\vec{u} = \vec{u}_{plate}; \frac{dp}{dy} = 0$) where $\vec{u}_{plate}$ is the velocity of the plate defined by the first derivation of Eq. 6 (mentioned after Figure 2).

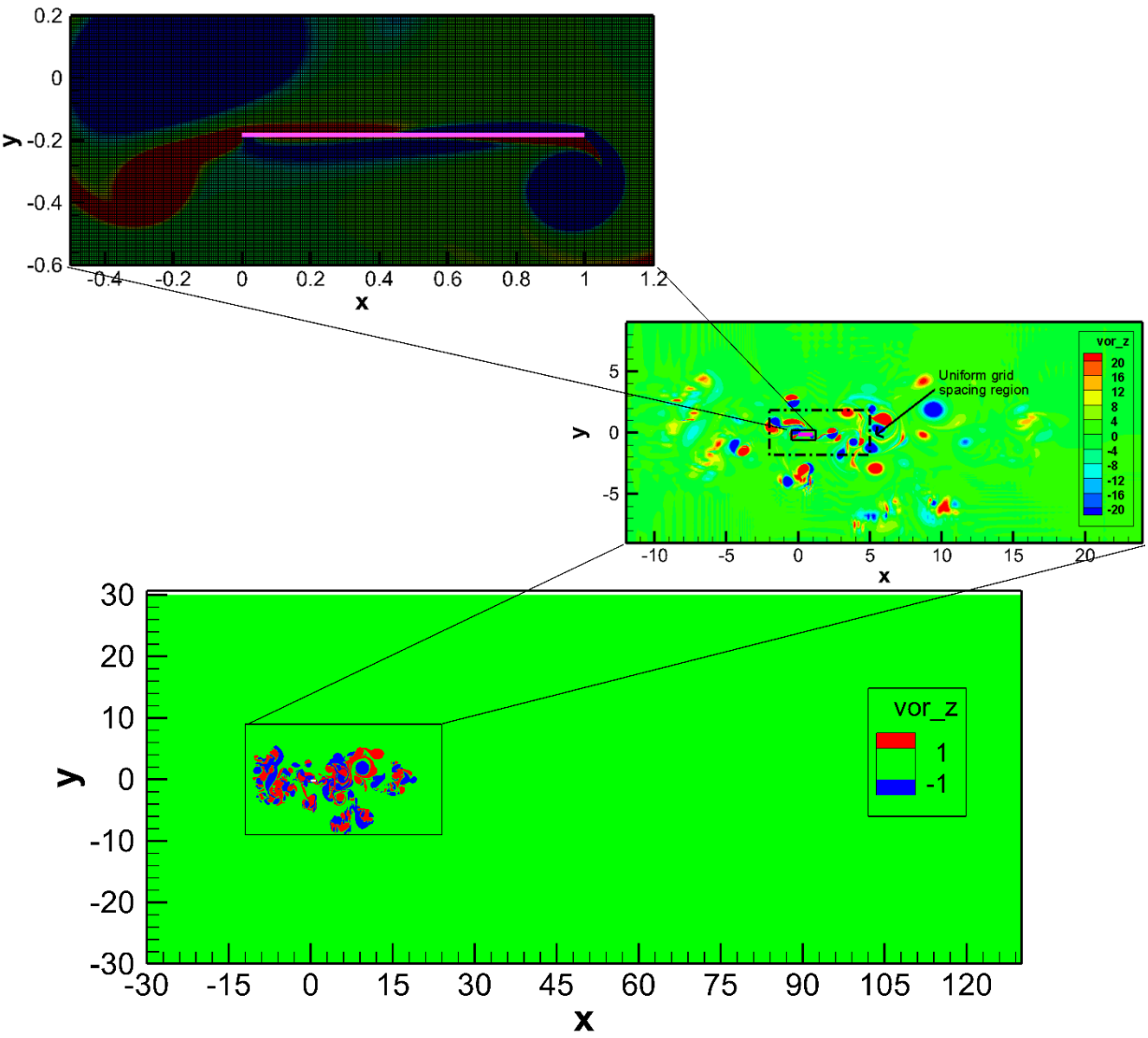

Figure 2: Instantaneous vorticity field (z-vorticity (ω)) at kh = 4. Insets show the extent of the vortices generated by the plate relative to the size of the domain and to the size of the grid spacing

.

The flat plate oscillates in a pure plunge motion which is governed by a sinusoidal equation (Eq. 6). Initially the plate is located at y = 0 and the plunging motion starts with the plate moving upwards.

$$Y^* = Y_0^* + a^* \sin(2\pi f^* t^*) \quad (6)$$

where,

Y^* = position of the plate at any time t (m)

Y_0^* = Initial position of the plate = 0 (m)

a^* = Plunge amplitude (m)

f^* = Plunge frequency (Hz)

t^* = time (s)

The full extent of the grid line ($-30 \leq x \leq 130$) (versus only$0 \leq x \leq 1$) is being oscillated with the plate in order to maintain orthogonality of the grid throughout the plunge cycle.

Table 2: Summary of calculations and time-averaging

k	***h***	**Cycles considered in time avaraging**
0.25	1.0, 2.0, 4.0, 8.0	9 - 16
0.5	0.5, 1.0, 2.0, 4.0	9 - 16
1	0.25, 0.5, 1.0, 2.0, 4.0	9 - 16
2	0.125, 0.25, 0.5, 1.0, 2.0	9 – 16
4	0.0625, 0.125,0.25,0.5,1.0	9 – 16
8	0.0625, 0.125,0.25,0.5	9 – 16
10	0.05, 0.1,0.2,0.4	11 - 20
12	0.04167, 0.083,0.167,0.333	13 - 24
16	0.03125, 0.0625,0.125,0.25	17 - 32

Table 2 summarizes the different combinations of reduced frequency, k (Eqn. 1) and different plunge amplitudes ($h=a/c$) (Eq. 2) simulated in the present study. The investigation is done for a wide range of reduced frequency ($0.25 \leq k \leq 16.0$) and plunge amplitude ($0.03125 \leq h \leq 8.0$). The flat plate oscillates with reduced frequencies of 0.25, 0.5. 1, 2, 4, 8, 10, 12 and 16 and amplitudes ranging from 8 to 0.03125 for all the frequencies, thus producing a working range of plunge

velocity between $0.25 \leq kh \leq 4$. The computational time of the numerical simulation increases as kh increases. However, the increase is more significant with increase in amplitude than with frequency increase. It ranges from 2 hours of wall-clock time per oscillation cycle for $kh = 1$ ($k = 16$, $h = 0.0625$) to 52 hours for the most compute intensive case for $kh = 4$ ($k = 1$ and $h = 4$) on 20 Haswell 2xE5 2.5 GHz cores.

When traced back to dimensional values, the current study covers the frequency and amplitude range of a variety of biological flyers and propulsors. For example, a chord length of millimeter scale corresponds to a broad frequency range of 400 to 7000 Hz in air and 30 to 500 Hz in water capturing the insect flying frequency range [31] and beat frequency of micro-organisms like ascidian larvae [32], [33]. The velocity attributed to this regime is 100 cm/s in air and 10 cm/s in water which are analogous to the flying speed of Dragon-fly or Damsel-fly [34] and swimming speed of small crustaceans like copepod or shrimp [35]. As Figure 3 shows, centimeter range chord length-scales yield frequencies and velocities of birds in air and fishes like Lake Sturgeon [36] and Herring [35] in water.

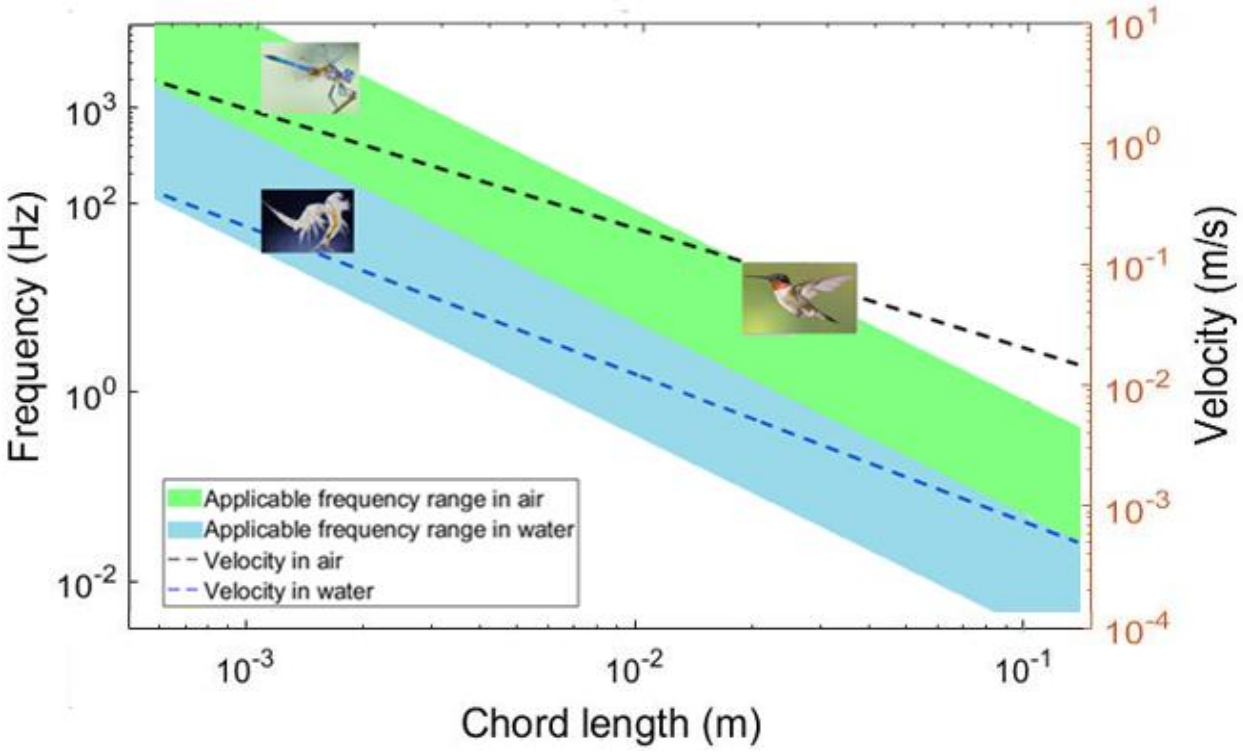

Figure 3: Range of applicability of present study; shaded area encompasses frequency range while dashed lines depict velocity range in air and water for chosen characteristic length (=chord = plate length); different animal pictures depict the characteristic lengths, velocities, and frequencies of respective animals.

The majority of previous studies have worked with small non-dimensional amplitudes ranging from 0.005 to 0.6 which is representative of insect flight. But if bird or bat flight is to be mimicked, the functional non-dimensional amplitude is generally greater than one. It is safe to say that the larger the wingbeat frequency, the smaller the amplitude is for a biological flyer. Hence, a wide plunge amplitude (h) range, covering the flight range from insects to birds and swimming range of marine microorganisms to regular fish was studied. The shaded area of Figure 3 encompasses the applicable range of the current study.

Of primary interest in this study is the mean thrust coefficient defined as:

$$C_T = \frac{\bar{T}}{\frac{1}{2}\rho U_\infty^2 c} \tag{7}$$

where, $\bar{T}$ is the time-averaged thrust force. The time-averaged thrust coefficient is calculated over multiple cycles once the flow oscillations have reached a stationary state. Typically, time-averaging is performed over 8 cycles, but for highly energetic flows at high frequency and/or high amplitude oscillations, the time-averaging is performed over more plunge cycles as shown in Table 2.

4. RESULTS AND DISCUSSION

4.1 Grid Independency Study

Because of the strong non-linearity in the flow resulting from vortex-vortex interactions as *kh* increases, an extensive grid independency study has been conducted. Six grid levels were tested to establish grid independency. Table 3 shows the details of the six grids. Along with varying the number of grid points, different grid distribution strategies were also investigated.

Table 3: Details of grid independency tests

	Grid 1	**Grid 2**	**Grid 3**	**Grid 4**	**Grid 5**	**Grid 6**
Number of grid Points along the plate length	100	132	200	250	250	300
Total number of cells (millions)	0.14	0.25	0.56	1.77	2.18	2.97
Remark **UGS** = Uniform Grid Spacing	UGS $0<x<1$	UGS $0<x<1$	UGS $0<x<1$	UGS $2<x<5$	UGS $2<x<5$ $-1.8<y<1.8$	UGS $2<x<5$ $-1.8<y<1.8$
Remark **GGC** = Gradual Grid Coarsening	GGC starting from the	GGC starting from the	GGC starting from the	GGC starting from the	No GGC in the vicinity of the plate	No GGC in the vicinity of the plate

	plate in y direction	plate in y direction	plate in y direction	plate in y direction

To test the grid independency, some representative cases from the three largest plunge velocity (kh = 1, 2 and 4) were simulated using all six grids. These choices were motivated by cases which exhibited regular (kh = 1) as well as large chaotic fluctuations in the instantaneous thrust coefficient (kh = 2 & 4). The time averaged (averaging period mentioned in Table 2) value of thrust coefficient is shown in Table 4 for the three representative cases. They show good comparison among the three finer grids considering the fact that there are large positive and negative fluctuations in instantaneous C_T and the mean value is much smaller than the amplitude of these fluctuations as seen in the representative case of k = 8, h = 0.125 in Figure 4.

Table 4: Comparison of results among six different grid resolutions.

			Grid-1	**Grid-2**	**Grid-3**	**Grid-4**	**Grid-5**	**Grid-6**
	k	h	C_T	C_T	C_T	C_T	C_T	C_T
***kh* = 1**	8	0.125	0.711	0.710	0.693	0.693	0.683	0.680
***kh* = 2**	12	0.167	1.46	0.837	0.776	0.659	0.517	0.515
***kh* = 4**	16	0.25	0.711	0.629	0.570	0.317	0.243	0.240

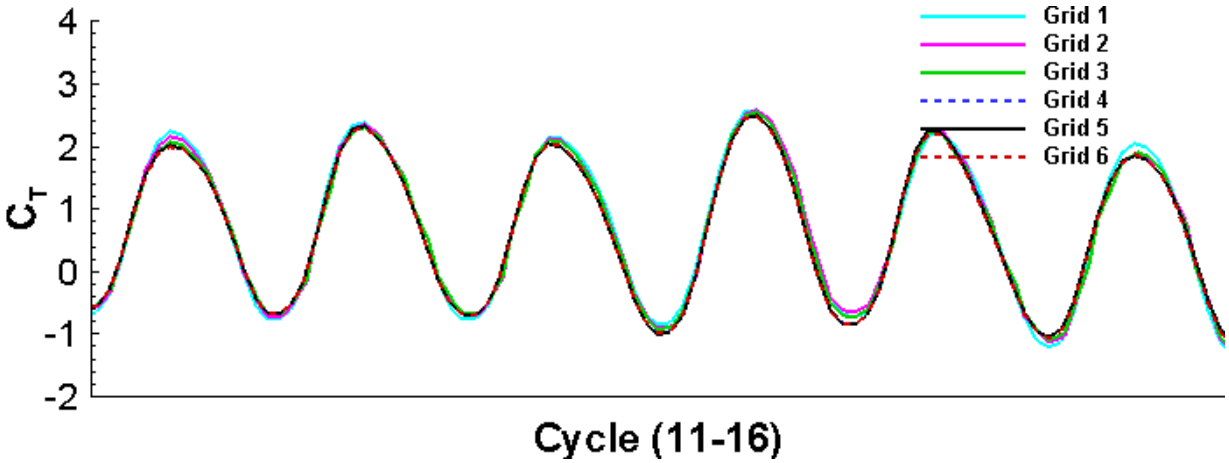

Figure 4: Instantaneous thrust coefficient (C_T) for k = 8, h = 0.125 with good comparison among the three finer grids (grid 4, 5 and 6); the mean C_T value is much smaller than the amplitude of positive and negative fluctuations.

As evident from Table 4, the percentage difference of mean thrust coefficient calculated on Grid-5 in comparison with the finest grid (Grid-6) is within 1.5% for most cases. Since computational cost increases as the square of the total number of grid cells, Grid-5 is chosen as the base grid on which all results are presented.

4.2 Validation with Literature

As the current study is in the low Reynolds number regime, no previous experimental or numerical study was found to exactly match the conditions in this investigation. Moreover, to include the flying range of both insect and birds, the focus of this work was at higher plunge amplitudes whereas the majority of previous works were in the lower range. Thus the current work is validated in Figure 5 against a viscous calculation ($Re = 2x10^4$) [17] and two sets of experimental measurements ($Re = 10^4$) [18,37].

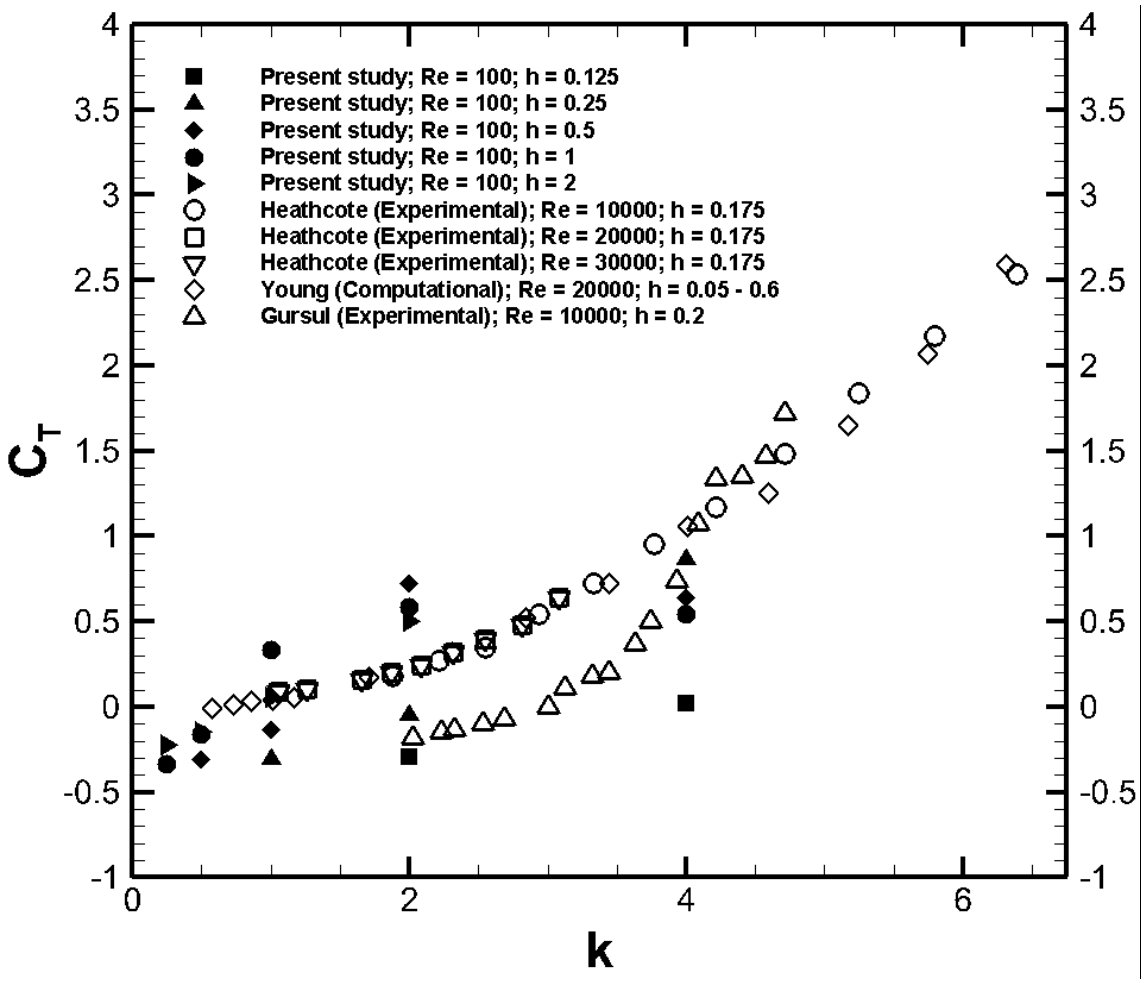

Figure 5: Comparison of thrust coefficient from present study with past studies in the literature

The present study mostly follows the trend of increasing thrust coefficient with increasing reduced frequency as observed in the literature. This work shows reasonable comparison with Gursul et al. [37] where the plunge amplitude is comparable. The discrepancy at smaller reduced frequency can be attributed to the large difference in *Re*, the effect of which is more visible when the oscillating flow is less energetic and the plunge induced velocities are comparatively smaller as is the case with smaller reduced frequencies. A higher amplitude case ($h=2$) of the current study shows better comparisons with Young et al. [17] as the reduced frequency approaches similar values. Considering the fact that the present study was conducted at a very low Reynolds number

compared to previous studies, Figure 5 shows reasonable agreement. Moreover, the studies of Young, Heathcote, and Gursul were all conducted on a NACA 0012 airfoil, whereas the current study is based on a flat plate geometry. The difference in the oscillating surface topology will also influence the thrust coefficient values.

4.3 Variation of Mean Thrust Coefficient

The primary objective of this study is to relate the thrust coefficient to plunge frequency and amplitude. Lai and Platzer [22] found that thrust coefficient increases with increasing plunge velocity (kh). Whereas Lewin et al. [28] identified reduced frequency (k) to be the primary factor in governing the vortex topology and hence efficiency with kh being the secondary factor. But their work concentrated on a relatively narrow band of small amplitudes (h ranging from 0.0125 to 0.75). The current study however works with a larger range of amplitudes (h ranging from 0.03125 to 8) and reveals that the thrust coefficient does not increase monotonically with increasing k, h or kh. Rather it exhibits an increasing trend for increasing k, h or kh until some optimum k and h combination and then exhibits a gradual decreasing trend at high k, h or kh. The behavioral trend of thrust coefficient with increasing k and h is shown in Figure 6 in which the thrust coefficient is plotted against plunge velocity (kh) for constant k (6-a) and versus k for constant kh (6-b). As can be seen from Figure 6-a, for all the frequencies (k) tested, C_T increases until a certain h or kh value and then decreases. Irrespective of the plunge velocity (kh), low frequency oscillations at $k = 0.25$ fail to produce any thrust. Nominal thrust production occurs at $kh = 0.5$ when $k \geqslant 4$. It is only after $kh \geqslant 1$ that thrust production is prevalent; but as the amplitude gets larger the increasing trend in C_T is reversed that could revert back to drag production. For a given frequency (e.g. k = 1, 2, 4 etc.), the amplitude associated with kh = 1 almost always experiences the highest thrust coefficient. The variation of C_T with h (or kh) for a constant k and

with *k* (or *h*) for a constant *kh* is explained in detail in sections 4.4.1 and 4.4.2 with examples from *k* = 1, 2, 4 and 8.

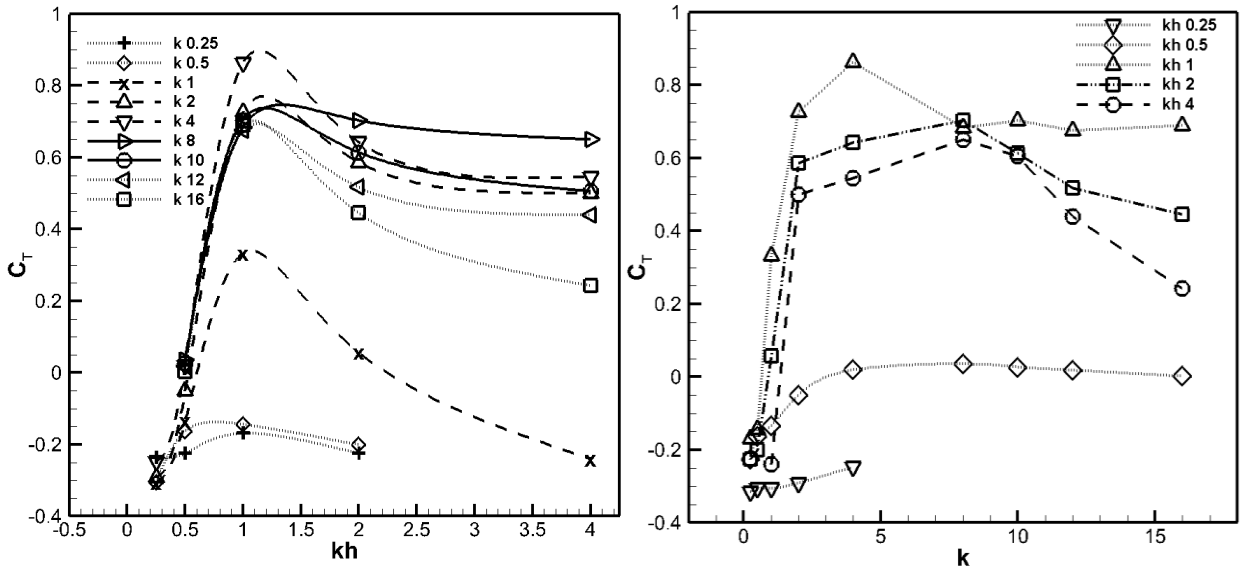

(a) **(b)**

Figure 6: Variation of mean thrust coefficient with (a) varying plunge velocities (*kh*) for constant reduced frequencies (*k*); (b) with varying reduced frequencies (*k*) for constant plunge velocities (*kh*).

It is clearly evident from Figure 6 that neither *kh* nor *k* is not the sole parameter influencing thrust production when working with a frequency and amplitude range as wide as in the current study. These trends in thrust coefficient can be directly related to the vorticity dynamics at the oscillating plate and is explained in detail in the following sections.

4.4 Vorticity Dynamics and Thrust Coefficient

The effect of reduced frequency (k) and plunge amplitude (h) on vortex structure is discussed first. An upward motion of the plate creates a counterclockwise vortex at the leading edge and a clockwise vortex at the trailing edge on the bottom side of the plate as shown in Figure 7. Likewise,

a downward motion creates a clockwise vortex at the leading edge and a counterclockwise vortex at the trailing edge on the top side of the plate. The extent to which these vortices are attached to the plate during the duration of the plunge cycle determines whether a net thrust or a net drag will result. Unlike the production of instantaneous lift which is dominated by pressure differences between the top and bottom sides, for the plate geometry thrust or drag is only dependent on shear forces acting on it. Thrust is obtained if the vortex induced velocities tend to push or pull the plate in a direction opposing the approach flow for a majority of time in the cycle. Whereas, drag results if the vortices force the plate in the same direction as the inflow. An example of LEV induced negative shear stress corresponding to thrust production as well as TEV induced positive shear stress corresponding to drag production is shown in Figure 7 on the bottom surface of the plate for a representative case of $k = 1$, $h = 0.5$. The LEV induces negative velocity near the plate surface whereas the TEV induces positive velocity. The quantitative velocity profiles depicted by the black lines in Figures 7 show negative and positive velocity profiles peaking up to 5 units in the vicinity of the leading and trailing edge. The resulting negative shear from the LEV acts to push the plate up stream. Thus, in general leading edge vortices (LEVs) contribute towards thrust while trailing edge vortices (TEVs) towards drag as surmised from Figure 7 where LEVs and TEVs are represented by z-vorticity (ω) contours.

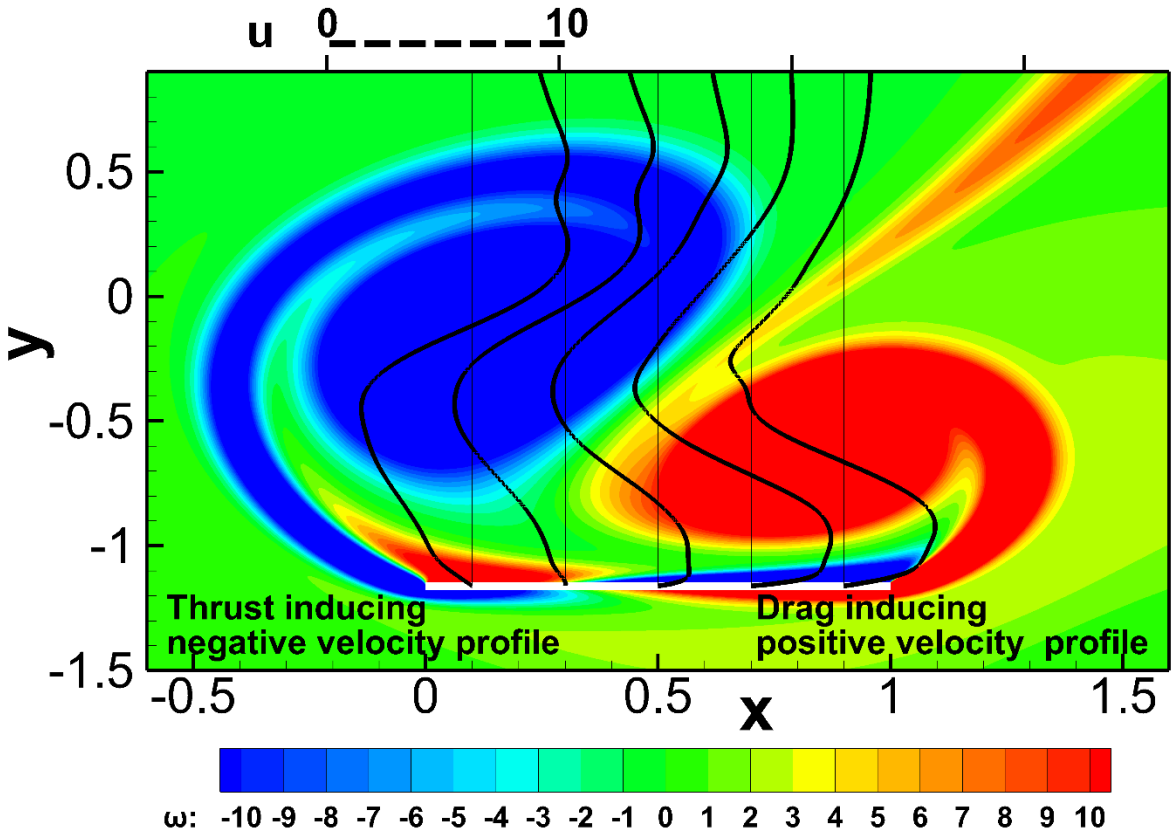

Figure 7: Instantaneous *u*-velocity profiles at different chord positions (x = 0.1, 0.3, 0.5, 0.7 and 0.9) in the presence of LEV and TEV shown in terms of z-vorticity (ω). LEVs induce negative velocity gradients (depicted by black lines) adjacent to the plate (e.g. at x = 0.1 and 0.3) to produce thrust while TEVs induce positive velocity gradients (depicted by black lines) adjacent to the plate (e.g. at x = 0.5, 0.7 and 0.9) to produce drag. The scale marked by the dashed black line above the contour denotes the u-velocity (u) scale used in the figure.

The production of drag or thrust also manifests in the wake characteristics. It was shown by Jones et al. [23] that the wake structures behind an airfoil plunging sinusoidally at relatively low plunge velocities (kh = 0.15) have clockwise rotating vortices in the upper row and counterclockwise rotating vortices in the lower row indicating a drag producing wake. On the other hand, they

showed that when the plunging airfoil is oscillated at a sufficiently high *kh* (= 0.6), the upper row of vortices are counterclockwise rotating while the lower row of vortices are clockwise rotating indicating a thrust producing wake. It is also evident from their work that if the counterclockwise and clockwise vortices are arranged alternatively in the same row, the resultant force would be neither drag nor thrust but neutral.

4.4.1 Comparison of Vorticity Dynamics at Constant *k*, Varying *h* and Its Relation to Thrust Production

The work of Lewin et al. [28] described the vortex dynamics at various combinations of frequency and amplitude for a plunging airfoil, but did not relate that with thrust generation. In an effort to do so, we first analyze a case of reduced frequency $k = 1$ for which four plunge amplitudes ($h = 0.25,\ 0.5, 1$ and 2) for $kh = 0.25, 0.5, 1,$ and 2 are investigated in Figure 8. By definition (Eq. 1) the reduced frequency is a measure of the ratio of the convective time scale of the approach flow to travel the length of the plate to the time taken for the plate to traverse half a cycle (π radians). It is noted that the physical significance of the reduced frequency diminishes as vortex induced velocities start influencing the convection of vortices over the plate which does happen as h increases or as the plunge velocity (kh) increases. For the two smaller amplitudes ($h = 0.25$ and 0.5) LEVs that form on the plate are convected downstream by the approach flow and shed as TEVs into the wake. This is evident in Figure 8-a and 8-b where h = 0.25 and h = 0.5, respectively. In both these cases, at the start of the down stroke a negative clockwise LEV starts forming on the top surface of the plate which grows during the downstroke and convects to the trailing edge at the end of the downstroke. On the upstroke the vortex convects further into the wake and finally sheds into the wake at the end of the upstroke. A similar cycle is evident for the LEV that starts forming at the bottom surface at the beginning of the upstroke which finally sheds

into the wake at the end of the downstroke. Although Figures 8-a and 8-b show both LEVs to be in close proximity to the plate as they convect downstream, at low amplitudes as in these cases, the LEVs do not build up enough strength to induce a negative flow in the boundary layer of the plate. That is why low amplitudes and low reduced frequencies usually result in net drag. Thus at all instances during the cycle, the flow on the plate is drag inducing as denoted by the "D" in Figure 8-a and 8-b. Comparing the vortex structures between $h = 0.25$ and $h = 0.5$, the LEVs associated with $h = 0.5$ are stronger compared to the ones for $h = 0.25$. This is reflected in the lower drag value for h = 0.5 as the stronger LEVs, although not strong enough to induce a net thrust, decrease the contribution towards drag. The regular shedding of two vortices per plunge cycle is captured in the drag producing [23] von Karman wake characteristics with alternating positive or counterclockwise vortices in the lower row and negative clockwise vortices in the upper row in Figure 9-a. Counterclockwise and clockwise vortices arranged alternatively almost in the same row in Figure 9-b indicates small magnitude of drag.

Figure 8-c shows the time evolution of vortices at a higher plunge amplitude of $h = 1$. While the size of the vortices increase, the basic shedding cycle observed for $h = 0.5$ still persists. However, asymmetries between the upstroke and down stroke begin to appear in the force profile during which the latter half of the down stroke and first half of the upstroke generate thrust. During this time it can be observed that the LEV formed on the top surface dominates the flow near the plate and induces negative velocities at the plate to generate thrust. In contrast the LEV that forms on the bottom surface during the upstroke is much smaller in size while the TEV is larger and in closer proximity to the plate than during the thrust producing interval, which together result in drag. Accordingly, we get a wake structure consisting of counter clockwise vortices in the upper row

and clockwise vortices in the lower row (Figure 9-c). This structure results in a momentum surfeit and is a thrust producing wake[23].

As the plunge amplitude increases further to $h = 2$, the vortex interactions get more complex. Whereas in the low amplitude cases, only LEVs form and convect along the plate, at higher amplitudes both LEVs and TEVs form during the down stroke and upstroke. Not only do the vortices increase in size, but their induced velocities become larger than the approach velocity. Thus a pair of vortices (LEV+TEV) are shed upstream of the plate at the end of the down stroke and another pair is shed at the end of the upstroke into the wake. The vortices shed upstream are eventually redirected downstream by the main flow. This phenomenon can be inferred in the first snapshot and the second-to-last and last snapshot in the series (Figure 8-d). As a consequence of the strong vortex-vortex interactions, the transient thrust coefficient enters a chaotic regime. The generation of TEVs negates any thrust production tendency of LEVs and it is found that the mean thrust coefficient regresses back to drag at this stage. Due to the highly nonlinear vortex dynamics, the wake is also irregular and cannot easily be characterized as either drag or thrust producing. In Figure 9-d, a weak trend of clockwise vortices in the upper row and counter clockwise vortices in the lower row are visible, thus indicating a net drag of small magnitude.

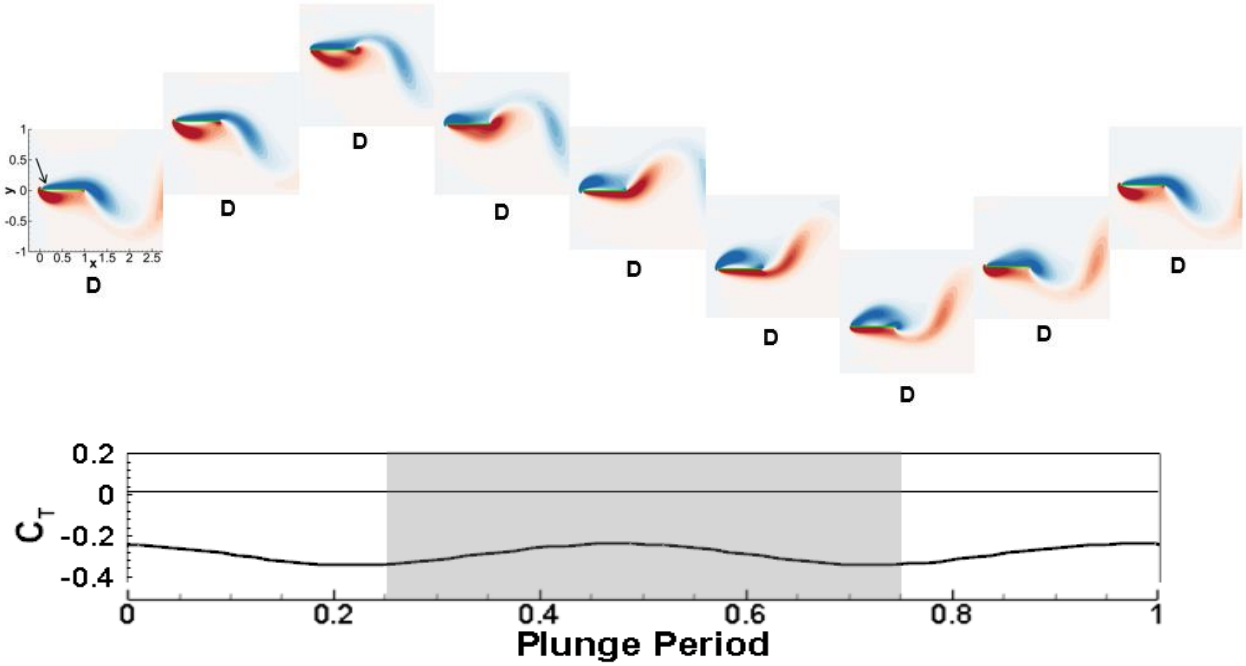

(8-a) $k = 1,\ hk = 25;\ kh = 0.25$

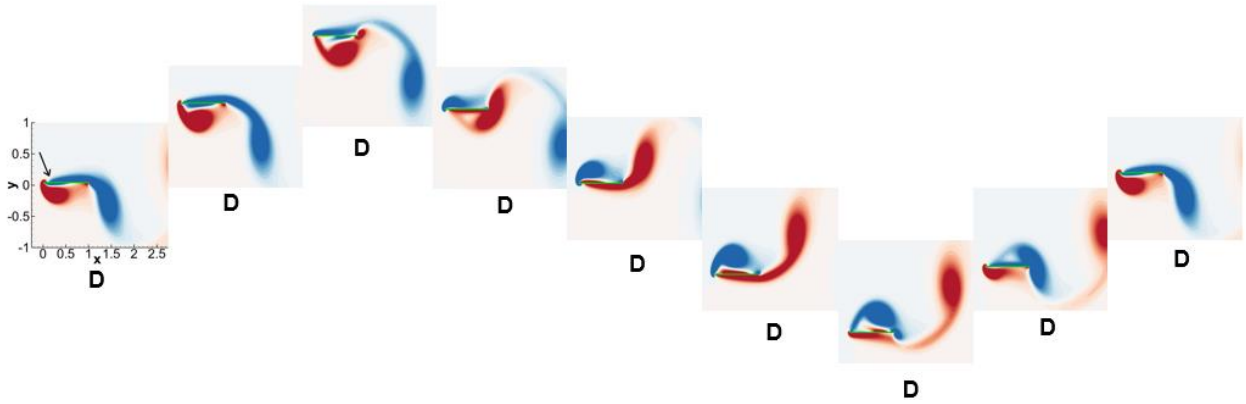

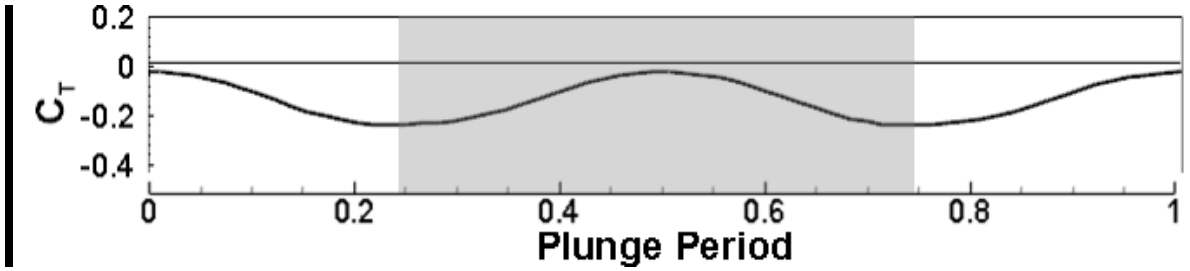

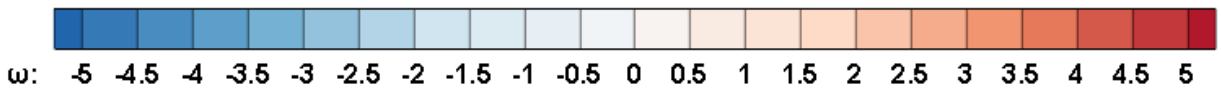

(8-b) $k = 1,\ hk = 5;\ kh = 0.5$

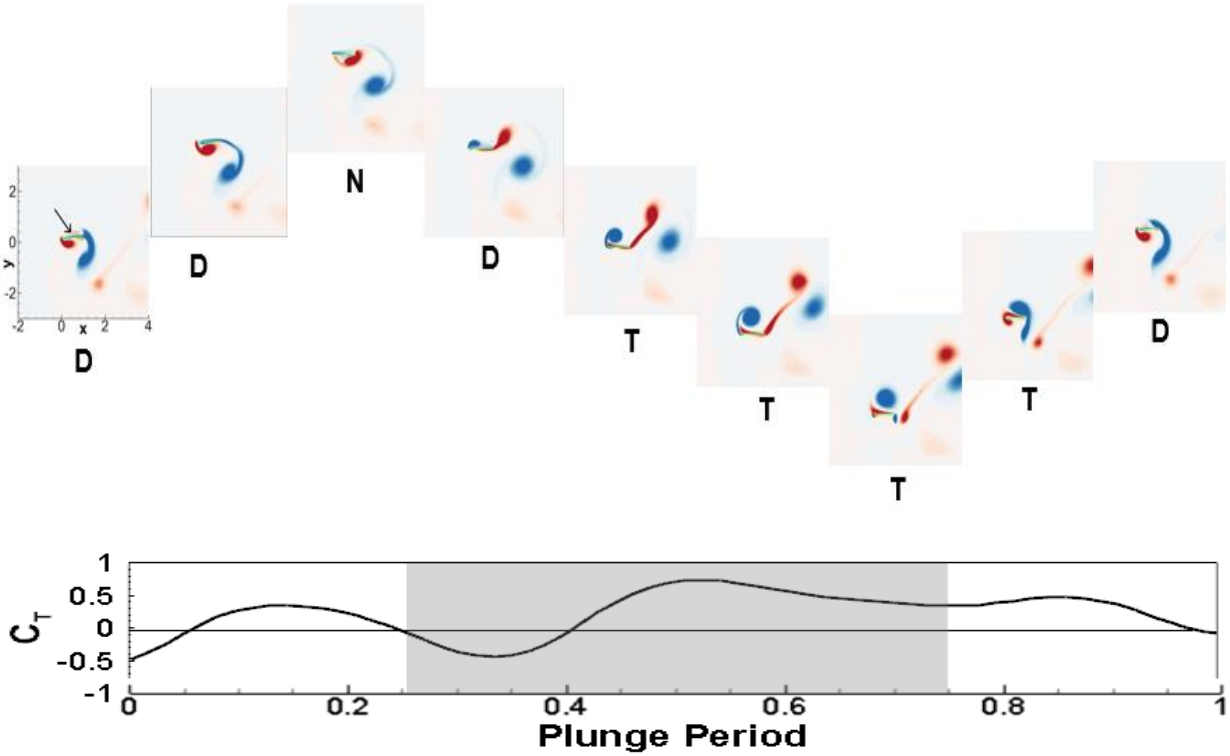

(8-c) $k = 1,\ hk = kh = 1$

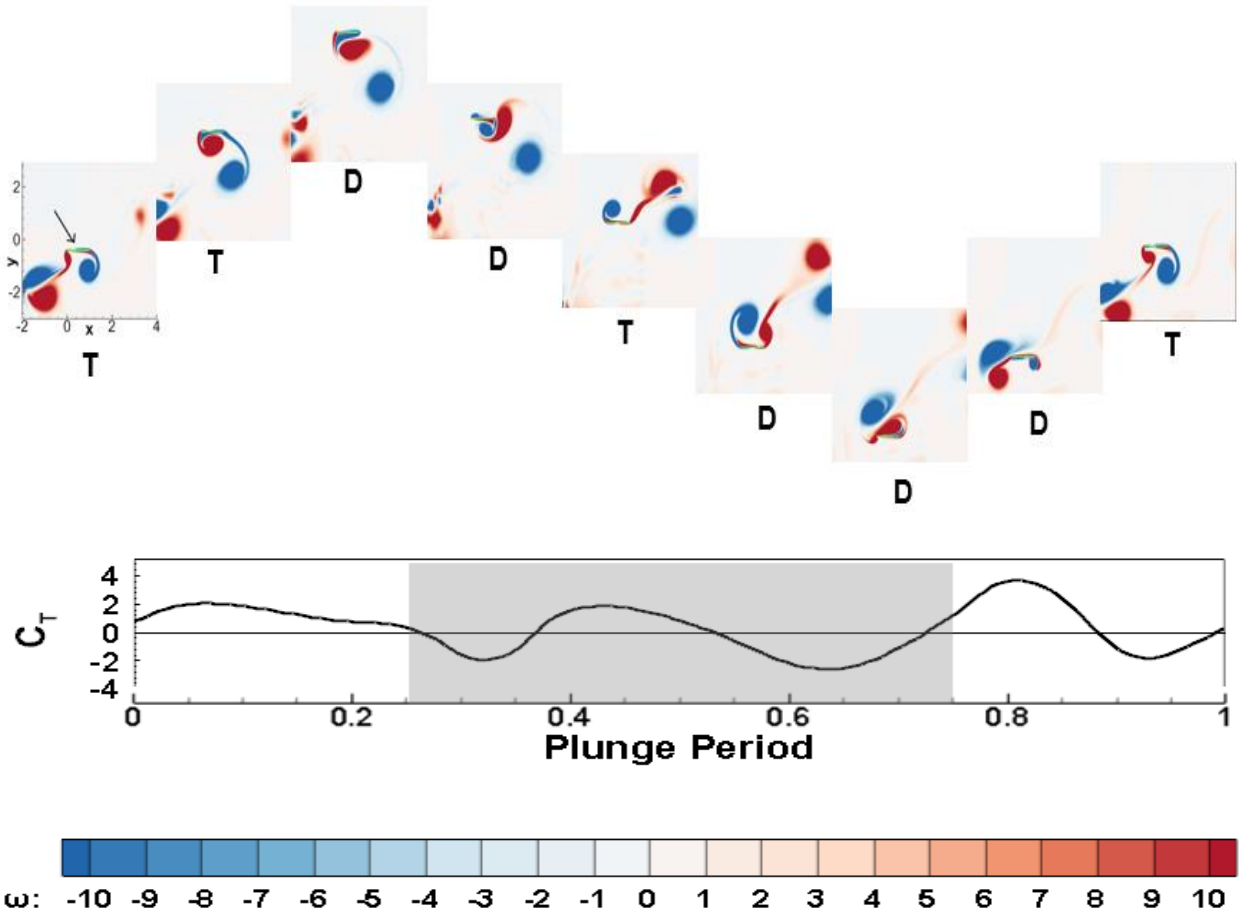

(8-d) $k = 1,\ hk = kh = 2$

Figure 8: Distribution of vortices at discrete time instances for a representative plunge cycle at $k = 1,\ h = 0.25(a),$ 0.5(b), 1.0(c) and 2.0(d) together with the thrust coefficient signals. Entire cycle is discretized in nine time intervals for vorticity plots; vertical position of each inset represents instantaneous position of plate in plunge cycle; arrow on the first inset points to the plate; snapshots of (a) and (b) has same special resolution and scale shown after (b) whereas snapshots of (c) and (d) has same special resolution and scale shown after (d). Subscripts '**D**', '**T**' and '**N**' indicate instantaneous forces as drag, thrust, or neutral experienced by the plate. Shaded region in thrust coefficient signal depicts down stroke

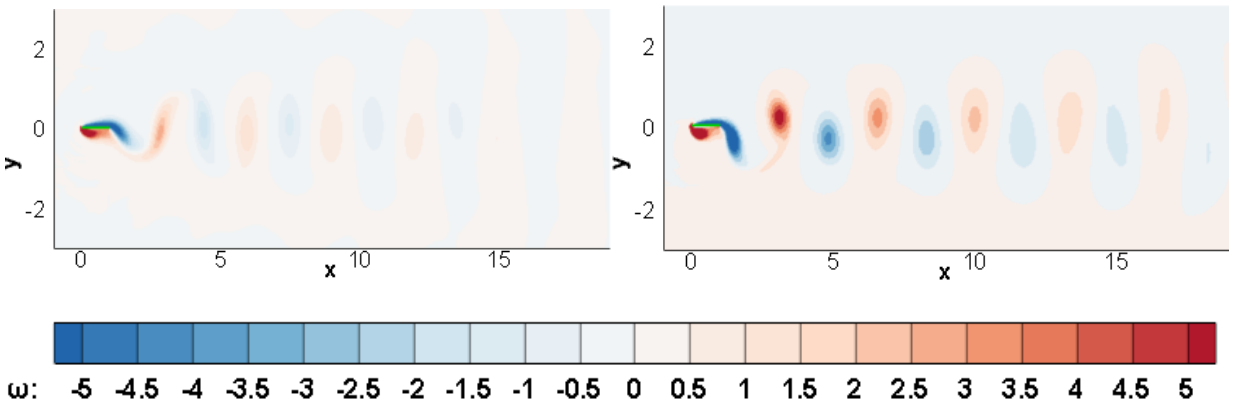

(9-a) $k = 1,\ hk = 25;\ kh = 0.25$ (9-b) $k = 1,\ h = 0.5;\ kh = 0.5$

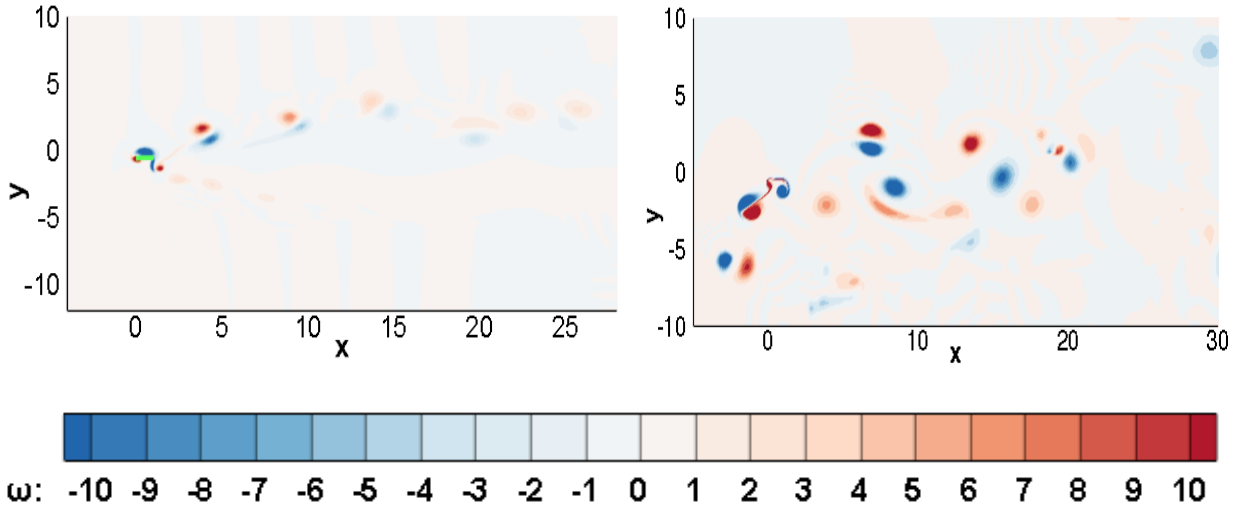

(9-c) $k = 1,\ h = 1;\ kh = 1$ (9-d) $k = 1,\ h = 2;\ kh = 2$

Figure 9: Vortex structure in the wake behind the plunging flat plate for $k = 1, h = 0.25$ (a) 0.5 (b), 1.0 (c) and 2.0 (d)

As the reduced frequency increases to k = 2, the time scale of the oscillation decreases in relation to vortex convection, hence increasing the residence time of the vortex on the plate than when oscillating at k = 1. The vorticity dynamics are shown in Figure 10a-d and the corresponding wake

in Figure 11a-d. At the smaller amplitudes (h = 0.125 and 0.25), the vortex dynamics is very similar to that observed in Figure 8-a, b (k = 1 and h = 0.25 and 0.5). LEVs of opposite signs form and shed into the wake during each half of the cycle. The small amplitude of oscillation does not allow them to gain sufficient strength before they are shed into the wake. As a result, the vortex induced velocity of the LEV is not high enough to induce thrust producing velocities at the plate resulting in a drag producing von Karman wake structure (Figure 11-a, b). As h increases to 0.5, both a LEV and TEV of opposite sign form at the start of the down stroke. However, the much smaller TEV is quickly subsumed by the LEV from the upstroke which has convected to the trailing edge of the plate. This dynamic occurs for both the upstroke and downstroke. The LEV which forms at the beginning of the stroke grows and gathers strength during the stroke while remaining near the plate surface as it convects towards the trailing edge of the plate. The strength and proximity of the LEV to the plate induces negative velocities at the plate throughout the oscillation cycle. Thus in this case, thrust is produced throughout the cycle (Figure 10-c), which is also reflected in the wake structure in Figure 11-c.

As the amplitude increases further to h = 1, the strength of the vortices increase as both LEVs and TEVs form during each of the strokes. However, the vorticity dynamics shown in Figure 10-d igure 10-d is somewhat different from k = 1 and h = 2 in Figure 8-d. At the beginning of the downstroke, the remnant of the LEV which has formed during the upstroke and the LEV formed during the downstroke combine to shed upstream of the plate. Similarly, at the beginning of the upstroke, the newly formed TEV combines with the TEV formed during the downstroke to shed in the wake. Contrary to the equivalent case with the same plunge velocity (k = 1, h = 2) which produces net drag, the present case (k = 2, h = 1) results in net thrust production during the cycle, albeit lower than k = 2, h = 0.5. The increase in thrust over k = 1, h = 2, is due to two reasons, one

of them being the longer residence time of LEVs relative to the oscillation frequency and the other is that the TEVs have a shorter residence time near the plate than the LEVs. At the same time, the thrust is lower than $k = 2$, $h = 0.5$ because of the stronger interaction between vortices which result in shorter residence times of LEVs in the vicinity of the plate. The instantaneous wake shown in Figure 11-d is quite complex and cannot be characterized easily.

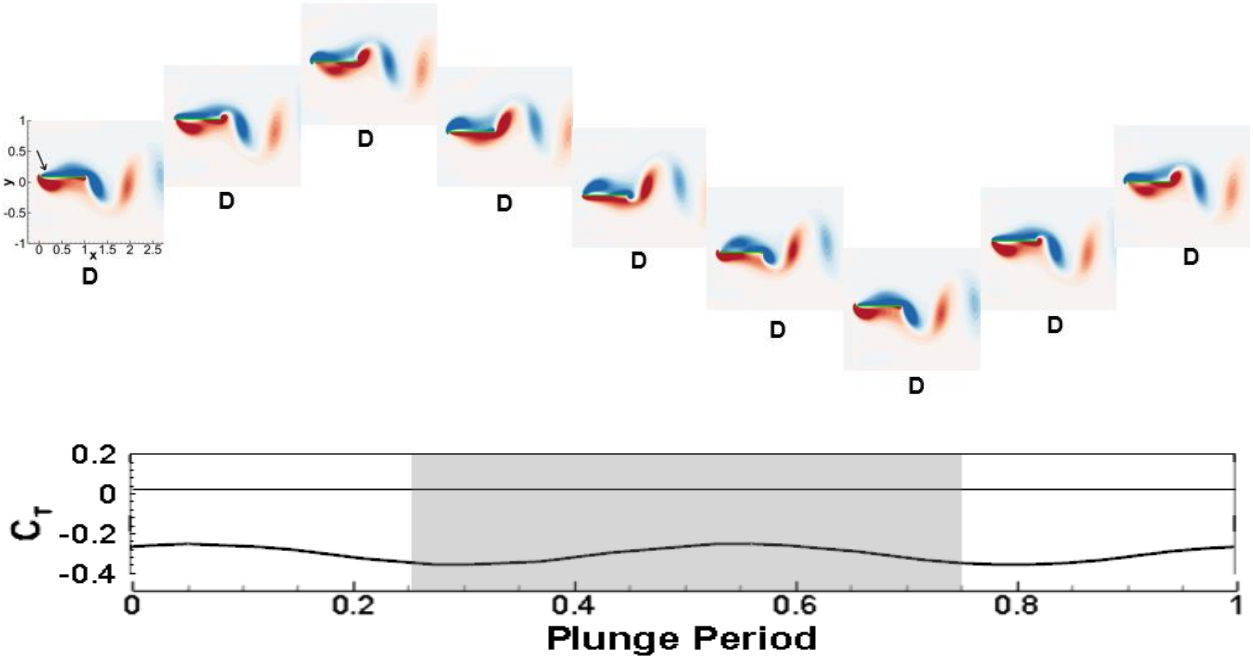

(10-a) $k = 2,\ hk = 125;\ kh = 0.25$

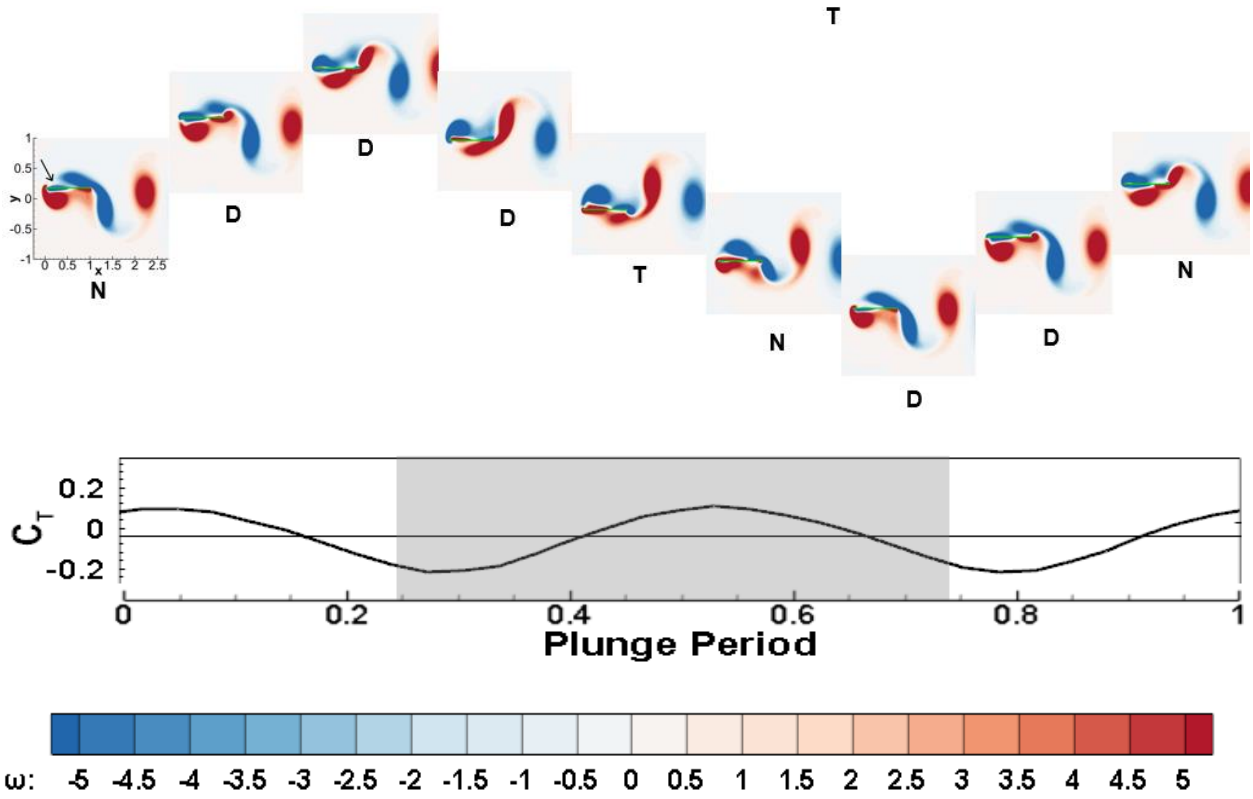

(10-b) $k = 2,\ hk = 25;\ kh = 0.5$

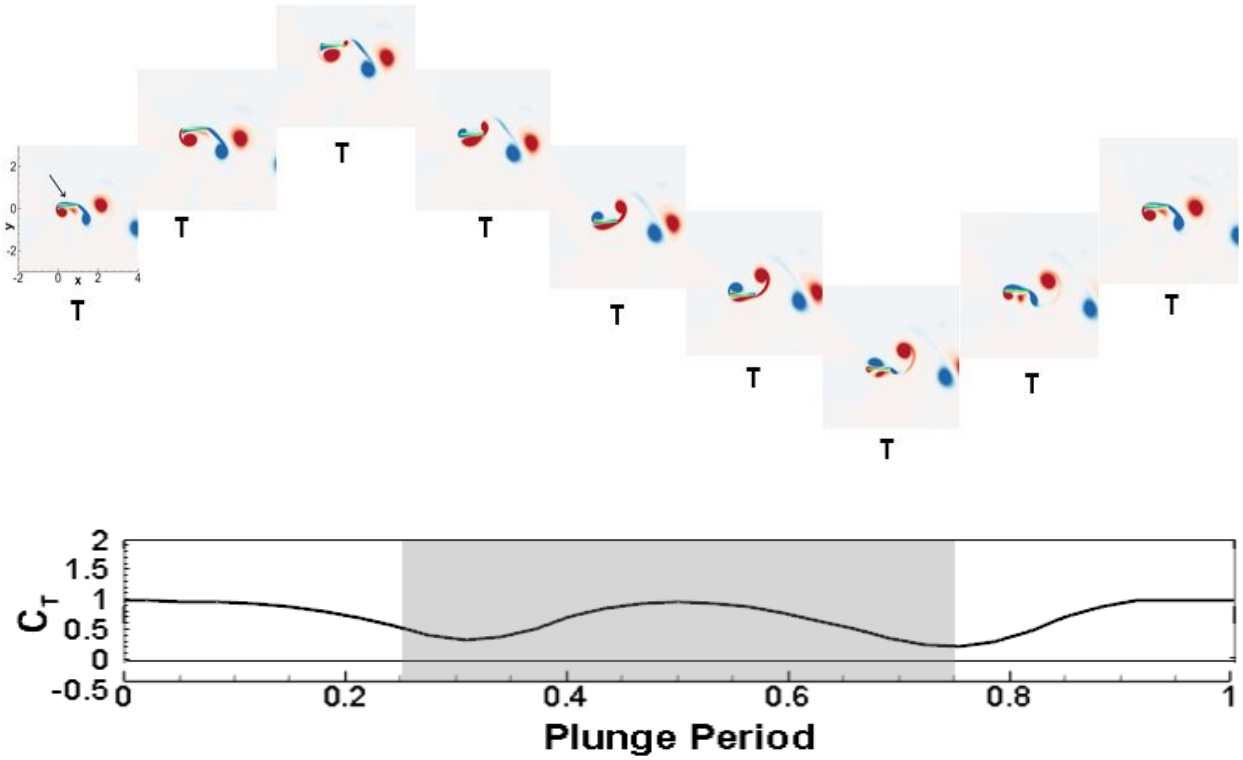

(10-c) $k = 2,\ hk = 5;\ kh = 1$

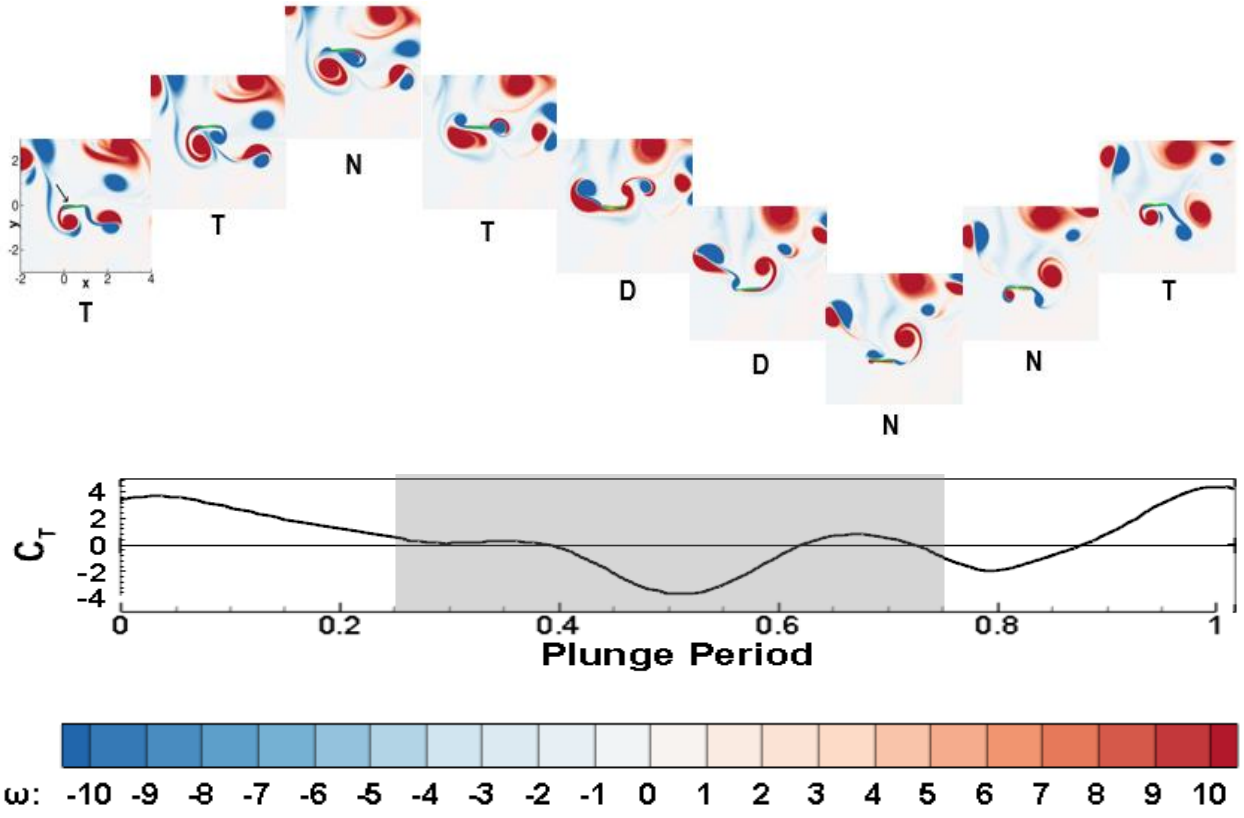

(10-d) $k = 2,\ hk = kh = 2$

Figure 10: Distribution of vortices at discrete time instances for a representative plunge cycle at $k = 2,\ h = 0.125(a),\ 0.25$(b), 0.5(c) and 1(d) together with the thrust coefficient signals. Entire cycle is discretized in nine time intervals for vorticity plots; vertical position of each inset represents instantaneous position of plate in plunge cycle; arrow on the first inset points to the plate; snapshots of (a) and (b) has same special resolution and scale shown after (b) whereas snapshots of (c) and (d) has same special resolution and scale shown after (d). Subscripts '**D**', '**T**' and '**N**' indicate instantaneous forces as drag, thrust, or neutral experienced by the plate. Shaded region in thrust coefficient signal depicts down stroke.

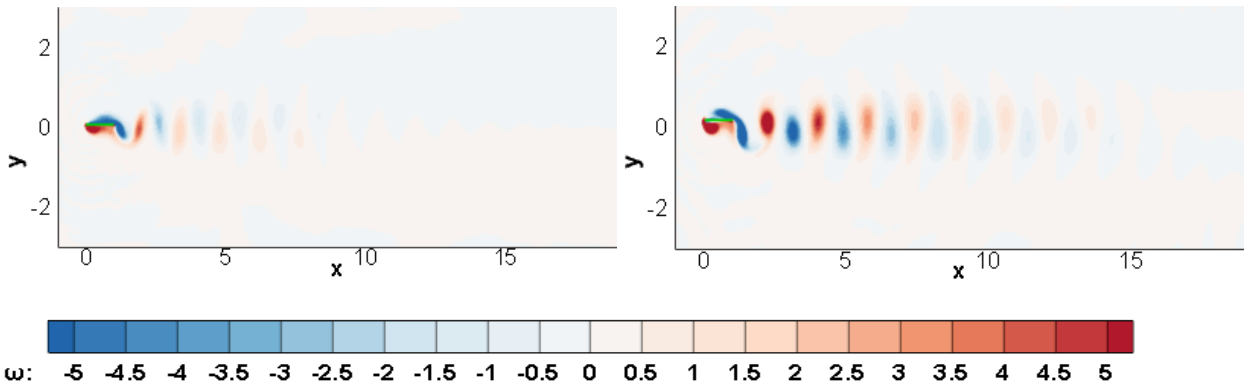

(11-a) $k = 2,\ hk = 125;\ kh = 0.25$ (11-b) $k = 2,\ hk = 25;\ kh = 0.5$

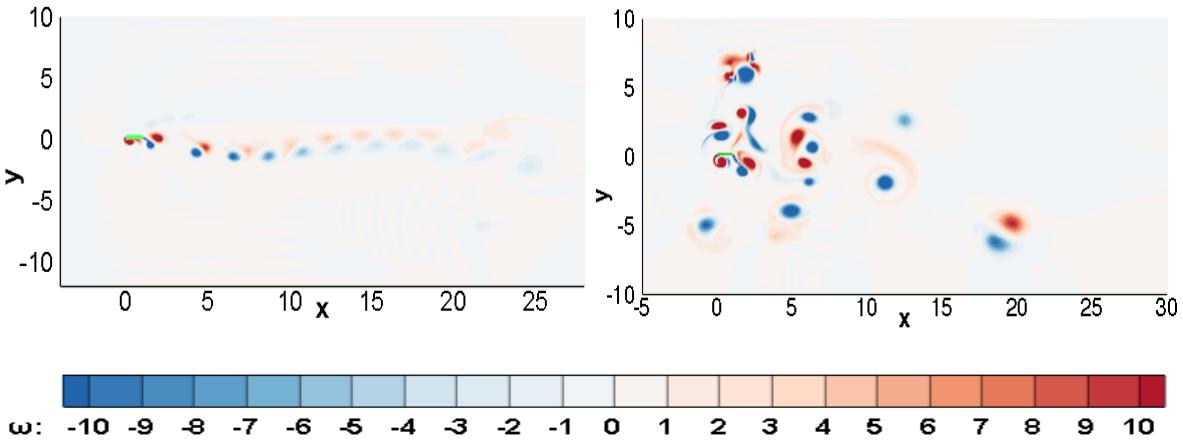

(11-c) $k = 2,\ hk = 5;\ kh = 1$ (11-d) $k = 2,\ hk = kh = 2$

Figure 11: Vortex structure in the wake behind the plunging flat plate for $k = 2, h = 0.125\ (a)$, 0.25 (b), 0.5 (c) and 1.0 (d)

From the analysis at *k* = 1 and *2*, the following main phenomenological observations can be made regarding the individual effects of *k* and *h*. Increasing *k*, increases the relative convection time of LEVs across the plate and offers greater potential for the LEVs to induce a thrust producing velocity field at the plate. These effects dominate at low *h* over a wide range of *k* as long as *kh* < *1*. Increasing *h*, increases the strength and size of LEVs offering a larger potential for thrust

production, however at the same time, it also increases the strength and size of TEVs which counter the thrust producing effect of LEVs on the plate surface. Previously, Young et al. [17], Visbal et al. [25], and Martin et al. [26]. explored the effect of plunge parameters on thrust production, but like most other previous studies, they only explored a very narrow regime of small amplitudes and provided explanations of thrust producing phenomena for an amplitude range of roughly 0.005 to 0.259. In this regime, when $kh < 1$ and h is small, the TEV is convected into the wake during formation and its effect on the plate is minimal which is mostly impacted by the convecting LEV. In this low amplitude regime, thrust increases with the plunge velocity, kh. As observed by Lai et al. [22] even for a comparatively wider range of kh (0.09- 4.65) thrust coefficient displays a direct and increasing relationship with kh as long as the considered h values are on the smaller side. Although Lai et al. [22] worked with plunge velocities ranging from 0.09-4.65, their plunge amplitude varied only from 0.0125 to 0.6 which is approximately one order of magnitude smaller than the amplitude range of the present study. The present study however indicates that TEVs of consequential strength are created at moderate-to-large amplitude plunging conferring a significant effect on the flow-field, irrespective of the kh value. The formation of these TEVs interferes with the monotonic increase of thrust coefficient with kh reported in previous studies due to non-linear interactions between the TEVs and LEVs which are elaborated on in section 4.4.3.

4.4.2 Comparison of Vorticity Dynamics at Constant *kh* and Relation to Thrust Production

To accentuate the observations in the previous section, Figure 12 compares the vorticity dynamics at different k and h values at the same plunge velocity kh. For $kh = 0.5$ and $k = 1$ we make the observation that the LEV that starts forming during the up stroke or downstroke sheds from the trailing edge at the end of the respective stroke or soon after and is only resident on the plate for half the oscillation cycle. Contrary to this, the LEV that forms for the plate oscillating at $k=4$ is

resident on the plate for the full cycle. We also note that there is no TEV formation at $k = 1$, but a TEV is formed at $k = 4$, which however does not directly interact with the LEV but is shed into the wake every half stroke.

For $kh = 1$, $k = 1$, the vortex dynamics on the plate is quite similar to $kh = 0.5$, $k = 1$, except that the size and strength of the vortices increase (as h increases). As in the $kh = 0.5$ cases, there is no separate formation of a TEV; the LEV that forms during one half of the stroke convects to the trailing edge and manifests as a TEV for the other half of the stroke. At $k = 4$ and $kh = 1$, similar to $kh = 0.5$, a separate TEV forms during each half of the stroke and the vorticity dynamics is very similar, except that since h has increased, the strength and size of vortices are larger. It is noted that for both $kh = 0.5$ and 1 at $k = 4$, in spite of the formation of TEVs, there is very little to no interaction between the TEV and LEV.

For $kh = 2$, $k = 1$, h increases further and the vortices generated by the plate gain in size and strength for each half stroke. Now, because of the higher plunge velocity kh, both $k = 1$ and $k = 4$, generate TEVs. The LEV and TEVs because of their induced velocity fields start interacting with each other and as a result have a detrimental effect on thrust production. The degree of interaction decreases as k increases from $k = 1$ to $k = 4$ or as h decreases from $h = 2$ to $h = 0.5$. Due to these nonlinear LEV-TEV interactions, the LEVs have a shorter residence time on the plate compared to the $kh = 1$ cases resulting in smaller thrust value than $kh = 1$. The vortex dynamics of $kh = 2$, $k = 4$ is very similar to that of $kh = 2$, $k = 2$ shown in Figure 10-d, thus the thrust coefficient values of these two cases are of comparable magnitude.

$\boldsymbol{kh} = \mathbf{0.5}$	**(12-a)** $\boldsymbol{k = 1}$, $\boldsymbol{h} = \mathbf{0.5}$	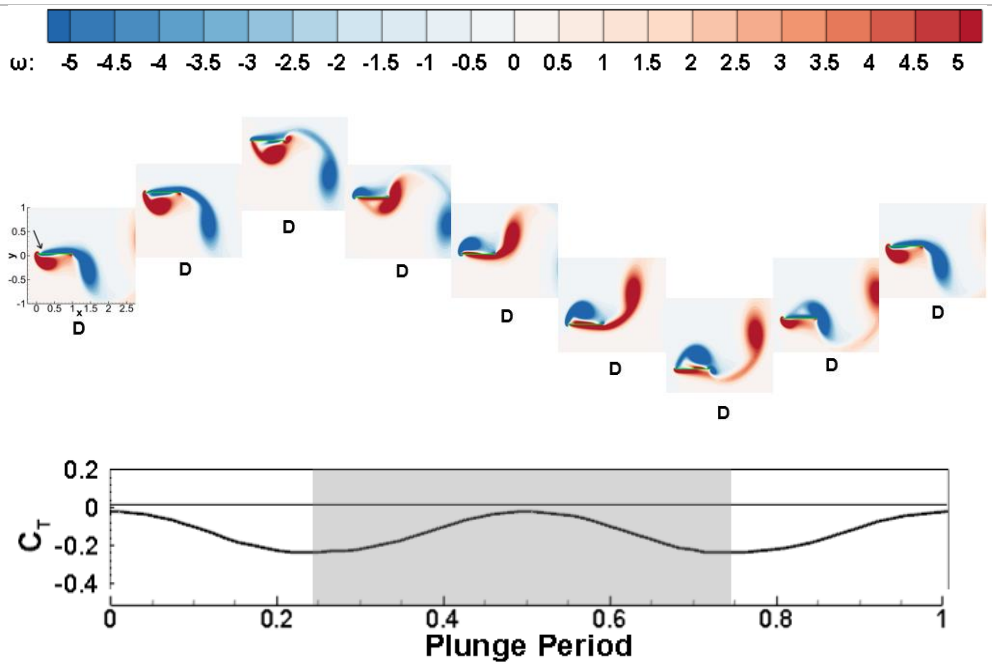
	(12-b) $k = 4$, $h = 0.125$	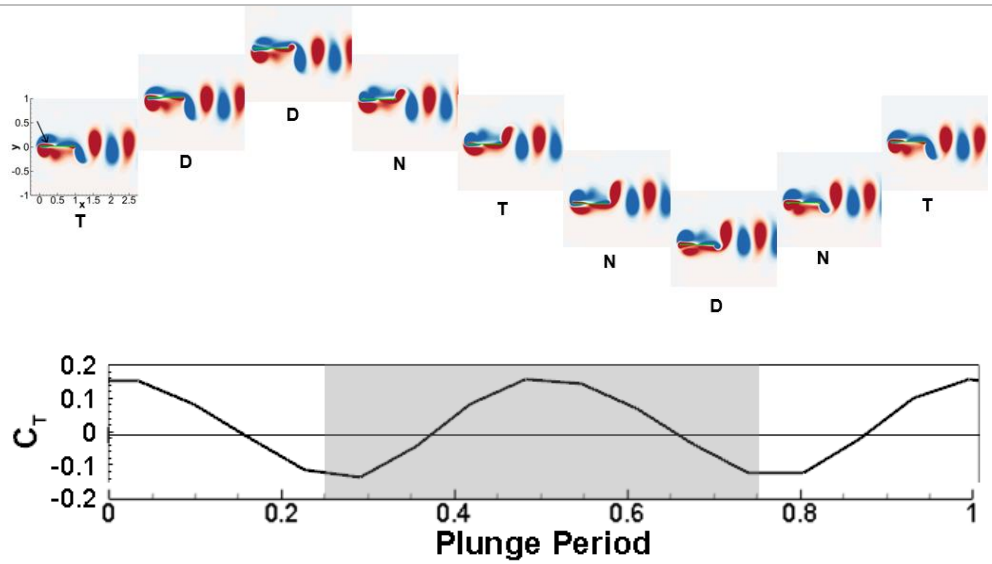

$kh = 1$	(12-c) $k = 1$ $h = 1$	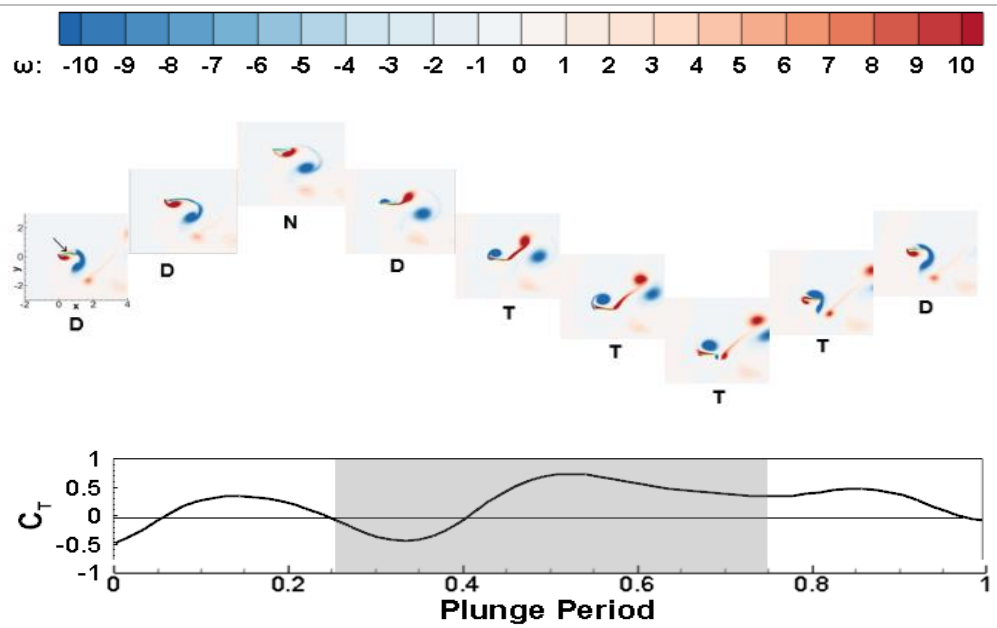
	(12-d) $k = 4$ $h = 0.25$	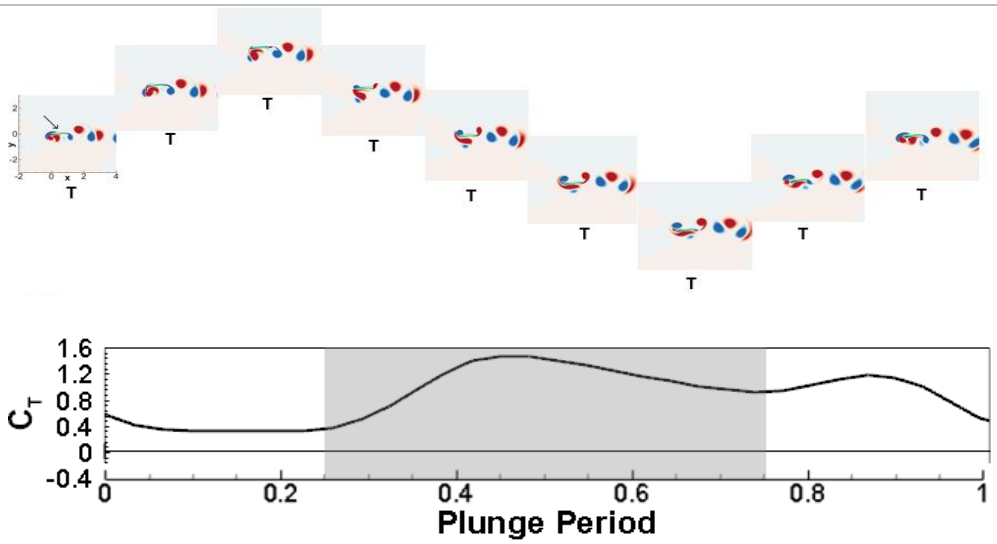

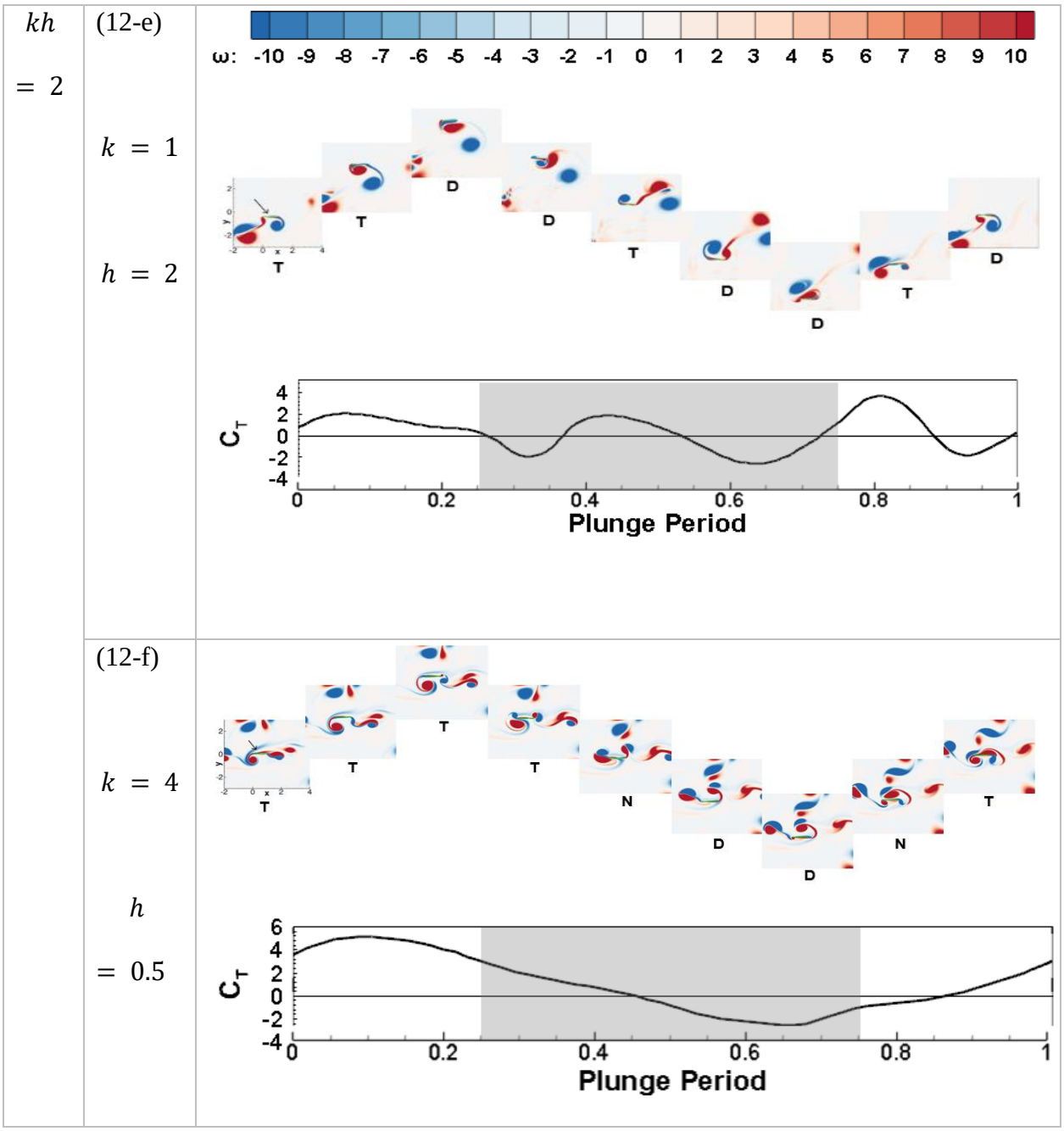

Figure 12: Comparison of vortex structures during plunge cycle and thrust coefficient signals between cases with same kh but with different combinations of k and h; respective scale is shown for each kh group

As *h* increases or as *kh* gets larger, the increasing strength and size of the LEV during each half-stroke, besides having a favorable effect on thrust production, will also by virtue of its induced velocity field draw the TEV on to the plate, thus having a detrimental effect on thrust production. For $kh > 1$, the interplay between LEVs and TEVs becomes the defining factor for thrust production which now enters a regime in which LEV-TEV interactions dominate. As *kh* increases to values much greater than unity, the interactions get more complex and non-linear effects dominate the flow and the mechanics of thrust production.

The detailed discussion on vorticity dynamics in sections 4.4.1 and 4.4.2 clearly shows that neither *kh* nor *k* can be attributed as a sole parameter influencing thrust production when working with a frequency and amplitude range as wide as in the current study. Thus the observations made by Lai el al. [22] and Lewin et al. [28] are limited to their respective working range. Findings from this study are not only robust and applicable to a wider parameter range, but also closely tie the irregular trend in thrust generation to the strong non-linear vortex dynamics observed. The details of the non-linear vortex dynamics characterization are presented in the following section.

4.4.3 Vortex Interactions at Large *kh*

Three pre-dominant vortex-vortex interaction mechanisms which influence thrust production for large *h* and *kh* are identified, all of which reduce the residence time of vortices near the plate. The first mechanism (Mechanism-1) is when an incipient vortex merges with an existing vortex from the previous cycle or stroke and is convected away from the plate, thus reducing the time it resides near the plate to sufficiently influence the shear stress at the plate surface. Whilst this phenomenon is favorable for thrust production when TEVs, which induce drag on the plate, get convected away, it is not favorable for thrust production when LE vortices merge and convect away from the plate. For LEVs, this shedding usually occurs upstream and for TEVs downstream of the plate. This

mechanism is present for LEVs in all the *kh* = 2 cases, shown in Figure 13 but in none of the *kh* = 1 cases (previously shown in Figure 8-c, 10-c and 12-c, d). This explains the reason behind the comparatively higher values of C_T for *kh* = 1 compared to *kh* = 2 as seen in Figure 6-b. Similarly, although this mechanism is not prevalent for TEVs at $k = 2$ and $h = 1$ (Figure 13-a), it is present in the subsequent cases of $k = 4, h = 0.5$ (Figure 13-b) and $k = 8, h = 0.25$ (Figure 13-c). Because the presence of TEVs induce drag, their faster convection results in an increment of thrust coefficient at higher *k* and lower *h* cases for a constant *kh*.

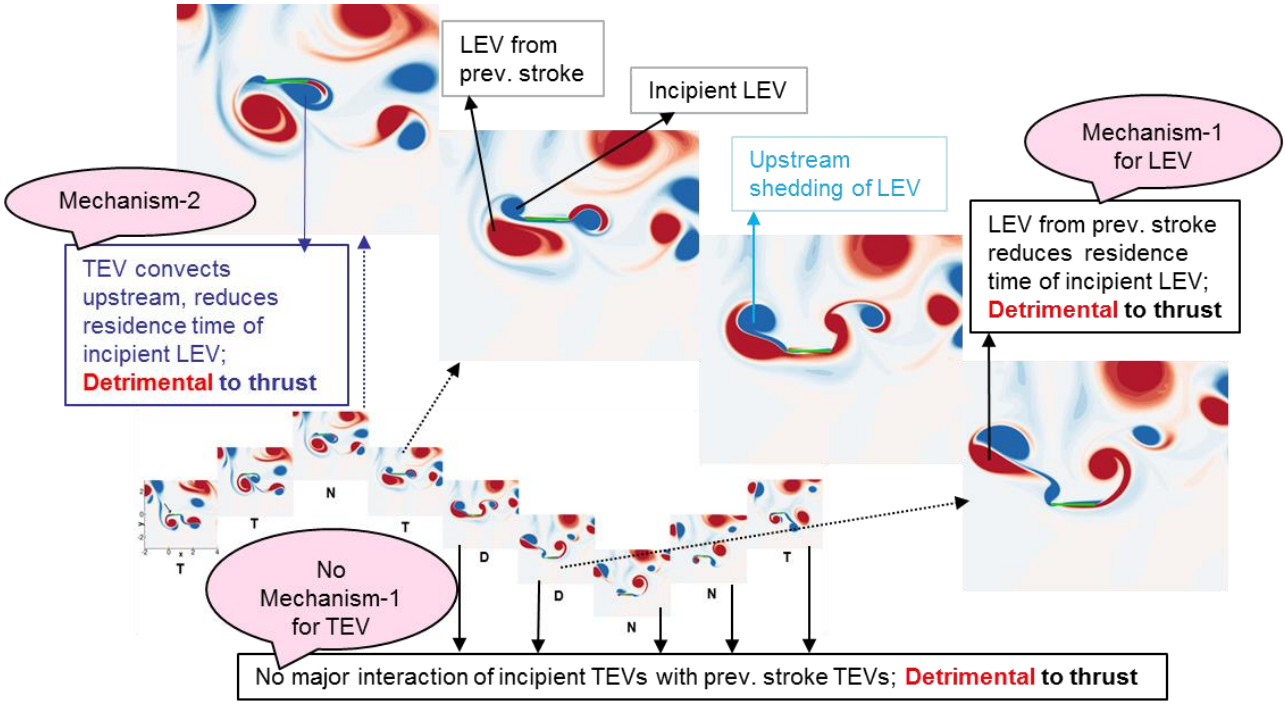

(13-a) $kh = 2;\ k = 2, h = 1$

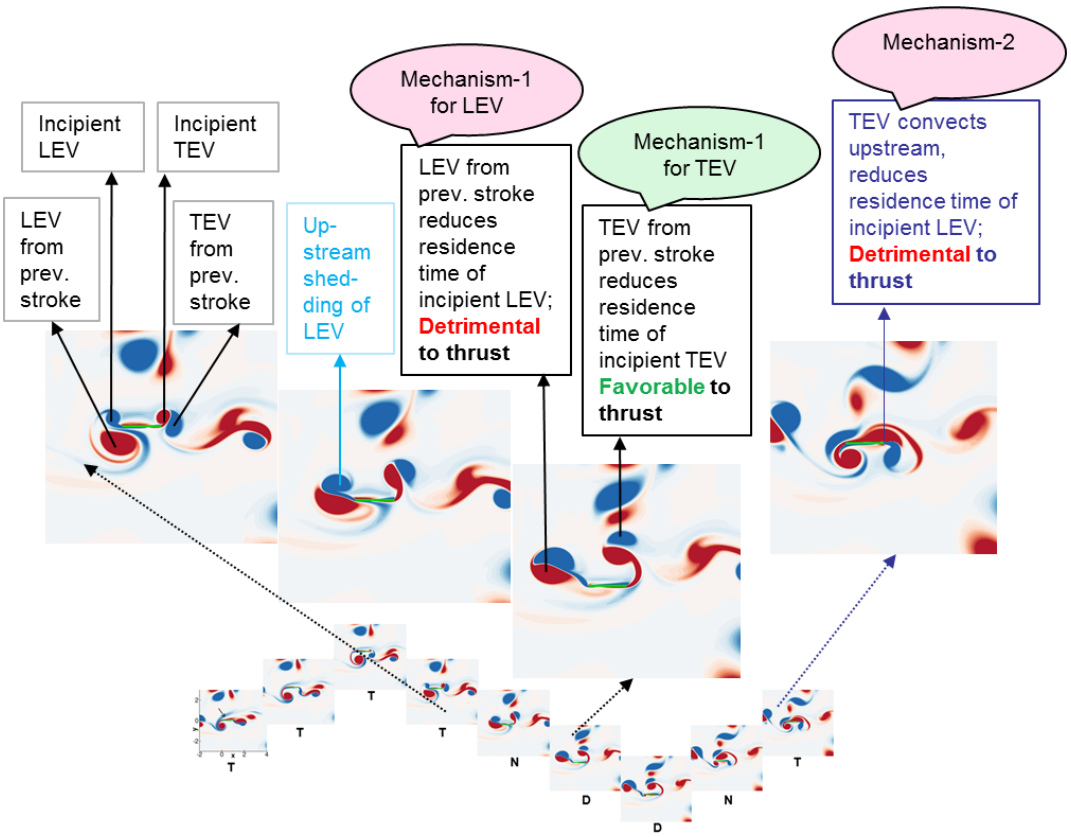

(13-b) $kh = 2;\ k = 4, h = 0.5$

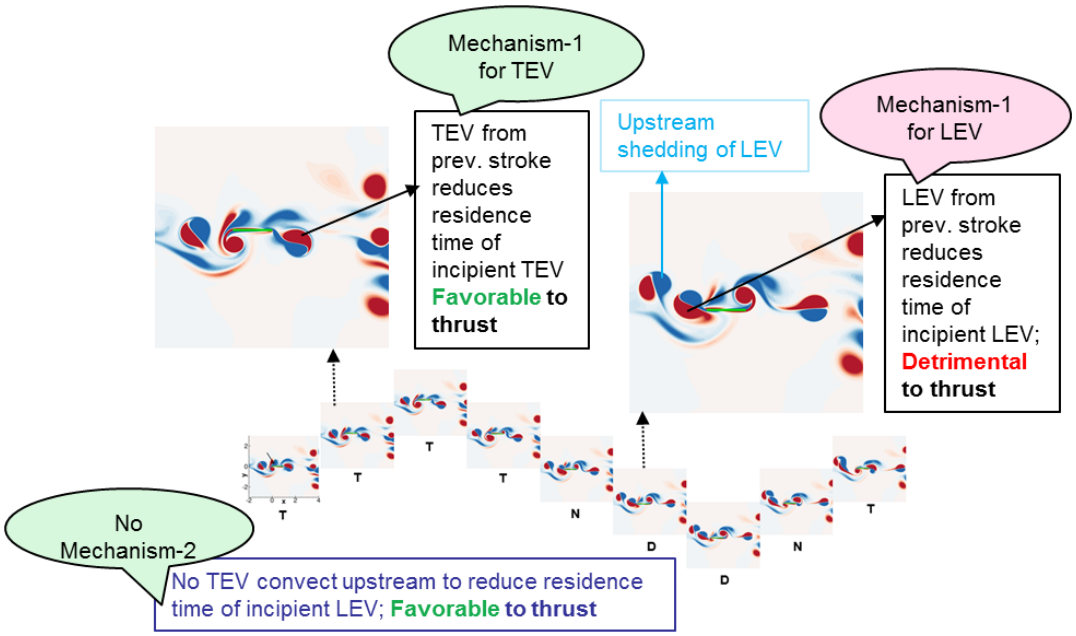

(13-c) $kh = 2;\ k = 8, h = 0.25$

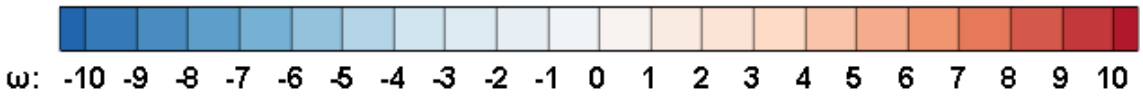

Figure 13: Distribution of vortices at discrete time instances for a representative plunge cycle at $kh = 2$, with different k and h combinations. $k = 2, h = 1$ (a), $k = 4, h = 0.5$ (b) and $k = 8, h = 0.25$ (c). Entire cycle is discretized in nine time intervals for vorticity plots; vertical position of each inset represents instantaneous position of plate in plunge cycle; arrow on the first inset points to the plate; all vorticity plots use the same scale shown after (c). Subscripts '**D**', '**T**' and '**N**' indicate instantaneous forces as drag, thrust, or neutral experienced by the plate. Black, violet and cyan color annotations respectively correspond to Mechanisms 1, 2, and 3.

Another mechanism (Mechanism-2) of vortex-vortex interaction is the merging of a TEV with the LEV of the next stroke that reduces the residence time of the LEV. This is seen in large amplitude cases in which the LEV induced velocity becomes large enough to draw the TEV to the leading edge of the plate, thus introducing a detrimental effect on thrust production. This phenomenon is analogous to the "negative reinforcement between vortices" by Anderson et al. [13]. Mechanism-2 is present in higher amplitude cases of $kh = 2$ as seen at the start of downstroke of $k = 2$; $h = 1$ (Figure 13-a) and at the middle of up-stroke of $k = 4$; $h = 0.5$ (Figure 13-b). Mechanism-2, TEV→LEV merges are not present for comparatively smaller amplitude cases (e.g. $k = 8$; $h = 0.25$ and $k = 16$; $h = 0.125$). This is because the size of LEV vortices reduce as h reduces and the induced velocity of the smaller vortices are not strong enough to draw TEVs to the leading edge of the plate. This is the reason that $k = 8$; $h = 0.25$ does not have the detrimental effect of TEV→LEV merges and exhibits a higher thrust value than the higher amplitude cases of the same kh (=2). However, as the plunge amplitude (h) decreases further (e.g. $k = 10$, $h = 0.2$; $k = 12$, $h = 0.167$ and

k = 16, h = 0.125), the smaller LEV vortices cease to have as large an effect on thrust production as at higher plunge amplitudes. This is one of the mechanisms that dictates the optimal combination of k and h that result in maximum thrust production.

Another pre-dominant mechanism (Mechanism-3) of vortex-vortex interaction involves interaction between a vortex shed several cycles or strokes before and an existing LEV. As can be seen from Figure 13a-c, all the different k, h combinations of kh = 2 experience the shedding of a vortex pair upstream of the plate that eventually convects back to the plate to interact with an incipient LEV forming at the leading edge. The difference between mechanism-1 and -3 is in the fact that for Mechanism-1, the incipient LEV interacts with an LEV that was shed from the immediate preceding stroke. The result of Mechanism-1 is often a pair of LEVs of opposite signs resulting from two consequent strokes or one cycle convecting away from the plate together. This is shown by the blue box annotation in Figure 13-c. Whereas in Mechanism-3, the shed LEV pair (can be a result of Mechanism-1) that was shed multiple strokes or cycles before, returns to interact with an incipient LEV. Mechanism-3 is depicted in Figure 14 where the mechanism takes place over a duration of 5 consecutive strokes, 3 down and 2 up denoted as D1, U1, D2, U2 and D3 in Figure 14-a. Figure 14-a shows the interaction of a LEV pair that has shed multiple strokes (four strokes for this particular case) ago with an incipient LEV. The previously shed LEV pair is circled in red in order to show its path. In their path to come back to the plate, the vortex pair of opposing signs might separate (as can be seen in D2 of Figure 14-a) to finally interact with an incipient LEV as a single vortex (negative in sign for all the instances shown in Figure 14). The interaction caused by Mechanism-3 too reduces the residence time of the LEV and reduces thrust. Mechanism-3 interaction is more prevalent at low frequencies (e.g. k = 2; h = 1 or k = 4; h = 0.5) than at higher frequencies. As k $(= \frac{\pi f c}{U_\infty})$ becomes larger, the time scale on which LEVs are shed becomes smaller

than the time scale associated with the free-stream that convects the shed vortices back to the plate. In effect, it takes a relatively longer time for the shed vortices to return to the plate and interact with the incipient LEV. During this time, their (shed vortices) strength decays and hence they have a weaker interaction with the incipient LEV and subsequently have less of a detrimental effect on thrust compared to lower *k*. This decaying effect of mechanism-3 is shown in Figure 14-b where the strength of the returning vortices for k = 2, 4 and 8 is roughly half, one-fourth, and one-eighth of the strength of the incipient vortex.

But similar to Mechanism-2, for constant plunge velocity (kh) when the frequency is much higher (e.g. k = 10, 12 or 16) the amplitude decreases (e.g. h = 0.2, 0.167 or 0.125) and consequently so does the size of vortices. Hence the thrust coefficient again decreases beyond the optimum combination of k = 8; h = 0.25.

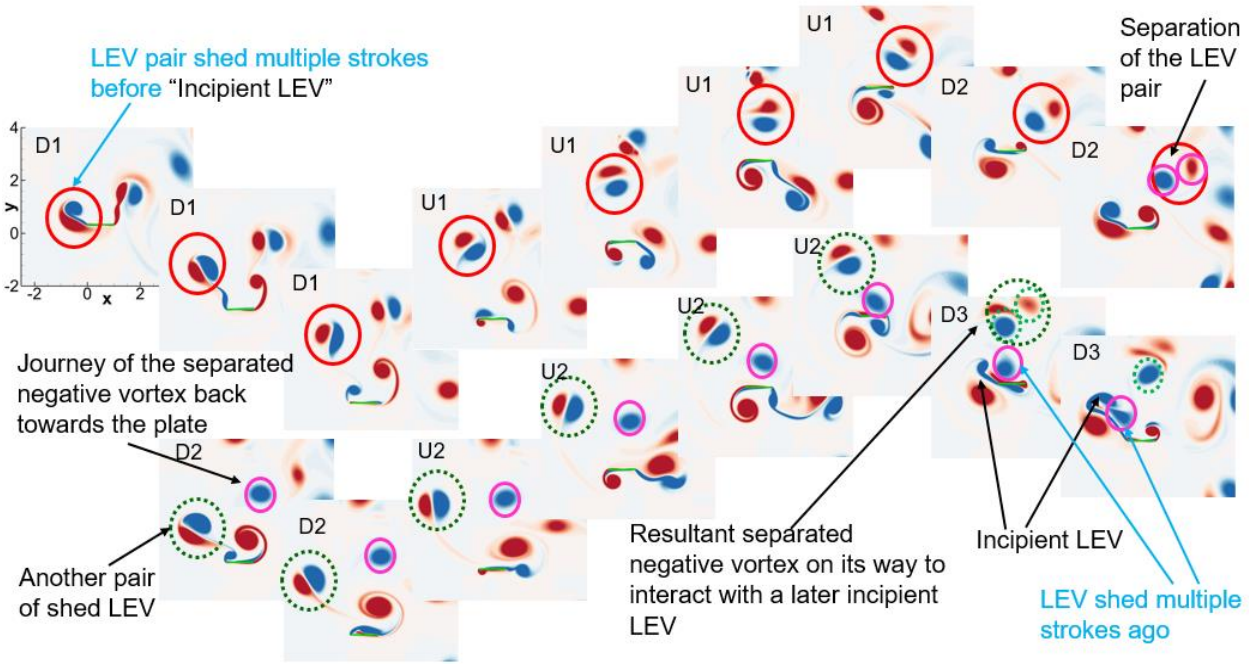

(14-a)

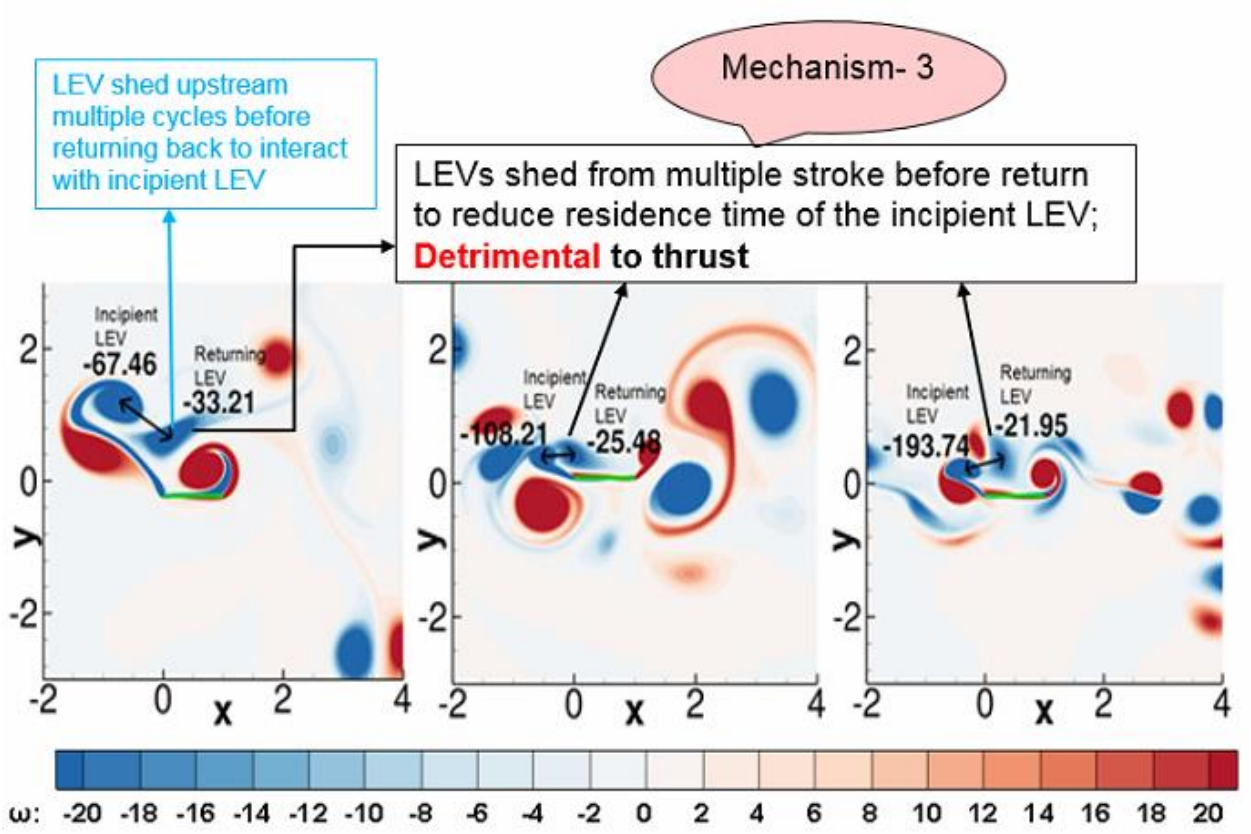

(14-b)

Figure 14: Mechanism-3. (a) The dynamics of the mechanism taking place in 5 consecutive strokes, 3 down and 2 up denoted as D1, U1, D2, U2 and D3; plate is highlighted in green line; dynamics of the interaction of a LEV pair shed multiple strokes ago with an incipient LEV is circled in red and pink; the vortex pair in red circle lost adhesion in D2, hence-forth circled by pink and interacted with the incipient LEV as a single negative vortex in D3; within these 5 strokes, another vortex pair circled in green dots convects upstream near the end of D2 and starts to come back on the way towards the plate at the end of D3; green circled LEV interacts with a later incipient LEV which has not been shown. (b) Comparison of strength of returning and incipient vortices for $kh = 2$. $k = 2$; $h = 1$, $k = 4$; $h = 0.5$ and $k = 8$; $h = 0.25$ from left to right; arrows

indicate pair of returning and incipient vortices which interact; return time of vortices increase from left to right, reducing relative strength of vortices as indicated.

4.5 Wake Characterization

As stated earlier, thrust or drag production by the oscillating plate is reflected in the structure of the wake. Negative or clockwise rotating vortices in the upper row and positive or counter-clockwise rotating vortices in the lower row indicate a drag producing wake. On the other hand, a thrust producing wake is characterized by negative vortices in the upper row and positive vorticity in the lower row giving rise to a momentum surfeit indicative of energy added to the flow. Figure 15 summarizes the wake behavior for different plunge velocities (*kh)*. For $kh = 0.25$, the presence of clockwise vortices in the upper row and counterclockwise vortices in the lower row result in a drag producing velocity deficit in the wake, irrespective of the individual *k* and *h* combinations. In contrast, at $kh = 1$, the wake structures are clearly thrust producing. However, at even higher $kh = 2$ or 4 the associated flow-fields become more energetic leading to complex vortex-vortex interactions. Hence, the wake structures corresponding to high *kh* values are chaotic in nature and cannot be characterized easily.

A common characteristic of all the wakes is that they become narrower as the amplitude (*h)* decreases. In Figure 15, at the same *kh*, this effect manifests when *k* increases. As the reduced frequency increases and amplitude decreases for fixed *kh* values, not only does the wake narrow, but the strength and spacing between same sign vortices in the wake also change.

We define *D* to be the distance between two vortices of same sign (i.e. a pair of consecutive positive or negative vortices as marked in Figure 15-a). Figure 16-a shows the relationship between *D* and *h* for different *k*. The distance between two same sign wake vortices is directly proportional

to h and can be approximated by a linear dependence with h. Similarly, Figure 16-b shows the relationship between D and k for different h. The distance D is inversely proportional to k and decreases as ~1/k. Considering the trends observed in Figure 16-a, b it can be said that the distance *(D)* between two same sign vortices in the wake is a strong function of k and h and follows Eq. 8. Figure 16-c shows that D varies as $\sqrt{(\frac{h}{k})}$ and the data points are in good agreement with the power-law fitted function with a squared correlation coefficient, R^2 = 0.89. It should be noted that the chaotic wake structures pertaining to high kh values (= 2 and 4 e.g. shown in Figure 15-c and f) were not considered in Figure 16 and Eq. 8 as getting a definite and meaningful value of D for these cases is challenging.

$$D = f(\frac{h}{k}) = 5\sqrt{h/k} \quad \text{for} \quad \begin{cases} 1 \le k \le 16 \\ 0.0625 \le h \le 2 \\ kh \le 2 \end{cases} \tag{8}$$

Increa ↓ -sing h	$\boldsymbol{k = 1}$	$\boldsymbol{k = 4}$
$\boldsymbol{kh = 0.25}$	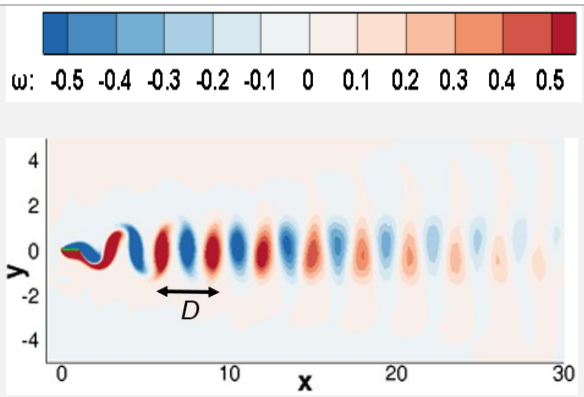 (15-a) $k = 1,\ hk = 25$	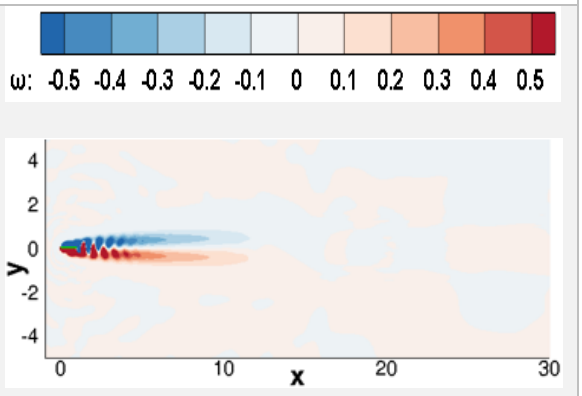 (15-d) $k = 4,\ hk = 0625$

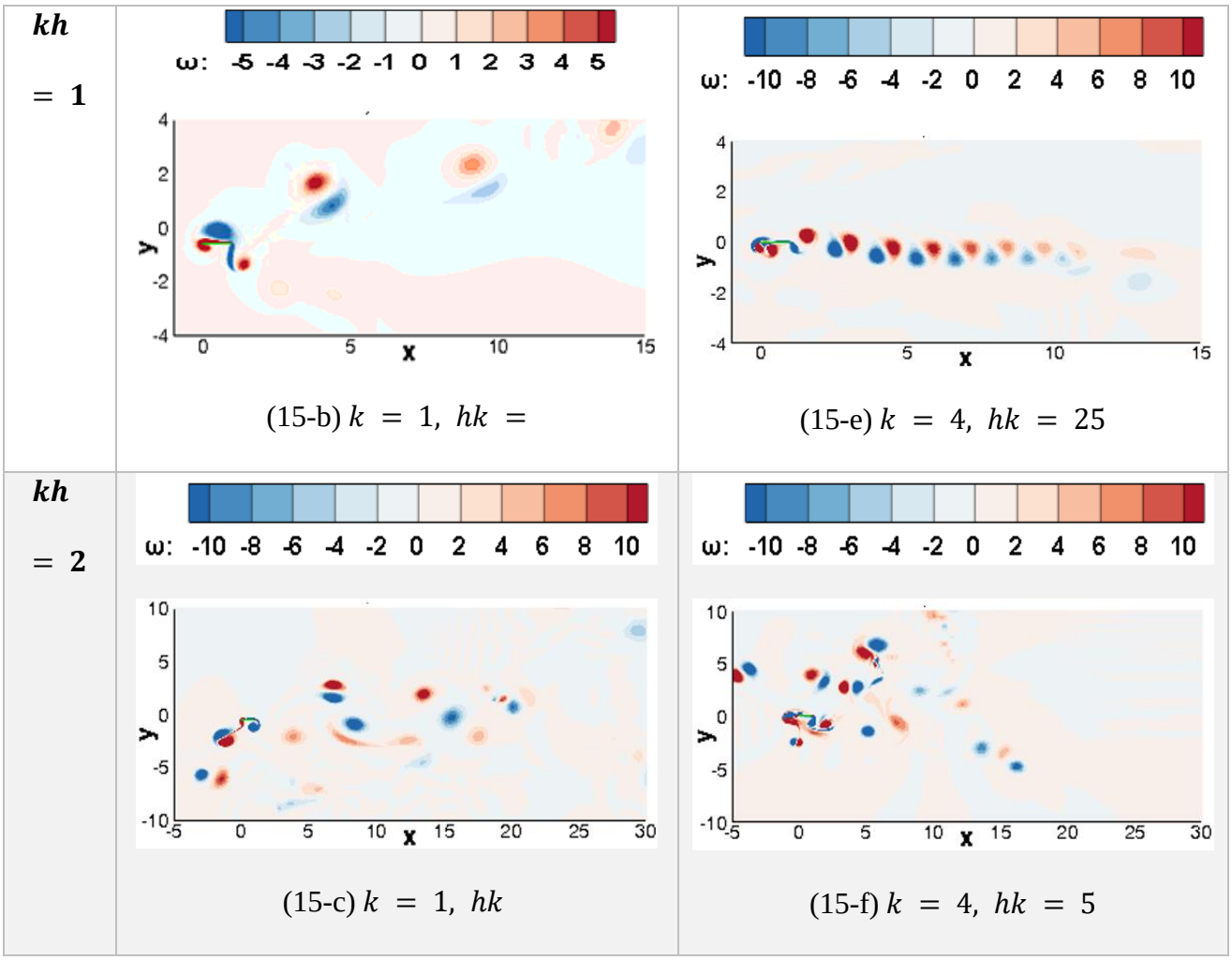

Figure 15: Comparison of vortex structure in the wake between cases with same kh but with different combinations of k and h

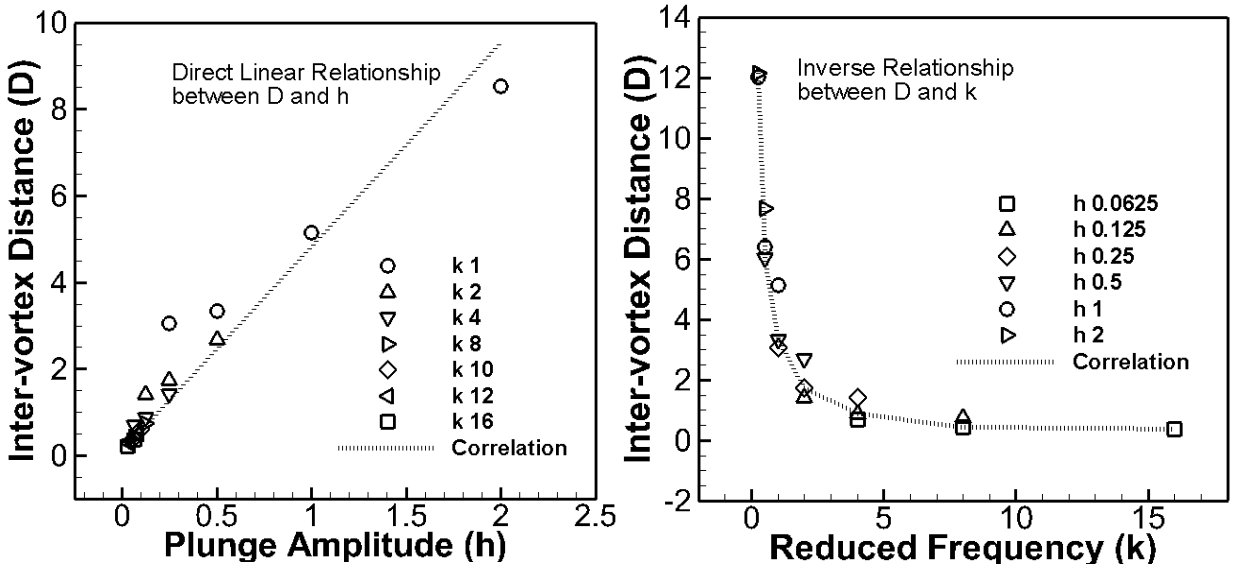

(a)

(b)

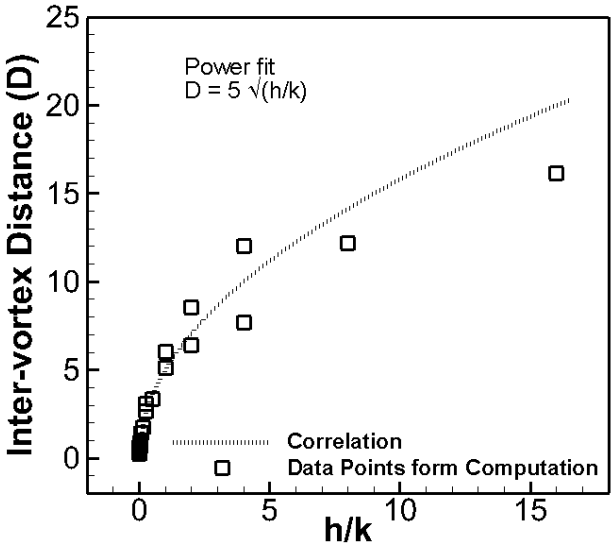

(c)

Figure 16: Variation of inter-vortex distance with (a) varying plunge amplitudes for constant reduced frequencies; (b) with varying reduced frequencies for constant plunge amplitudes; (c) as a combined function of reduced frequency and plunge amplitude

Similar to inter-vortex distance *(D)*, strength of vorticity *(S)* can also be parametrized using *k* and *h*. One representative positive vortex is chosen consistently at a time instance when it is about to shed for each of the 39 test cases. The strength *(S)* is measured at the vortex core. Figure 17 shows that the vortex strength *(S)* is a strong function of reduced frequency *(k)* and the functional relationship is near linear for different plunge velocities *(kh)* with increasing slope as *kh* increases. The squared correlation coefficient (R^2) for the different linear fits for different *kh* values varies between 0.89 to 0.99.

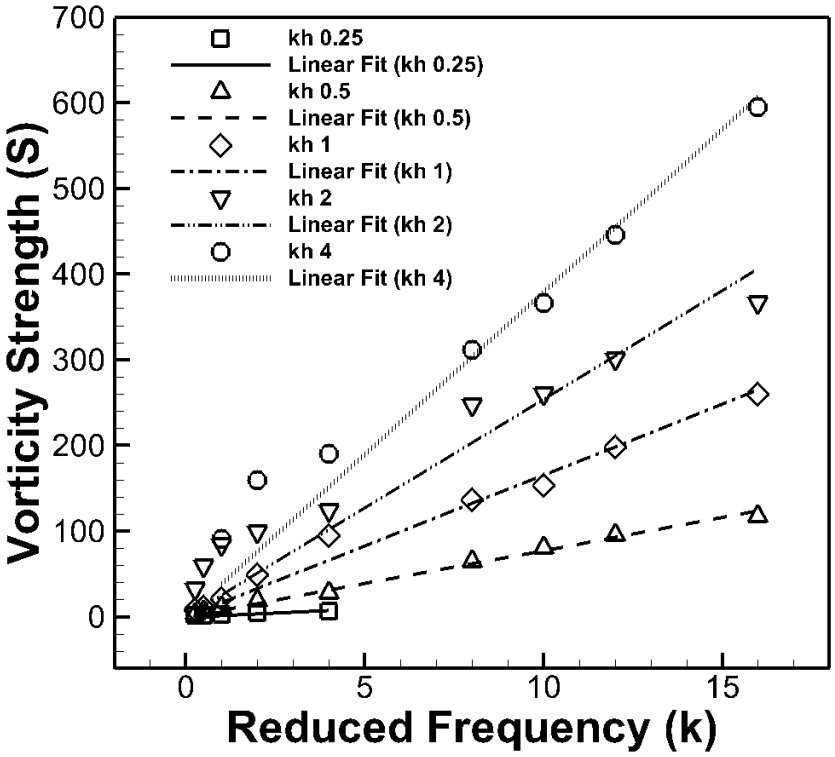

Figure 17: Variation of vorticity strength with varying reduced frequencies for constant plunge velocities.

5 SUMMARY AND CONCLUSIONS

The canonical case of a plunging flat plate at Re =100 is investigated over a wide range of reduced frequencies $0.25 \leq k \leq 16$ and plunge amplitudes $0.03125 \leq h \leq 8$ to give plunge velocities ranging

from $0.25 \leq kh \leq 4$. It is found that at $kh = 0.25$, the plunging motion does not result in any thrust production for any combination of k and h. As kh increases to 0.5, the wake transitions from drag producing to thrust producing and some nominal thrust is produced as the reduced frequency increases. At $kh \geq 1$, for $k > 0.5$ and $h < 2$, all combinations of k and h produce thrust. However, thrust does not increase monotonically with kh but reaches a maximum at $kh = 1$ for most combinations of k and h and reduces thereafter. The rate at which thrust production drops is dependent on h – decreasing rapidly at large plunge amplitudes when the reduced frequency is small, so much so that at low k and high kh the force produced reverts back to drag.

It is shown that LEVs contribute to thrust production by inducing counter flow velocities near the plate, whereas TEVs do the opposite. At low $kh < 1$, the LEVs do not have the strength to induce a counter-flow at the plate even though they convect down the plate to the trailing edge and the TEVs are shed directly into the wake. As kh increases, the LEVs increase in size and have enough strength to induce a counter-flow near the plate as they convect over the plate. At the same time, the induced velocities of both LEVs and TEVs are not high enough for the TEVs to become consequential by convecting upstream and influence the flow at the plate. Thrust production is maximum in this regime. As kh increases further, particularly as h increases, the strength and size of LEVs and TEVs increase enough to counter the mainstream flow and enter into a regime in which vortex-vortex interactions dominate. Three main mechanisms of such vortex-vortex interactions are identified, the net effect of which is to decrease the residence time of LEVs near the plate and reduce thrust.

This analysis is followed by a detailed parameterization of some wake characteristics with the different plunge attributes. The inter-vortex distance in the wake is found to correlate directly with plunge amplitude and inversely with frequency. On the other hand, vortex strength is found to be

a strong function of reduced frequency *(k)* where the functional relationship is near linear for different plunge velocities *(kh)* with increasing slope as *kh* increases.

The current study establishes that findings from previous investigations that thrust coefficient and vortex dynamics is predominantly governed by plunge velocity (kh) [22] or reduced frequency (k) [28] is valid only for their respective relatively narrow band of small amplitudes. As this study covers a relatively larger range of amplitudes (h ranging from 0.03125 to 8), it is shown that the thrust coefficient does not increase monotonically with *kh*, which eventually hinders the possibility of parameterizing a simple relationship between frequency, amplitude, and thrust production. An additional conclusion that can be reached is that if the formation of TEVs can be prevented by flow control, only LEV formation and shedding will result in a monotonic increase in thrust coefficient with *kh* as indicated by the identified mechanisms of vortex-vortex interactions.

ACKNOWLEDGEMENTS

This research did not receive any specific grant from funding agencies in the public, commercial, or not-for-profit sectors. The authors would like to acknowledge Advanced Research Computing (ARC) at Virginia Tech for providing computational resources.

REFERENCES

[1] Shyy W, Berg M, Ljungqvist D. Flapping and flexible wings for biological and micro air vehicles. vol. 35. 1999. doi:10.1016/S0376-0421(98)00016-5.

[2] Pornsin-Sirirak T, Tai Y, Nassef H. Unsteady-state aerodynamic performance of MEMS

wings. Symp Smart 2000. doi:10.1.1.4.6786&rep=rep1&type=pdf.

[3] Shyy W, Aono H, Chimakurthi SK, Trizila P, Kang CK, Cesnik CES, et al. Recent progress in flapping wing aerodynamics and aeroelasticity. Prog Aerosp Sci 2010;46:284–327. doi:10.1016/j.paerosci.2010.01.001.

[4] Knoller R. “Die Gesetze des Lufrwiderstandes,.” Flug- Und Mot 1909;3:1–7.

[5] Betz A. “Ein Beitrag zur Erklaerung des Segelfluges,.” Z Flugtech Mot 1912;3:269–72.

[6] Katzmayr R. Effect of periodic changes of angle of attack on behavior of airfoils. NACA TM 1922;147.

[7] Ober S. Note on the Katzmayr Effect on Airfoil Drag. NACA Tech Note 1925;214.

[8] Garrick I. E. Propulsion of a Flapping and Osccilating airfoil. NACA Rept 1936;567.

[9] Katz J, Weihs D. Behavior of vortex wakes from oscillating airfoils. J Aircr 1978;15:861–3. doi:10.2514/3.58463.

[10] Lai JCS, Yue J, Platzer MF. Control of backward-facing step flow using a flapping foil. Exp Fluids 2002;32:44–54. doi:10.1007/s003480200005.

[11] Tuncer I, Lai J, Platzer M. A computational study of flow entrainment over a stationary/flapping airfoil combination in tandem. 36th AIAA Aerosp Sci Meet Exhib 1998. doi:10.2514/6.1998-109.

[12] Koochesfahani MM. Vortical patterns in the wake of an oscillating airfoil. AIAA J 1989;27:1200–5. doi:10.2514/3.10246.

[13] Anderson JM, Streitlien K, Barrett DS, Triantafyllou MS. Oscillating foils of high propulsive efficiency. J Fluid Mech 1998;360:41–72. doi:10.1017/S0022112097008392.

[14] Choudhuri PG, Knight DD, Visbal MR. Two-dimensional unsteady leading-edge separation on a pitching airfoil. AIAA J 1994;32:673–81. doi:10.2514/3.12040.

[15] Ekaterinaris JA, Platzer MF. Computational prediction of airfoil dynamic stall. Prog Aerosp Sci 1998;33:759–846. doi:10.1016/S0376-0421(97)00012-2.

[16] Isogai K, Shinmoto Y, Watanabe Y. Effects of Dynamic Stall on Propulsive Efficiency and Thrust of Flapping Airfoil. AIAA J 1999;37:1145–51. doi:10.2514/2.589.

[17] Young J, S. Lai JC. Oscillation Frequency and Amplitude Effects on the Wake of a Plunging Airfoil. AIAA J 2004;42:2042–52. doi:10.2514/1.5070.

[18] Heathcote S, Wang Z, Gursul I. Effect of spanwise flexibility on flapping wing propulsion. J Fluids Struct 2008;24:183–99. doi:10.1016/j.jfluidstructs.2007.08.003.

[19] Cleaver DJ, Wang Z, Gursul I. Investigation of High-Lift Mechanisms for a Flat-Plate Airfoil Undergoing Small-Amplitude Plunging Oscillations. AIAA J 2013;51:968–80. doi:10.2514/1.J052213.

[20] Cleaver DJ, Wang Z, Gursul I, Visbal MR. Lift enhancement by means of small-amplitude airfoil oscillations at low Reynolds numbers. AIAA J 2011;49:2018–33. doi:10.2514/1.J051014.

[21] Freymuth P. Propulsive Vortical Signature of Plunging and Pitching Airfoils. AIAA J 1988;26:881–3. doi:10.2514/3.9982.

[22] Lai JCS, Platzer MF. Jet Characteristics of a plunging airfoil. AIAA J 1999;39:531–4. doi:10.2514/3.14764.

[23] Jones KD, Dohring CM, Platzer MF. Experimental and Computational Investigation of the Knoller-Betz Effect. AIAA J 1998;36:1240–6. doi:10.2514/2.505.

[24] Gopalakrishnan P, Tafti DK. Unsteady Aerodynamic and Aeroelastic Analysis of Flapping Flight. 2008. doi:etd-12182008-134215.

[25] Visbal MR. High-fidelity simulation of transitional flows past a plunging airfoil. AIAA J

2009;47:2685–97. doi:10.2514/1.43038.

[26] Martín-Alcántara A, Fernandez-Feria R, Sanmiguel-Rojas E. Vortex flow structures and interactions for the optimum thrust efficiency of a heaving airfoil at different mean angles of attack. Phys Fluids 2015;27. doi:10.1063/1.4926622.

[27] Lai JCS. Characteristics of a Plunging Airfoil at Zero Freestream Velocity 2000;39:531–4. doi:10.2514/2.1340.

[28] Lewin GC, Haj-Hariri H. Modelling thrust generation of a two-dimensional heaving airfoil in a viscous flow. J Fluid Mech 2003;492:339–62. doi:10.1017/S0022112003005743.

[29] Tafti DK. GenIDLEST - A scalable parallel computational tool for simulating complex turbulent flows. ASME-IMECE, vol. 256, 2001, p. 347–56.

[30] Gopalakrishnan P, Tafti DK. A parallel boundary fitted dynamic mesh solver for applications to flapping flight. Comput Fluids 2009;38:1592–607. doi:10.1016/j.compfluid.2009.01.006.

[31] Wang ZJ. Dissecting insect flight. Annu Rev Fluid Mech 2005;37:183–210. doi:10.1146/annurev.fluid.36.050802.121940.

[32] McHenry MJ. The morphology, behavior, and biomechanics of swimming in ascidian larvae. Can J Zool 2005;83:62–74. doi:10.1139/z04-157.

[33] Mchenry MJ, Patek SN. the Evolution of Larval Morphology and Swimming Performance 2009;58:1209–24. doi:10.1111/j.0014-3820.2004.tb01701.x.

[34] Tennekes H. The Simple Science of Flight: From Insects to Jumbo Jets. 2009. doi:10.1017/CBO9781107415324.004.

[35] Jørgensen BB. Bacteria and Marine Biogeochemistry. 2006. doi:10.1007/3-540-32144-6.

[36] Videler JJ, Wardle CS. Fish swimming stride by stride: speed limits and endurance. Rev Fish Biol Fish 1991;1:23–40. doi:10.1007/BF00042660.

[37] Gursul I, Cleaver DJ, Wang Z. Control of low Reynolds number flows by means of fluid-structure interactions. Prog Aerosp Sci 2014;64:17–55. doi:10.1016/j.paerosci.2013.07.004.

Chapter 3: Effect of Leading-Edge Vortices (LEVs) on Thrust Coefficient of a Plunging Flat Plate

Aevelina Rahman

Danesh Tafti[2]

Department of Mechanical Engineering, Virginia Tech, Blacksburg, VA 24061.

ABSTRACT

Plunging motion, characterized by frequency and amplitude is a key component in the kinematics of many flying and swimming organisms. We studied plunging of a flat plate with a broad range of reduced frequencies $0.25 \leq k \leq 16$ and plunge amplitudes $0.03125 \leq h \leq 8$ giving plunge velocities of $0.25 \leq kh \leq 4$ at $Re = 100$. This study observed that, unlike previous investigations for small plunge amplitudes, thrust does not increase monotonically with kh but reaches a maximum and then decreases. It is shown that Leading Edge Vortices (LEVs) are responsible for thrust production whereas Trailing Edge Vortices (TEVs) induce drag on the plate. At higher kh, vortex induced velocities dominate the flow with strong nonlinear vortex-vortex interactions (VVI). Predominant forms of VVI include TEV interactions that reduce the residence time of LEVs on the plate and adversely affect thrust production. Thus, in order to estimate the sole effect of LEVs on thrust coefficient, TEVs are eliminated by introducing a splitter plate in the wake of the primary plate. With only the LEVs present in the flow field, the thrust coefficient (C_T) increases monotonically. A parametrization of thrust coefficient is then done with frequency (k) and

[2] Corresponding author: 213E Goodwin Hall, 635 Prices Fork Road, Blacksburg, VA 24061; Tel: +1 (540) 231-9975; email: dtafti@exchange.vt.edu

amplitude (h) [$C_T = A.k^{1.4}h - B$ where A and B are constants, with a R^2 = 0.96 for the proposed equation].

Keywords: Plunging flat plate, low Reynolds number, thrust coefficient, vortex dynamics, LEV effect, parameterization

Declarations of interest: none

1. INTRODUCTION

This study investigates the separate effects of vortices generated on the leading edge and trailing edge of a plunging flat plate. The study covers a broad range of reduced frequencies $0.25 \leq k \leq 16$ and plunge amplitudes $0.03125 \leq h \leq 8$ to give plunge velocities ranging from $0.25 \leq kh \leq 4$. The individual effect of Leading Edge Vortices (LEVs) and Trailing Edge Vortices (TEVs) on thrust production is identified and it is shown that LEVs have a positive impact on thrust production. At high amplitude and frequency, the detrimental dynamics of plunge induced vortex-vortex interactions involving TEVs is identified. To investigate the sole effect of LEVs on thrust production, TEVs are eliminated through numerical experiments. It is shown that in the absence of TEVs, thrust increases monotonically with plunge frequency and amplitude.

The literature review, governing equations, methodology, computational geometry and parametric range remains the same as chapter 1 and is not repeated.

2. RESULTS AND DISCUSSION

The grid independency study and the validation with literature is presented in the previous chapter. Following sections emphasis results that separate the individual effect of Leading Edge Vortices (LEVs) and Trailing Edge Vortices (TEVs) on thrust production and leads to a representative parameterization of thrust with varying plunging attributes.

2.1. Variation of Mean Thrust Coefficient

The primary objective of this paper is to categorize the effects of leading edge and trailing edge vortices on thrust coefficient. Lai and Platzer [21] found that thrust coefficient increases with increasing plunge velocity (kh). Whereas Lewin et al. [28] identified reduced frequency (k) to be the primary factor in governing the vortex topology and hence efficiency with kh being the secondary factor. But their work concentrated on a relatively narrow band of small amplitudes (h ranging from 0.0125 to 0.75). Moreover, these works did not identify or isolate the individual effects of LEVs and TEVs on thrust production. The current study however works with a larger range of amplitudes (h ranging from 0.03125 to 8) and reveals that the thrust coefficient does not increase monotonically with increasing k, h or kh. Rather it exhibits an increasing trend for increasing k, h or kh until some optimum k and h combination and then exhibits a gradual decreasing trend at high k, h or kh. The behavioral trend of thrust coefficient with increasing k and h is shown in Figure 5 in which the thrust coefficient is plotted against plunge velocity (kh) for constant k (3-a) and versus k for constant kh (3-b). As can be seen from Figure 3-a, for all the frequencies (k) tested, C_T increases until a certain h or kh value and then decreases. Irrespective of the plunge velocity (kh), low frequency oscillations at $k = 0.25$ fail to produce any thrust. Nominal thrust production occurs at $kh = 0.5$ when $k \geq 4$. It is only after $kh \geq 1$ that thrust production is prevalent; but as the amplitude gets larger the increasing trend in C_T is reversed that could revert back to drag production. For a given frequency (e.g. $k = 1, 2, 4$ etc.), the amplitude associated with $kh = 1$ almost always experiences the highest thrust coefficient.

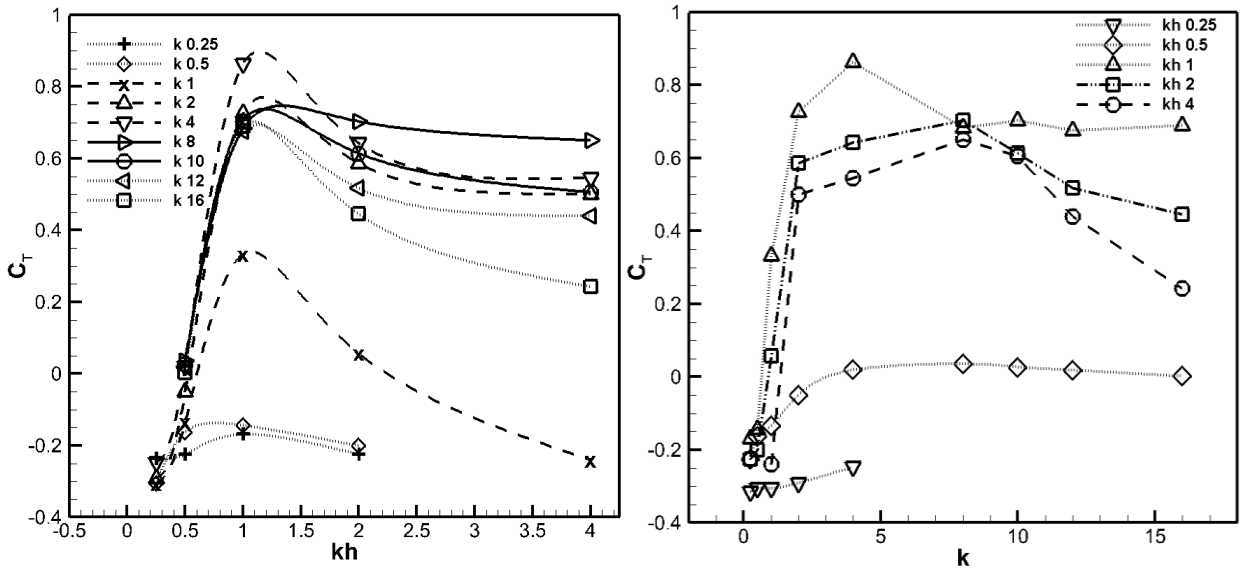

(a) **(b)**

Figure 3: Variation of thrust coefficient with (a) varying plunge velocities (*kh*) for constant reduced frequencies (*k*); (b) with varying reduced frequencies (*k*) for constant plunge velocities (*kh*).

It is clearly evident from Figure 3 that neither kh nor k is the sole parameter influencing thrust production when working with a frequency and amplitude range as wide as in the current study. These trends in thrust coefficient can be directly related to the vorticity dynamics at the oscillating plate and is explained in detail in the following sections. The following sections explain that the irregularity in the trends shown in Figure 3 can be directly attributed to trailing edge vortices (TEVs) and can be avoided by considering the effects of only leading edge vortices (LEVs) on the flow field.

2.2. Vorticity Dynamics and Thrust Coefficient

The effect of vortex dynamics on thrust production is discussed first. An upward motion of the plate creates a counterclockwise vortex at the leading edge and a clockwise vortex at the trailing

edge on the bottom side of the plate. Likewise, a downward motion creates a clockwise vortex at the leading edge and a counterclockwise vortex at the trailing edge on the top side of the plate. The extent to which these vortices are attached to the plate during the duration of the plunge cycle determines whether a net thrust or a net drag will result. Unlike the production of instantaneous lift which is dominated by pressure differences between the top and bottom sides, for the plate geometry thrust or drag is only dependent on shear forces acting on it. Thrust is obtained if the vortex induced velocities tend to push or pull the plate in a direction opposing the approach flow for a majority of time in the cycle. Whereas, drag results if the vortices force the plate in the same direction as the inflow. An example of LEV induced negative shear stress and net instantaneous thrust production is shown in Figure 4 on the top surface of the plate for a representative case of $k = 1$, $h = 0.5$. The LEV induces negative velocity near the plate surface. The resulting negative shear from the LEV acts to push the plate up stream. Thus, in general leading edge vortices (LEVs) contribute towards thrust while trailing edge vortices (TEVs) towards drag as surmised from Figure 4 where LEVs and TEVs are represented by z-vorticity (ω) contours.

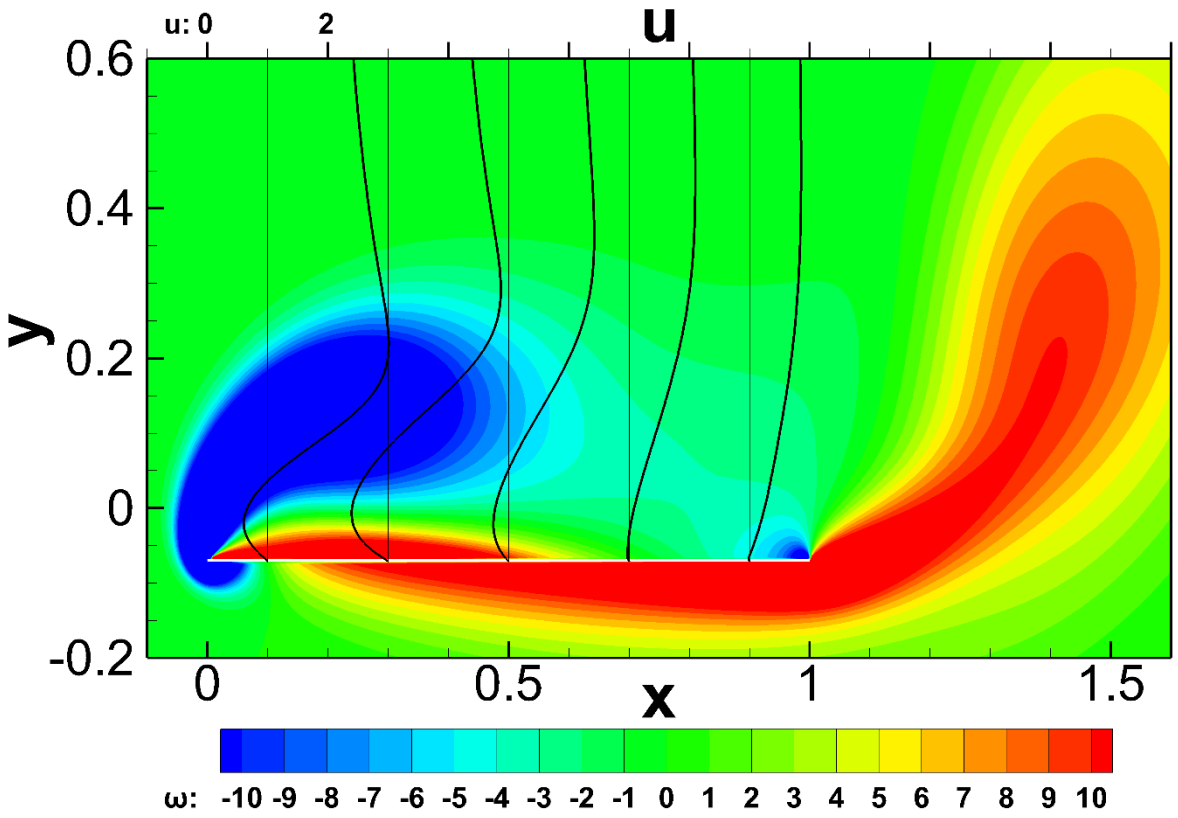

Figure 4: Instantaneous *u*-velocity profiles at different chord positions (x = 0.1, 0.3, 0.5, 0.7 and 0.9) in the presence of LEV and TEV shown in terms of z-vorticity (ω). LEVs induce negative velocity gradients (depicted by black lines) adjacent to the plate (e.g. at x = 0.1, 0.3 and 0.5) to produce thrust. The scale marked above the contour denote the u-velocity (u) scale used in the figure.

The work of Lewin et al. [28] described the vortex dynamics at various combinations of frequency and amplitude for a plunging airfoil, but did not relate that with thrust generation. In an effort to do so, we analyzed plunging plates of increasing amplitude (h) or plunge velocity (kh) for all the reduced frequencies (k). The main phenomenological observations made in those analyses regarding the individual effects of k and h are discussed below.

Increasing *k*, increases the relative convection time of LEVs across the plate and offers greater potential for the LEVs to induce a thrust producing velocity field at the plate. Increasing *h*, increases the strength and size of LEVs offering a larger potential for thrust production, however at the same time, it also increases the strength and size of TEVs which counter the thrust producing effect of LEVs on the plate surface. These effects dominate at low *h* over a wide range of *k* as long as $kh < 1$. Previously, Young et al. [10], Visbal et al. [26], and Martin et al. [12]. explored the effect of plunge parameters on thrust production, but like most other previous studies, they only explored a very narrow regime of small amplitudes and provided explanations of thrust producing phenomena for an amplitude range of roughly 0.005 to 0.259. In this regime, when $kh < 1$ and *h* is small, the TEV is convected into the wake during formation and its effect on the plate is minimal which is mostly impacted by the convecting LEV. In this low amplitude regime, thrust increases with the plunge velocity, *kh*. As observed by Lai et al. [21] even for a comparatively wider range of *kh* (0.09- 4.65) thrust coefficient displays a direct and increasing relationship with *kh* as long as the considered *h* values are on the smaller side. Although Lai et al. [21] worked with plunge velocities ranging from 0.09-4.65, their plunge amplitude varied only from 0.0125 to 0.6 which is approximately one order of magnitude smaller than the amplitude range of the present study.

As *h* increases and thus *kh* gets larger, the increasing strength and size of the LEV during each half-stroke, besides having a favorable effect on thrust production, will also by virtue of its induced velocity field draw the TEV on to the plate, thus having a detrimental effect on thrust production. For $kh > 1$, the interplay between LEVs and TEVs becomes the defining factor for thrust production which now enters a regime in which LEV-TEV interactions dominate. As *kh* increases to values much greater than unity, the interactions get more complex and non-linear effects dominate the flow and the mechanics of thrust production.

The discussion on vorticity dynamics clearly shows that neither kh nor k can be attributed as a sole parameter influencing thrust production when working with a frequency and amplitude range as wide as in the current study. Thus the observations made by Lai el al. [21] and Lewin et al. [28] are limited to their respective working range. Findings from current study are not only robust and applicable to a wider parameter range, but also closely tie the irregular trend in thrust generation to the strong non-linear vortex dynamics observed. The details of the non-linear vortex dynamics characterization are presented in the following section.

2.3. Vortex-Vortex Interactions at Large *kh*

At large h and kh, pre-dominant vortex-vortex interaction mechanisms influence thrust production by reducing the residence time of Leading edge vortices (LEVs) near the plate. The first form of interaction occurs when an incipient vortex merges with an existing vortex from the previous cycle or stroke and is convected away from the plate. This reduces the time it resides near the plate to sufficiently influence the shear stress at the plate surface. This phenomenon is favorable for thrust production when involving TEVs, as they get convected away and thus can induce limited drag. However, the phenomenon is not favorable for thrust production when Leading edge vortices merge and convect away from the plate. For LEVs, this shedding usually occurs upstream and for TEVs downstream of the plate. This mechanism is present for LEVs in all the $kh = 2$ cases, shown in Figure 5. However, although this mechanism is not prevalent for TEVs at $k = 2$ and $h = 1$ (Figure 5-a), it is present in the subsequent cases of $k = 4, h = 0.5$ (Figure 5-b) and $k = 8, h = 0.25$ (Figure 5-c). Because the presence of TEVs induce drag, their faster convection results in an increment of thrust coefficient at higher k and lower h cases for a constant kh.

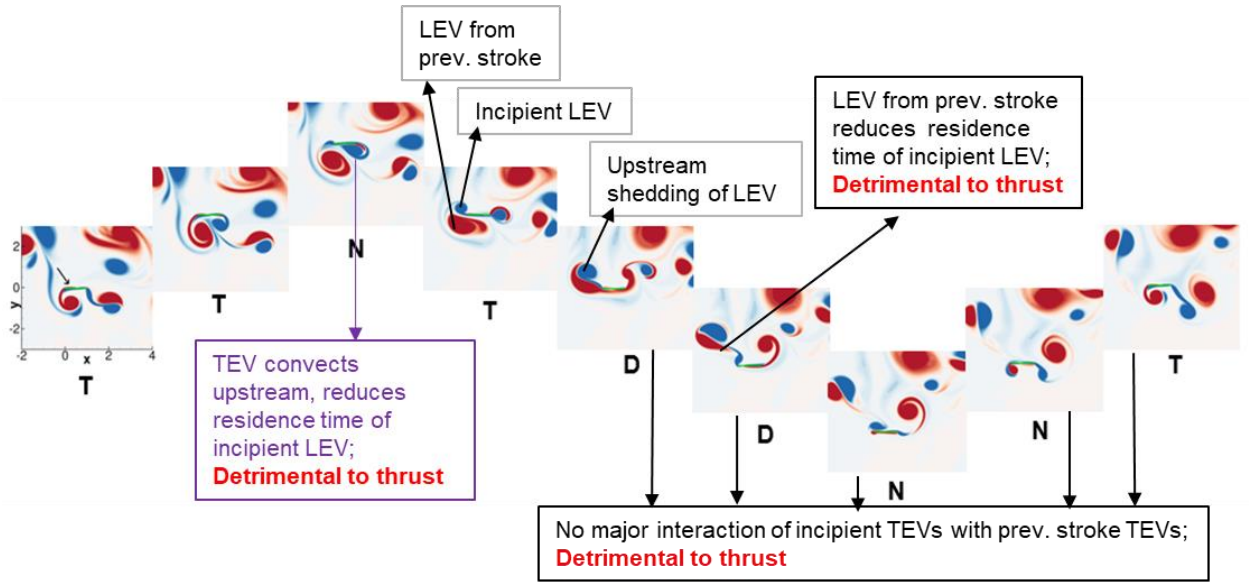

(5-a) $kh = 2;\ k = 2, h = 1$

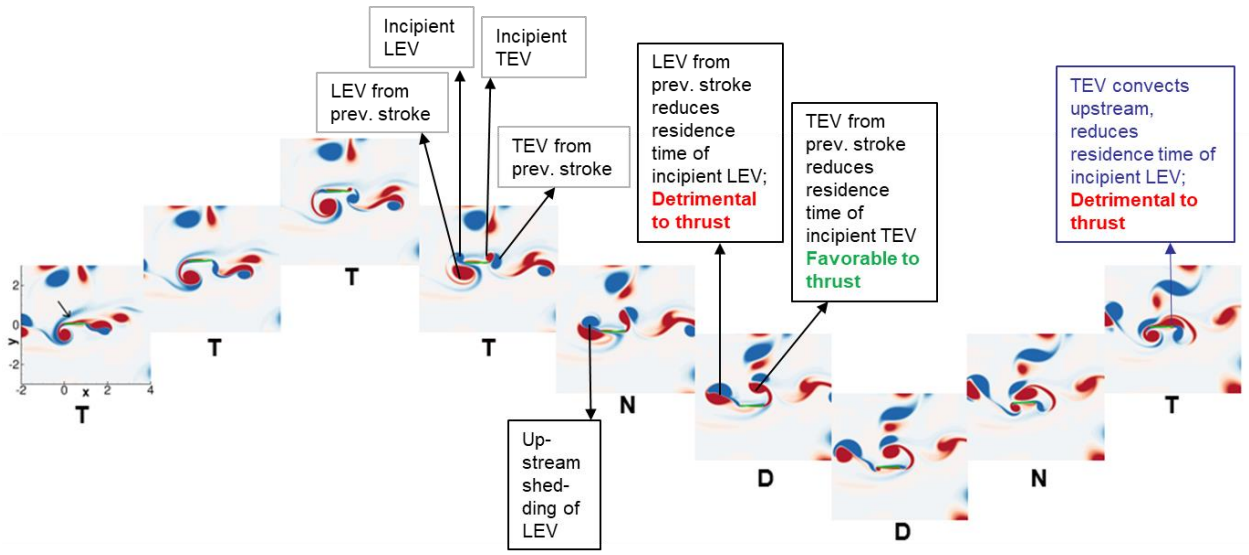

(5-b) $kh = 2;\ k = 4, h = 0.5$

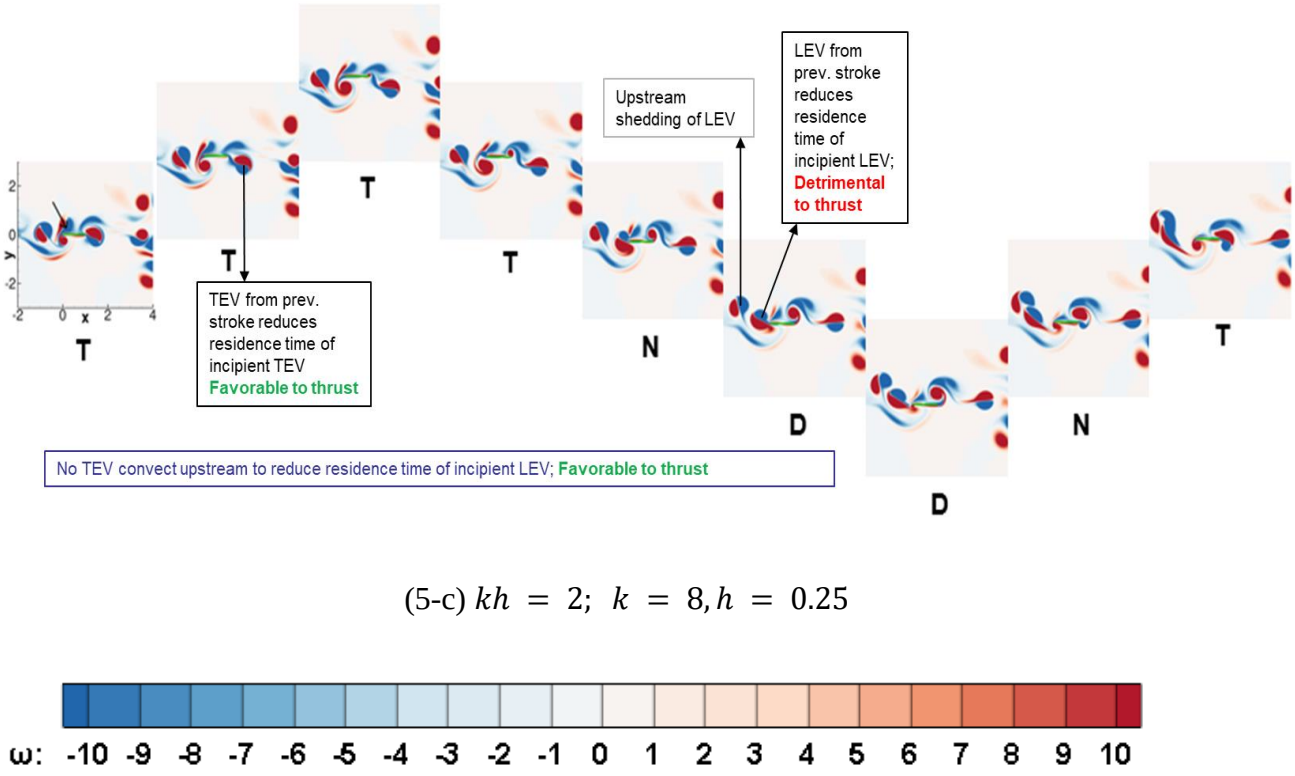

(5-c) $kh = 2;\ k = 8, h = 0.25$

Figure 5: Distribution of vortices at discrete time instances for a representative plunge cycle at $kh = 2$, with different k and h combinations. $k = 2, h = 1$ (a), $k = 4, h = 0.5$ (b) and $k = 8, h = 0.25$ (c). Entire cycle is discretized in nine time intervals for vorticity plots; vertical position of each inset represents instantaneous position of plate in plunge cycle; arrow on the first inset points to the plate; all vorticity plots use the same scale shown after (c). Subscripts '**D**', '**T**' and '**N**' indicate instantaneous forces as drag, thrust, or neutral experienced by the plate. Black and violet color annotations respectively correspond to interaction forms one and two.

Another form of vortex-vortex interaction entails the merging of a TEV with the LEV of the next stroke. This also reduces the residence time of the LEV on the plate. This is seen in large amplitude cases in which the LEV induced velocity becomes large enough to draw the TEV to the leading edge of the plate, thus introducing a detrimental effect on thrust production. This phenomenon is

analogous to the "negative reinforcement between vortices" by Anderson et al. [16]. This form of LEV-TEV merging occurs in higher amplitude cases of $kh = 2$ as seen at the start of downstroke of $k = 2$; $h = 1$ (Figure 5-a) and at the middle of up-stroke of $k = 4$; $h = 0.5$ (Figure 5-b). TEV→LEV merges are not present for comparatively smaller amplitude cases (e.g. $k = 8$; $h = 0.25$ and $k = 16$; $h = 0.125$). This happens because the size of LEV vortices reduce as h reduces and the induced velocity of the smaller vortices are not strong enough to draw TEVs to the leading edge of the plate. This is the reason that $k = 8$; $h = 0.25$ does not have the detrimental effect of TEV→LEV merges and exhibits a higher thrust value than the higher amplitude cases of the same kh (=2). However, as the plunge amplitude (h) decreases further (e.g. $k = 10$, $h = 0.2$; $k = 12$, $h = 0.167$ and $k = 16$, $h = 0.125$), the smaller LEV vortices cease to have as large an effect on thrust production as at higher plunge amplitudes. This is a major phenomenon that dictates the optimal combination of k and h resulting in maximum thrust production.

2.4. Isolating the Effects of LEVs by Eliminating TEVs

As stated earlier, the primary objective of this study is to individualize the effect of leading edge and trailing edge vortices on thrust coefficient. Along the way, the current study also aims to find a relationship between thrust coefficient and a representative parameterization of plunging frequency (k) and amplitude (h). However, the nonlinear interactions between LEVs and TEVs described in the previous section result in an irregular trend of thrust coefficient with increasing frequency and amplitude as shown in Figure 3. The vortex dynamics presented in the previous sections established that thrust production is positively influenced by Leading Edge Vortices only. Thus, in order to estimate the sole effect of LEV strength on thrust coefficient, TEVs are eliminated by introducing a splitter plate which extends far downstream of the primary plate of interest.

The role of the splitter plate is to make sure that the TEVs form far downstream of the primary plate and do not influence the vorticity dynamics on the primary plate which is only influenced by the LEVs shed at the leading edge of the plate. To ensure an optimum and effective length for the splitter plate, three different lengths were tried; 50c, 60c and 70c for a representative case of $k = 2$ and $h = 0.5$. The length of 60c was found to be adequate as the percentage difference between the thrust coefficients between a splitter plate of length 60c and 70c is significantly low. The validation of an adequate splitter plate length is shown in table 5.

Table 5: Thrust coefficient (C_T) for different splitter plate lengths

50c		**60c (base length)**		**70c**	
C_T	% diff.	C_T	% diff.	C_T	% diff.
10.6	8.6	11.2	3.4	11.6	0

In the calculations with the splitter plate, a coarser grid is used to balance the computational cost. The resolution of the coarser grid was adequate to ascertain that the thrust producing vortices (LEVs) are well resolved. Similar to the actual chord, cases with varying reduce frequency and amplitude are simulated with the splitter plate in place. All the characteristic parameters are kept the same as the p plate case, namely $Re = 100$, based on inflow velocity and length of the actual chord. All the splitter plate cases were run for a significant number of cycles with an initial period of development before time averaging was initiated as mentioned in Table 2. As the force calculation was done only on the first chord length from the leading edge, only the effect of LEVs was captured in the calculated thrust coefficient. Figure 6 shows the calculated thrust coefficient after being scaled appropriately.

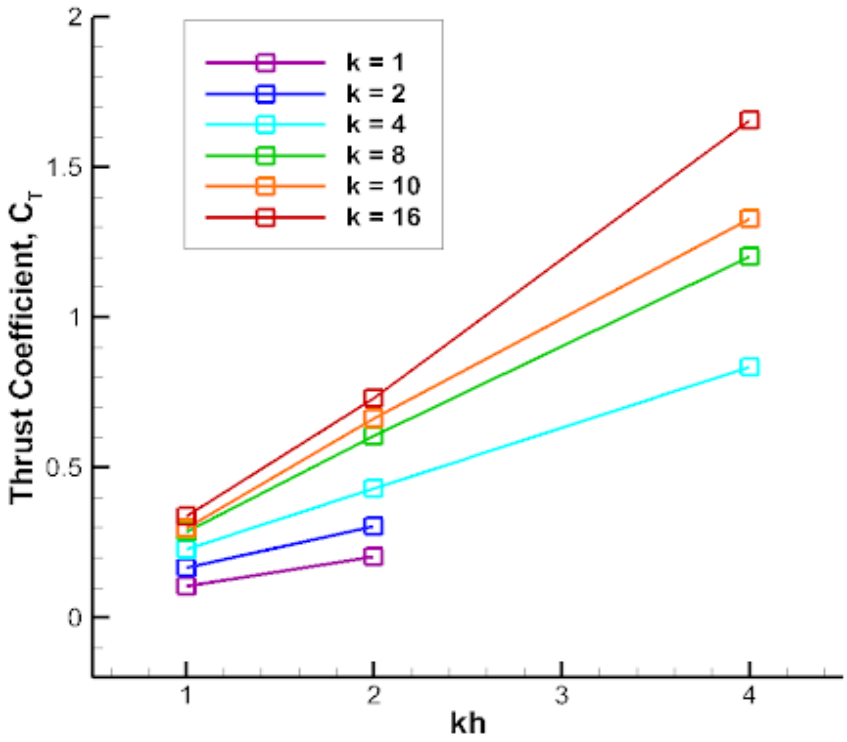

Figure 6: Behavioral trend of thrust coefficient with varying plunge velocity for the splitter plate cases

Thrust coefficient exhibits a regular increasing trend with increasing amplitude (*h*) for all the different frequencies (*k*) tested.

For all the amplitudes tested, the thrust increment is always in a factor more than two (depicted by Ratio (*R*)) for doubled frequency as shown in Table 6. The rate of thrust increment decreases slightly at larger frequencies which is depicted by decreasing values of ratio (*R*) for a constant amplitude. Ratio (*R*) depicts the ratio of C_T between increasing (with a factor of two) frequencies of same amplitude.

Table 6: Trend of thrust coefficient increase for increasing reduced frequency at different plunge amplitudes

h	k	C_T	Ratio (R)
0.125	4	0.11	
	8	0.29	2.64
	16	0.74	2.55
0.25	2	0.08	
	4	0.23	2.88
	8	0.61	2.65
	16	1.59	2.60
0.5	1	0.06	
	2	0.17	2.83
	4	0.44	2.59
	8	1.13	2.56
1	1	0.11	
	2	0.31	2.82
	4	0.85	2.74
2	1	0.21	
	2	0.55	2.62

This indicates that the dependence of thrust coefficient is not entirely linear with both frequency and amplitude. However, it is found that thrust coefficient varies linearly with plunge amplitude (h) and as a power of 1.4 with reduced frequency (k).

With the regular increasing trend of thrust coefficient in the flow field with only LEVs, a direct parameterization is now achievable between thrust coefficient (C_T) and the non-dimensional parameters of reduced frequency (k) and plunge amplitude (h). The parametric equation is given in Eq. 9. As seen in figure 7, the different data points of observed C_T for various k and h in the presence of LEVs only shows very good agreement with the correlation given by Eq. 9. Here, A and B are constants, with a R^2= 0.96 for the proposed equation.

$$C_T = Ak^{1.4}h - B \tag{9}$$

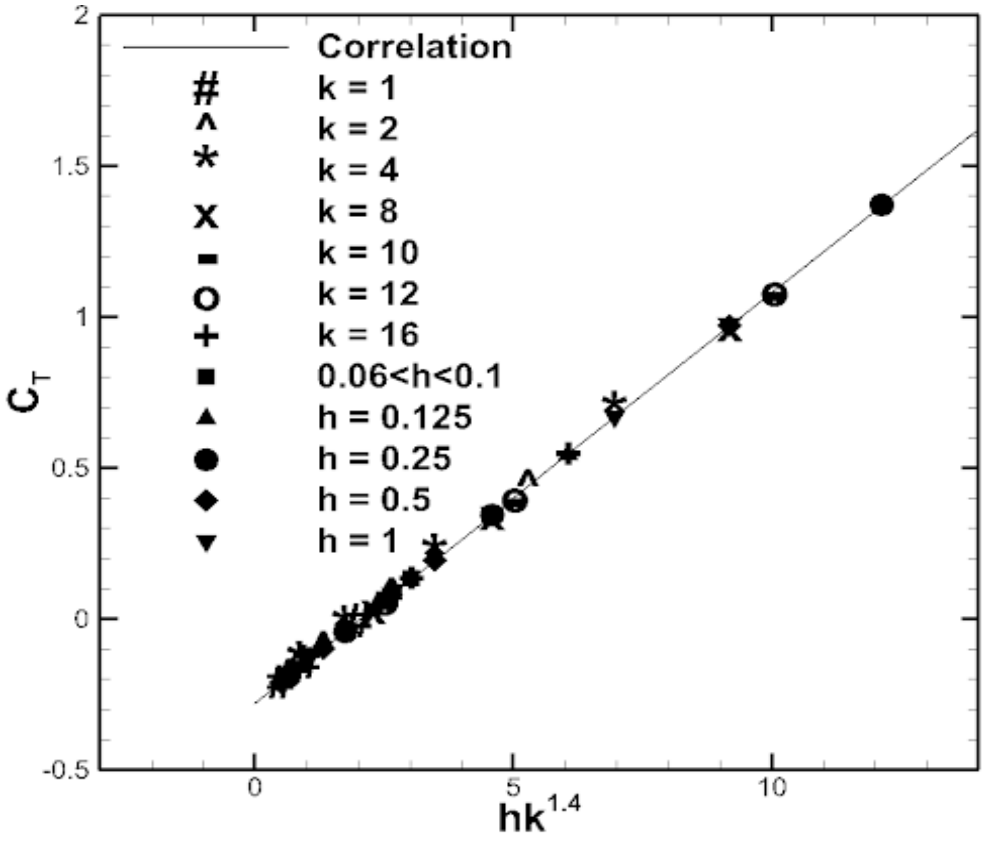

Figure 7: Parameterization of thrust coefficient for a "no TEV" flow

Upon consideration of the vortex field in the presence of the splitter plate, similar observations are made as without the splitter plate. The upstream convection of LEVs is still present for high amplitude cases. However, with only LEVs present in the flow field, the primary contribution of TEVs towards drag is eliminated. Moreover, with no TEVs to negatively interact with LEVs and reduce their residence time on the plate, the net result is a significant amount of thrust even for higher amplitude cases of kh >1.

This result indicates the potential of only having leading edge vortices in the flow field. If this is achievable by removing trailing edge vortices via flow control, then a regular increasing trend will be observed for thrust coefficient over a broad range of plunge frequency and amplitude.

3. SUMMARY AND CONCLUSIONS

The canonical case of a plunging flat plate at Re =100 is investigated over a wide range of reduced frequencies $0.25 \leq k \leq 16$ and plunge amplitudes $0.03125 \leq h \leq 8$ to give plunge velocities ranging from $0.25 \leq kh \leq 4$. It is found that thrust does not increase monotonically with kh but reaches a maximum at $kh = 1$ for most combinations of k and h and reduces thereafter. The rate at which thrust production drops is dependent on h – decreasing rapidly at large plunge amplitudes when the reduced frequency is small, so much so that at low k and high kh the force produced reverts back to drag.

It is shown that LEVs contribute to thrust production by inducing counter flow velocities near the plate, whereas TEVs do the opposite. At low $kh < 1$, the LEVs do not have the strength to induce a counter-flow at the plate even though they convect down the plate to the trailing edge and the TEVs are shed directly into the wake. As kh increases, the LEVs increase in size and have enough strength to induce a counter-flow near the plate as they convect over the plate. At the same time, the induced velocities of both LEVs and TEVs are not high enough for the TEVs to become consequential by convecting upstream and influence the flow at the plate. Thrust production is maximum in this regime. As kh increases further, particularly as h increases, the strength and size of LEVs and TEVs increase enough to counter the mainstream flow and enter into a regime in which vortex-vortex interactions dominate. Some predominant forms of such vortex-vortex interactions are identified, the net effect of which is to decrease the residence time of LEVs near the plate and reduce thrust.

In order to estimate the sole effect of LEV strength on thrust coefficient, TEVs are eliminated by introducing a splitter plate in the wake of the primary plate. This splitter plate is nothing but

numerical experimentation to eliminate the immediate effect of TEVs on the plate. With only LEVs present in the flow field, the thrust coefficient (C_T) increases monotonically with kh for all the tested frequencies. With this regular trend, a parametrization of thrust coefficient is possible with frequency (k) and amplitude (h). Observed values of C_T closely follow the proposed parametric equation with an excellent R^2 value.

The current study identifies separate and opposite effects of leading edge and trailing edge vortices in thrust production and thus relates vortex dynamics with thrust production in rigorous detail compared to previous studies. Finally, this study successfully claims that, if the formation of TEVs can be prevented by flow control, only LEV formation and shedding results in a monotonic increase in thrust coefficient with kh and thus allows for a predictive parameterization of C_T with frequency (k) and amplitude (h).

ACKNOWLEDGEMENTS

This research did not receive any specific grant from funding agencies in the public, commercial, or not-for-profit sectors. The authors would like to acknowledge Advanced Research Computing (ARC) at Virginia Tech for providing computational resources.

REFERENCES

[1] Shyy W, Berg M, Ljungqvist D. Flapping and flexible wings for biological and micro air vehicles. vol. 35. 1999. doi:10.1016/S0376-0421(98)00016-5.

[2] Pornsin-Sirirak T, Tai Y, Nassef H. Unsteady-state aerodynamic performance of MEMS wings. Symp Smart 2000. doi:10.1.1.4.6786&rep=rep1&type=pdf.

[3] Shyy W, Aono H, Chimakurthi SK, Trizila P, Kang CK, Cesnik CES, et al. Recent

progress in flapping wing aerodynamics and aeroelasticity. Prog Aerosp Sci 2010;46:284–327. doi:10.1016/j.paerosci.2010.01.001.

[4] Knoller R. “Die Gesetze des Lufrwiderstandes,.” Flug- Und Mot 1909;3:1–7.

[5] Betz A. “Ein Beitrag zur Erklaerung des Segelfluges,.” Z Flugtech Mot 1912;3:269–72.

[6] Katzmayr R. Effect of periodic changes of angle of attack on behavior of airfoils. NACA TM 1922;147.

[7] Ober S. Note on the Katzmayr Effect on Airfoil Drag. NACA Tech Note 1925;214.

[8] Garrick I. E. Propulsion of a Flapping and Osccilating airfoil. NACA Rept 1936;567.

[9] Katz J, Weihs D. Behavior of vortex wakes from oscillating airfoils. J Aircr 1978;15:861–3. doi:10.2514/3.58463.

[10] Young J, S. Lai JC. Oscillation Frequency and Amplitude Effects on the Wake of a Plunging Airfoil. AIAA J 2004;42:2042–52. doi:10.2514/1.5070.

[11] Heathcote S, Wang Z, Gursul I. Effect of spanwise flexibility on flapping wing propulsion. J Fluids Struct 2008;24:183–99. doi:10.1016/j.jfluidstructs.2007.08.003.

[12] Martín-Alcántara A, Fernandez-Feria R, Sanmiguel-Rojas E. Vortex flow structures and interactions for the optimum thrust efficiency of a heaving airfoil at different mean angles of attack. Phys Fluids 2015;27. doi:10.1063/1.4926622.

[13] Lai JCS, Yue J, Platzer MF. Control of backward-facing step flow using a flapping foil. Exp Fluids 2002;32:44–54. doi:10.1007/s003480200005.

[14] Tuncer I, Lai J, Platzer M. A computational study of flow entrainment over a stationary/flapping airfoil combination in tandem. 36th AIAA Aerosp Sci Meet Exhib 1998. doi:10.2514/6.1998-109.

[15] Koochesfahani MM. Vortical patterns in the wake of an oscillating airfoil. AIAA J

1989;27:1200–5. doi:10.2514/3.10246.

[16] Anderson JM, Streitlien K, Barrett DS, Triantafyllou MS. Oscillating foils of high propulsive efficiency. J Fluid Mech 1998;360:41–72. doi:10.1017/S0022112097008392.

[17] Choudhuri PG, Knight DD, Visbal MR. Two-dimensional unsteady leading-edge separation on a pitching airfoil. AIAA J 1994;32:673–81. doi:10.2514/3.12040.

[18] Ekaterinaris JA, Platzer MF. Computational prediction of airfoil dynamic stall. Prog Aerosp Sci 1998;33:759–846. doi:10.1016/S0376-0421(97)00012-2.

[19] Isogai K, Shinmoto Y, Watanabe Y. Effects of Dynamic Stall on Propulsive Efficiency and Thrust of Flapping Airfoil. AIAA J 1999;37:1145–51. doi:10.2514/2.589.

[20] Freymuth P. Propulsive Vortical Signature of Plunging and Pitching Airfoils. AIAA J 1988;26:881–3. doi:10.2514/3.9982.

[21] Lai JCS, Platzer MF. Jet Characteristics of a plunging airfoil. AIAA J 1999;39:531–4. doi:10.2514/3.14764.

[22] Jones KD, Dohring CM, Platzer MF. Experimental and Computational Investigation of the Knoller-Betz Effect. AIAA J 1998;36:1240–6. doi:10.2514/2.505.

[23] Gopalakrishnan P, Tafti DDK. Unsteady Aerodynamic and Aeroelastic Analysis of Flapping Flight. 2008. doi:etd-12182008-134215.

[24] Cleaver DJ, Wang Z, Gursul I. Investigation of High-Lift Mechanisms for a Flat-Plate Airfoil Undergoing Small-Amplitude Plunging Oscillations. AIAA J 2013;51:968–80. doi:10.2514/1.J052213.

[25] Cleaver DJ, Wang Z, Gursul I, Visbal MR. Lift enhancement by means of small-amplitude airfoil oscillations at low Reynolds numbers. AIAA J 2011;49:2018–33. doi:10.2514/1.J051014.

[26] Visbal MR. High-fidelity simulation of transitional flows past a plunging airfoil. AIAA J 2009;47:2685–97. doi:10.2514/1.43038.

[27] Lai JCS. Characteristics of a Plunging Airfoil at Zero Freestream Velocity 2000;39:531–4. doi:10.2514/2.1340.

[28] Lewin GC, Haj-Hariri H. Modelling thrust generation of a two-dimensional heaving airfoil in a viscous flow. J Fluid Mech 2003;492:339–62. doi:10.1017/S0022112003005743.

[29] Tafti DK. GenIDLEST - A scalable parallel computational tool for simulating complex turbulent flows. ASME-IMECE, vol. 256, 2001, p. 347–56.

[30] Gopalakrishnan P, Tafti DK. A parallel boundary fitted dynamic mesh solver for applications to flapping flight. Comput Fluids 2009;38:1592–607. doi:10.1016/j.compfluid.2009.01.006.

[31] Rahman A, Tafti D. Characterization of heat transfer enhancement for an oscillating flatplate-fin. Int J Heat Mass Transf 2020;147. doi:10.1016.

[32] Gursul I, Cleaver DJ, Wang Z. Control of low Reynolds number flows by means of fluid-structure interactions. Prog Aerosp Sci 2014;64:17–55. doi:10.1016/j.paerosci.2013.07.004.

Chapter 4: Turning-Ascending Flight of a *H. pratti* Bat

Aevelina Rahman
Peter Windes[3]
Danesh Tafti[4]

Department of Mechanical Engineering, Virginia Tech, Blacksburg, VA 24061

ABSTRACT

Bats exhibit a high degree of agility and provide an excellent model system for bioinspired flight. The current study investigates an ascending right turn of a *H. pratti* bat and elucidates on the kinematic features and aerodynamic mechanisms used to effectuate the maneuver. To initiate and sustain the turn, the bat utilizes roll and yaw rotations of the body to different extents synergistically to generate the centripetal force for a stable turn. The turning moments are generated by drawing the wing inside the turn closer to the body, by introducing phase lags in force generation between the wings and redirecting force production to the outer part of the wing outside of the turn. Deceleration in flight speed, an increase in flapping frequency, shortening of the upstroke, and thrust generation at the end of the upstroke was observed during the ascending maneuver. The bat consumes about 0.67 W power to execute the turning ascending maneuver which is approximately two times the power consumed by similar bats during level flight. Upon comparison with a similar maneuver by a *H. armiger* bat (Windes et al. [1]), some commonalities as well as differences were observed in the detailed wing kinematics and aerodynamics.

Keywords: Flapping flight, Aerodynamics, Maneuvering bat flight, Ascending and turning bat flight, Maneuvering techniques

[3] Current address: Eastman Chemical Company, **Kingsport, TN 37660**
[4] Corresponding author: 213E Goodwin Hall, 635 Prices Fork Road, Blacksburg, VA 24061; Tel: +1 (540) 231-9975; email: dtafti@exchange.vt.edu

Declarations of interest: none

1. INTRODUCTION

Bats exhibit excellence at maneuvering due to their highly articulated skeletal structures and pliant wing membrane that provides flexibility and control over aerodynamic force generation [2]. They show agility in air which is an important element for survival for most flying species as it is critical for capturing prey, avoiding predators, or navigating through cluttered habitats. The natural agility and maneuverability allow bats to rapidly initiate a turn, to execute a turn within a tight radius or to re-direct it's trajectory within a wing beat. These flight traits are consequential in bioinspired micro air vehicle (MAV) design, and to this purpose birds and insects have been studied extensively in attempts to emulate desirable flight capabilities like speed, efficiency, quietness, endurance, durability, gust tolerance, light weight, control mechanisms and agility [3–16]. Studies regarding bat flights have received less attention in the literature compared to insects [9,13,15,17] mainly due to the challenges associated with measuring the complex wing articulation during flight. However, with recent advances in motion capturing technology [18,19], quite a few bat flight studies have been carried out providing a compelling model for highly agile and maneuverable MAV designs.

A significant portion of prior bat flight aerodynamics research has primarily focused on different aspects of straight flight such as wing and bone structure [2,20–23], flight efficiency and performance [24–30], complexity in wing kinematics [31–33] and aerodynamics [34–42]. These studies have provided tremendous insight into wing structure and articulation during flight and its effect on aerodynamic force generation. Maneuvering flight on the other hand, brings in elements in wing articulation and aerodynamics not present in straight flight which are very worthy of investigation in spite of the challenges associated with capturing the wing kinematics during such

flight and its aerodynamic interpretation [43–47]. Norberg et al. [43] studied two bat species performing a 180◦ roll maneuver and a sideslip with a single camera. Although, there were no 3D kinematic data generated, a common mechanism was observed for both maneuvers with pronation of one wing and supination of the other. Multiple cameras were used by Aldridge et al. [47] to record the flight of six different species in a flight tunnel. 3D reconstructions were done for several of them which resulted in correlations between turning radius and various morphological parameters. Iriarte-D´ıaz et al. [45] investigated 90◦ turns of fruit bats in an L-shaped tunnel with 3D motion capture and were able to reconstruct detailed kinematic data. They observed that the right turn maneuver was effected by a combined bank and yaw rotation of the body. They also reported various kinematic parameters throughout the duration of the turn which shed light on the details of the turn. Henningson et al. [46] investigated side maneuvers of a brown long-eared bats using particle image velocimetry (PIV) and 3D motion capture which enabled for a coupled analysis of kinematics and the resulting flow field. They observed most maneuvers to be initiated during the upstroke than during the down-stroke with the most common use of asymmetries in drag or thrust. They also reported the time histories of wing amplitude, lift, thrust, wing length, angle of attack, and body orientation for several maneuvers. Boerma et al. [48] investigated the recovery maneuver from disruptive forces like aerial stumbles for fruit bats and reported that the bats primarily responded by adjusting extension of wing-joints, and recovered pre-disturbance body orientation and symmetrical wing motions very fast, over the course of just one wingbeat cycle. They also used a simplified dynamical model that showed that the inertial torques generated during recovery drives the observed body reorientation. The same group also investigated landing maneuvers and linked roosting ecology with landing biomechanics [49]. These studies while providing important insights into maneuvering flight, also highlight some of the inherent

challenges. To start with, data collection on flight kinematics in a wind tunnel suppresses the bat's ability to perform maneuvers with significant heading change. For example, the shallow turn investigated by Henningson et al. [46] resulted in a heading change of only 4°. Although the static L-shaped flight tunnel used by Iriarte-D´ıaz et al. [45] allowed complex maneuvers with a heading angle change of as large as 45°, it could not allow for the use of PIV flow measurements for aerodynamic analysis.

Using measured wing kinematic data as input boundary conditions to run detailed aerodynamic simulations provides a powerful option for establishing the causal relationship between wing motion and force generation to effect the maneuver. Thus, the current study follows a computational approach to deconstruct the detailed kinematic-aerodynamic nuances of a maneuvering bat flight. This approach has been used in the literature mostly for level flight [32,36,40] and recently for maneuvering flight by Windes et al. [1,50]. Using measured kinematics and aerodynamic simulations, Windes et al. [1] investigated a right ascending sweeping turn of a large insectivorous bat (*Hipposideros armiger*) and found simultaneous and synergistic banking and yawing to be the fundamental turning mechanism. Later, an analysis of a U-turn of the same bat revealed that active control of the velocity along with the body rotations allows the bat to achieve the centripetal force for the 180-degree turn [50].

The current study is motivated by the desire to investigate a specific maneuver in a different bat species than done in previous works. In this paper we investigate a *Hipposideros Pratti* (*H. pratti*) or Pratt's Roundleaf bat while executing an ascending right sweeping turn. Combined kinematic and aerodynamic studies on bat maneuvers are rare in the literature and provide a much needed gateway for a deeper characterization of the relationship between wing motions and the ensuing aerodynamics, which is the dominant force producing mechanism over the course of the maneuver.

The primary focus is to elucidate on the following: mechanism used to generate force asymmetries; dominance of lift, thrust or drag asymmetries; difference in mechanism between the initiation and rest of the turn; role of body rotations; contribution of banking and yawing; the relative contribution of upstrokes and down strokes; and the energy cost of achieving the maneuver. These are investigated by a combined effort of kinematic measurements and detailed computational analysis of the aerodynamic forces generated during the turn. The kinematic data is collected in a flight tunnel using a 3D optical motion capture system [29,36,44] while the numerical simulations are run using the wing kinematic data as an input boundary condition to calculate the flow and pressure field around the maneuvering bat's wings, giving access to accurate spatially and temporally resolved force data on the wing surface throughout the entirety of the maneuver. Aerodynamic forces and rotational moments are analyzed in two main reference frames; the global coordinate system and a body fixed local coordinate system. This framework allows for investigating the underlying mechanisms causing body rotations and turning forces.

A secondary aim of this paper is to compare the current flight characteristics to that of Windes et al. [1] in which a *H. armiger* bat performs a similar maneuver. This is done with several caveats: to have a living creature perform the exact same maneuver in all its attributes is highly unlikely; even within the same species different bats will exhibit different individual traits that will influence their kinematics; and the same bat may have variations in how it performs the same maneuver. One way to eliminate these variations would be to take the mean of several flight experiments performing the same maneuver by measuring only a few characteristic data points on the body and wings. While this method will give macro-flight kinematic parameters, it will not yield the detailed wing kinematics needed to elucidate on the aerodynamic forces produced by the wing articulation to effect the maneuver. In spite of these caveats, because there are only a handful of investigations

in the literature on aerodynamic characterization of maneuvering bats, any insights into similarities and differences between flights, however limited, will contribute to a more comprehensive understanding of bat flight.

2. METHODS

2.1. Experimental Set-up and Motion Capture

The bat used for current study is an adult female Pratt's roundleaf bat (*Hipposideros pratti*) weighing 55 g. The animal was kept with a group of conspecifics in a controlled indoor environment designed to allow natural movement given its typical flight behavior. Ethical procedures according to Virginia Tech's Institutional Animal Care and Use Committee (protocol number 15-067) were followed. Kinematic data were collected using an optical 3D motion capture system put together inside a 1.2 m×1.2 m×5 m open-ended flight tunnel. The system comprised of 21 synchronized video cameras arranged in 3 rings located about 40 cm apart. The details of the camera specification and their arrangement is given in a prior work [36]. After being released, the bat flew without interruption through the tunnel and the camera arrays recorded the flight featuring different maneuvers at 120 frames per second and in 1920×1080 pixel resolution. The camera array was calibrated using the Svoboda multi-camera self-calibration method [51].

The recorded flight path [53 ("Maneuvering_flight_trajectory.mp4")] consists of 3 full wingbeat cycles and an extra half-cycle at the end, i.e., 3.5 wingbeat cycles, captured over 55 video frames during which the bat executes an ascending right turn with deceleration in the flight direction similar to Windes et al. [1]. Each cycle is defined to start with an upstroke and end with a down-stroke. The last half cycle (upstroke) is included in spite of the second half of the cycle (down-stroke) being incomplete as the bat continues to ascend outside the range of the motion capture

system. After the last upstroke that was analyzed in the current paper, the bat completes two full flaps before perching on the ceiling of the tunnel.

In order to track the wing motion, about 150 small white circular markers made of medical tape were set to the bat's wings to capture the detailed spatio-temporal kinematic features of the wing as it effectuates the maneuver. Stereo triangulation was performed for the 55 frames of the current flight using a custom MATLAB code to achieve a total of (150 points) × (55 frames) ~ 8250 points in 3D space. In the event of spatial or temporal occlusions among those points, a temporal spline curve and a spatial implicit surface reconstruction [32] was used to fill in the missing data. Afterwards a 3D reconstruction was done using a MATLAB code where a semi-automated technique was used to define point correspondences between frames, the details of which are described in previous works [1,32,36,53 ("Raw data for an ascending right turn of Hipposiderous Pratti")]

2.2. Reference Frames

For kinematic and aerodynamic analysis, two reference frames are defined initially. The global or ground reference frame (x_g, y_g, z_g) is a fixed, inertial coordinate system with x_g directed along the longitudinal tunnel axis, z_g directed upward opposing gravity, and y_g directed normal to both x_g and z_g.

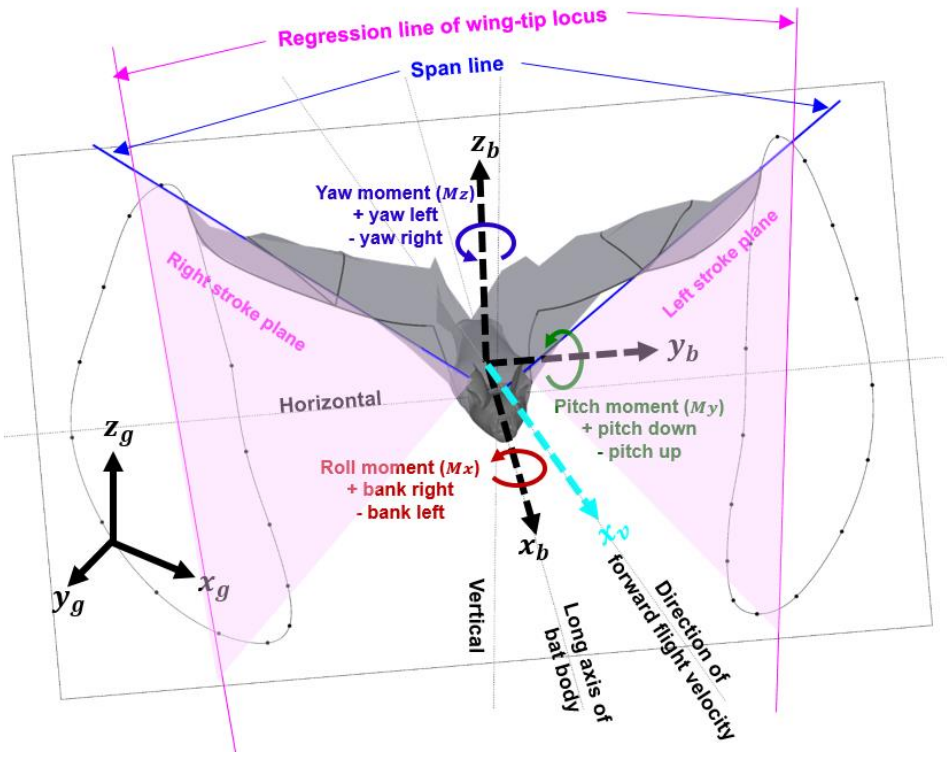

Figure 1: Definition of the global, body-fixed and velocity-based coordinate system with bat body orientation at an arbitrary point during flight.

The local or body-fixed reference frame (x_b, y_b, z_b) is defined based on the instantaneous orientation of the bat's body and changes with time. The non-inertial body-fixed reference frame moves with the bat as it flies along; one such instance is shown in Figure 1. The origin is set at the center of mass (COM) of the bat body. The +ve y_b vector points laterally toward the left wing while the +ve x_b points along the axis of the bat body with perpendicularity enforced between the basis vectors x_b and y_b. Lastly, the z_b upward pointing vector is found by taking a right-handed cross-product between x_b and y_b. Detailed definition and description of the three basis vectors in the body-fixed coordinate system is presented in Windes et al. [1]. The stroke plane, local aerodynamic forces and moments are all calculated using the instantaneous body-fixed coordinate system.

Another local coordinate system, aligned with the velocity vector is also defined, as the long axis of the body might not always be aligned with the velocity vector of a maneuvering trajectory. For example, in the current flight, the long axis of the body mostly lies inside the trajectory of the turn. The velocity-based reference frame (x_v, y_v, z_v) is defined based on the instantaneous velocity vector which changes with time. Figure 1 shows such an instantaneous velocity vector in cyan which is also the direction of the +ve x_v vector. The +ve y_v vector again points laterally towards the left wing with orthogonality enforced with the x_v direction. The +ve z_v vector points upwards and is found by taking a right-handed cross-product between x_v and y_v.

Figure 1 also defines the span (blue) as the line connecting the shoulder to the wingtip. The wingtip loci for the right and left wings are shown for a wingbeat cycle with two regression lines (pink) fitted through them. These regression lines along with a fixed root at the two sides of the wing make up the respective stroke planes shown in pale pink. Euler rotations about the body fixed x_b, y_b and z_b axes are defined respectively as roll, pitch, and yaw with right-roll, left-yaw and pitch-down as positive. The rotations apply in an orderly manner with yaw first, then pitch and then roll. The negative of the pitch angle is presented later in the paper as the elevation angle to denote pitch-up by a positive value.

2.3. Aerodynamic Analysis

Following the kinematic data collection and pre-processing, the in-house incompressible Navier–Stokes solver, GenIDLEST [52] was used to simulate the aerodynamic flow around the bat during the maneuvering flight. The Immersed Boundary Method (IBM) is used to resolve the wing motion which is represented by a triangulated surface mesh immersed in a volumetric mesh. The location and spatial orientation of the surface mesh is advanced in time based on the wing kinematics [53

("ctr_pts.ucd", " surfgrid.s001", " splines.dat", " ibm_movement_bat.f90")]. No slip boundary conditions are enforced on the wing surface.

The in-house Navier–Stokes solver has been utilized and validated for a diverse field of applications like bio-locomotion [54], bio-fluid mechanics [55], multiphase fluid-particulate system [56], turbo-machinery [57][58], heat transfer augmentation [59] etc. The IBM formulation specifically has been validated and applied to many different geometries and flow conditions, e.g. [60–62]. For further details about the computational setup used for the current paper, please refer to prior work on bat flight aerodynamics [1,36,40,50]. The computational domain extends from 8 chord lengths upstream to 24 chord lengths downstream in the x_g direction with a cross-section of 16 x 16 chord lengths in the y_g and z_g directions, respectively, representing the tunnel cross-section. In order to reduce the computational complexity of having to resolve the flying bat which would require a very fine mesh throughout the computational domain, a moving reference frame is used to limit the movement of the bat in the computational domain. The moving reference frame follows the mean velocity of flight, 2.40 m/s in the x_g-direction, 0.36 m/s in the y_g-direction, and 0.54 m/s in the z_g-direction. Perturbations on the mean flight velocities are reflected in the kinematics of the bat wings. The perturbed wing motion is shown in an animation in the supplementary documents [53 ("animation1.avi")]. After the completion of the simulations, the results are post-processed by adding back the moving reference frame velocity. Figure 2 shows the background and surface grid distribution.

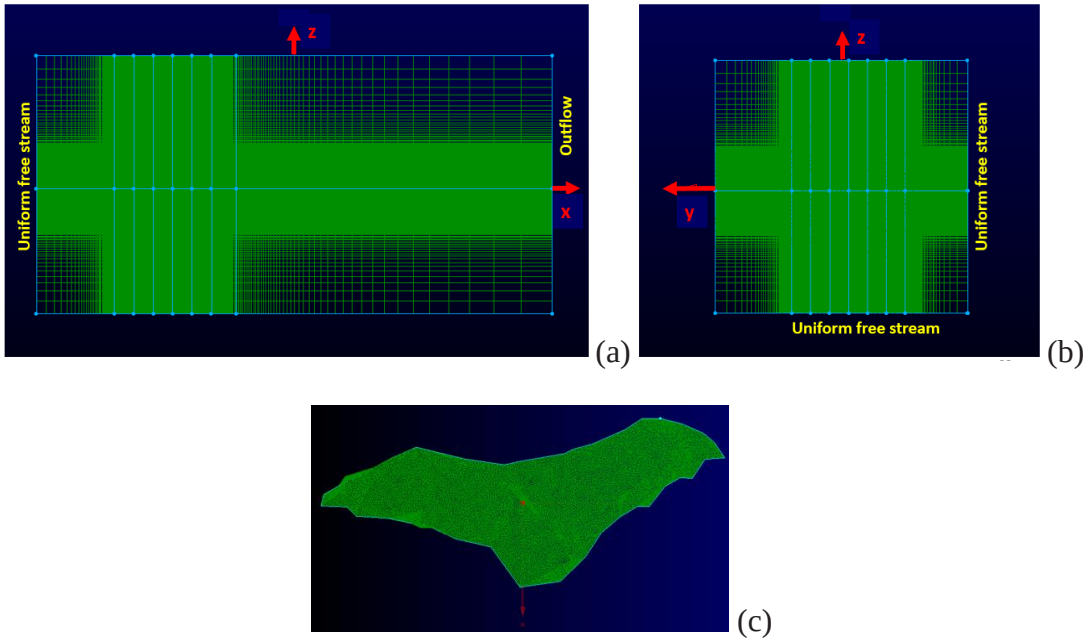

Figure 2: Schematic of computational grid (a) front view of background grid (38.2 million cells), (b) side view of background grid and (c) bat surface grid (42,000 surface elements).

2.4. Validation

In order to characterize the accuracy of the kinematic data from the motion capture methodology, the resulting lengths of two relatively rigid arm bones (bone 1: shoulder to elbow and bone 2: elbow to wrist) are compared at different time instances within the flight by using the derived spatial locations of shoulder, elbow and wrist markers. This is done for both the left and the right wing bones. The comparisons are done at the most outstretched frames of each downstroke. Figure 3 shows that the derived bone lengths from both wings are within 5% of each other over different cycles validating the motion capture methodology and the extracted kinematic data from the raw measurements. Considering that the diameter of each white marker used was 3 mm and the bone lengths measured are ~50 mm (shoulder to elbow) and ~90 mm (elbow to wrist), the observed difference could very likely be due to the uncertainty associated with identifying the center of each

marker location. As will be shown later, the ability of the simulated aerodynamic forces to reproduce the experimental flight trajectory of the bat further validates the accuracy of the extracted kinematic data which is used as input to the aerodynamic simulations.

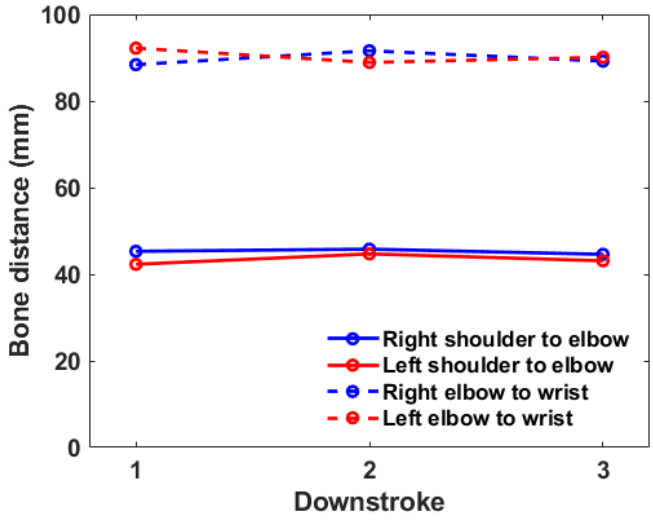

Figure 3: Comparison of right and left wing bone lengths at three time instances during downstrokes of the wing beat cycles.

To validate the aerodynamic analysis, four different grid sizes are tested for their ability to predict the time-dependent forces generated by the bat during the recorded flight. These are summarized in Table 1. The coarsest background grid resolves the bat with 20 cells per wing chord length, whereas the finest grid uses up to 50 cells per chord length, with approximately 42,000 triangular surface elements (Δ~0.022 chord) defining the wing surface. The temporal evolution of generated forces in the x_g-, y_g-, and z_g- directions are presented in Figure 4 (a-c). Some difference at force peaks and valleys where the temporal gradients are high for the two coarsest grids of 20 and 30 cells per chord length are evident. These differences are mitigated considerably as the grid is refined further to 40 cells per chord length. Figure 4 (d) shows the percentage difference of the integrated net fluid force exerted over the full recorded flight compared to the finest grid of 50

cells per chord length. For the two coarsest grids the force varies by about 4% and 1% percent, respectively, while the difference is negligible when using the third (1/40 chord length grid spacing) grid. Based on this study, results from the 40 cells per chord length are presented in this paper.

Table 1: Summary of different background grids evaluated.

Cells per chord length / Δs	Background grid size	Processors used
20 / 0.05	4.98 million	32
30 / 0.033	13.8 million	64
40 (Base grid) / 0.025	38.2 million	128
50 / 0.020	64.6 million	256

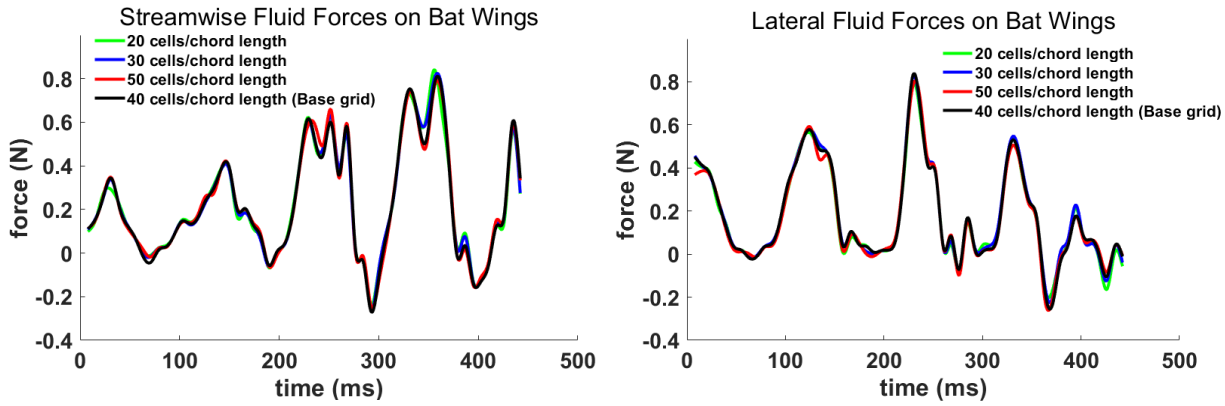

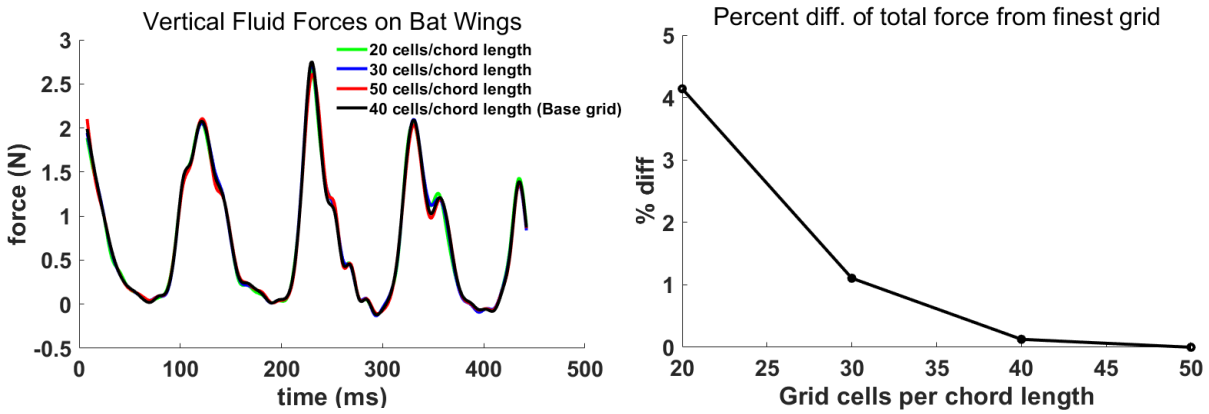

Figure 4: Fluid forces in the global coordinate system on the bat wing on background grids of different resolution along with percentage difference of net force from the finest grid

To supplement the validation of the digitization of 2D motion capture video frames to 3D spatio-temporal data, and the grid independency study of the aerodynamic solver, additional validation is done by treating the bat as a simple lumped mass system and using the calculated aerodynamic forces [53 ("ibm_force_all.dat")] to predict its trajectory in comparison to the measured trajectory in the global reference frame. Note that this validation requires both, the accurate representation of the actual wing kinematics as well as the accurate reproduction of forces driving the flight. The lumped mass dynamics analysis is based on Newton's second law, $\frac{d^2\vec{x}}{dt^2} = \frac{\vec{F}}{m}$. The bat mass is approximated as a point mass at the center of mass (COM) which is approximated by the body location and wing posture [63]. The net time-dependent forces are obtained from the numerical simulations. The velocity and position of the COM is then predicted by integrating the acceleration once and twice with respect to time. The comparison of the predicted path of the bat's body obtained from the aerodynamic simulation with the measured path of the bat body marker point is presented in Figure 5.

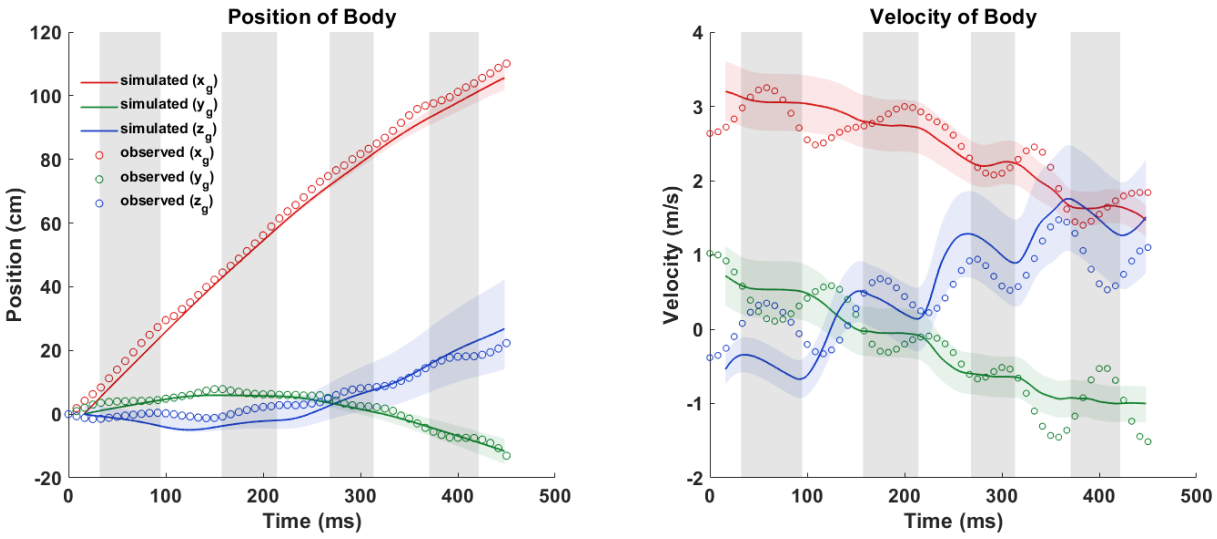

Figure 5: Comparison between the observed and predicted flight trajectory of the bat body in the global coordinate system; (a) position of the bat body and (b) velocity of the bat body; simulated velocities and positions are calculated from integrating the simulated force; gray shaded regions denote upstrokes while white denotes down strokes; red, green and blue shaded regions enveloping the predicted trajectory and velocity represents $\pm 15\%$ of the computed values from aerodynamic force, withing which the observed position and velocity from kinematics lie

Good comparison is obtained between the predicted and observed values of the body position and velocity in the $y_g -$ and $z_g -$ directions. The under prediction of the velocity and consequently the position in the $x_g -$ direction indicates the under prediction of $x_g -$ directional force by the simulation model. As pointed out by Windes et al. [1] and expressed in Figure 5 by the shaded regions, even a small discrepancy in the predicted force will accumulate in time while calculating the velocity and position as they are calculated via temporal integration of acceleration. The shaded regions enveloping the predicted trajectory and velocity are representative of the observed values varying within $\pm 15\%$ of the predicted values. Another discrepancy, also observed by Windes et al. [1], is the relative insensitivity of the model to variations within a single wingbeat cycle. This

trait is particularly characteristic of variations in the $x_g -$ and $y_g -$ directions and could be attributed to the simplicity of the lumped mass model, the much smaller aerodynamic forces produced in these directions compared to the $z_g -$ direction, and to inertial forces which are not included in the model. In spite of these differences, it is established that the overall trajectory over the recorded flight is reproduced with good accuracy, giving confidence in the fidelity of kinematic measurements and aerodynamic simulations.

3. RESULTS & DISCUSSION

Of primary interest is relating the dynamics of the turning ascending maneuver with the relevant wing kinematics. First we introduce relevant morphological parameters of the bat and the flight trajectory followed by the aerodynamic analysis of the related wing kinematics. Wherever relevant we also compare and contrast the kinematic and aerodynamic traits of the flight of the *H. armiger* by Windes et al. [1].

3.1. Morphological Parameters

The measured morphological parameters of the *H. pratti* in flight over the recorded 3.5 wing beat cycles are presented in Table 2 along with equivalent data from Windes et al. [1] for a *H. armiger* bat for comparison.

Definitions of the different parameters are as follows:

- **Wing area:** The wing area is the maximum total surface area during the downstroke (when the wing is fully stretched), averaged over several wingbeat cycles. The value in parenthesis indicate the averaged area over the entire up and downstrokes.
- **Planform area:** The planform area is the mean wing area during downstroke and upstroke projected onto the local body-fixed $x_b - y_b$ plane, averaged over several wingbeat cycles.

- **Span:** The span is measured as the maximum wingtip to wingtip distance averaged over the wingbeat cycles.
- **Mean Chord:** The mean chord of the bat wing is calculated by dividing the maximum planform area within a cycle by the span distance and averaged over the several wingbeat cycles.
- **Aspect Ratio:** Aspect ratio (AR) is span squared over planform area
- **Wing Loading:** Wing loading is weight over planform area.

The current bat exhibits a much larger mass and wingspan than some prior work on maneuvering bat flight in the literature by Iriarte-Díaz et al. (mass ~ 33 g) [45], and Henningsson et al. (mass of ~10 g) [46]. However, the morphological parameters of the current study are in the same range as that of Windes et al. [1][50] in spite of the bat being from a different species. The mass (1% heavier) and span (3% larger) are almost identical, but the *H. pratti* bat in the current study has a wing area larger by 20%, and thus a 15% larger planform area. This leads to a larger mean chord (14%), smaller aspect ratio (6%) and smaller wing loading (11%) compared to the bat in the study of Windes et al. [1].

Table 2. Morphological parameters

	Mass (g)	Span (cm)	Wing Area (cm^2)	Planform area (cm^2)	chord (cm)	AR	Wing loading (N/m^2)
Current Flight	55	53	522 (mean = 398)	459	8.91	6.12	11.98
Windes et al. [1]	54.5	51	434	398	7.8	6.5	13.4

3.2. General Flight Description

In order to provide context for the presented results, this section describes the measured flight trajectory. Figure 6 shows the wing position at mid-downstroke of 7 consecutive wingbeat cycles

in the flight trajectory. Among them, 3 downstrokes (shown enclosed in the green box) and 4 upstrokes which constitute the right-turn maneuver is studied in the current paper. Two wingbeat cycles later it performs an upside-down 180° somersault to perch on the ceiling of the tunnel. While the bat is still climbing, the preparation for the perch is expected to influence the flight during the latter stages of the recorded flight.

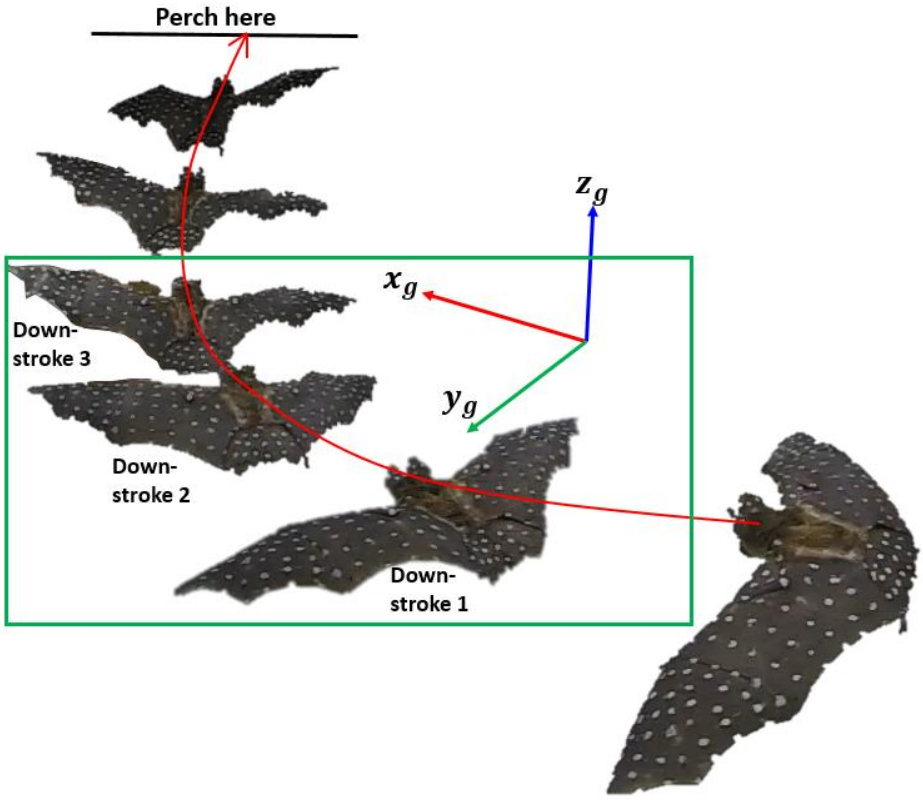

Figure 6: Flight trajectory (shown in red) with wing placement on 6 consecutive downstrokes. Current paper studies the three downstrokes (along with 4 upstrokes in between) shown in the green box. The bat perches on the ceiling of the flight tunnel on the third upstroke after downstroke 3.

The analyzed flight consists of 3.5 wingbeat cycles spread over 450 ms of flight time. Figure 7 provides planar top and side views of the flight trajectory identifying the upstrokes and down strokes and the velocity magnitude along the flight trajectory. Among other things, Figure 5 (a) (in

section 2.4) shows the details of the flight trajectory observed from the kinematic data (denoted by open circle symbols). Taking the starting position as the origin, the bat first veers to the left (maximum of 4 cm left from origin at 158 ms) as indicated by the lateral y_g-displacement. It then makes a sustained right turn (maximum of 15 cm right from origin at 450 ms or at the end of the recorded flight). The entire flight is associated with a cumulative 46.4 degree change in bearing in the x_g-y_g plane. The maneuver is tightest at about 335 ms when the radius of curvature of the turn is smallest (= 61.5 cm). During the course of the 110 cm recorded flight, the x_g-directional velocity of the bat decreases from 2.95 m/s to 2.15 m/s. The initial mostly level flight (slight loss in altitude up to 150 ms), is followed by a gradual increase in elevation, becoming steeper at around 250 ms. During the recorded ascent, the bat gains an elevation of 19 cm. The maximum ascent angle is 26.9 degrees during the last half cycle. One interesting trait to note is that the dominant maneuvers in the lateral and vertical direction start at the same time (~ 150 ms) as shown in Figure 5 (a). This trait was also present in the maneuvering flight of Windes et al. [1] indicating that perhaps, a change in altitude is often accompanied by a turning maneuver or vice-versa. Figure 7(c) shows the forward velocity of the bat in the local velocity based co-ordinate system (as opposed to the global co-ordinate system used for Figure 5(b)) in order to provide a clearer understanding of the effective velocities contributing to the current flight. It is seen that, during the climb and turn, the bat loses some of its forward momentum and decelerates from ~2.5 m/s to ~1.8 m/s.

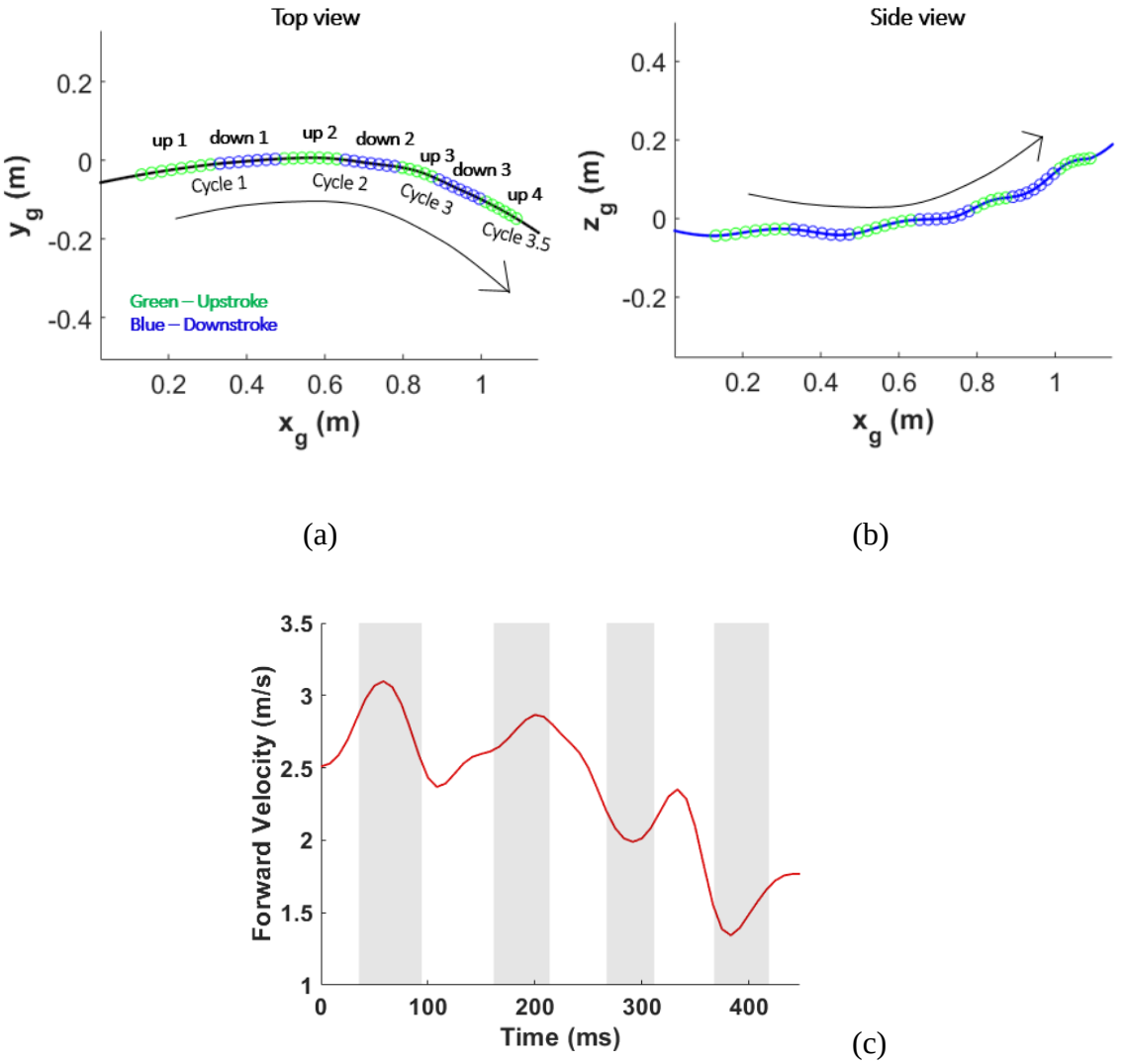

Figure 7: Flight trajectory (a-b) Top and side views, green and blue dots depict individual frames of the video recording; (c) Forward velocity in the local velocity based coordinate system

The quantitative flight parameters are noted in Table 3 along with equivalent data from Windes et al. [1] for a *H. armiger* bat. The bat is flying much faster (about 45%) in the current flight and also decelerating more along its curved path when compared to the maneuvering flight studied in Windes et al. [1]. The 2.64 m/s mean turning flight velocity in the present study is slightly higher but in the same range as the 2.0 m/s mean velocity observed by Iriate-Díaz et al. [45] and the wind tunnel velocity of 2.5 m/s used by Henningsson et al. [46].

Table 3. Comparison of flight parameters between current and a similar previous maneuver

	Flight duration (s)	Total # of full wingbeat cycles	Mean velocity (m/s)	Mean acceleration (m/s^2)	Wingbeat frequency (Hz)
Current Flight	0.450	3.5	2.64	-1.78	9.08
Windes et al. [1]	0.558	5.0	1.81	-0.86	9.7

The average wingbeat frequency does not differ much between the two flights, although it is about 6% lower for the current flight. Analyzing the angle of ascent and flight path curvature in Figure 8 provides more perspective on the term "strongest maneuver" in the vertical and lateral directions, respectively. In general, both the angle of ascent and curvature show an increasing trend during downstrokes and a decreasing or neutral trend during upstrokes, indicating that the majority of kinematic features fueling both the upward and lateral maneuver take place during downstrokes. There is a clear synergy between the vertical ascent angle and lateral curvature. The angle of ascent has the steepest gradient during downstrokes followed by a levelling-off in the rate during upstrokes. Accordingly, the radius of curvature follows the same trend as the ascent angle, increasing and decreasing in synch with the rate of ascent. The curvature reaches a maximum at near mid third downstroke indicating the tightest part of the turn in the lateral direction and drops off precipitously after that indicating that the bat has straightened out of the turn. During this time, the bat keeps climbing but at a slower rate. The last part of the flight kinematics could be in response to the bat sensing the tunnel walls and preparing for the ceiling perch.

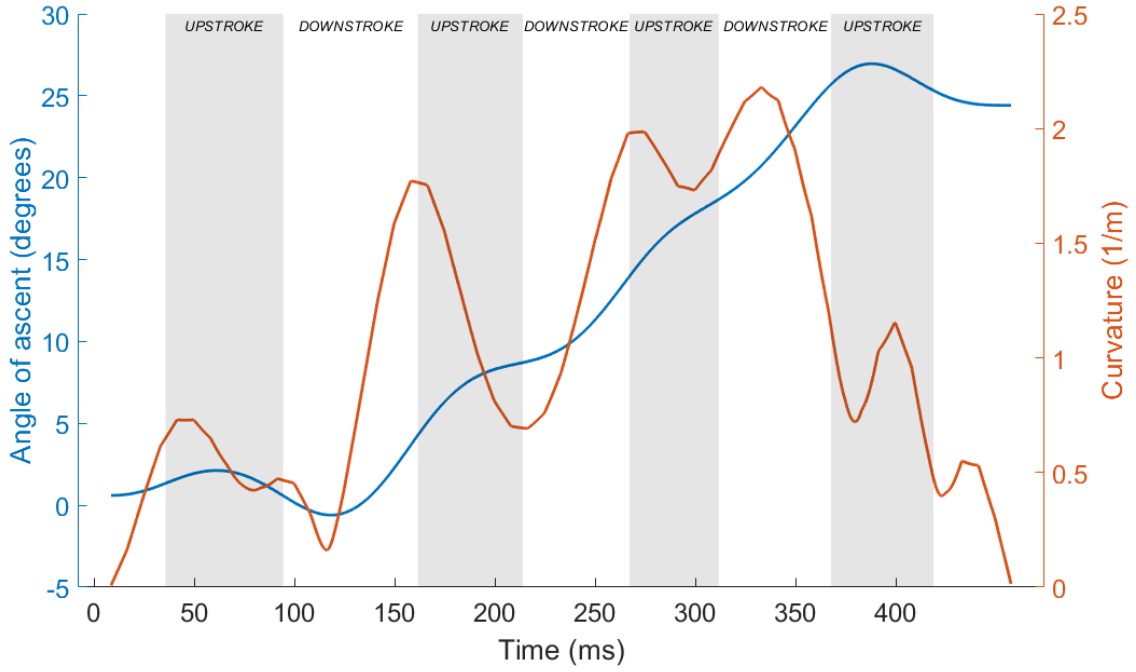

Figure 8: Angle of ascent and curvature over flight time; curvature is inverse of the radius of curvature (ROC), the tightest turn occurs when the ROC is smallest, or curvature is largest.

3.3. Flight Aerodynamics

The integrated aerodynamic forces for the turning flight are first presented in the body-fixed coordinate system in Figure 9(a) supplemented with the gravitational force components in the three directions. During straight, level, constant speed flight the aerodynamic forces supplemented with gravitational forces should balance out to be zero on a cycle averaged basis. However, for a turning, ascending and decelerating flight as the current one, significant forces are expected as shown by Figure 9(a). The x_b-direction of the body frame is aligned with the direction of the longitudinal axis of the bat's body. Hence, the positive x_b-component of the force is a major contributor to net thrust while the negative component to net drag. Positive peaks in $F_{x,b}$ (meaning

instantaneous thrust is more than drag) are observed during the downstrokes. During the first two upstrokes minimal net drag or a neutral value is observed. But during the major turning-climbing maneuver which starts at the second downstroke, small thrust peaks appear during 3rd and 4th upstrokes to supplement the thrust generated during the downstrokes. Previously Johansson et al. [41] also reported thrust generation at the end of the upstroke and related it to effective pitch and yaw control. This feature was also observed by Viswanath et al. [64] during ascending flight of a fruit bat.

The z_b-component of the force is the major contributor to the lift force and is substantially larger than the other two components in order to support the weight of the bat and to perform the climb. The body coordinate z-directional force is maximum during the 2nd downstroke to facilitate the steep climb in the subsequent cycles. The force generated during upstrokes is very small in magnitude, positive in the first two downstrokes and negative in the last two. The lateral force $(F_{y,b})$in the body fixed coordinate system remains near zero during the flight. On comparing $F_{x,b}$ and $F_{z,b}$ with Windes et al. [1], the magnitude of $F_{x,b}$ is comparatively smaller in the current flight while that of $F_{z,b}$ is comparatively larger. This could be because the rate of ascent of the current flight is higher than that of the *H. armiger* in Windes et al. [1]. Upon consideration of the gravitational force components, all the three directional body-fixed forces decrease or exhibit larger negative values.

At first glance, the overall positive force in the x_b direction seems counterintuitive to the overall deceleration observed in the current flight. However, as the direction of the long axis of the bat body is often different from the direction of the velocity vector, the force components calculated in the velocity based coordinate system can provide a clearer relation with the observed bat motion. The velocity coordinate system is constructed by using the direction of the velocity vector as the

x_v-direction, followed by defining the y_v and z_v coordinate directions as outlined in section 2.2 for the body-fixed coordinate system. Forces in the velocity-based coordinate system are plotted in Figure 9(b).

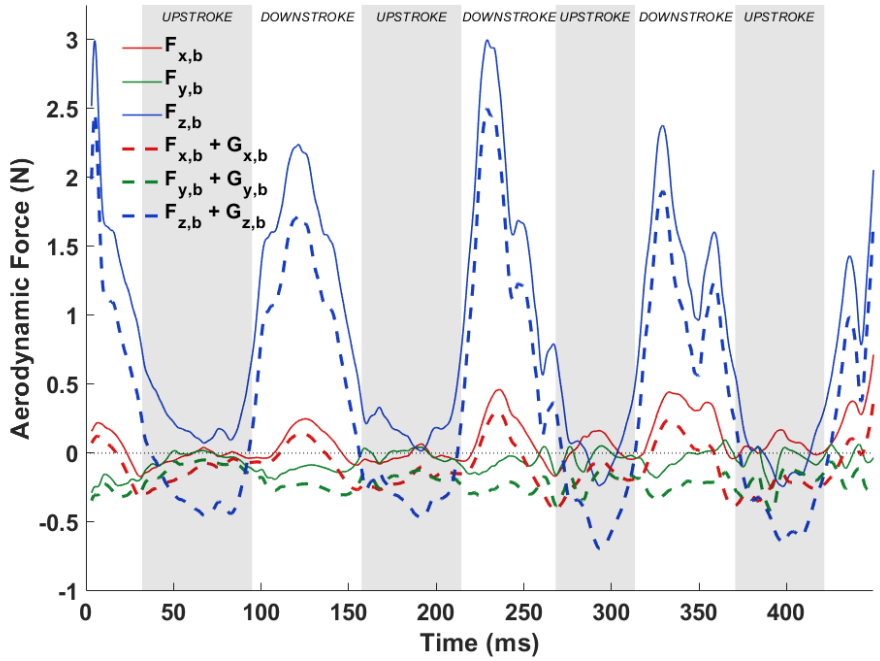

(a)

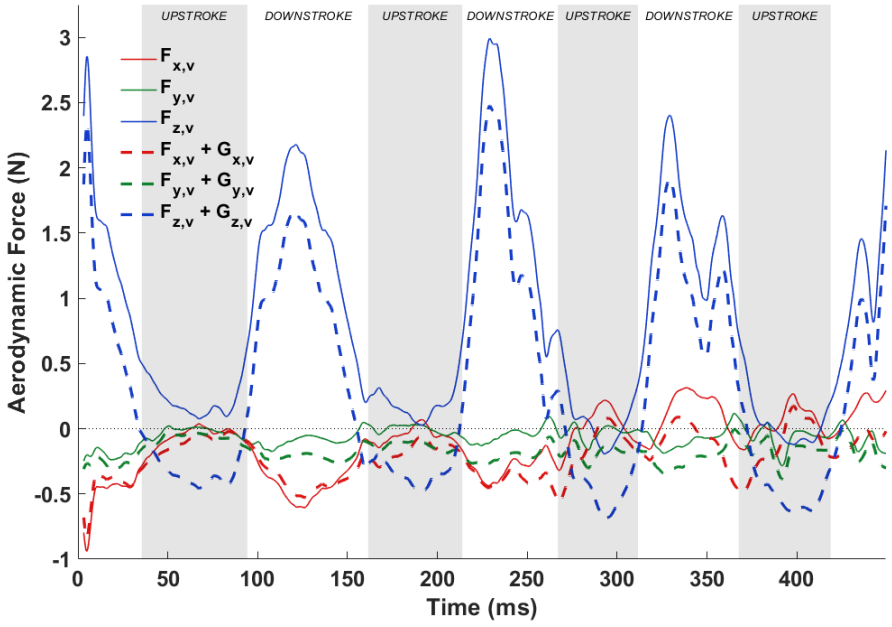

(b)

Figure 9: Forces in the (a) body and (b) velocity coordinate system with gravity components. F denotes aerodynamic forces and G denotes gravitational force components.

The biggest difference in the body-fixed versus velocity based forces is evident in the forward direction. While the net $F_{x,b}$ force in the body frame is mostly positive, the forward component in the direction of velocity is mostly drag force. This is consistent with the observed motion of the bat slowing down. The manifestation of a net drag force $F_{x,v}$ in the velocity frame in spite of a net thrust force, $F_{x,b}$, in the body frame is explained by the relative orientation of the force components in the two coordinate systems shown in Figure 10 (a). $F_{z,b}$, by far the largest force in the body frame, has a large positive contribution to $F_{z,v}$ in the velocity frame, but at the same time has a significant negative contribution to $F_{x,v}$ to overwhelm the component of positive $F_{x,b}$. The small thrust peaks observed on both up- and down-strokes from the 3rd cycle onwards result from the larger positive $F_{x,b}$ force. Figure 10 (b) also shows that $F_{z,b}$ contributes a negative component to the velocity frame lateral force $F_{y,v}$, increasing its magnitude.

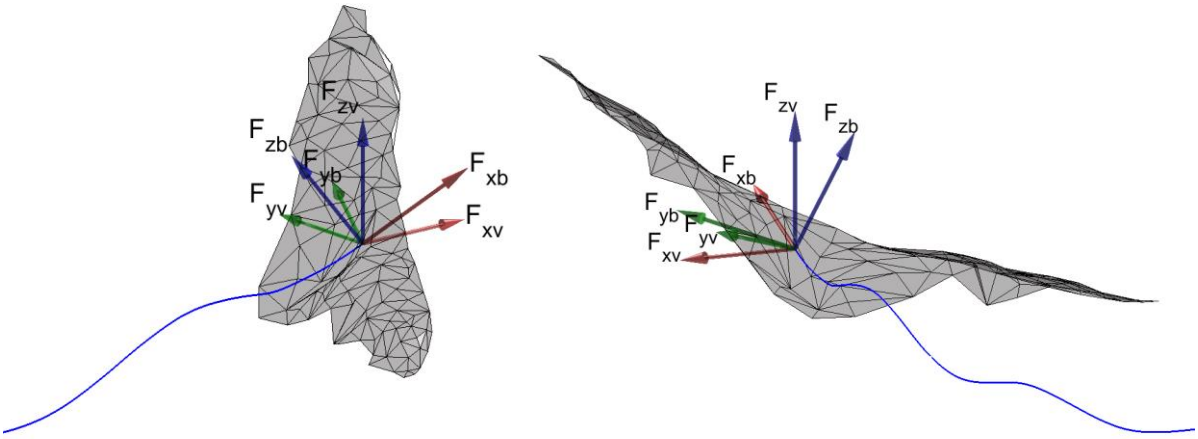

(a) (b)

Figure 10: Contributions of forces in body-fixed coordinate system to forces in the velocity-based coordinate system; two different views (a and b) complement each other to show the contributions in the three different directions.

The inward pointing lateral force ($F_{y,v} + G_{y,v}$) along the bat trajectory plays an instrumental role in a stable turn by balancing the centrifugal acceleration felt by the bat as it traverses the turn. From Figure 11, the net lateral or radial force during the turn from 158 ms to 450 ms is calculated to be ~0.21 N (shown by the green dashed line). The centrifugal force generated is calculated from the mass, velocity, and radius of turn in Eqn. 1 and found to be 0.24 N. This balance between the forces acting on the turn radius assures a stable turn.

$$F_{rad} = ma_c = \frac{mv_{tan}^2}{r} \approx \frac{(0.055\ kg)(\ 2.27\ ms^{-1})^2}{1.15\ m} = 0.24\ N \qquad \text{Eq. 1}$$

where,

m = total bat mass

a_c = centrifugal acceleration

v_{tan} = approximate flight velocity magnitude averaged over the flight time

r = approximate radius of curvature averaged over the flight time

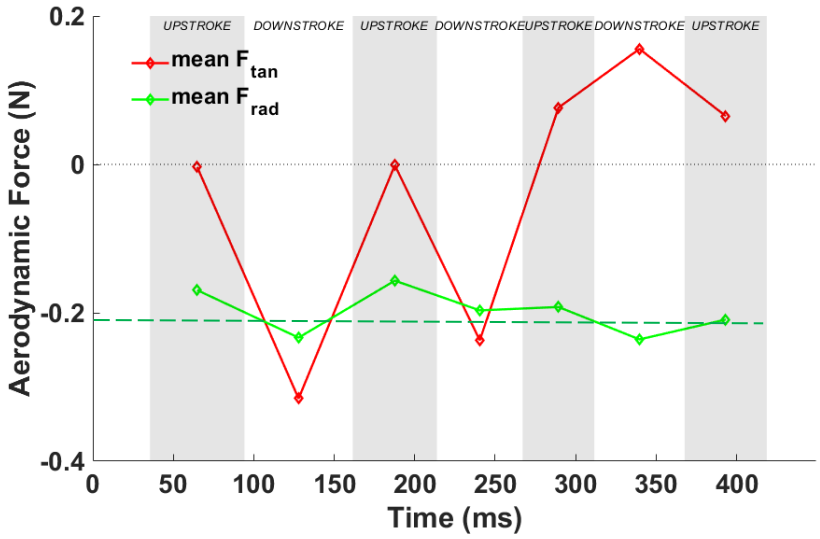

Figure 11: Half-cycle averaged tangential and radial force

It is to note that, the radial force shown in Figure 9 (b) and 11 results from the simulation whereas the centrifugal force is obtained from the kinematic data; the close agreement between the two is yet another validation of the overall methodology. Discrepancies between the estimated (from kinematic data) and calculated (from aerodynamic simulations) values can result from the fact that the bat is not in a steady state, constant radius, constant velocity turn and is also gaining elevation.

3.4. Orientation of Bat Body

Another aspect of the turning mechanism comes from the orientation angles of the bat body and velocity. The direction of the net force vector is the most significant driver that allows the bat to follow a curved trajectory. This direction is predominantly controlled by the rotational orientation of the bat in space. The relative orientation of the body-fixed frame to the ground frame represents the angular rotation of the bat, described by the three Euler angles as—the roll, pitch, and yaw as introduced in section 2.2. When the bat changes its angular orientation, it changes the direction of

the flight path through yaw and redirects the force so that a radial acceleration is achieved through roll.

As the direction of a flight does not always follow the body orientation, we define three additional angles based on the velocity coordinate system. Equivalent to the roll angle in the body-fixed coordinate, a bank angle is defined as the absolute angle between y_v-axis and the horizontal. Also defined is a climb angle which is the inclination of the x_v-axis with the horizontal and a bearing angle as the angle between the initial and current flight direction projected on the horizontal $x_g - y_g$ plane.

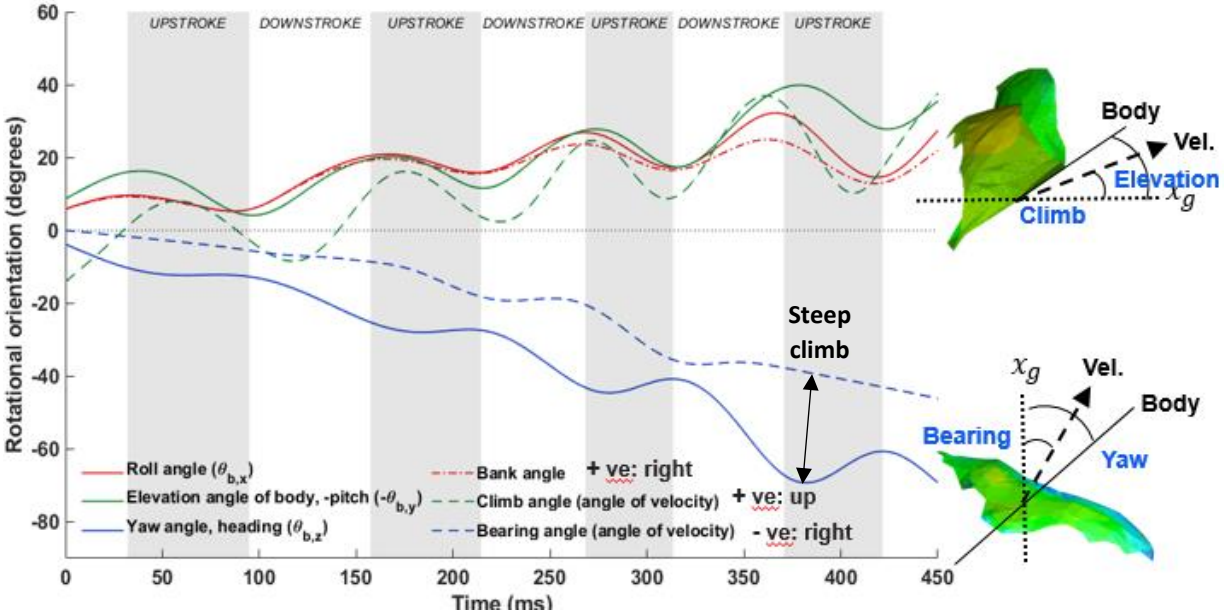

Figure 12: The angular orientation of the bat's body and velocity vector relative to the ground, slope of lines indicates angular velocity and concavity indicates angular acceleration. Schematics on the right show a representative (non-scaled) deviation of the longitudinal body axis and velocity vector and the resultant angles.

The Euler angles of the bat body rotation (yaw, pitch, and roll) are shown in Figure 12 along with the orientation of the velocity vector (bearing, climb, and bank). The bank angle, although closely related to the roll angle, is not an Euler angle. As Euler rotations are applied sequentially, the roll angle is usually affected by the pitch and yaw angles. However, the bank angle is free from any such effect and can simply be calculated as the absolute angle between the instantaneous y_v axis and the horizontal. At small pitch angles, the roll and bank angles do not differ much as the effect of pitch on roll is minimal. This is evident at the start of the flight where pitch angles are smaller. However, towards the end of the flight, after the 2nd cycle, the bat undergoes a steep climb, thus obtaining a significant pitch which in turn affects the roll angle. Therefore, there is significant difference between the bank and roll angles towards the end of the flight. Figure 12 also shows the elevation angle which is defined as a negative pitch angle for convenience. Positive values of the elevation angle represent an upward inclination of the bat body. The velocity counterpart of the elevation angle is the climb angle which has been defined above. The last angle describing the flight velocity in Figure 12 is the bearing angle, which is solely based on the flight direction, whereas the yaw angle is based on the body orientation only. The distinction between the body and velocity angles plays a fundamental role in explaining the maneuver mechanics below.

The body rotations allow the bat to redirect the net force vector so that a turning maneuver can be achieved. The most direct way to incline the force vector laterally to activate a turn is through rolling of the body and banking. A positive roll angle of around 7 degrees from the start of the flight indicates that the bat is preparing for a right turn. During the flight, the roll angle increases gradually up to around 20 degrees until the third cycle after which it grows rapidly to 37 degrees towards the end. This is consistent with the curvature plot shown in Figure 8 which indicates that the tightest portion of the turn starts at around the third cycle. Although roll is the most direct way

to incline the net force vector in favor of a lateral turn, a combined yaw-roll action is more effective. Yaw allows the center of the turn radius to be shifted back and thus produces a tighter turn. In absence of yaw, only roll can result in a gradual turn, but not a tighter one. Similarly, only yaw without roll is not optimal for a tighter turn as the lift force remains vertical and does not impart any component towards the turn. Thus, only the significantly smaller thrust force imparts a radial component if there is no roll and only yaw. The current maneuver was achieved by a synergistic effect of roll and yaw. A negative yaw and a positive roll drives the bat to turn right as is seen for the current flight in Figure 12. As yaw facilitates a rotated axis for subsequent roll to be performed around, it is a crucial component to initiate the turn. Therefore, the yaw angle in Figure 12 shows a gradual increment in the first 2 cycles, when the lateral turn is not very tight. But when the third cycle starts, there is a steep increase in the yaw angle facilitating the tighter turn despite the bearing angle not following suit. The comparatively gradual behavior of the bearing angle towards the end, is consistent with the overhead flight trajectory of Figure 7, showing that the bat bearing change is comparatively gradual throughout the entire flight time. Even after the collaborative effect of roll and yaw initiates the steep turn around the third cycle, the bearing angle does not align with the heading. This indicates that the body axis of the bat is always positioned inside the trajectory of the turn for the current flight.

The bat body pitches up during downstroke and pitches down during upstroke. As seen in Figure 12, the increase in elevation during downstroke is larger than the decrease during upstroke allowing the bat to gain altitude with the steepest gain occurring during the 3rd stroke. At the start there is a ~37° difference between the elevation and climb angle but during the maneuver the velocity is nearly aligned with body axis. In contrast, Windes et al. [1] reported a somewhat consistent difference of 20 degrees between the body elevation angle and the velocity inclination

angle for both the maneuver as well as straight flight for the *H. armiger*, implying that the noted difference between how a bat positions its body with respect to its trajectory could possibly be an individual trait of the bat.

3.5. Rotational Moments

Thus far, we have established that the bat turns by generating a lateral force which provides the needed centripetal acceleration. This lateral force is produced when the net force vector is re-orientated by the combined effect of body yawing and banking. The moments created on the three axes of the body frame is yet another important aspect to explain the turning mechanism. The net rotational moment based on the bat's COM is estimated from the spatial distribution of the aerodynamic force on the wing surface. Figure 13 shows the roll, negative pitch or elevation and yaw moment created in the body fixed co-ordinate system both in a transient (a) as well as half-cycle averaged (b) time axis. According to a right-handed system, a negative yaw and positive roll moment is necessary to make a right turn while a negative pitch (or positive elevation) moment takes the bat upwards as shown in Figure 13.

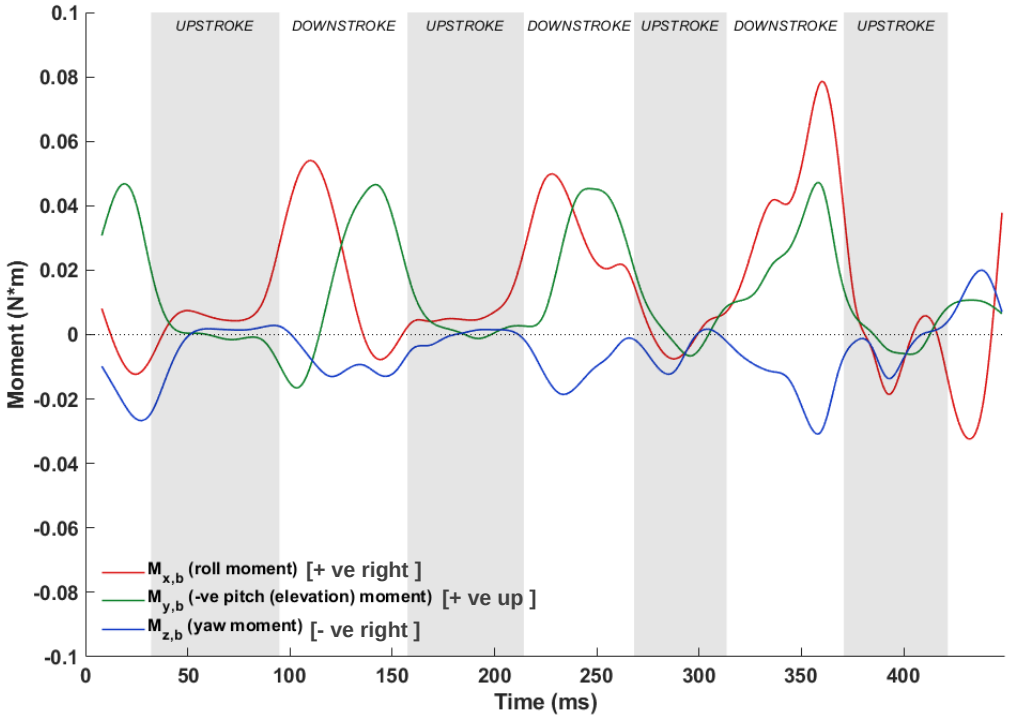

(a)

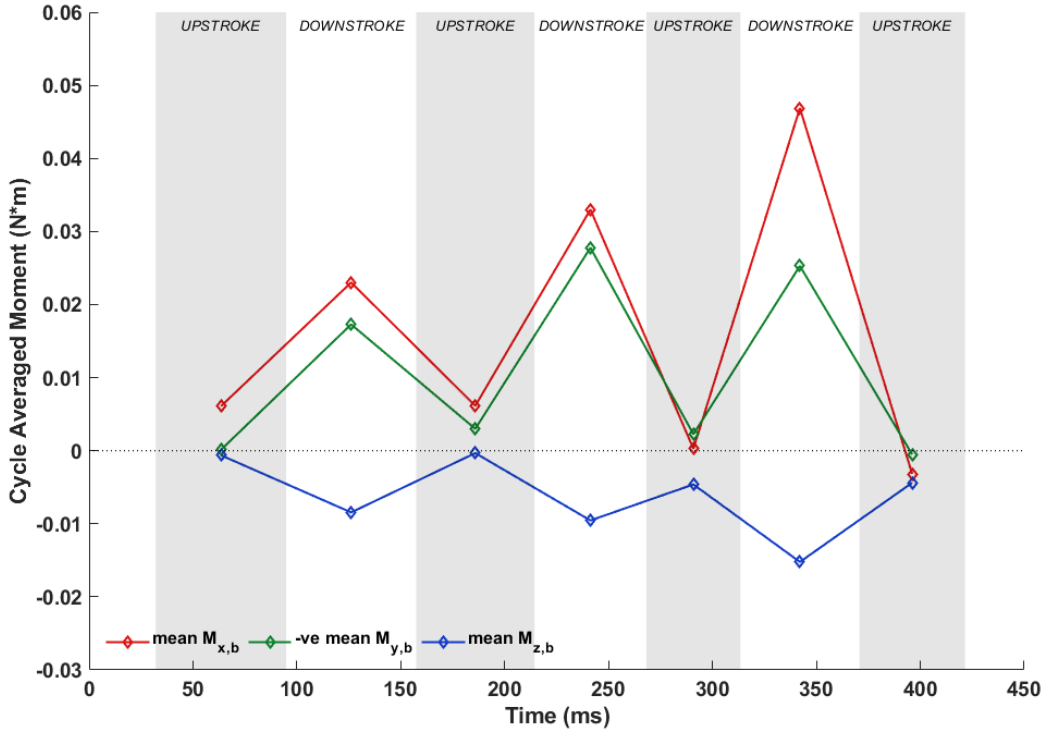

(b)

Figure 13: Body-frame rotational moments relative to the center of mass; (a) – instantaneous, (b) - cycle-averaged

The yaw and roll moments are the main drivers for the lateral turn. The cycle averaged plot shows that the yaw moment experiences a gradual increment in the first two wingbeat cycles and then a significant increase starting from the 3rd cycle. This is consistent with the increasing trend of the body yaw rotation seen in Figure 12. The highest roll moment is also recorded towards the end of the flight where the tightest turn occurs. Towards the very end of the recorded flight, in the 4th upstroke and the subsequent downstroke, a correction can be seen in the form of a negative roll moment in the instantaneous plot which is surmised to be preparation for the perch in the following cycles. The positive cycle averaged elevation moment fuels the overall upward motion of the bat. Within each wingbeat cycle, during the downstroke the predominantly positive elevation moment fuels the bat's upward pitch. Towards the end of every downstroke, the bat starts to pitch down which persists to a steady and gradual decrease of the elevation moment during upstrokes. The highest rate of the elevation moment increment is seen between downstrokes 0 and 2 with the peak magnitude achieved just before the steepest ascent begins. It is noted that the bulk of the moments that effectuate the maneuver are generated during the downstroke when the aerodynamic forces are at their highest, whereas the upstroke plays a minor role.

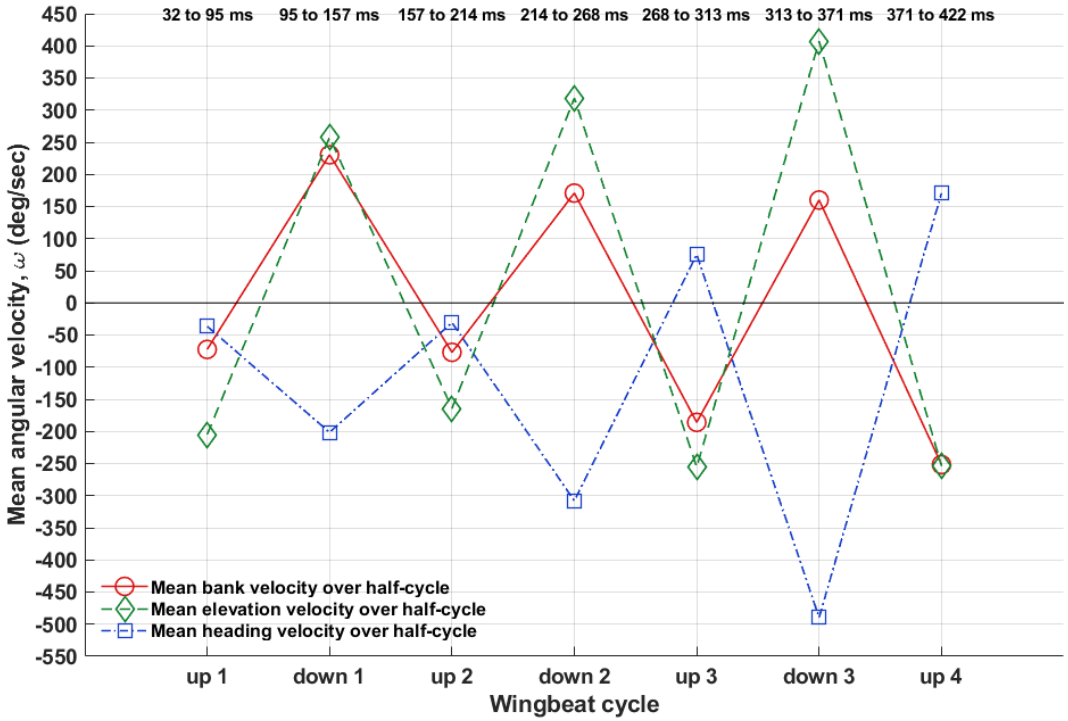

Figure 14: Half-cycle averaged angular velocities.

These aerodynamic moments give rise to angular acceleration or changes in angular velocities which is presented in Figure 14 from the experimental kinematic data with a half-cycle averaged time axis for easier visualization. Angular acceleration or the change in angular velocity can be caused by aerodynamic moments, inertial moments, or a combination of the two. The yaw or heading angular velocity is always net negative meaning that the bat nose is moving inward of the turn. In accordance with the yaw moment, the yaw or heading angular velocity increases to a maximum of 500 deg/s of yaw rotation during the initiation of the tightest turn (at around the 3rd cycle). The angular bank velocity changes from net positive to slightly net negative towards the end of the flight in accordance with the corrective negative roll moment observed in preparation for the perch. The elevation angular velocity is overall positive and increases with the upward

motion, peaking up to 400 deg/s of pitch rotation nearing the end of the flight. This is consistent with the steep ascent observed towards the end of the current flight.

3.6. Spatial Distribution of Aerodynamic Forces and their Effect on Rotational Moments and Turning Mechanism

The body rotations and moments are created when the wing kinematics cause asymmetries between the forces generated by the left and right wings as well as between different regions of the wing surface (inner and outer). The different regions of the wing on which the force distribution and thus moment generation is analyzed are specified in Figure 15.

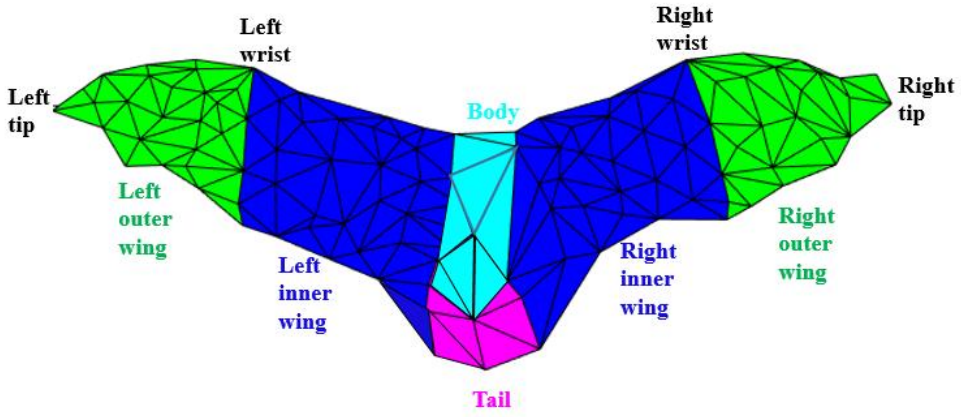

Figure 15: Spatial segmentation of the wing.

To better understand the effect of the spatial distribution of forces on moment generation, forces on inner and outer wings in the body-fixed local co-ordinate system are presented.

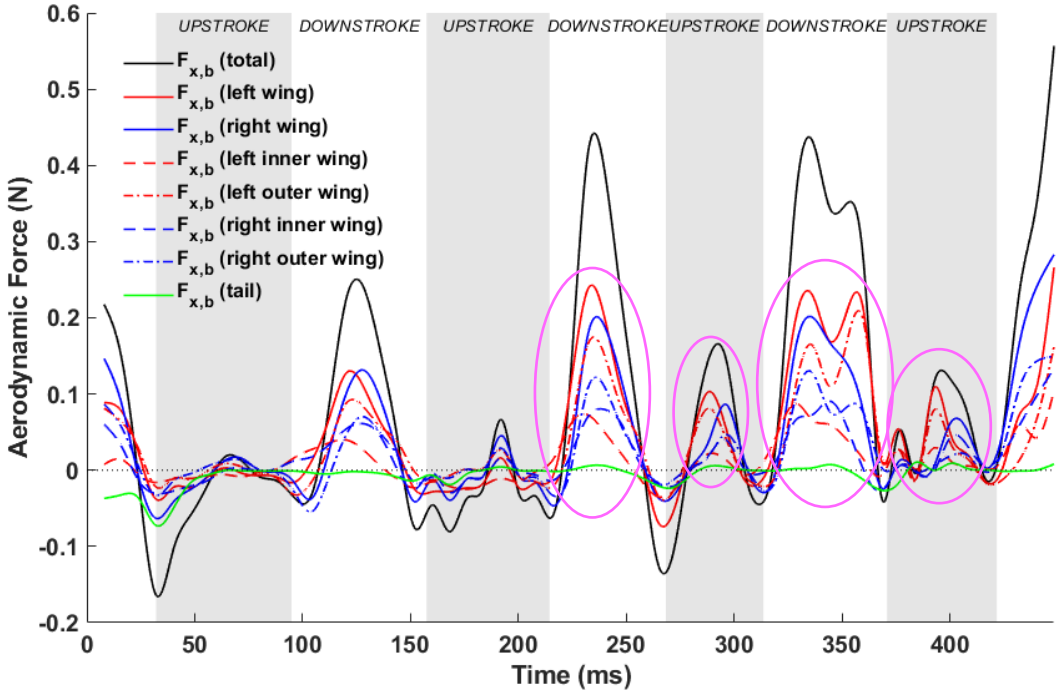

Figure 16: $F_{x,b}$ component of aerodynamic force broken down by different wing sections; pink circled regions encompass the asymmetries observed between the left and right wing.

Figure 16 shows the body-coordinate x-directional force acting on different regions of the wing. Imbalance in the thrust generated by the left and right wing is a major contributor to the yaw moment and body rotation. Starting from the 2nd downstroke, three types of asymmetries are noted in the force distributions. The first is a phase lag between left and right wing, the second is the left wing producing a larger positive force than the right wing, and the third is the left outer wing consistently producing more force than its right counterpart. These trends are persistent during the 2nd and 3rd strokes and are marked by pink circled regions. The asymmetries contribute to a large extent to the negative yaw moment (rotates the nose into the turn) that allows the subsequent roll to be acted on an already rotated longitudinal axis. Similar observations were made by Windes et al. [1].

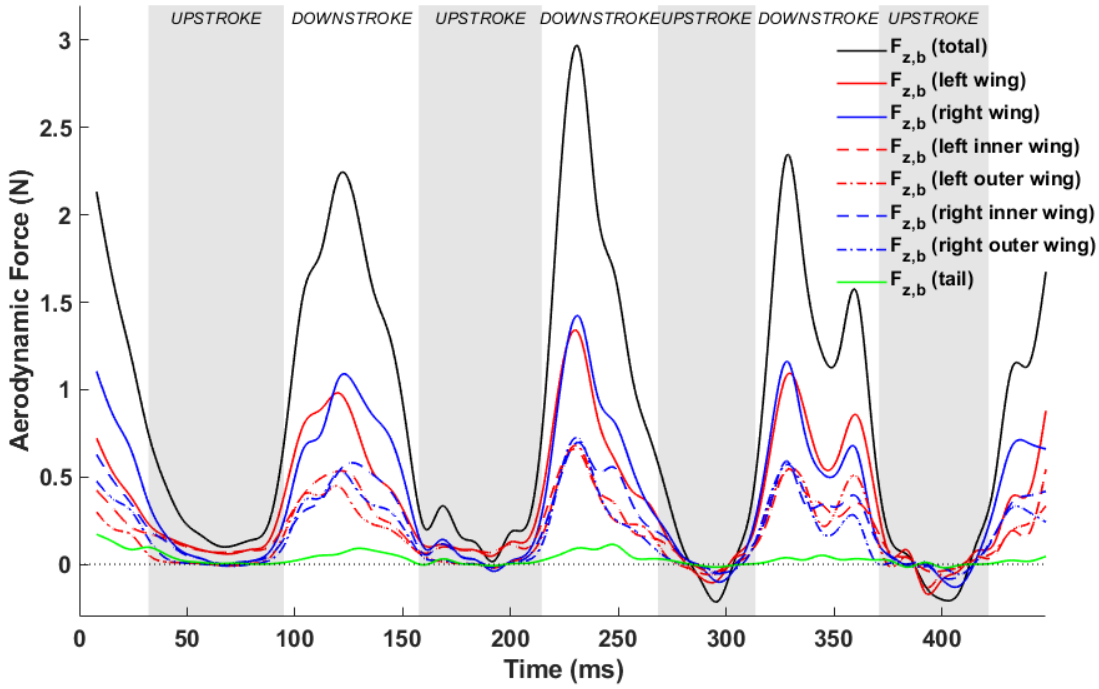

Figure 17: $F_{z,b}$ component of aerodynamic force broken down by different wing sections.

Figure 17 shows the body-coordinate z-directional force acting on different regions of the wings. An imbalance in the force generated by the left and right wing contributes to the roll moment in the body frame. $F_{z,b}$ has a slightly larger contribution from the right wing during down-strokes 1 and 2 and from the left wing during down-stroke 3 and 4. Otherwise, the contribution of the left-right and the outer-inner wings show relative symmetry in the force generated in the body-coordinate system and cannot be clearly and consistently related to the generation of roll moments presented in Figure 13. In this case the bat effectuates the required roll moment by positioning the two wings differently and changing the moment arm between the left and right wing during the right-turn maneuver. This is reflected in the roll moments generated by the individual wings shown in Figure 18. It will be shown in section 3.8 that during the right turn, the right wing moves closer to the body thus reducing the moment arm on which the aerodynamics forces act, thus effectuating a right roll.

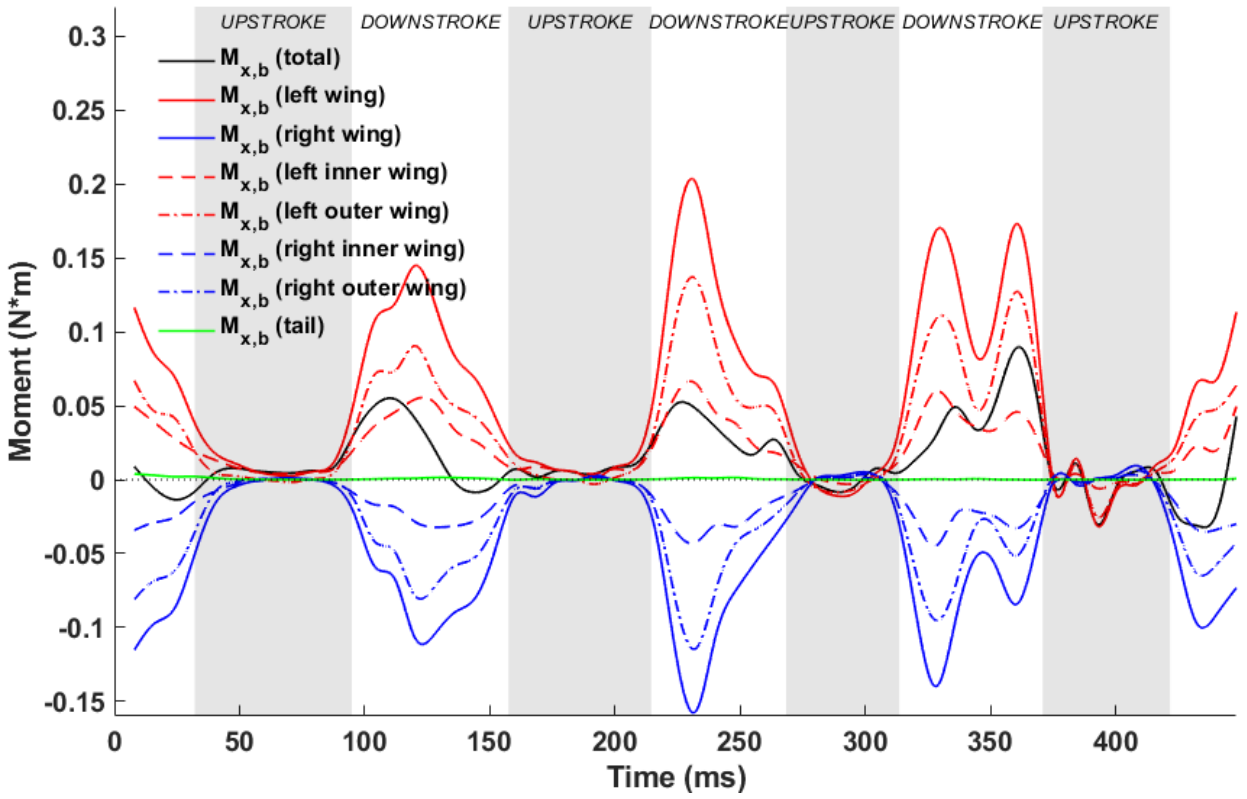

Figure 18. Roll moment generated by wings

3.7. Wing Kinematic Traits

In this section we investigate different kinematic traits of the bat flight. We also focus on comparing these traits to the right-ascending turn studied by Windes et al. [1]. In the full spectrum of maneuvers that a living bat could possibly undertake, the maneuver studied in this paper and that by Windes et al. are quite similar. In both cases the bats, which morphologically are also quite similar, start out at near level flight and initiate an ascending right turn maneuver in a similar, if not exactly the same flight tunnel environment. During the 450 ms duration of the recorded flight, the bat ascends about 20 cm, while travelling a distance of 110 cm along the length of the tunnel and moves 17 cm laterally to the right. In contrast, the bat in [1] travels 87 cm along the length of the tunnel, ascending 18 cm with a lateral displacement of 32 cm during the recorded flight of 550

ms. While the rate of lateral movement between the two bats is approximately the same, the current bat is more aggressive in the rate of ascent and travels faster in forward flight. Given these similarities and differences we seek to identify any general traits in their kinematic signatures noting that in the current study the bat perches on the ceiling two flaps past the end of the recorded flight and this action is bound to impact the kinematics towards the end of the recorded sequence.

Figure 19(a) shows the flapping frequencies for different wingbeat cycles. It is notable that the frequency increases at the initiation of and during the maneuver. This occurs at the start of the second cycle in the current flight during which the bat starts ascending. Thus, an increase in flapping frequency can be categorized as one of the mechanisms bats use to increase the power needed to effectuate the maneuver but may not be singular to this particular maneuver. A similar observation was made in Windes et al. [1]. There lies an aerodynamic limit to the maximum amount of lift that can be generated in a single stroke. Thus, to get additional lift for ascent a bat needs to execute more downstrokes per unit time (i.e. increase flapping frequency). This is done by increasing the downstroke velocity and by shortening the duration of the upstroke. Figure 19 (b) shows that the tip velocity of the current bat for both wings increases, peaking at the 3rd cycle when the maximum frequency is observed (Figure 19(b)). Additionally, the bat also spends less time on upstrokes (again lowest in the 3rd cycle) as shown in Figure 19 (c) by increasing the upstroke wing velocity more than the corresponding increase in downstroke velocity. This allows the downstrokes to be longer to accommodate the excess lift generation needed for the ascent.

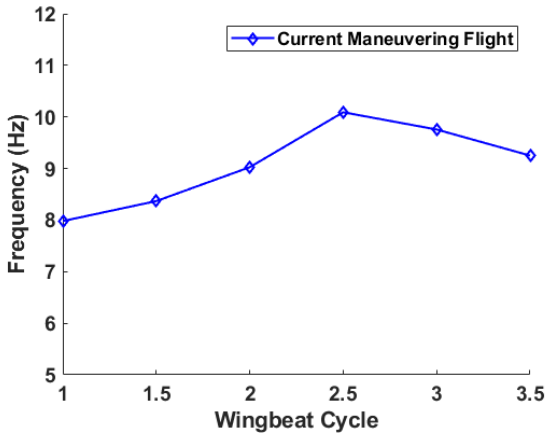

(a)

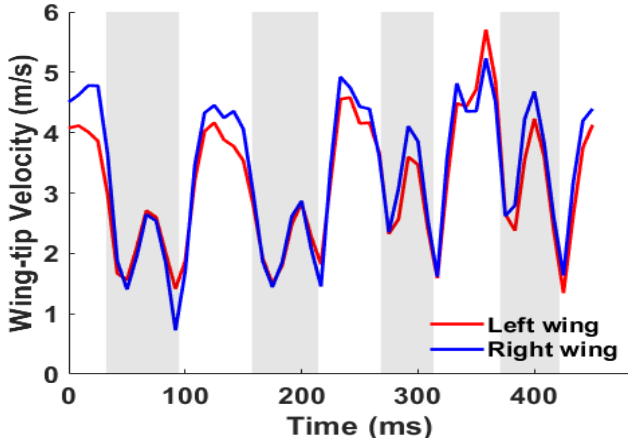

(b)

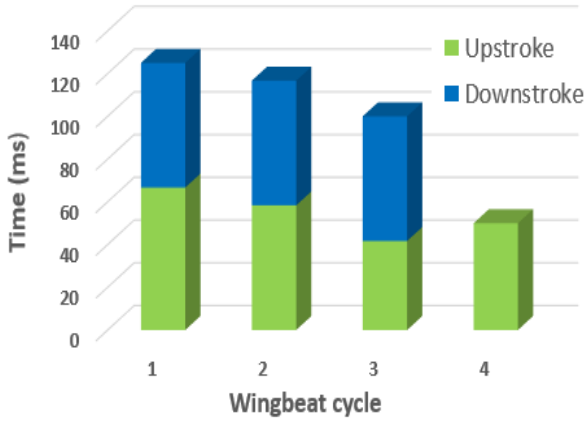

(c)

Figure 19: (a) Temporal trend in wing beat frequency shown at each half-cycle; (b) Tip velocity for the left and right wing; (c) Time spent in upstrokes and downstrokes in consequetive wingbeat cycles. The fourth upstroke was not analyzed in the current study.

The wing kinematics define the shape and orientation of the bat wings over the duration of flight. The mechanisms by which bats generate lift to stay aloft and thrust to propel forward, as well as the forces and moments to maneuver are controlled by the wing kinematics. In order to provide a holistic view of the kinematic data and identify specific maneuvering traits, several parameters

which characterize important aspects of wing motion are presented. Before going into the detailed kinematic markers, it is worth mentioning that a consistent difference observed between the current flight and that of Windes et al. [1], was the positioning of the body with respect to the velocity vector. Figure 12 shows that the bearing angle has a larger negative value than the heading angle, implying that the body long axis is oriented inside the trajectory of the turn. In the previous sweeping turn, during initiation the body was positioned outside the turn but quickly aligned with the velocity vector during the rest of the sweeping turn. This basic difference could instigate differing kinematic mechanisms to effectuate a similar maneuver.

3.8. Orientation of Stroke Planes and Associated Angles

Stroke plane is defined in section 2.2 (schematic in Figure 1) as the plane formed by the regression line through the wing-tip loci of a complete wingbeat cycle and the root of the wing. Two separate stroke planes are calculated for the right and left wings. A new stroke plane is calculated at each half wingbeat cycle, for e.g. a stroke plane at wingbeat cycle 1 is calculated using the 1^{st} upstroke+1^{st} downstroke, cycle 1.5 is calculated using 1^{st} downstroke+2^{nd} upstroke, and so on. Figure 20 shows the different stroke planes calculated for the 1^{st} and 3^{rd} wingbeat cycles for the left and right wings.

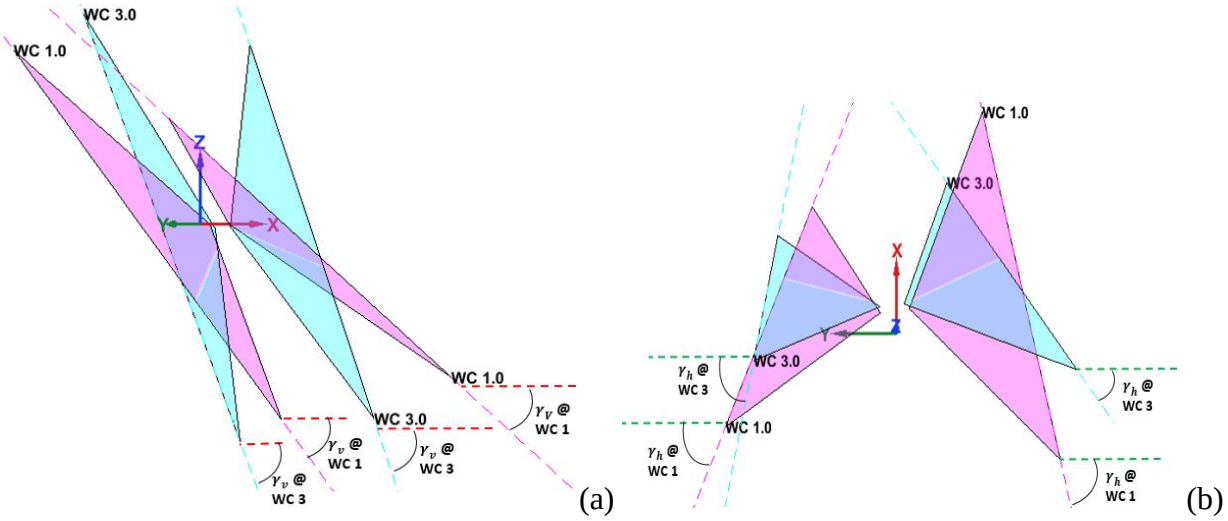

Figure 20: Stroke planes for 1st (magenta) and 3rd (cyan) wingbeat cycles for the left and right wings; WC = wingbeat cycle; The dashed lines show the regression line of the wingtip loci for respective cycles. (a) and (b) shows different views of the stroke planes for better perspective of the vertical (γ_v) and horizontal (γ_h) stroke plane angles.

In spite of the fact that bat wings are not rigid planar surfaces but highly deformable membrane wings, the orientations of these planes are used to identify macro adjustments that the bat makes during maneuvers. The orientation of the stroke plane is described by the horizontal (γ_h) and vertical (γ_v) stroke plane angles. The horizontal stroke plane angle γ_h is obtained by projecting the wingtip loci regression line onto the body-fixed $x_b - y_b$ plane. The angle between the projected regression line and the y_b axis is taken as the horizontal stroke plane angle which represents the in-out or lateral movement of the wingtip in relation to the body. The projection of the regression line onto the body-fixed vertical ($x_b - z_b$) plane defines the vertical stroke plane angle γ_v as the angle between the projected line and the x_b axis. It can vary from 0 to 90 degrees with higher angles facilitating more thrust and lower angles more lift. It signifies the forward-backward movement of the wingtip. Symmetry between the left and right stroke plane angles is

expected during straight flight, while asymmetries initiate the imbalance in force usually seen in maneuvering flights.

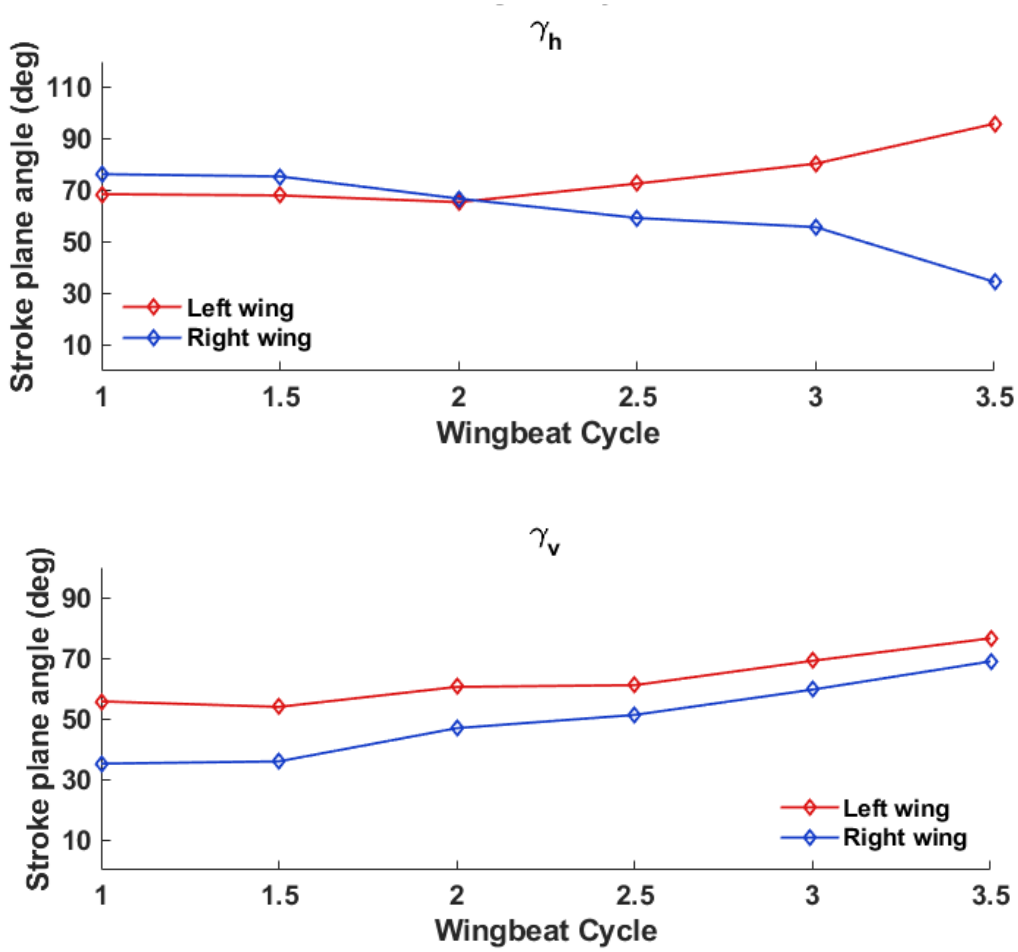

Figure 21: The vertical (γ_v) and horizontal (γ_h) stroke plane angles for the right and left wings

The horizontal and vertical stroke plane angles for the current maneuvering flight are presented in Figure 21. The horizontal angle, γ_h exhibits near symmetry between right and left wings with a nominal value of 70° during the first flap cycle, which is close to the value observed by Windes et al. [36] during straight descending flight. However, in turning flight they observed a large asymmetry between the two wings, with the wing inside the turn (right) exhibiting a much lower

value ($40° \leq \gamma_h \leq 60°$), indicating more lateral movement of the wing tip, accompanied by a nominal increase to about 80° for the left wing. The asymmetry was largest at the initiation of the maneuver but was reconciled gradually over 5 flap cycles as the bat settled into the turning-ascending maneuver. In the current flight, as the bat initiates the maneuver in the second cycle, asymmetry develops between the two wings which keeps increasing during the rest of the recorded fight. During this two flap duration, γ_h tends to $95°$ and $35°$ for the left and right wings, respectively. It means that the left wing flaps in a plane which is outward tilted from the long axis of the body (x_b) whereas the right wing flaps much closer to the body. Thus, the nature of the asymmetry observed by Windes et al. [1] and Iriarte-Díaz et al. [45], that during initiation and into the turn, the wing on the inside of the turn exhibits smaller horizontal stroke plane angles than the wing on the outside of the turn is confirmed in this study as well. This identifies a general trait that the wing inside of a turn flaps closer to the body in the body-horizontal plane when the bat maneuvers a turn. This particular action reduces the moment arm of the right wing and could be a key factor in generating the roll moment.

Figure 21 also shows the progression of the vertical stroke plane angles during the maneuvering flight. The current bat flies with progressively increasing vertical angles (γ_v) for both wings whereas the previous sweeping turn [1] had somewhat stable values for most of the flight time. The magnitude of γ_v measured in previous studies by Windes et al. [36] [1] and Sekhar et al. [40] for similar sized bats and by Iriarte-Díaz et al. [45] for a much smaller bat, in straight as well as maneuvering flight, has ranged between 40◦ and 60◦. Whereas, the current bat shows a clear asymmetry between the right and left wings, with the left wing angle increasing from 55◦ to 74◦ and the right wing angle from 35◦ to 67◦. During the entire flight, the current bat has a smaller vertical stroke plane angle for the right wing indicating that the wing outside the turn (left wing)

consistently flaps in a plane which is steeper with respect to the body-horizontal plane. The difference of ~20◦ between the left and right wing at the start of the recorded flight reduces to about ~7◦ towards the end. Considering that the right turn ascending maneuver is initiated at the 2nd stroke of the current flight, the observed asymmetry between the two wings is a common phenomenon between the current and previous sweeping turn [1]. During the initiation of the right turn maneuver of a *H. armiger* at the beginning of the flight, Windes et al. also observed an asymmetry between the vertical stroke plane angles of the two wings. However, in that sweeping turn, the right wing exhibited a higher vertical stroke plane angle than the left wing (by approximately 10◦) as opposed to the current flight. Thus, it is not possible to draw an unequivocal conclusion on the general role of the vertical stroke plane angle in effectuating the turning-ascending maneuver except noting that a higher value is more favorable towards thrust production and as a consequence, the left wing produces larger F_{xb} (Figure 16) and contributes to generating a yaw moment.

Additional kinematic markers are shown in Figure 22(a-c). The stroke plane deviation angle is defined as the angle between the actual span-line and its projection onto the stroke plane. Positive values indicate that the wingtip is in front of the stroke plane, while negative values indicate that it is behind the stroke plane. The flap angle is a measure of the flapping amplitude in the stroke plane. The half-span represents the instantaneous distance between the wing tip and the respective shoulder joint. While there are drastic differences between the left and the right wing starting at the 3rd downstroke, the observed traits are more likely related to the bat positioning itself for the impending perch on the tunnel ceiling. The flap angle of the right wing excurses dramatically down to -80°, about 20° more than the left wing with its half span dropping below 10 cm, with a much larger than normal stroke plane deviation angle of -20°. During this time, the left wing remains

extended out and does not retract towards the body as it normally does at the end of the downstroke. Closer observation of the curvature and ascent angle in Figure 8 reveals that although the bat is still climbing, it seems to have straightened its trajectory in preparation for the perch which would require it to execute a 180° somersault. This is why during the 3rd downstroke, there is a steep increase in the ascent angle but the curvature reaches a maximum before reducing to minimal values as the bat rapidly straightens its trajectory. These kinematic traits have a distinct force signature as well – both F_{xb} and F_{zb} forces exhibit a secondary peak into the 3rd downstroke. Interestingly, in spite of the large difference in the kinematic traits between the two wings, both wings contribute to the secondary peaks as observed in Figures 16 and 17 with the left outer wing having a noticeably larger contribution to the secondary peak in F_{xb}.

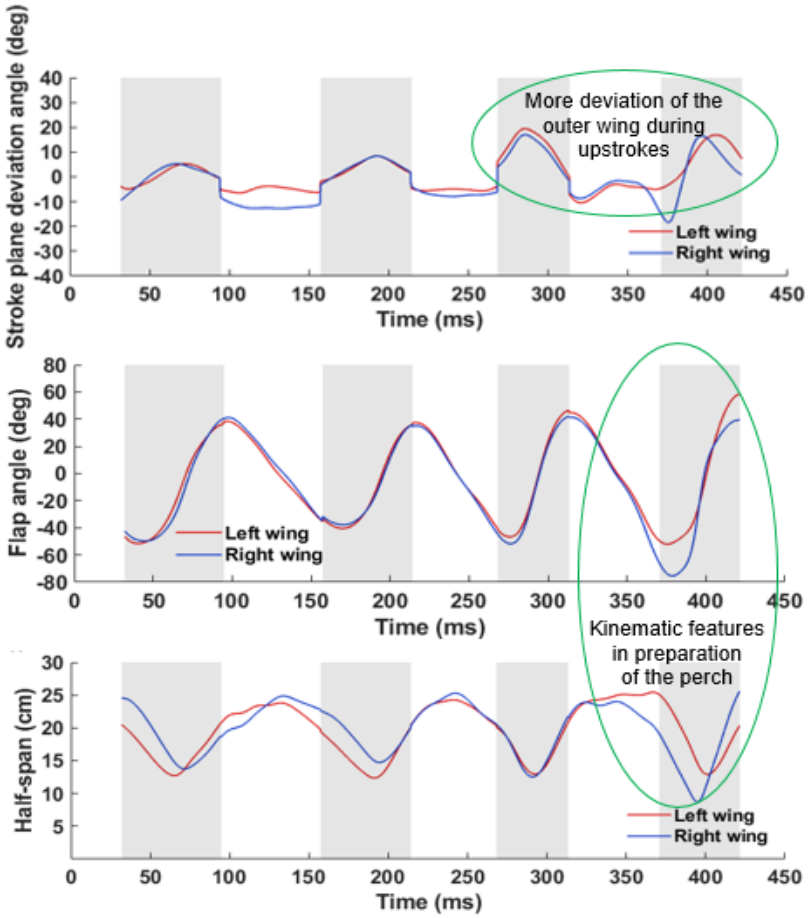

Figure 22: Kinematic features of left and right wings (a) Stroke plane deviation angle (b) flapping angle and amplitude (c) half span. Upstrokes are designated by the shaded regions; Circled regions indicate kinematic traits associated with the maneuver and impending perch.

In contrast to the relatively benign differences observed during most of the turning-ascending maneuver, Windes et al. (Fig. 4 in [1]) found significant consistent differences in the *H. armiger*. They observed that the right wing exhibited higher positive and negative stroke plane deviation angles at mid-upstroke and at end-of-downstroke, respectively, in almost all of the flap cycles during the turning-ascending maneuver. They also observed that the right wing had a larger flapping amplitude moving further down in the stroke plane to end the downstroke than the left wing, followed by the observation that the right wing tip also consistently pulled closer to the body than the left wing tip at mid-upstroke.

3.9. Energy and Power Analysis

While flying, the bat generates power to stay aloft, overcome drag, and to maneuver through air. For a straight level flight at constant velocity, the basic power required covers two aspects: producing lift to balance its weight and overcoming drag during forward motion. For maneuvering flight however, additional power in excess of the base power is needed to turn, climb, or accelerate. In this section, we present a total energy analysis to study the power expenditure of the ascending right turn. Figure 23-a presents the change in potential energy (PE) and kinetic energy (PE) during the flight. The climbing decelerating bat gains PE (energy gain) and loses KE (energy loss). Since the loss in KE is larger than the gain in PE, the bat experiences a net energy expenditure during the maneuver. Figure 23-b presents the power expenditure budget for the current maneuvering flight. The first element considered is the aerodynamic power which represents the rate of work

done on the air by the wing. The aerodynamic power is obtained from the flow simulation using $P = \vec{F} \cdot \vec{v}$ on the differential elements of the wing followed by a full surface integration. In addition to the aerodynamic power, the rate of change of kinetic energy (KE) and potential energy (PE) also need to be considered as both the altitude and velocity of the bat changes in the maneuvering flight. In case of descent or deceleration, less aerodynamic power is needed whereas ascent or acceleration increases the power load on the bat. Figure 23 shows the evolution of PE and KE and the net power required for the current maneuver which is the aerodynamic power plus or minus the rate of change of PE and KE.

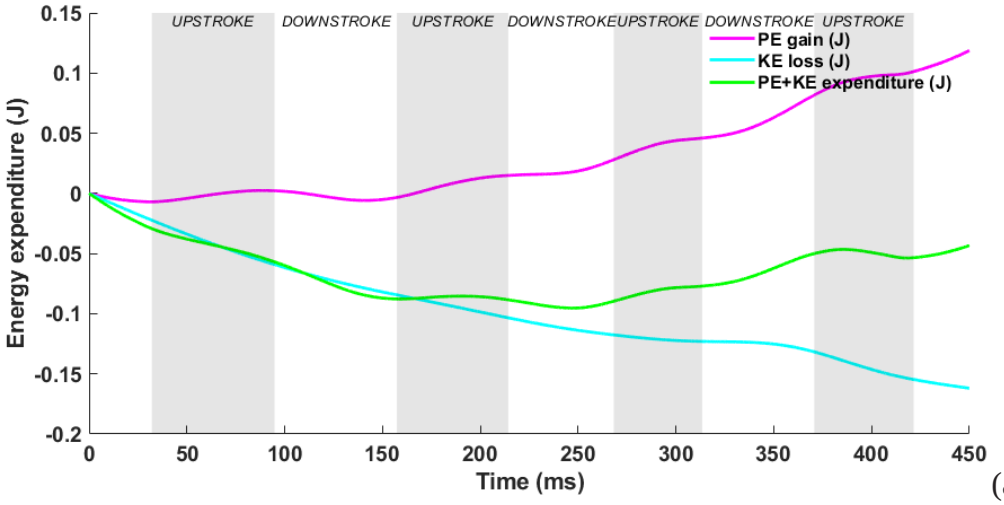

(a)

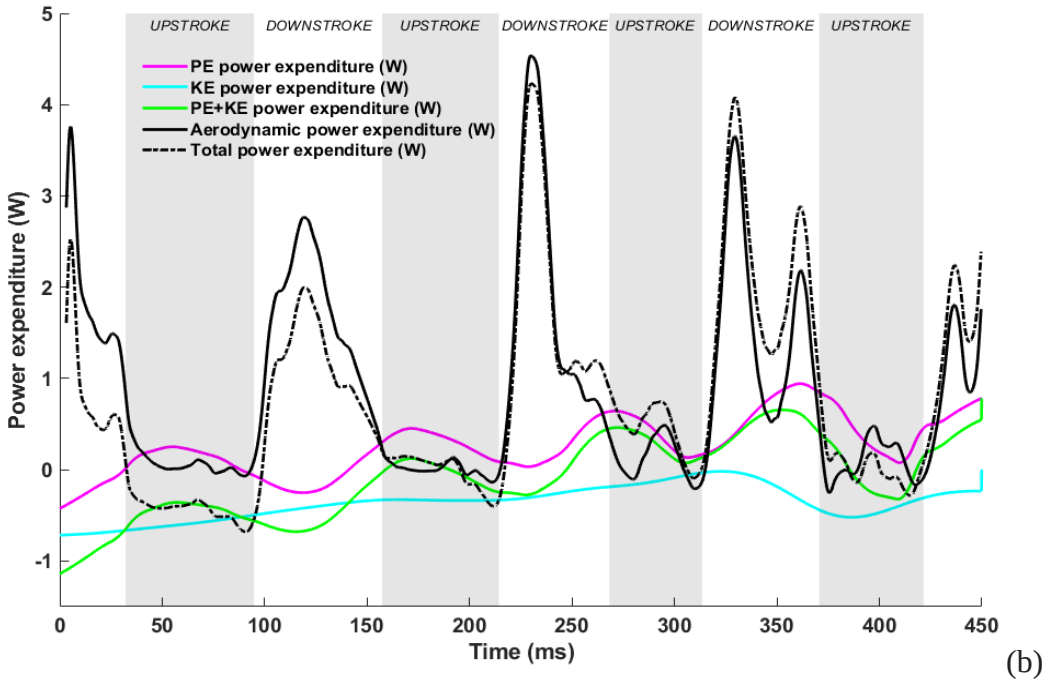

(b)

Figure 23: (a) Kinetic and potential energy loss and gain; (b) total power expenditure for the maneuvering flight.

In the current maneuver, the bat is ascending (increased power expenditure), turning (increased power expenditure) and decelerating (decreased power expenditure or effective power gain). The ascent is steady from an early stage of the flight with a steep ascent at the third cycle. The turn starts around midflight and becomes tightest at the third cycle, while the deceleration is not so prominent until the second cycle and peaks around the third cycle. At the beginning of the flight, when the bat is only preparing for the maneuver but has not entered the turn yet, the rate of conversion of potential energy into flight energy is lower than the gain resulting from the decceleration. Thus, the total power expenditure is less than the calculated aerodynamic power expenditure. However, during the maneuver, additional power is required on top of the base power expenditure as a cost of turning and climbing. With the bat slowing down, the resulting gain in kinetic energy decreases the power load. However, the energy required to make the ascent and turn

is more than the gain from the deceleration and a net increase of power load results. Thus, when the bat performs the maneuver, the total power expenditure is elevated beyond the aerodynamic power. The average total power expenditure for the current flight is 0.67 W which is comparable to the power observed during the maneuvering flight of Windes et al. [1] which shows a 94% increase compared to a straight flight.

4. SUMMARY AND CONCLUSIONS

We have investigated the kinematics and dynamics of a *H. pratti* performing a turning ascending maneuver. Special attention has been given to the mechanics of executing the maneuver and to identify commonalities with the previous investigation of Windes et al. [1] in which a *H. armiger* performed a similar maneuver under comparable conditions. Both bats utilized roll and yaw rotations of the body synergistically to redirect the force vector inward to provide the required centripetal force to control the turn. While both yaw and roll rotations can be clearly identified and related to the force moments generated by the wing kinematics, the timing and relative importance of one versus the other varies between the two flights and in general is expected to depend on the initial state of flight entering the turn, the extent of the turn, velocity, etc. For example, the roll moment and roll angle utilized by the *H. pratti* in the current study are larger than that observed in *H. armiger*, in spite of a similar rate of turn. In generating the roll and yaw moments, the bats utilize force as well as moment-arm asymmetries between the two wings. There is evidence in both flights that the wing inside the turn is drawn closer to the body while executing the turn to reduce the moment arm and accentuate force asymmetries. Force asymmetries are created by introducing phase lags in force generation between the wings and also redirecting force production to different parts of the wing. For example, there is evidence in both flights that the yaw moment is produced by thrust asymmetries on the outer part of the wing.

A common trait noted in both flights was that during the initiation of the maneuver, there was a marked increase in the flapping frequency and a shortening of the upstroke compared to the downstroke. Most probably this trait is to power the ascent since a turn can be achieved by introducing force or moment-arm asymmetries which may not require a lot more power over and above what is expended by the bat during straight flight. The ascent is characterized by an increase in the lift force in the body coordinate system. Another observation in both flights was the generation of a small thrust force in the upstroke during the maneuver, which is absent in level flight. The thrust peak appeared consistently through the maneuver of the *H. armiger* and appeared during the latter half of the flight of the *H. pratti*. A similar peak was also observed by Viswanath et al. [64] in a climbing flight of a fruit bat with no lateral maneuver. This indicates that the smaller thrust peaks observed during upstrokes are mostly associated with the elevation gain and compensate for the negative component of lift force in the body frame which acts against forward motion on the inclined climbing trajectory of the bat.

The power expended by the *H. pratti* in the current study for the turning and ascending maneuver is quite similar to that calculated for the *H. armiger* in Windes et al. [1]. In both cases, the average power during the maneuver is about 0.67 W and 0.66 W, which is approximately twice (~1.91-1.94) the power needed for level flight (0.34 W in Windes et al. [1]).

Bat flight provides a compelling model for bioinspired MAV designs for agile flight. Thus it is important to extract the kinematic and aerodynamic features which bats use to effectuate a certain maneuver. This is one of few studies which directly relate kinematics to aerodynamic force generation, which is a critical component for identifying kinematic traits used across different bat species and individuals for a specific maneuver. The current study has demonstrated many common traits and features for one maneuver, but has also identified kinematic features with

markedly different trends; wing kinematic markers such as stroke plane angle, stroke plane deviation angle, flapping amplitude, half span showed many differences between the two flights. Differences were also observed in the relative body orientation with respect to the respective flight trajectories. Further methodical investigation of different maneuvers across species and individuals will significantly add to a more comprehensive understanding of kinematic asymmetries, aerodynamic forces, and power loadings and the inter-dependence with bat wing morphology.

ACKNOWLEDGEMENTS

The authors acknowledge Advanced Research Computing at Virginia Tech for providing computational resources for the numerical simulations (URL: http://www.arc.vt.edu). The authors would also like to acknowledge Prof. Rolf Mueller and Xiaozhou Fan for the flight measurements. This project was supported on NSF CBET Grant No. 1510797.

REFERENCES

[1] P. Windes, D.K. Tafti, R. Müller, Kinematic and aerodynamic analysis of a bat performing a turning-ascending maneuver, Bioinspiration and Biomimetics. 16 (2020). doi:10.1088/1748-3190/abb78d.

[2] J.A. Cheney, N. Konow, K.M. Middleton, K.S. Breuer, T.J. Roberts, E.L. Giblin, S.M. Swartz, Membrane muscle function in the compliant wings of bats, Bioinspir. Biomim. 9 (2014) 025007. doi:10.1088/1748-3182/9/2/025007.

[3] J. Young, S.M. Walker, R.J. Bomphrey, G.K. Taylor, A.L.R. Thomas, Details of insect wing design and deformation enhance aerodynamic function and flight efficiency.,

Science. 325 (2009) 1549–52. doi:10.1126/science.1175928.

[4] T. Nakata, H. Liu, Aerodynamic performance of a hovering hawKmoth with flexible wings: A computational approach, Proc. R. Soc. B Biol. Sci. 279 (2012) 722–731. doi:10.1098/rspb.2011.1023.

[5] M.J.C. Smith, Simulating moth wing aerodynamics: Towards the development of flapping-wing technology, AIAA J. 34 (1996) 1348–1355. doi:10.2514/3.13239.

[6] H. Liu, C.P. Ellington, K. Kawachi, C. van den Berg, A.P. Willmott, A computational fluid dynamic study of hawkmoth hovering, J. Exp. Biol. 201 (1998). https://jeb.biologists.org/content/201/4/461 (accessed March 31, 2021).

[7] H. Wan, H. Dong, K. Gai, Computational investigation of cicada aerodynamics in forward flight, J. R. Soc. Interface. 12 (2014). doi:10.1098/rsif.2014.1116.

[8] Y. Ren, H. Dong, X. Deng, B. Tobalske, Turning on a dime: Asymmetric vortex formation in hummingbird maneuvering flight, Phys. Rev. Fluids. 1 (2016) 050511. doi:10.1103/PhysRevFluids.1.050511.

[9] T. Nakata, H. Liu, Y. Tanaka, N. Nishihashi, X. Wang, A. Sato, Aerodynamics of a bio-inspired flexible flapping-wing micro air vehicle, Bioinspir. Biomim. 6 (2011) 045002. doi:10.1088/1748-3182/6/4/045002.

[10] L. Zheng, T.L. Hedrick, R. Mittal, Time-Varying Wing-Twist Improves Aerodynamic Efficiency of Forward Flight in Butterflies, PLoS One. 8 (2013) e53060. doi:10.1371/journal.pone.0053060.

[11] M. Maeda, T. Nakata, I. Kitamura, H. Tanaka, H. Liu, Quantifying the dynamic wing

morphing of hovering hummingbird, R. Soc. Open Sci. 4 (2017). doi:10.1098/rsos.170307.

[12] W. Shyy, M. Berg, D. Ljungqvist, Flapping and flexible wings for biological and micro air vehicles, 1999. doi:10.1016/S0376-0421(98)00016-5.

[13] B.N.L. Lentink D., Jongerius S.R., The Scalable Design of Flapping Micro-Air Vehicles Inspired by Insect Flight, Springer, Berlin, Heidelberg, 2009.

[14] J.W. Gerdes, S.K. Gupta, S.A. Wilkerson, A review of bird-inspired flapping wing miniature air vehicle designs, J. Mech. Robot. 4 (2012) 1–11. doi:10.1115/1.4005525.

[15] Y. K. Ma, P. Chirarattananon, B. S. Fuller, and J. R. Wood, Controlled Flight of a Biologically Inspired, Insect-scale Robot, Science (80-.). (2013) 603–607.

[16] G.K. Taylor, R.L. Nudds, A.L.R. Thomas, Flying and swimming animals cruise at a Strouhal number tuned for high power efficiency, Nature. 425 (2003) 707–711. doi:10.1038/nature02000.

[17] S.J. Chung, M. Dorothy, Neurobiologically inspired control of engineered flapping flight, J. Guid. Control. Dyn. 33 (2010) 440–453. doi:10.2514/1.45311.

[18] A.L.A. and R.M. Y. Lin, Y. Xu, H. Chen, M. J. Bender, Optimal Threshold and LoG Based Feature Identification and Tracking of Bat Flapping Flight, in: IEEE Winter Conf. Appl. Comput. Vis. (WACV), St. Rosa, CA, USA, 2017, Pp. 418-426, Doi 10.1109/WACV.2017.53., 2017. doi:10.1371/journal.pone.0218672.

[19] M.J. Bender, H.G. McClelland, G. Bledt, A. Kurdila, T. Furukawa, R. Mueller, Trajectory estimation of bat flight using a multi-view camera system, AIAA Model. Simul. Technol.

Conf. 2015. (2015) 1–13. doi:10.2514/6.2015-1806.

[20] J.A. Cheney, N. Konow, A. Bearnot, S.M. Swartz, A wrinkle in flight: The role of elastin fibres in the mechanical behaviour of bat wing membranes, J. R. Soc. Interface. 12 (2015). doi:10.1098/rsif.2014.1286.

[21] J.A. Cheney, J.J. Allen, S.M. Swartz, Diversity in the organization of elastin bundles and intramembranous muscles in bat wings, J. Anat. 230 (2017) 510–523. doi:10.1111/joa.12580.

[22] S.M. Swartz, Skin and bones functional, architectural, and mechanical differentiation in the bat wing, Bat Biology and Conservation, 1998. doi:10.1371/journal.pone.0218672.

[23] J.W. Bahlman, R.M. Price-Waldman, H.W. Lippe, K.S. Breuer, S.M. Swartz, Simplifying a wing: diversity and functional consequences of digital joint reduction in bat wings, J. Anat. 229 (2016) 114–127. doi:10.1111/joa.12457.

[24] Y. Winter, O. Von Helversen, The energy cost of flight: Do small bats fly more cheaply than birds?, J. Comp. Physiol. - B Biochem. Syst. Environ. Physiol. 168 (1998) 105–111. doi:10.1007/s003600050126.

[25] R. Von Busse, R.M. Waldman, S.M. Swartz, C.C. Voigt, K.S. Breuer, The aerodynamic cost of flight in the short-tailed fruit bat (Carollia perspicillata): Comparing theory with measurement, J. R. Soc. Interface. 11 (2014). doi:10.1098/rsif.2014.0147.

[26] F.T. Muijres, G.R. Spedding, Y. Winter, A. Hedenström, Actuator disk model and span efficiency of flapping flight in bats based on time-resolved PIV measurements, Exp. Fluids. 51 (2011) 511–525. doi:10.1007/s00348-011-1067-5.

[27] F.T. Muijres, L.C. Johansson, M.S. Bowlin, Y. Winter, A. Hedenström, Comparing Aerodynamic Efficiency in Birds and Bats Suggests Better Flight Performance in Birds, PLoS One. 7 (2012) e37335. doi:10.1371/journal.pone.0037335.

[28] U.M. Norberg, T.H. Kunz, J.F. Steffensen, Y. Winter, O. von Helversen, The cost of hovering and forward flight in a nectar-feeding bat, Glossophaga soricina, estimated from aerodynamic theory, J. Exp. Biol. 182 (1993). https://jeb.biologists.org/content/182/1/207 (accessed March 16, 2021).

[29] A. Hedenström, L.C. Johansson, G.R. Spedding, Bird or bat: comparing airframe design and flight performance, Bioinspir. Biomim. 4 (2009) 015001. doi:10.1088/1748-3182/4/1/015001.

[30] N. Konow, J.A. Cheney, T.J. Roberts, J. Iriarte-Díaz, K.S. Breuer, J.R.S. Waldman, S.M. Swartz, Speed-dependent modulation of wing muscle recruitment intensity and kinematics in two bat species, J. Exp. Biol. 220 (2017) 1820–1829. doi:10.1242/jeb.144550.

[31] D.K. Riskin, D.J. Willis, J. Iriarte-Díaz, T.L. Hedrick, M. Kostandov, J. Chen, D.H. Laidlaw, K.S. Breuer, S.M. Swartz, Quantifying the complexity of bat wing kinematics, J. Theor. Biol. 254 (2008) 604–615. doi:10.1016/j.jtbi.2008.06.011.

[32] P. Windes, D.K. Tafti, R. Müller, Determination of spatial fidelity required to accurately mimic the flight dynamics of a bat, Bioinspiration and Biomimetics. 14 (2019). doi:10.1088/1748-3190/ab3e2a.

[33] T.Y. Hubel, N.I. Hristov, S.M. Swartz, K.S. Breuer, Wake structure and kinematics in two insectivorous bats, Philos. Trans. R. Soc. B Biol. Sci. 371 (2016). doi:10.1098/rstb.2015.0385.

[34] L.C. Johansson, M. Wolf, A. Hedenström, A quantitative comparison of bird and bat wakes, J. R. Soc. Interface. 7 (2009) 61–66. doi:10.1098/rsif.2008.0541.

[35] M. Wolf, L.C. Johansson, R. Von Busse, Y. Winter, A. Hedenström, Kinematics of flight and the relationship to the vortex wake of a Pallas' long tongued bat (Glossophaga soricina), J. Exp. Biol. 213 (2010) 2142–2153. doi:10.1242/jeb.029777.

[36] P. Windes, X. Fan, M. Bender, D.K. Tafti, R. Müller, A computational investigation of lift generation and power expenditure of Pratt's roundleaf bat (Hipposideros pratti) in forward flight, PLoS One. 13 (2018) 1–26. doi:10.1371/journal.pone.0207613.

[37] F.T. Muijres, L. Christoffer Johansson, Y. Winter, A. Hedenström, Leading edge vortices in lesser long-nosed bats occurring at slow but not fast flight speeds, Bioinspir. Biomim. 9 (2014) 025006. doi:10.1088/1748-3182/9/2/025006.

[38] L.C. Johansson, M. Wolf, R. von Busse, Y. Winter, G.R. Spedding, A. Hedenström, The near and far wake of Pallas' long tongued bat (Glossophaga soricina)., J. Exp. Biol. 211 (2008) 2909–18. doi:10.1242/jeb.018192.

[39] A. Hedenström, L.C. Johansson, M. Wolf, R. von Busse, Y. Winter, G.R. Spedding, Bat Flight Generates Complex Aerodynamic Tracks, Science (80-.). 316 (2007) 894–897. doi:10.1126/SCIENCE.1142281.

[40] S. Sekhar, P. Windes, X. Fan, D.K. Tafti, Canonical description of wing kinematics and dynamics for a straight flying insectivorous bat (Hipposideros pratti), 2018. doi:10.1371/journal.pone.0218672.

[41] L.C. Johansson, J. Håkansson, L. Jakobsen, A. Hedenstrom, Ear-body lift and a novel

thrust generating mechanism revealed by the complex wake of brown long-eared bats (Plecotus auritus), Sci. Rep. 6 (2016) 1–9. doi:10.1038/srep24886.

[42] C. Schunk, S.M. Swartz, K.S. Breuer, The influence of aspect ratio and stroke pattern on force generation of a bat-inspired membrane wing, Interface Focus. 7 (2017). doi:10.1098/rsfs.2016.0083.

[43] U.M. NORBERG, Some Advanced Flight Manoeuvres of Bats, J. Exp. Biol. 64 (1976). https://jeb.biologists.org/content/64/2/489 (accessed March 16, 2021).

[44] A.J. Bergou, S.M. Swartz, H. Vejdani, D.K. Riskin, L. Reimnitz, G. Taubin, K.S. Breuer, Falling with Style: Bats Perform Complex Aerial Rotations by Adjusting Wing Inertia, PLOS Biol. 13 (2015) e1002297. doi:10.1371/journal.pbio.1002297.

[45] J. Iriarte-Díaz, S.M. Swartz, Kinematics of slow turn maneuvering in the fruit bat Cynopterus brachyotis., J. Exp. Biol. 211 (2008) 3478–89. doi:10.1242/jeb.017590.

[46] P. Henningsson, L. Jakobsen, A. Hedenström, Aerodynamics of manoeuvring flight in brown long-eared bats (Plecotus auritus), J. R. Soc. Interface. 15 (2018). doi:10.1098/rsif.2018.0441.

[47] H.D. Aldridge, Turning flight of bats, J. Exp. Biol. 128 (1987). https://jeb.biologists.org/content/128/1/419 (accessed March 16, 2021).

[48] D.B. Boerma, K.S. Breuer, T.L. Treskatis, S.M. Swartz, Wings as inertial appendages : how bats recover from aerial stumbles, (2019). doi:10.1242/jeb.204255.

[49] D.B. Boerma, J.P. Barrantes, C. Chung, G. Chaverri, S.M. Swartz, Specialized landing maneuvers in Spix ’ s disk-winged bats (Thyroptera tricolor) reveal linkage between

roosting ecology and landing biomechanics, (2019). doi:10.1242/jeb.204024.

[50] P. Windes, D.K. Tafti, R. Müller, Analysis of a 180-degree U-turn maneuver executed by a hipposiderid bat, PLoS One. 15 (2020) 1–23. doi:10.1371/journal.pone.0241489.

[51] T. Svoboda, D. Martinec, T. Pajdla, A convenient multicamera self-calibration for virtual environments, Presence Teleoperators Virtual Environ. 14 (2005) 407–422. doi:10.1162/105474605774785325.

[52] D.K. Tafti, GenIDLEST - A scalable parallel computational tool for simulating complex turbulent flows, in: ASME-IMECE, 2001: pp. 347–356.

[53] D. Rahman, Aevelina; Windes, Peter; Tafti, Data used for analyzing a turning-ascending flight of a H. pratti bat, (n.d.). doi:10.5061/dryad.mcvdnck2c.

[54] A. Rahman, D. Tafti, The role of vortex–vortex interactions in thrust production for a plunging flat plate, J. Fluids Struct. 96 (2020) 103011. doi:10.1016/J.JFLUIDSTRUCTS.2020.103011.

[55] H. Hosseinzadegan, D.K. Tafti, A Predictive Model of Thrombus Growth in Stenosed Vessels with Dynamic Geometries, J. Med. Biol. Eng. 39 (2019) 605–621. doi:10.1007/s40846-018-0443-5.

[56] H. Elghannay, D. Tafti, K. Yu, Evaluation of physics based hard-sphere model with the soft sphere model for dense fluid-particle flow systems, Int. J. Multiph. Flow. 112 (2019) 100–115. doi:10.1016/J.IJMULTIPHASEFLOW.2018.12.004.

[57] D. Tafti, C. Dowd, X. Tan, High Reynold number LES of a rotating two-pass ribbed duct, Aerospace. 5 (2018). doi:10.3390/aerospace5040124.

[58] K. Yu, H.A. Elghannay, D. Tafti, An impulse based model for spherical particle collisions with sliding and rolling, Powder Technol. 319 (2017) 102–116. doi:10.1016/J.POWTEC.2017.06.049.

[59] A. Rahman, D. Tafti, Characterization of heat transfer enhancement for an oscillating flatplate-fin, Int. J. Heat Mass Transf. 147 (2020). doi:10.1016.

[60] K. Nagendra, D.K. Tafti, K. Viswanath, A new approach for conjugate heat transfer problems using immersed boundary method for curvilinear grid based solvers, J. Comput. Phys. 267 (2014) 225–246. doi:10.1016/j.jcp.2014.02.045.

[61] Z. Cao, D.K. Tafti, M. Shahnam, Modeling drag force in ellipsoidal particle suspensions with preferential orientation, Powder Technol. 378 (2021) 274–287. doi:10.1016/j.powtec.2020.09.067.

[62] T.K. Oh, D. Tafti, K. Nagendra, LES-conjugate heat transfer analysis of a ribbed cooling passage using the immersed boundary method, Proc. ASME Turbo Expo. 5A-2019 (2019) 1–16. doi:10.1115/GT2019-90397.

[63] J. Iriarte-Díaz, D.K. Riskin, D.J. Willis, K.S. Breuer, S.M. Swartz, Whole-body kinematics of a fruit bat reveal the influence of wing inertia on body accelerations., J. Exp. Biol. 214 (2011) 1546–53. doi:10.1242/jeb.037804.

[64] K. Viswanath, K. Nagendra, J. Cotter, M. Frauenthal, D.K. Tafti, Straight-line climbing flight aerodynamics of a fruit bat, Phys. Fluids. 26 (2014). doi:10.1063/1.4864297.

Chapter 5: Role of Wing Inertia on Maneuvering Bat Flights

Aevelina Rahman

Danesh Tafti[5]

Department of Mechanical Engineering, Virginia Tech, Blacksburg, VA 24061

ABSTRACT

The individual effects of aerodynamics and wing inertia on the motion dynamics for maneuvering flight of *H. armiger* and *H. pratti* bats have been investigated. Comparative studies among a straight flight, two ascending right turns, and a U-turn reveal that inertial forces play an essential and sometimes crucial role in effecting the maneuvers. The maneuvering trajectory of the bat is mostly driven by the aerodynamic forces generated by the wings along the flight path, whereas inertial forces for the most part drive the intra-cycle fluctuations. Inertial forces were also found to contribute non-trivially to the ascending motion of the *H. armiger*. Similar to translation, while aerodynamic moments account for the general rotational trends in roll, pitch and yaw angles exhibited by the bat body, inertial moments influence intra-cycle fluctuations. In addition, inertial moments play a dominant and crucial role for effecting yaw rotation during maneuvers for the sweeping turns as well as the U-turn. The moment resulting from the Coriolis force is deemed essential in accurate yaw prediction for lateral maneuvers. Finally, as the maneuver gets more complex or extreme such as in a 180° U-turn, the importance of the Coriolis and centrifugal moments increase, with the largest effect of centrifugal moments evidenced in the U-turn.

Keywords: Inertia, distributed wing-mass, aerodynamics, dynamic equation of motion, rotation

[5] Corresponding author: 213E Goodwin Hall, 635 Prices Fork Road, Blacksburg, VA 24061; Tel: +1 (540) 231-9975; email: dtafti@exchange.vt.edu

Declarations of interest: none

1. INTRODUCTION

Natural flyers i.e. insects, birds and bats have been a consistent inspiration for designing biomimetic micro-air vehicles [1] and thus studied in-depth. During flying, these animals flap their wings to produce aerodynamic forces that keep them aloft as well as propel them to the desired maneuver. As the wings themselves have some mass, the animals need to exert some portion of their total energy expenditure to articulate their wings into the complex kinematics required for the desired maneuver. The force expended to accelerate or decelerate the wings through air is termed as the inertial force. Thus, the total force active in animal flight has both the aerodynamic and the inertial counterparts associated with its motion dynamics [2].

Among the wide range of flying animals, insect flights have been extensively studied in the literature to understand the versatile effects of wing flapping kinematics and their diverse response in flight aerodynamics [3–10]. Considerable progress in the area of aerodynamic force mechanisms of insect flapping wings, has encouraged researchers to study the dynamics in detail. Early comparative studies on the stability of gliding and flapping flights concluded that, flapping can potentially enhance the static stability compared to gliding flights at certain speeds [11,12]. While studying insect flight dynamics, a common assumption made is to ignore the inertial forces associated with wing mass which is generally less than 5% of the body mass [13][14]. However, Sun et al. showed that, although the effects of the wings on an insect body are small, there could still exist a per flap-cycle change in the body orientation due to the inertial coupling of the wings that can influence the motion dynamics [15]. Another common simplification is done by treating the insect wing as a “rigid body” so that the linear theory of aircraft flight dynamics is applicable

[13,16]. Some studies treated the body and the two wings separately as three rigid bodies instead of just one rigid body [15,17]. But, their model still falls short in portraying the flight of an animal when the wings undergo considerable deformation while flying. Thus, none of the above mentioned simplifications are valid for a flying system where the wing mass is a significant percentage of the whole body mass like in birds or bats; and the wing shape deforms significantly as opposed to being "rigid" during flapping.

Studies investigating larger flyers has accumulated the knowledge of flapping flight by high-lighting additional features exhibited by virtue of their larger wing structures. As bird wings have some degree of flexibility, a rigid body assumption is often modified to account for their wing flexion [18–21]. Hedrick et al. showed that the re-configurability of bird wings allowed for inertial and aerodynamic modes of reorientation, both of which played important roles in the low speed turning flight of the rose-breasted cockatoo [22,23].

When it comes to flight maneuverability, agility and efficiency, the flights of bats has obtained special attention mainly due to their highly articulated bone structures and pliant wing membranes that provide flexibility and control over aerodynamic force and moment generation [24–26]. A number of studies have been done in literature to understand the intricate mechanisms of bat flight, most of which primarily focused on different aspects of straight flight such as wing and bone structure [24,27–30], flight efficiency and performance [31–37], complexity in wing kinematics [26,38,39] and aerodynamics [25,40–47]. Maneuvering bat flight on the other hand, brings in additional elements which are very worthy of investigation. Hence, although not as intensively studied as straight flight, different maneuvers of bats have also been researched in an effort to

identify common turning mechanisms such as pronation and supination of wings, asymmetries in drag or thrust, establish correlations between turn-radius and morphological parameters, identify individual roles of upstrokes and down-strokes in initiating maneuvers, understand the effect of instantaneous body orientation on attempted maneuvers and so on [16–19]. The inertial counterpart of bat flight, has however received less attention.

Aldridge et al. recommended that the instantaneous acceleration experienced by a bat during flight has three components- aerodynamic, gravitational and inertial. But their work concentrated on identifying the effect of upstroke 'tip-reversal" in thrust generation and only approximated the inertial contribution by body acceleration to better estimate the wing kinematics of different bat species [53]. Iriarte et al. considered the effect of the distributed mass on inertia. By modelling the mass distribution of a lesser dog faced fruit bat, they estimated the center of mass (COM) and tracked the change of its position through time. Upon comparing it with the measured COM via accelerometers set on specific points on the body, they concluded that inertial forces significantly affect the movement of COM [54]. Later, Riskin et al. used a more accurate mass distribution obtained from actual measurements of a bat carcass to investigate the inertial cost of wing flexion [55] and suggested that it could be substantial in comparison to the cost of moving the wings through the air. Dongfu et al. also used a computational mass model to investigate the individual effects of different bones and membrane of the bat wing on inertial force and power generation [56]. Although these studies shed light on the interplay between whole-body kinematics and the coupled inertial consequences, they lacked consideration of one key component, the flight aerodynamics. Bergou et al. presented a detailed study of bats performing complex aerial maneuvers by primarily manipulating wing inertia. They showed through a comparative study that

bat maneuvers did not rely on aerodynamic forces but a fruit fly, with nearly massless wings, would have to rely on aerodynamic forces to facilitate similar turns [49]. Boerma et al. also investigated the recovery maneuver from disruptive aerial stumbles for fruit bats and reported that the bats primarily responded by adjusting extension of wing-joints and recovered pre-disturbance body orientation and symmetrical wing motions very fast by using inertial moments [57]. However, these studies oversimplified the aerodynamics with a quasi-steady drag model considering a generalized coefficient and only the mean chord*span as wing area and thus fail to capture the intricate coupled dynamics of inertial and aerodynamic forces. Although Fan et al. incorporated both aerodynamic and inertial forces in the motion dynamics of a lesser-nosed-dog-faced fruit bat, the use of a lower order technique such as the blade element momentum theory (BEMT) to model the aerodynamics impairs the accuracy [58]. BEMT has been previously used for modeling the aerodynamics of insect [12] or bird [22] flights where the wing deformation is either non-existent or marginal as compared to bats.

One unique feature of bat flight is the highly stretchable wing membrane that can deform itself to allow for optimum capture and release of air to maximize aerodynamic force generation. While deriving the non-linear dynamics for flapping wing micro air vehicles, Orlowski et al. showed that the various aerodynamic modeling choices significantly impact the motion dynamics [59]. Lower order approximations cannot resolve these intricate features thus bat flight aerodynamics needs to be fully resolved by solving the Navier-strokes flow equations. Although some previous studies have used computational fluid dynamics, they have used rigid wing kinematics of insect flight as the boundary condition influencing the aerodynamics [15,16]. Thus far, there is no research done where the total wing kinematics have been used as the boundary condition to fully resolve the

aerodynamic forces so that it can be included in detailed motion dynamics. Motivated by this, the current investigation follows a computational approach to deconstruct the detailed kinematic-aerodynamic nuances of a maneuvering bat flight. This approach has been previously used for both level flight [39,42,45] and various maneuvering flights [60–62]. By using measured wing kinematic data as input boundary conditions to run detailed aerodynamic simulations, the current study strongly establishes the causal relationship between wing motion and force generation to effect the maneuver. The measured wing kinematics along with a detailed mass distribution are then utilized to account for the inertial consequences of the complete motion dynamics. The primary objective is to investigate the comparative/ individual role of aerodynamic and inertial forces and moments in effectuating the complete maneuver encompassing both translational and rotational aspects.

2. METHODOLOGY

To investigate the role of inertial versus aerodynamic forces in effecting bat flight trajectories, multiple bat flights have been experimentally recorded and analyzed. These feature a straight-descending flight path [61], two ascending right turns or sweeping turns [60,61], and a 180° U-turn [62]. The flights were performed by two different but morphologically similar bats coming from two different species, namely *H. armiger* and *H. pratti*. Table 1 lists the morphological parameters of the two individuals used in the current study.

Table 1. Morphological parameters of the bats used

Species	Performed maneuvers	Mass (g)	Span (cm)	Wing Area (cm^2)	Planform area (cm^2)	chord (cm)	AR	Wing loading (N/m^2)
Hipposideros pratti	Sweeping turn	55	53	522	459	8.91	6.12	11.98

Hipposideros armiger	Straight flight, Sweeping turn, U-turn	54.5	51	434	398	7.8	6.5	13.4

Definitions of the different parameters presented in Table 1 are as follows:

- **Wing area:** The wing area is defined as the maximum total surface area during the downstroke (when the wing is fully stretched), averaged over several wingbeat cycles.
- **Planform area:** The planform area is defined as the mean wing area during downstroke and upstroke projected onto the local body-fixed $x_b - y_b$ plane, averaged over several wingbeat cycles.
- **Span:** The span is defined as the maximum wingtip to wingtip distance averaged over the wingbeat cycles.
- **Mean Chord:** The mean chord is defined by dividing the maximum planform area within a cycle by the respective span distance and averaged over several wingbeat cycles.
- **Aspect Ratio:** Aspect ratio (AR) is defined as span squared over planform area
- **Wing Loading:** Wing loading is defined as the bat weight divided by the planform area.

The mass and span of the two individuals are almost identical varying just 1% and 3% respectively. The wing area of the *H. pratti* bat however is larger, leading to a larger mean chord, smaller aspect ratio and smaller wing loading compared to the *H. armiger* bat.

The straight flight consisted of 2.5 wingbeat cycles (42 video frames) spread over 342 ms of flight time. During this flight, the bat accelerated to travel ~65 cm in the flight direction. There was no lateral maneuver whatsoever, but the bat descended by about 11 cm. While the primary interest of current work is to investigate the interplay between inertial and aerodynamic forces and moments

on maneuvering flight, the straight flight is analyzed to establish a baseline case for nominal flight behavior. Being individual living animals, bats always show some irregularities in the wing-motion from flap to flap. Comparing the complex maneuvering flights to a straight flight facilitates identifying significantly distinctive features made to effectuate the maneuvers while ignoring the small irregularities. The two sweeping flights studied were ascending right turns consisting of 3.5 and 5 wingbeat cycles (55 and 68 video frames) spread over 450 and 558 ms of flight time for the *H. pratti* and *H. armiger* bats, respectively. Both bats decelerated in the course of travelling 110 cm (*H. pratti*) and 80 cm (*H. armiger)* to accommodate the maneuver. Both of them traversed slightly towards the left and then took a big turn towards the right achieving 19 cm (*H. Pratti*) and 32 cm (*H. armiger*) of lateral displacement with a cumulative 46 and 53 degrees bearing change in the horizontal plane, respectively. During these flights, the bats gained a height of 19 cm (*H. Pratti*) and 18 cm (*H. armiger*). The U-turn consisted of 6 wingbeat cycles (90 video frames) spread over 690 ms of flight time and was segmented into 4 sections. While approaching the U-turn, the bat decelerated to execute a gradual right turn and started to climb which lasted for the first two cycles. During the initiation of the U-turn, the bat tightened the turn radius rapidly and continued to climb and decelerate, lasting for the next two cycles. The apex of the turn occurred at the 5^{th} cycle with rapid change of bearing angle accompanied by maximum height gain (36 cm), minimum turn radius, and minimum flight velocity. Finally, the bat egressed the U-turn with an acceleration and nominal descent (3 cm down from apex at completion of cycle 6). The three flights performed by the *H. armiger* bat were segregated from one continuous flight recording during which the bat did the sweeping turn first, followed by the U-turn and the straight flight. Table 2 summarizes the general flight parameters for the four different flights analyzed while Figure 1 provides the planar top and side views of their trajectories.

Table 2. Detailed parameters for all the flights analyzed

Maneuver	Flight duration (s)	Total # of full wingbeat cycles	Mean velocity (m/s)	Mean acceleration (m/s^2)	Wingbeat frequency (Hz)
Straight Flight	0.342	2.5	2.02	0.76	9.4
Sweeping turn (*H. pratti*)	0.450	3.5	2.64	-1.78	9.08
Sweeping turn (*H. armiger*)	0.558	5.0	1.81	-0.86	9.7
U-turn	0.690	6.0	1.18	-1.72	8.7

The mean flight velocities vary from 2.64 m/s to 1.18 m/s and lie in the same range as that reported by Iriate-Díaz et al. [50] and Henningsson et al. [51] for their respective maneuvering flights. While the wing inertia studied by Fan et al. was for a higher velocity flight of a bat [58], Hedrick et al. covered a wide range of velocities (including those for current study) for birds [23,63]. There are some consistent trends visible among the maneuvering flights investigated in the current study. In effectuating the sweeping turn and the U-turn, the bats combine these maneuvers with ascension and a gain in height. For the sweeping turns, the right turn and ascent start at about the same time (cycle 2 for sweeping turn 1 and cycle 3 for sweeping turn 2) while for the U-turn the apex and maximum ascent was gained simultaneously during the 5^{th} cycle as shown in Figure 1(b, c, d). It is postulated here that the change in direction is the primary maneuver. Ascension accompanying a change in flight direction is only used to decelerate against gravity and to reduce the flight velocity quickly to limit the centrifugal forces that arise during the turning maneuver. The tighter (smaller radius) the maneuver, the larger is the needed reduction in velocity. Interestingly, in all three maneuvers, the calculated centrifugal forces are in the same range of 0.2-0.25 N [60–62]

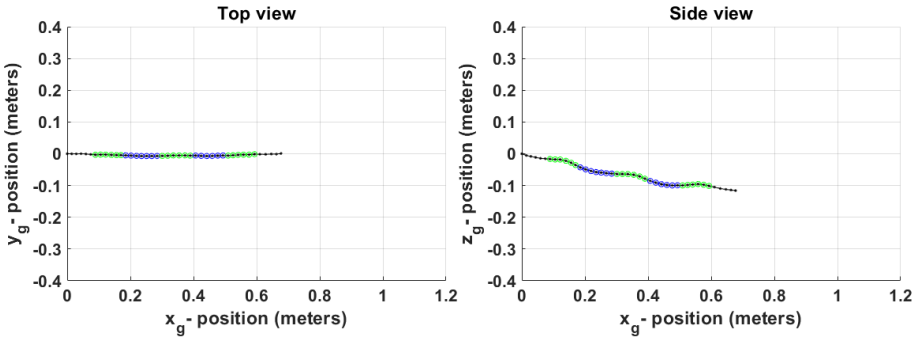
Top view
Side view
y_g - position (meters)
z_g - position (meters)
x_g - position (meters)
x_g - position (meters)

(a)

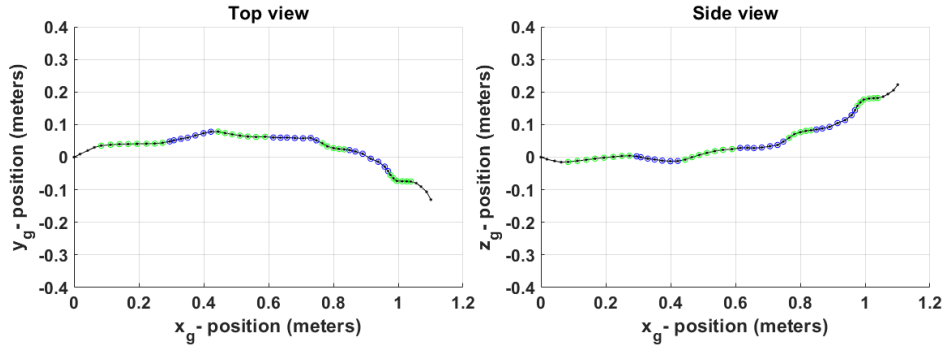
Top view
Side view
y_g - position (meters)
z_g - position (meters)
x_g - position (meters)
x_g - position (meters)

(b)

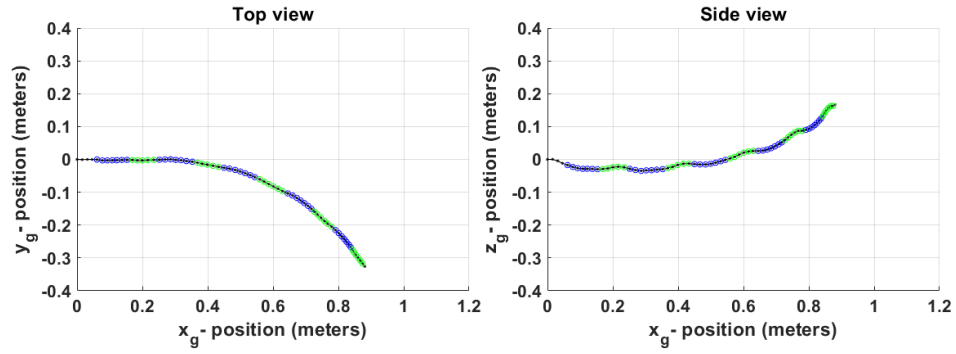
Top view
Side view
y_g - position (meters)
z_g - position (meters)
x_g - position (meters)
x_g - position (meters)

(c)

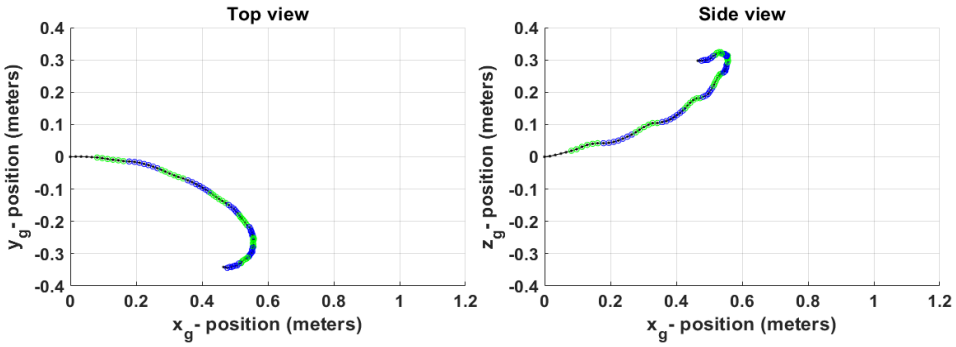
Top view
Side view
y_g - position (meters)
z_g - position (meters)
x_g - position (meters)
x_g - position (meters)

(d)

Figure 1: Planar top and side views of the flight trajectories; (a) Straight flight, *H. armiger;* (b) Sweeping turn (*H. Pratti*); (c) Sweeping turn (*H. armiger*)*;* (d) U-turn, *H. armiger*. Green and blue dots depict individual frames in upstrokes and downstrokes of the video recording.

2.1. Experimental Set-up and Motion Capture

The bats used for the current study were kept with a group of conspecifics in a controlled indoor environment designed to allow natural movement. Ethical codes were followed according to Virginia Tech's Institutional Animal Care and Use Committee (protocol number 15-067). Kinematic data were collected using an optical 3D motion capture system assembled inside an open-ended flight tunnel (1.2 m×1.2 m×5 m). The motion capture system had 21 synchronized video cameras, the details of which are given in a prior work [42]. For each flight, the bats flew without interruption through the tunnel after being released allowing the camera array to record at 120 frames per second and in 1920×1080 pixel resolution.

In order to track the wing motion, small white circular markers made of medical tape were set to the bats' wings to capture the detailed spatio-temporal kinematic features performed during the maneuvers. Stereo triangulation was performed for the recorded frames using a custom MATLAB code to achieve a digital representation of the bat wings in 3D space over the flight time. In the event of occlusions, a temporal spline curve and a spatial implicit surface reconstruction [39] was used to fill in the missing data. Afterwards a 3D reconstruction was done using a semi-automated MATLAB code in order to define point correspondences between frames. The details of these processes are described in previous works [1,32,36,53].

2.2. Mass Distribution

The two bats used for current study were an adult female Pratt's roundleaf bat (*Hipposideros pratti*) and an adult male great roundleaf bat (*Hipposideros armiger*) weighing 55 g and 54.5 g respectively. During data collection, small white circular markers made of medical tape were set to the bats' wings to capture the detailed spatio-temporal kinematic features performed during the maneuvers. 150 marker points were set to the *H. pratti* wing whereas 240 to the *H. armiger* wing. A spatial fidelity study was done to establish the relationship between the density of wing surface points and several aerodynamic metrics [39]. Their results indicated that the number of marker points set on the bats of current study was enough to resolve the aerodynamic parameters with adequate accuracy and capture the aerodynamic behavior observed during their complex wing kinematics. Figure 2 shows the white marker points and their digital reconstruction for a representative wing.


(a)
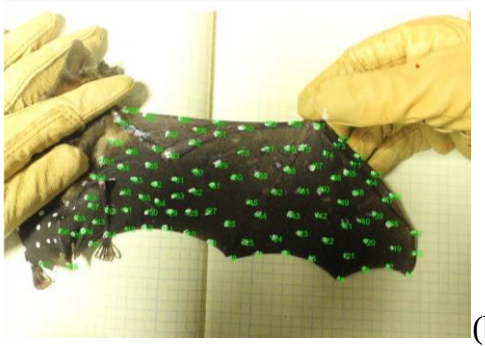
(b)

Figure 2: (a) Marker points set on a wing surface for flight recording experiments; (b) Green numeric depict the digitally reconstructed marker points.

In order to study the effect of wing inertia, detailed mass distribution of the bat wings was measured. After one of the bats (*H. armiger*) used for flight experiments died of natural causes, it's mass was measured using a mass scale accurate to $1/10^{th}$ of a microgram. Between the time of

living (during flight experiments) and after death mass measurements, the bat carcass lost some mass which was factored in in all the mesurements taken. Afterwards, the bat was sequentally dissected to different parts so that the mass mesurements of the head, body, leg-tail section, two separate wings, each wing-bone and the wing membrane could be recorded individually. Figure 3 shows the dissected portions of the bat carcass along with the breakdown of the mesured mass.

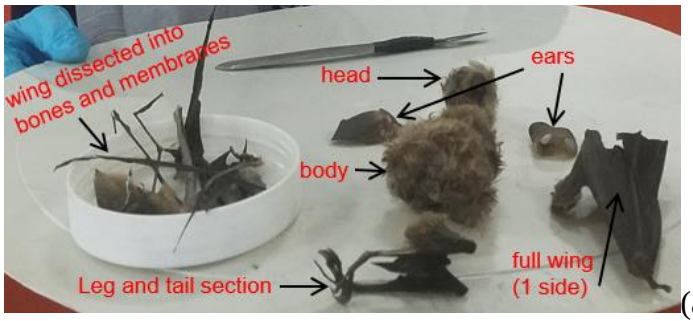

(a)

Body parts		Mass (g)
head		9.70
body		27.87
wing bones	Humerus (0.71 x 2)	1.42
	radius-ulna (1.71 x 2)	3.42
	thumb + digit-2 (0.16 x 2)	0.32
	digit-3 (0.44 x 2)	0.88
	digit-4 (0.31 x 2)	0.62
	digit-5 (0.22 x 2)	0.44
	femur + tibia-fibula + claws (0.82 x 2)	1.64
wing membrane (3.78 x 2)		7.56
Tail		0.63
Total		**54.5**

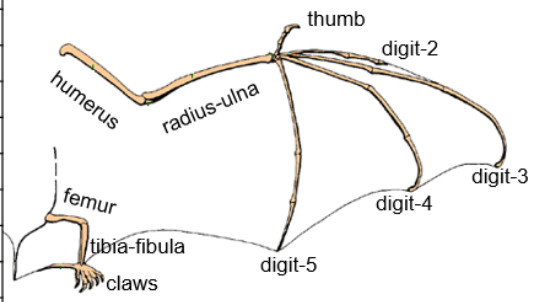

(b)

Figure 3: (a) Dissected portions of the bat carcass; (b) Breakdown of measured mass along with wing-bone schematic

The head and body accounted for the majority of the mass with the wings contributing ~31% of the entire mass. Within the wings, the membrane accounted for 48% of the wing mass. After the masses of the individual bones and membrane sections were recorded, the mass was uniformly

distrubuted to the marker points on the part. The bone joints got contributions from multiple bones making them the heaviest points among the distributed mass array. While distributing the mass, it was assumed that the left and right wings had the same mass. Although the mesurements were taken on the *H. armiger* bat, a similar distribution was assumed to be true for the *H. pratti* bat. The fact that both bats had nearly the same mass aided this assumption. However, the difference between the wing planform areas of the two bats (*H. pratti* was larger by a factor of ~1.2 than *H. armiger*) is factored in by redistributing the wing to body mass ratio for the *H. pratti*, finally resulting in more mass assigned to the wing of the *H. pratti* as compared to the *H. armiger* bat. Despite this, it is acknowledged that there might be some level of uncertainty associated with the mass distribution for the *H. pratti* bat. As getting dissected body-part measurements from an animal is challenging and involves ethical concerns, a similar approach was previously used where the mass measurements from one species was imparted to the inertial analyses of another species [55]. Figure 4 shows the final mass distribution used in the current study for the *H. pratti* bat.

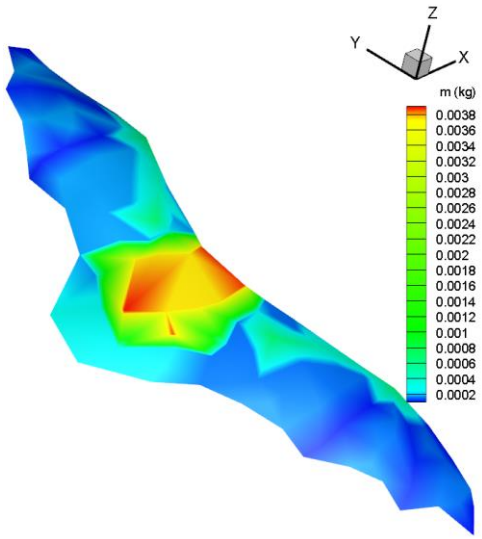

Figure 4: Distribution of mass assigned to marker points on the *H. pratti* bat body and wing. Bone mass is distributed over more marker points on digits 2 to 5.

2.3. Reference Frames

For kinematic, aerodynamic and inertial analysis, two reference frames are defined. The global or ground reference frame (x_g, y_g, z_g) is a fixed, inertial coordinate system with x_g directed along the longitudinal tunnel axis, z_g directed upward opposing gravity, and y_g directed normal to both x_g and z_g. The local or body reference frame (x_b, y_b, z_b) is fixed on the bat body and defined based on its time dependent instantaneous orientation. Throughout this paper, suffix g and b are used to refer to the variables in the global and body-fixed reference frames, respectively. The non-inertial body-fixed reference frame moves with the bat as it flies along; one such instance is shown in Figure 5 (a). With the origin set at the center of mass (COM) of the bat, the +ve y_b vector points laterally toward the left wing and +ve x_b along the body axis with perpendicularity enforced between the basis vectors x_b and y_b. Lastly, the upward pointing z_b vector is found by taking a right-handed cross-product between x_b and y_b. Figure 5(b) shows how the orientation of the non-inertial reference frame progresses with time along one representative flight trajectory. Detailed definition and description of the three basis vectors in the body-fixed coordinate system is presented in Windes et al. [61]. The local aerodynamic forces, inertial contributions and moments are all calculated using the instantaneous body-fixed coordinate system.

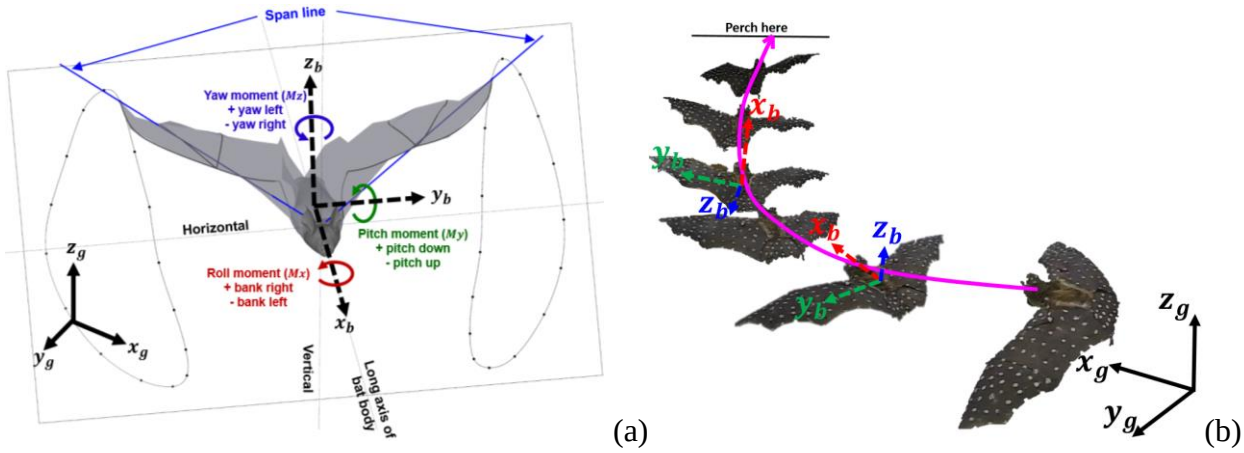

Figure 5: (a) Definition of the inertial (global) and non-inertial (body-fixed) coordinate system with bat body orientation at an arbitrary point during flight, span (blue line) is defined as the line connecting the shoulder to the wingtip, wingtip loci for the right and left wings are shown for a representative wingbeat cycle. (b) Flight path of *H. pratti* and body coordinate system along flight path.

The center of mass of the bat is calculated by $\boldsymbol{r}_{com,g} = \frac{\sum(m_i \boldsymbol{r}_{i,g})}{m}$, where $\boldsymbol{r}_{i,g}$ is the distance of point mass m_i from the global origin and m is the total bat mass. To test the accuracy of the calculated COM, we made use of the fact that $\sum(m_i \boldsymbol{r}_{i,b}) = 0$, where $\boldsymbol{r}_{i,b}$ is the distance of point mass m_i in the body frame from the calculated COM. The sum is divided by the mass of the bat and the span distance to normalize between different flights. As similar results were obtained for all the four flights, only the straight flight result is shown in Figure 6 which shows that $\sum(m_i \boldsymbol{r}_{i,b})_{nd}$ has a mean value of 0.095 for the straight flight which is sufficiently close to zero. Further, a sensitivity analysis was done by shifting the COM by ±2% and ±10% of span distance in all three coordinate directions. None of the combinations yielded a smaller $\sum(m_i \boldsymbol{r}_{i,b})_{nd}$ residue as shown in Figure 6 validating that the calculated COM is accurate.

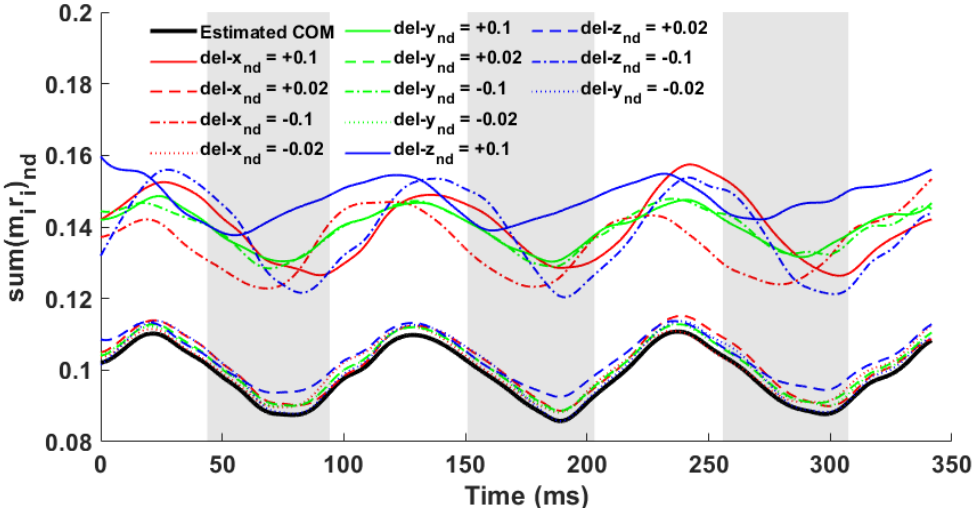

Figure 6: Accuracy of the center of mass; black line shows $\sum(m_i \boldsymbol{r}_{i,b})_{nd}$ for the COM used in the study, colored lines represent test cases where the COM was shifted to different locations.

The Euler rotations about the body fixed x_b, y_b and z_b axes are defined respectively as the roll, pitch, and yaw angles. Positive yaw, pitch and roll are directed towards left, down, and right. The negative of the definition of pitch angle is presented later in the paper as the pitch angle to denote upward motion by a positive value.

2.4. Aerodynamic Analysis

Using the detailed kinematics of the bat wings along the flight trajectory, a time-dependent aerodynamic analysis is conducted to obtain a detailed distribution of the external forces acting on the bat wings. An in-house incompressible Navier–Stokes solver, GenIDLEST [65] is used to simulate the aerodynamic flow around the bat during all the flights. This solver has been utilized and validated for a diverse field of applications like bio-locomotion [66], bio-fluid mechanics [67], multiphase fluid-particulate system [68], turbo-machinery [69,70], heat transfer augmentation [71] etc. The Immersed Boundary Method (IBM) is used to resolve the wing motion which is represented by a triangulated surface mesh immersed in a background volumetric mesh. The

spatial orientation of the surface mesh is advanced in time based on the wing kinematics with no slip boundary conditions enforced on the wing surface. The IBM formulation has also been specifically validated and applied to many geometries and flow conditions, e.g. [72–74].

For all the flights analyzed in current paper, the computational domain extended substantially upstream, downstream and in the cross-section to represent the flight tunnel. In the simulations, resolving the flying bat would require a very fine mesh throughout the computational domain. In order to avoid this computational complexity, a moving reference frame is used to limit the movement of the bat in the computational domain so that a limited region of fine mesh would suffice. This moving reference frame followed the mean velocities of the respective flights, in the x_g, y_g and z_g-directions. Perturbations on the mean flight velocities are reflected by the kinematics of the bat wings which are supplied as boundary conditions to the simulations. After the simulations are complete, the results are post-processed by adding back the moving reference frame velocities. Figure 7 shows a representative background and surface grid distribution. The number of cells and elements needed in the background and surface mesh varied between flights and was strictly driven by wing kinematics. The computational grids used for the different flights used in current study consisted of 62.9, 38.2, 62.9 and 69.1 million fluid cells respectively in which the grid cell size in proximity to the bat surface had an edge length of chord/ (40 to 50). That is the mean chord distance spanned over 40 to 50 fluid cells. The bat surface was represented by a mesh comprising of 40,000 – 60,000 fine elements. Adequate validation was provided in terms of the accuracy of the kinematic data collection, the aerodynamic simulations and their combined implementation. For further details about the computational setup used and validation for each of the flights studied in the current paper, please refer to our prior work [42,45,60–62].

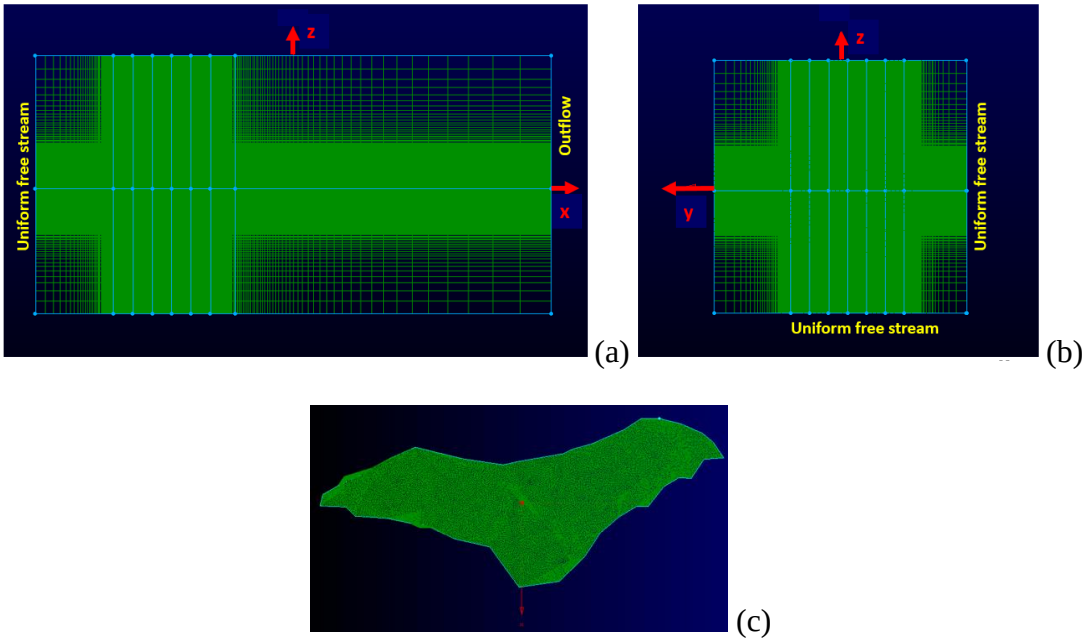

Figure 7: Schematic of computational grid; (a) front view of background grid (b) side view of background grid and (c) triangulated bat surface grid

2.5. Wing Inertial Analysis

Bat wings are capable of intricate articulation mainly due to the distribution of bones and muscles that make up the membrane hand wing structure. Thus they have much larger wing to body mass ratio in comparison to insects and it has been established previously that the motion of the heavy wings play a substantial role in the overall body dynamics during both steady and maneuvering flight [49,55,59]. As shown earlier, the bats' wings in the current analysis make up ~30% of the total bat mass. Thus it is expected that considerable force is required to accelerate the wings to execute the flapping and folding that effectuate the complex maneuvers. Likely, the acceleration felt by the different wing locations due to the wing perturbation is substantial and must be considered while doing the dynamical/ translational and rotational model of the analyzed flights.

2.5.1. Translational Analysis

To include the full effect (translational and rotational) of wing inertial accelerations in the dynamical equations describing the system motion, the measured mass of different body parts is distributed uniformly to the kinematic marker points that make up the part. Each point is then treated as a discrete mass with the collection of all markers making up the system. The flying bats with the marker points on their wings can be treated as a body comprised of multiple particle each with mass m_i. However, since the bat is deforming in the non-inertial body fixed frame while flying, an accurate dynamic analysis needs to cover two aspects. Firstly, treating the bat as a simple lumped mass system and using the calculated external aerodynamic forces to predict its trajectory in comparison to the measured trajectory in the global reference frame will account for the rigid body dynamics as done in our previous studies [60–62]. Secondly, additional inertial effects coming from the deformation of the wings needs to be considered. Thus, the dynamic equation can be written as

$$\boldsymbol{F}_{ext} = \boldsymbol{F}_{aero,g} + \boldsymbol{F}_{grav,g} = m_b \boldsymbol{a}_g = m_b \boldsymbol{a}_{o,g} + \sum m_i \boldsymbol{a}_{i,rel,g} \quad (1)$$

Where,

$\boldsymbol{F}_{ext}$ = external forces on bat COM integrated over wing marker points

$\boldsymbol{F}_{aero,g}$ = aerodynamic forces

$\boldsymbol{F}_{grav,g}$ = gravitational forces

$m_b = \sum m_i$ = total mass of the bat

$\boldsymbol{a}_g$ = total acceleration of COM

$\boldsymbol{a}_{o,g}$ = acceleration of COM using lumped mass approximation

m_i = mass assigned at individual marker points on the wings

$\boldsymbol{a}_{i,rel,g}$ = acceleration of the individual marker points on the wings relative to the COM

During implementation, the global co-ordinates of each wing point with respect to the bat COM are calculated and differentiated twice to get the global accelerations in all three directions ($\boldsymbol{a}_{i,rel.g}$). Then, the distributed mass is multiplied to each wing point acceleration and summed over the entire wing surface to finally get the inertial effect resulting from the wing motion.

2.5.2. Rotational Analysis

For rotational analysis, it is convenient to write the equations of motion in the body frame or non-inertial frame depicted in Figure 8. In Figure 8, O is the origin of the non-inertial frame located at the COM of the bat.

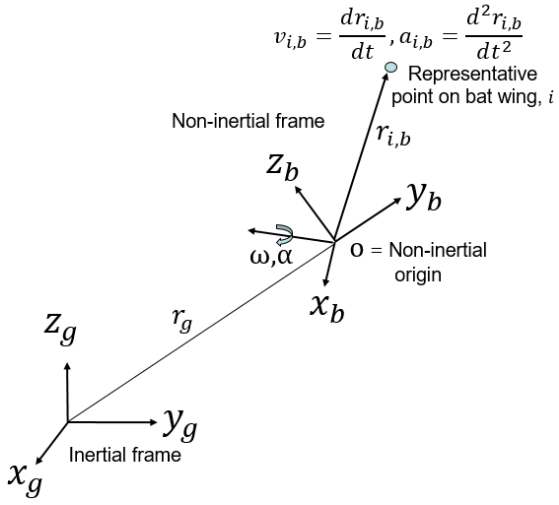

Figure 8: Schematic of the two reference frames and a representative wing point i. Suffix g and b refer to values in global and local or body reference frame, respectively.

Using the nomenclature in Figure 8, the equation of translational motion can be expressed in the inertial (global fixed) as well as the non-inertial (moving body frame) as follows:

$$\boldsymbol{F}_{aero,g} + \boldsymbol{F}_{grav,g} = m_b \boldsymbol{a}_g = m_b \boldsymbol{a}_{o,g} + \sum m_i \left(\boldsymbol{a}_{i,b} + \boldsymbol{\alpha} \times \boldsymbol{r}_{i,b} + 2\boldsymbol{\omega} \times \boldsymbol{v}_{i,b} + \boldsymbol{\omega} \times \left(\boldsymbol{\omega} \times \boldsymbol{r}_{i,b} \right) \right) \quad (2)$$

Acc. in inertial (global) frame | Acc. of non-inertial origin | Acc. in non-inertial (local) frame | Ang. acc. Term / Euler term | Coriolis acc. | Centrifugal acc.

where,

$\boldsymbol{a}_{i,b}$ = local acceleration in non-inertial body frame

$\boldsymbol{r}_{i,b}$ = radial vector relative to origin O

$\boldsymbol{v}_{i,b}$ = local velocity relative to origin O

$\boldsymbol{\omega}$ = angular velocity of the body frame

$\boldsymbol{\alpha}$ = angular acceleration of body frame

The second term on the right-hand side under the summation sign represents the inertial forces generated by the motion of the wings in the non-inertial rotating frame. The first term inside the summation represents inertial forces resulting from local accelerations of the wing point, the second term represents the forces generated by angular accelerations or rotations, and the third and fourth terms represent Coriolis and centrifugal forces experienced by the wing during the flapping motion. Note that the centrifugal acceleration depicted here is that of the wing with respect to the body frame origin and is different from the centrifugal acceleration experienced by the bat as a whole during a maneuvering turn.

The rotational motion of the bats' maneuvers is characterized by the three Euler angles namely roll, pitch and yaw defined in the body frame. Thus a modified form of Equation 2 in the body frame is used to formulate the moments in the rotational analysis

$$\sum \boldsymbol{r}_{i,b} \times \boldsymbol{F}_{aero,i,b} = \sum \boldsymbol{r}_{i,b} \times m_i \left(\boldsymbol{a}_{i,b} + \boldsymbol{\alpha} \times \boldsymbol{r}_{i,b} + 2\boldsymbol{\omega} \times \boldsymbol{v}_{i,b} + \boldsymbol{\omega} \times \left(\boldsymbol{\omega} \times \boldsymbol{r}_{i,b} \right) \right) \quad (3)$$

which can be reduced to Eqn. 4, the derivation of which is provided in the Appendix.

$$M_{aero,b} = \sum \boldsymbol{r}_{i,b} \times \boldsymbol{F}_{aero,i,b} = M_{loc} + [I]\boldsymbol{\alpha} + \left[\dot{I}\right]\boldsymbol{\omega} + \boldsymbol{\omega} \times [I]\boldsymbol{\omega} \quad (4)$$

where,

$[I] = \sum \boldsymbol{r}_{i,b} \times m_i \boldsymbol{r}_{i,b}$ is the moment of inertia matrix, $\left[\dot{I}\right] = \frac{d[I]}{dt}$, $M_{loc} = \sum \boldsymbol{r}_{i,b} \times m_i \boldsymbol{a}_{i,b}$ is the moment resulting from local accelerations in the body frame, $\left[\dot{I}\right]\boldsymbol{\omega}$ = moment from Coriolis acceleration and $\boldsymbol{\omega} \times [I]\boldsymbol{\omega}$ = moment due to centrifugal acceleration. Eqn. (4) is a second-order non-linear ODE in angular displacements. It is integrated explicitly in time using initial values estimated from the measured kinematics to find $\boldsymbol{\alpha}$, which is then further integrated to obtain $\boldsymbol{\omega}$ and subsequently the angular displacements,$\boldsymbol{\theta}$.

$$\boldsymbol{\alpha} = [I]^{-1}\left(\boldsymbol{M}_{aero,b} - \boldsymbol{M}_{loc} - \left[\dot{I}\right]\boldsymbol{\omega} - \boldsymbol{\omega} \times [I]\boldsymbol{\omega}\right) \quad (5)$$

In literature focusing on the control of wing motion, it is common to consider the angular accelerations ($\boldsymbol{\alpha}$) and velocities ($\boldsymbol{\omega}$) used in Eqn. 5 as the rotational variables associated with each wing. Most of those rotational analyses have primarily focused on insect flight in which the wings are treated as rigid bodies with representative angular accelerations ($\boldsymbol{\alpha}_{wg}$) and velocities ($\boldsymbol{\omega}_{wg}$) for the wings. In the current paper our focus is on understanding the primary roles of inertia and aerodynamics for effectuating a maneuver on the bat body. For bats, using a single wing-based angular acceleration ($\boldsymbol{\alpha}_{wg}$) and velocity ($\boldsymbol{\omega}_{wg}$) is deficient as the bat wings deform during the

entire flight time and do not behave as rigid bodies. Realizing this deficiency and the additional complexity of using multiple representative angular accelerations ($\boldsymbol{\alpha}_{wg}$) and velocities ($\boldsymbol{\omega}_{wg}$) for each wing segment, coupled to the fact that the focus of this study is on bat body rotations defining the maneuver, we have only used the rotational quantities associated with the body in Eqn. 5. It is postulated that the local moment, $\boldsymbol{M}_{loc}$ and moment due to Coriolis acceleration $[\dot{I}]\boldsymbol{\omega}$ in Eqns. 4 and 5, which are absent in rigid body rotation, represent the additional moments caused by the fact that the wing rotations are distinct from body rotations.

The rotational angles i.e. roll, pitch and yaw obtained from the above analysis are compared to the values from the kinematic data recorded from the flight experiments. This analysis allows for investigating the individual effects of the aerodynamic moment, local-acceleration moment, Coriolis moment and the centrifugal moment on the observed maneuver.

The inertia matrix, $[I]$, is calculated in the body frame for all the flights. Figure 9 presents the magnitudes of the different components of $[I]$ with the z_b- component (I_{zz}) being the highest, closely followed by the x_b- component (I_{xx}). The y_b- component (I_{yy}) is the lowest among the three moment of inertias for all the flights. In all the flights I_{zz} peaks just after mid-downstroke reducing to a minimum at the end of the upstroke. I_{xx} also peaks at mid-downstroke but reaches a minimum value at mid-stroke ahead of I_{zz}. I_{yy} on the other hand, peaks at stroke transitions and reduces to a minimum value at mid- upstroke and downstroke. The relatively high magnitude of the moments of inertia (diagonal components of the moment of inertia matrix, $[I]$) in comparison with the products of inertia (off-diagonal components) indicates that the body-axes (x_b, y_b, z_b) can be taken as the principal axes.

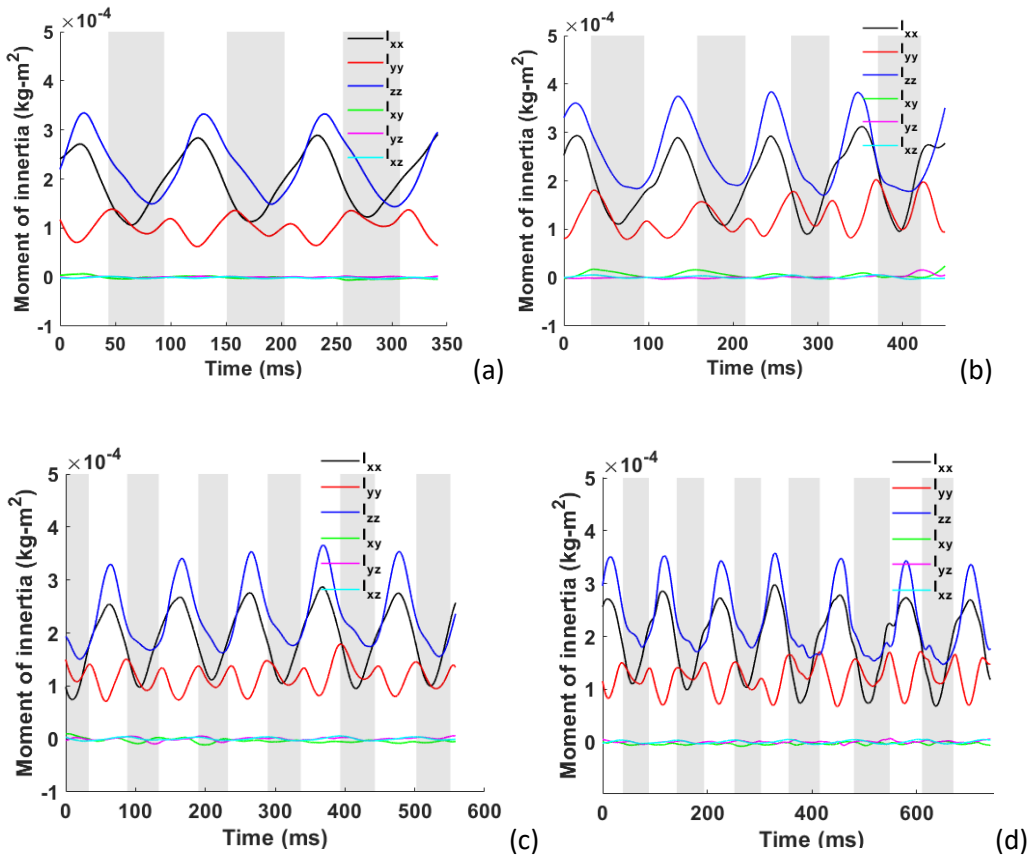

Figure 9: Magnitudes of the different components of the moment of inertia matrix for the (a) straight flight, (b) sweeping turn (*H. Pratti*), (c) sweeping turn (*H. armiger*), (d) U-turn. Upstrokes are depicted by the shaded regions.

3. RESULTS & DISCUSSION

The objective of this investigation is to identify the role of inertial forces and moments on translational and rotational dynamics of the bat in motion. Previous studies have investigated the relationship between aerodynamic forces and their moments on specific aspects of bat maneuvers [45,60–62]. As considerable mass is concentrated in the wings (~30%), here we focus on the role of time-varying inertial component on bat flight. Figure 10 shows the inertial forces ($\sum m_i \boldsymbol{a}_{i,rel,b}$ in Eqn. 1 in the body frame) resulting from wing accelerations in comparison to the aerodynamic forces for the four different flights analyzed. Inertial forces follow a predictable pattern in sync

with the wing flapping with a half-stroke phase difference between x_b- and z_b-directional forces. Common traits observed in all four flights is that while the aerodynamic forces peak near mid-downstroke when the wing area is maximum, the inertial forces always peak during stroke transitions when accelerations and decelerations are maximum as the wing undergoes pronation and supination. Also notable is the observation that the cycle averaged inertial force is small, resulting from negative and positive forces of nearly the same magnitude, compared to its aerodynamic counterpart and thus is expected to have a small effect on the trajectory of the bat over many flapping cycles, but is expected to strongly affect the trajectory within each flapping cycle.

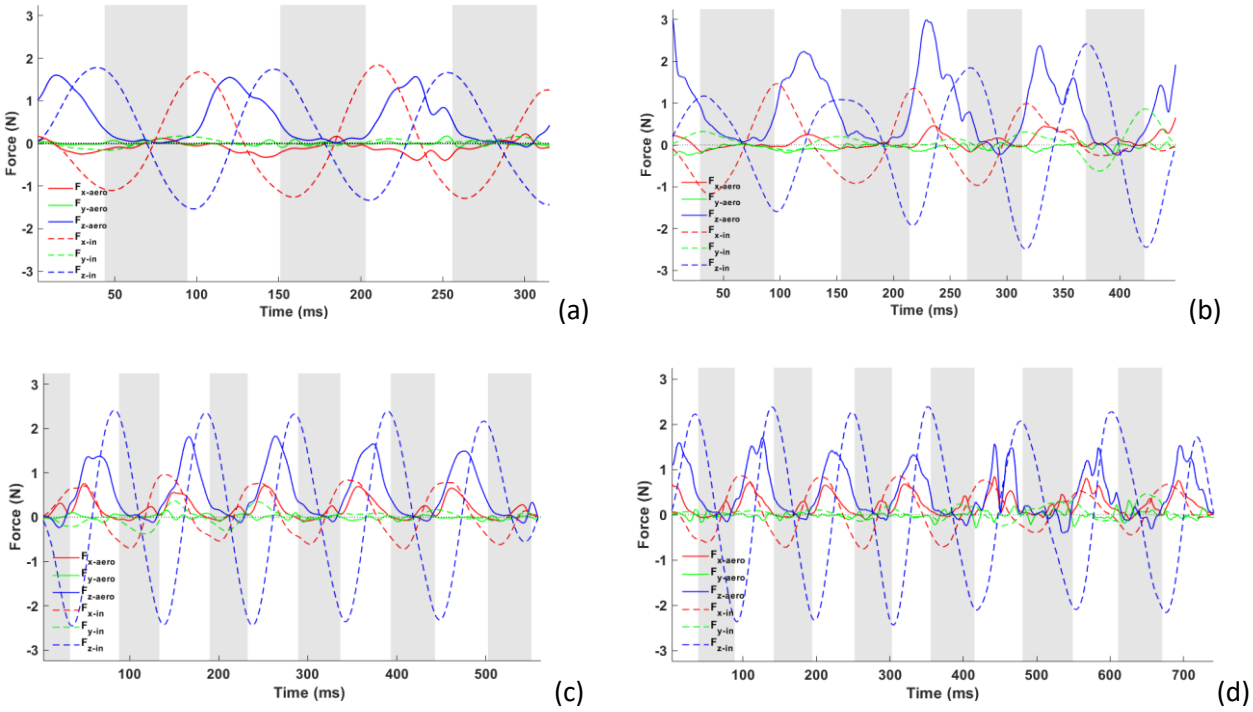

Figure 10: Wing inertial forces (dashed lines) in comparison to the aerodynamic forces (solid lines) in the body reference frame for (a) straight flight (*H. armiger*), (b) sweeping turn (*H.*

Pratti), (c) sweeping turn (*H. armiger*), (d) U-turn in the x_b-(red), y_b-(green) and z_b-directions (blue) of the body reference frame. Upstrokes are depicted by the shaded regions.

For all the flights investigated, at the start of every down-stroke, the wings quickly accelerate in the downward or *–ve* z_b direction, resulting in a *–ve* but increasing inertial force. After mid-downstroke, the wings start to decelerate to prepare for the direction change to the up-stroke. But as the wings are still moving downwards, the resultant force becomes positive and increases (due to the faster deceleration) from mid-downstroke till start of up-stroke. From the start of up-stroke till mid upstroke, the wings are accelerating in the upward or *+ve* z_b-direction, resulting in a *+ve* upward inertial force. After mid upstroke, the bat wings start to slow down to prepare for the upcoming direction change and this upward deceleration results in a *–ve* inertial force. Associated with the downward and upward motions during downstrokes and upstrokes, the natural flow of bat wings show a forward and backward movement, respectively in the x_b-direction. The forward acceleration and deceleration, during the downstroke results in a *+ve* but decreasing force till midstroke, after which the increasing deceleration results in a negative x_b-directional force. The reverse mechanism manifests in the upstroke as the wing retracts and moves backward, resulting in a negative force till mid-upstroke and a positive force to complete the upstroke. Table 3 summarizes the directions of the wing motions along with simultaneous acceleration or deceleration performed by the bat wings and the resultant inertial forces in both x_b and z_b directions.

Table 3: Wing motion directions with simultaneous acceleration or deceleration and the resultant inertial force

	z-direction			***x-direction***		
	Wing motion direction	Velocity change rate	inertial force	Wing motion direction	Velocity change rate	inertial force
DS start – DS mid	-	+	-	+	+	+
DS mid – US start	-	-	+	+	-	-
US start – US mid	+	+	+	-	+	-
US mid – DS start	+	-	-	-	-	+

In the straight-descending flight of the *H. armiger*, the peak inertial forces in x_b and z_b are of the same magnitude as the peak aerodynamic forces in the z_b-direction. This changes during maneuvering flight. The *H. pratti* in executing the sweeping right turn goes into the turn with x_b- and z_b- forces of about the same magnitude, but as the bat initiates the main part of the turn and starts ascending in the second cycle, the z_b-direction inertial force increases in magnitude while the x_b-direction force decreases. The difference in z_b- and x_b- direction forces are much more stark and consistent during the sweeping turn and U-turn execution of the *H. armiger* bat. In both these flights, the inertial forces in the z_b-direction dominate the force dynamics of flight. The z_b inertial force peaks at values of 2 or greater, which is more than twice the inertial force in x_b. This leads to the conclusion that the wings of the *H. armiger* and *H. pratti* accelerate and decelerate with larger magnitudes in the z_b-direction than the x_b-direction during maneuvers. Another distinguishing feature between the two species, is that the peak z_b-direction (lift) aerodynamic forces produced by the *H. pratti* are approximately 50% larger than that generated by the *H. armiger*. In comparison, y_b-direction forces are much smaller and the only time they seem to be of any significance is during the last recorded cycle of the *H. pratti* when the bat positions itself by a sharp ascent for the 180° back-flip to perch on the ceiling of the flight tunnel.

While Figure 10 presents the inertial forces in the body frame, more relevant to translational dynamics are the inertial forces in the global reference frame (x_g, y_g ,z_g). Figure 11 presents these forces in the global reference frame. The general oscillating nature of the inertial forces dominated by wing flapping remain the same, but accompanied by a change in the relative magnitudes of different directional components, which now depend on the actual trajectory of the bat in the global reference frame. The smallest differences are observed for straight flight as the body axes mostly remain aligned with the global axes. In the maneuvering flights all of which have the bat climbing or ascending in either a sweeping turn or 180° U-turn, the global components of inertial force vary markedly. In all the maneuvers, the x_g-direction inertia forces are comparable and often exceed the z_g- direction forces contributing to accelerating and decelerating the bat in the global x_g-direction, which aligns with the tunnel length. Not as much for the sweeping turn of *H. pratti* but more so for the *H. armiger*, substantial inertial forces manifest in the lateral y_g-direction for both the sweeping turn and the U-turn as the bat changes flight direction. During the sweeping turn of the *H. armiger*, high y_g inertial forces manifest during cycle 2 and 3 when the right sweeping turn is initiated. Similarly, the largest y_g forces are felt during cycles 4 and 5 when the bat is in the midst of the U-turn near the apex of the turn.

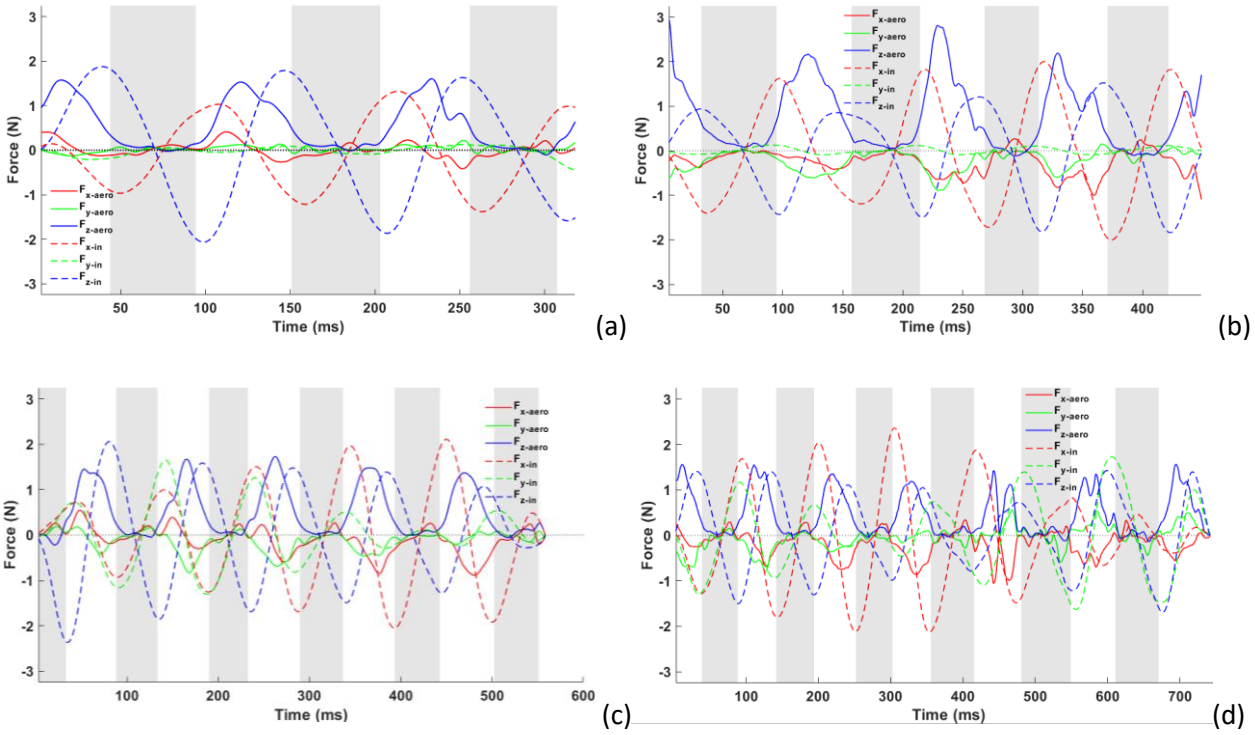

Figure 11: Wing inertial forces (dashed lines) in comparison to the aerodynamic forces (solid lines) in the global reference frame for (a) straight flight (*H. armiger*), (b) sweeping turn (*H. Pratti*), (c) sweeping turn (*H. armiger*), (d) U-turn in the x_g-(red), y_g-(green) and z_g-directions (blue) of the global reference frame. Upstrokes are depicted by the shaded regions.

3.1. Effect of wing inertia on the translational/ dynamic analysis

As shown by Figure 11 (a-d), in all the four flights, the inertial forces resulting from wing flapping are of the same order of magnitude and comparable to the aerodynamic forces. Hence, they should be expected to contribute substantially to the trajectory charted by the bat during flight. To isolate the effect of wing inertia on the translational dynamics, first the bat is treated as a lumped mass system concentrating the mass of the bat on the body at the COM and calculating the resulting acceleration of the system under the influence of aerodynamic and gravitational forces as given by

$m_b \boldsymbol{a}_{o,g}$ in Eqn. 1 [60–62]. This is followed by including the wing inertial force perturbation as given by $\sum m_i \boldsymbol{a}_{i,rel,g}$ in Eqn. 1, in which the summation of the mass distribution on the wing marker points with their respective relative accelerations with respect to the COM are included in the analysis as the wing flaps. In Eqn.1 and 2, the net time-dependent external or aerodynamic forces are obtained from the aerodynamic simulations which utilize the measured and digitized wing kinematics by integrating over the surface elements which make up the wing surface. The velocity and position of the bat COM is then predicted by integrating the predicted acceleration once and twice with respect to time, respectively, starting from initial conditions taken from the measurements. Two sets of predictions are presented for each of the four flights – one using the lumped mass system and the other with the inclusion of inertial perturbations. For each case, the predicted velocity and displacement of the COM are compared to measurements of the actual flight path and velocity.

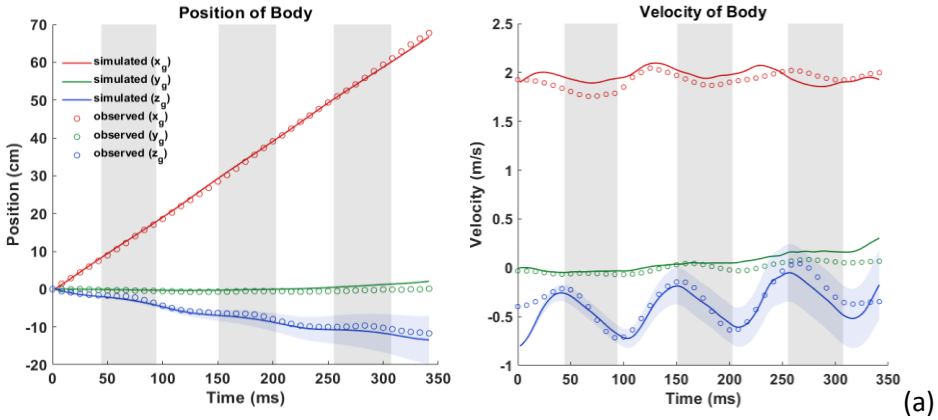

(a)

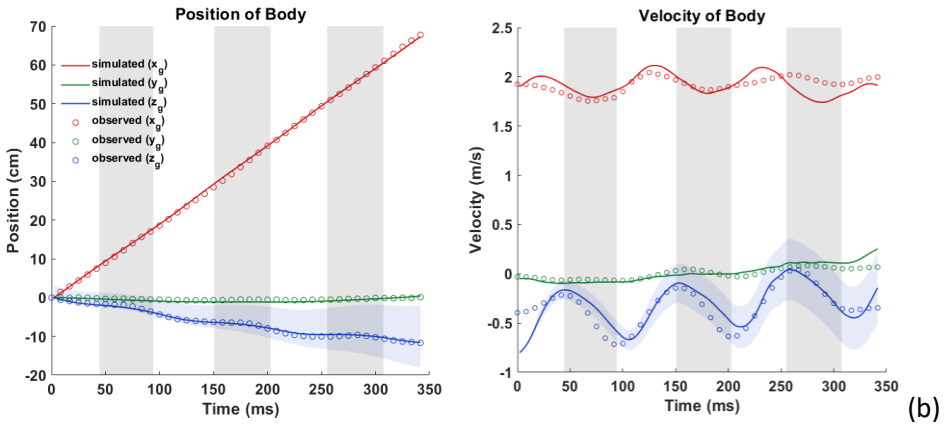

Figure 12: Comparison between the observed and predicted flight trajectory (position on left, velocity on right) of the bat COM in the global coordinate system (a) without and (b) with the effect of wing inertia for straight flight. Gray shaded regions denote upstrokes; shaded regions enveloping the predicted trajectory and velocity represent the range of possible values given by a $\pm 10\%$ uncertainty margin in computed aerodynamic forces in z-direction.

For the straight flight, good comparisons were obtained between the predicted (lines) and observed (circle symbols) values in all the three directions with the lumped mass model. However, after including the wing inertial effects the position predictions got even better to almost exactly match the measured values. The velocity predictions also get better especially in the x_g- and z_g-directions where the intra-cycle fluctuations are captured with significantly more accuracy. This results are according to expectation, that inertial forces because of their nearly equal and opposite positive and negative contributions affect the velocity and trajectory within a cycle much more than over many cycles.

For the sweeping turns, the comparisons between the measured data and trajectories predicted with just the aerodynamic forces and not considering the effect of wing inertia did not render as good an agreement as the straight flight. The disagreements were more acute in the x_g- and z_g- velocities

and z_g-positions. In case of the *H. pratti* flight, the predicted x_g-velocity with the lumped mass analysis could not capture the intra-cycle fluctuations recorded in the measured kinematics (Figure 13-a). When the wing inertial effects are included (Figure 13-b), the velocity fluctuations are captured with good fidelity. During the early phase of the flight the predicted x-fluctuations are out of phase with the measurements, but shows much better agreement towards the end the recorded flight. The lumped mass approximation does a relatively good job in predicting the intra-cycle velocity fluctuations in the z_g–direction. Adding the effects of inertia increases the amplitude of the cyclic fluctuations resulting in better predictions at the start of the recorded flight but leads to deviations from the measurements as the flight progresses further. Similar to straight flight, the y_g-velocity and displacement are not affected by wing inertia, indicating that aerodynamic forces are solely responsible for the lateral movement of the bat. The somewhat increased differences observed with measurement on inclusion of inertia terms in the flight of the *H. pratti* could be a result of the previously mentioned uncertainty associated with the wing mass distribution.

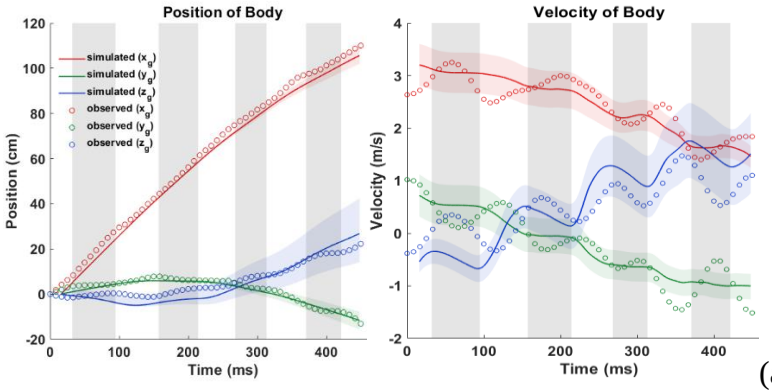

(a)

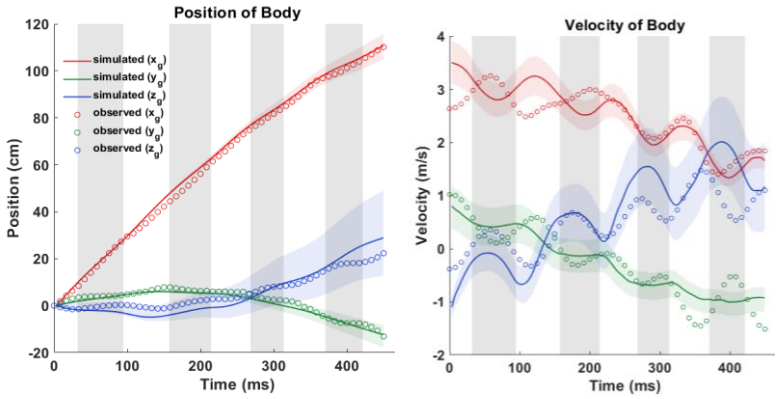

(b)

Figure 13: Comparison between the observed and predicted flight trajectory of the bat COM for sweeping flight of *H. pratti* ; (a) without and (b) with the effect of wing inertia. Shaded regions enveloping the predicted trajectory and velocity represent the range of possible values given by a $\pm 10\%$ uncertainty margin in computed aerodynamic forces in all three directions (as opposed to just the z-dircetion in case of the other three flights. As comparatively more deviations are observed for this maneuver in all directions, the shaded envelops serve to quantify those deviations)

The sweeping turn executed by the *H. armiger* bat is represented in Figure 14. The lumped mass model was able to replicate the location of the bat in the x_g- and y_g-direction quite accurately, but under predicted the vertical z_g location of the bat at the end of the recorded segment. The measured velocity fluctuations in the x_g- and y_g- directions are captured reasonably well by the lumped mass model albeit with phase differences. In the vertical z_g-direction, the fluctuating velocity is systematically under predicted by the lumped mass model which results in the model under predicting the height to which the bat flies. Including inertia makes the biggest improvement in the z_g direction by not only capturing the cyclic fluctuations in velocity with accuracy but also

increasing its magnitude to be more in line with the experimental measurements. This results in a large improvement in the predicted flight trajectory in the z_g-direction.

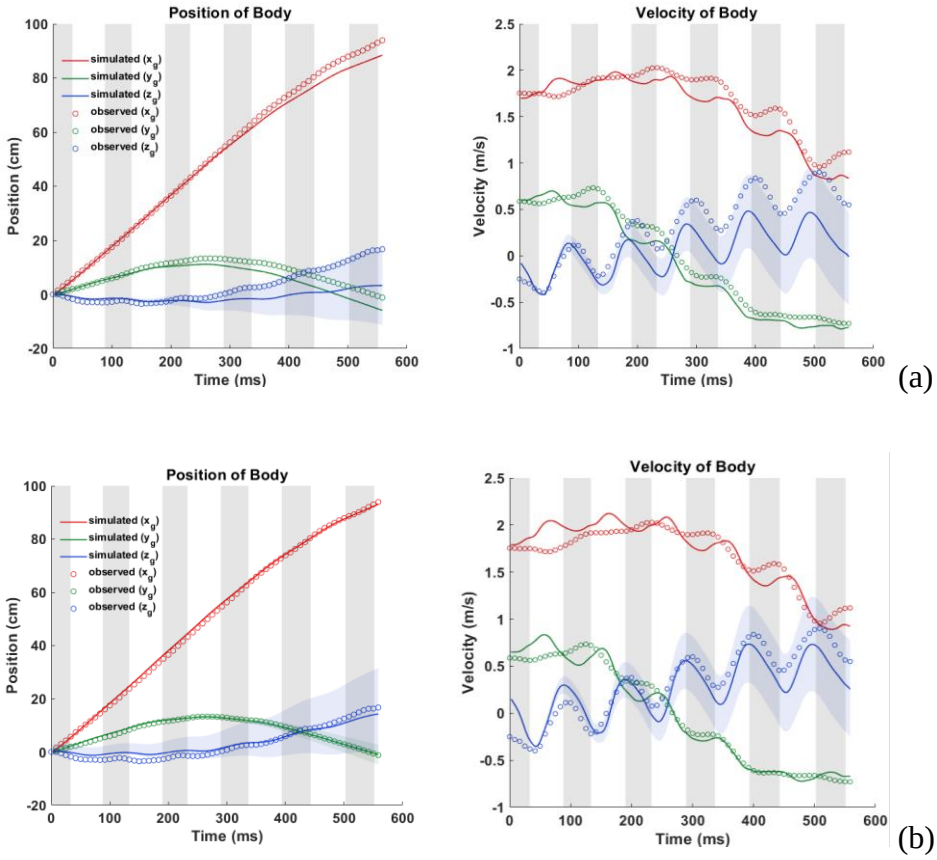

Figure 14: Comparison between the observed and predicted flight trajectory of the bat COM for sweeping flight of *H. armiger*; (a) without and (b) with the effect of wing inertia, shaded regions enveloping the predicted trajectory and velocity represent the range of possible values given by a $\pm 10\%$ uncertainty margin in computed aerodynamic forces in z-direction.

Finally similar trends are observed in the flight of the *H. armiger* executing the U-turn (Figure 15). The predicted velocity and trajectory are quite accurately captured in the x_g- and y_g- directions with the lumped mass representation and don't change considerably with the inclusion of inertia

forces. The largest effect of inertial forces manifest in the z_g- direction with very similar trends as that observed for the sweeping flight of the *H. armiger* in Figure 14.

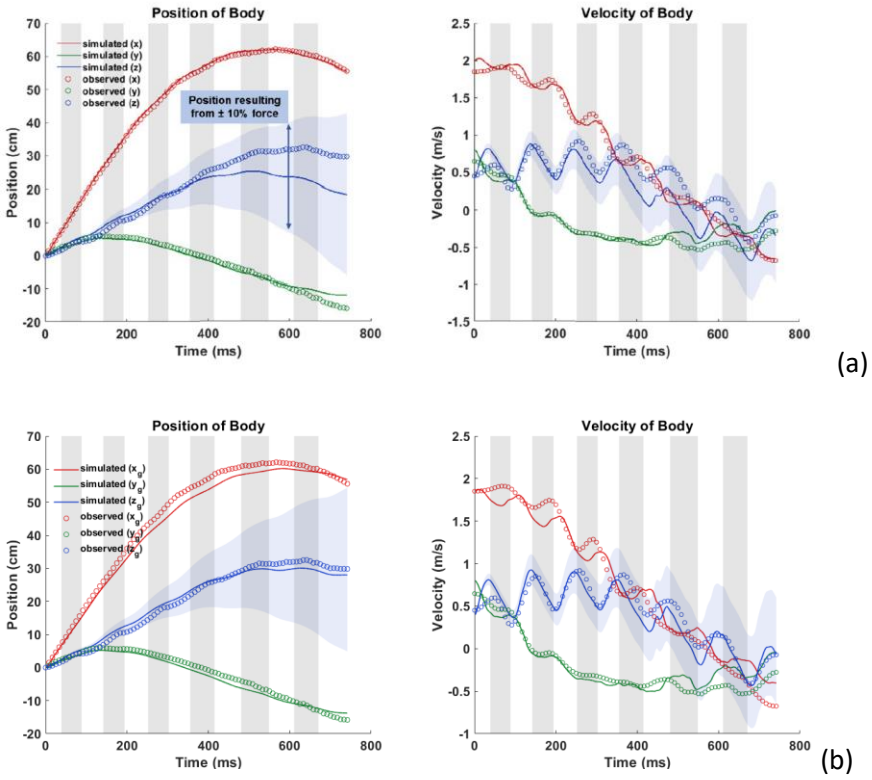

Figure 15: Comparison between the observed and predicted flight trajectory of the bat COM for a U-turn; (a) without and (b) with the effect of wing inertia, shaded regions enveloping the predicted trajectory and velocity represent the range of possible values given by a $\pm 10\%$ uncertainty margin in computed aerodynamic forces in z-direction.

Inclusion of wing inertia makes the largest impact in the z_g- directional velocity and position for the two maneuvers (sweeping and U-turn) performed by the *H. armiger* bat indicating that the flapping wings result in a net upward reaction force which helps the bat gain altitude. Figure 16 presents the half-cycle-averaged mean inertial forces experienced during up- and down-strokes for the *H. pratti* (a) and *H. armiger* (b-c) during their respective maneuvers. The averaged z_g-direction

inertial component of the *H. armiger* bat (Figure 16-b and c) is significantly more prominent than the x_g-directional component, explaining the most visible effect on the motion trajectories (seen in Figure 14 and 15). The averaged z_g-forces also show larger negative magnitudes which contribute towards increasing the z_g- elevation of the COM for the *H. armiger* bat as indicated by Eqn. 1. On the other hand, for the *H. pratti* bat (Figure 16-a) the x_g-directional component is more significant, the effect of which is seen in Figure 13 (inclusion of inertia influences the predicted x_g-velocity more than the z_g-velocity). In all three maneuvering flights, the y_g-directional inertial components are minimal which re-confirms that the aerodynamic forces are solely responsible for the lateral translation of the bat.

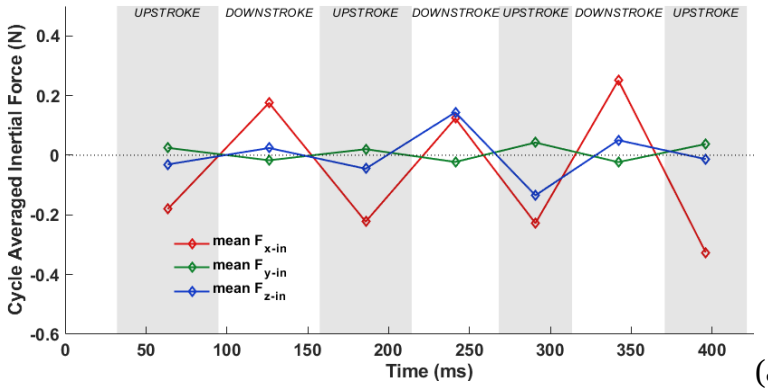

(a)

(b)

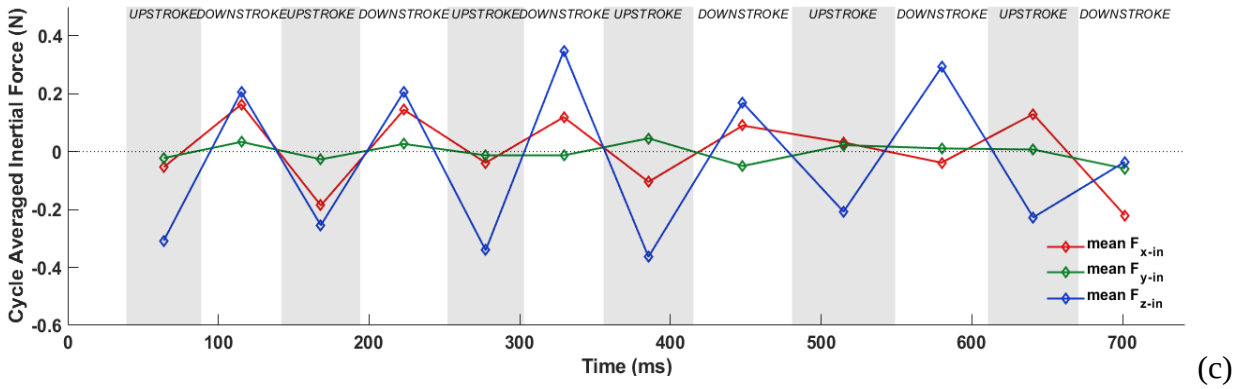

(c)

Figure 16: Half cycle averaged (separate for upstrokes and downstrokes) inertial forces for the maneuvering flights for (a) sweeping turn (*H. Pratti*), (b) sweeping turn (*H. armiger*), (c) U-turn in the x_g-(red), y_g-(green) and z_g-directions (blue) of the global reference frame. Upstrokes are depicted by the shaded regions.

From the four flights the following observations can be made regarding the effect of inertial forces on translational dynamics- i) the aerodynamic forces used with a lumped mass approximation provide a pretty good estimation of the overall velocity trends in all three directions but fail to capture the intricate dynamics that occur within a cycle, ii) the inertial effect of the wing perturbations are consequential in accurately describing the motion dynamics in maneuvering flights, iii) Wing inertia plays a key role in predicting the intra-cycle fluctuating trends of velocities and thus aid in better prediction of positions and finally, iv) the wing inertial effects are consistently more prominent in the direction of gravity (z_g-direction) when compared to the other two directions.

3.2. Effect of wing inertia on rotation

The rotational aspect of a maneuvering bat flight can be characterized by the three Euler angles namely roll, pitch, and yaw which identify the relative orientation of the body frame to the global

or inertial reference frame. These rotations are primarily driven by the aerodynamic and inertial moments experienced by the bat about the center of mass in the body frame as expressed by Eqn. 4 and 5.

In this section, the individual effects of aerodynamic as well as local inertial moments resulting from the wing flapping in effectuating a maneuver are investigated. In addition to that, the roles of the Coriolis ($[\dot{I}]\boldsymbol{\omega}$) and centrifugal ($\boldsymbol{\omega} \times [I]\boldsymbol{\omega}$) moments are also investigated to get a comprehensive picture of the maneuvers. This is done by selectively excluding terms from Eqn. 5 to solve for the angular acceleration in the four different flights (one straight and three maneuvering). The predicted angular accelerations are numerically integrated to arrive at the angular velocity and rotational angles by using initial values of each variable from the available kinematic data. Finally, the rotational angles i.e. roll, pitch and yaw are compared with the values from the kinematic data recorded from the flight experiments.

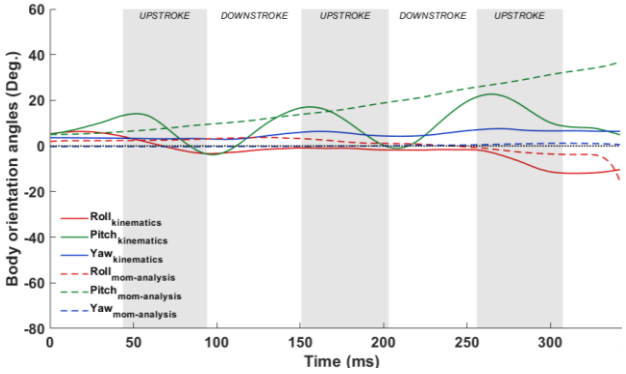

(a) $\boldsymbol{\alpha} = [I]^{-1}\left(M_{aero,b}\right)$

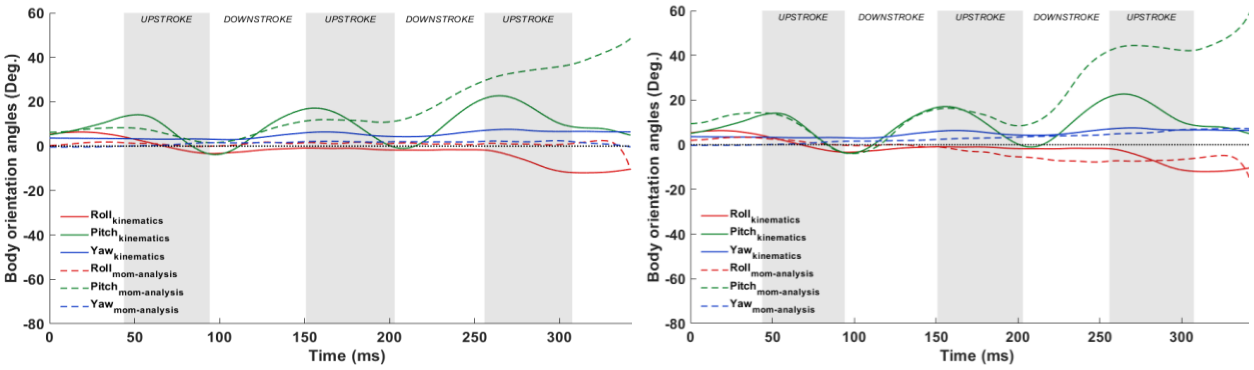

(b) $\boldsymbol{\alpha} = [I]^{-1}\left(M_{aero,b} - M_{loc}\right)$ (c) $\boldsymbol{\alpha} = [I]^{-1}\left(M_{aero,b} - M_{loc} - \left[\dot{I}\right]\boldsymbol{\omega} - \boldsymbol{\omega} \times [I]\boldsymbol{\omega}\right)$

Figure 17: Contribution of different terms in the rotational moment analysis to predict the body orientation angles for the straight flight. Solid lines depict measured values while dashed lines are predictions. Red, green, and blue, respectively, show roll, pitch, and yaw angles.

Figure 17 shows the predicted body orientation angles resulting from different approximations to Eqn. 5 compared to the experimentally recorded data. As there is no lateral maneuver, the measured roll and yaw angles were nominal with slightly increasing pitch angle even though the overall flight path is descending. By just including aerodynamic moments to predict the angular acceleration, both yaw and roll were under predicted whereas pitch angle monotonically increased and was over-predicted (Figure 17-a). The intra-cycle fluctuations with pitch angle increasing during down strokes (pitch up) and decreasing during upstrokes (pitch down) were only captured after the inclusion of the local inertial moment term (Figure 17-b). The addition of the Coriolis and centrifugal moments aided in better replication of the yaw and roll angles and also the cyclic pitching during the first two flapping cycles but tended to exacerbate the over-prediction of the pitch angle in the third flapping cycle (Figure 17-c).

Figure 18 compares the predicted and the measured angles for the ascending sweeping right turn maneuver of the *H. pratti*. As stated by Rahman et al. [60], the ascending sweeping turn is achieved by using yaw and roll synergistically to position the force vectors such that the bat is able to achieve a tight turn. The measured yaw angle indicates that the body axis of the bat changed direction by ~80° to the right with the roll angle changing by 30° towards the inside of the turn during the course of the flight. As the bat ascends, the pitch angle changes by about ~30°. The rate of change of the yaw angle gives an indication of how fast the bat is turning and the rate of change of the cycle averaged pitch angle an indication of how fast it is climbing. The measurements indicate that turning occurs at a higher rate during down strokes and at a lesser rate during upstrokes and the rate of turning increases sharply during the third down stroke. Similarly, the bat gains altitude faster during the down stroke but at a slower rate during the upstroke.

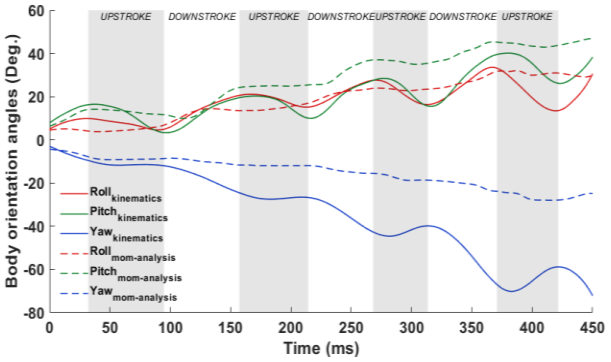

(a) $\boldsymbol{\alpha} = [I]^{-1}\left(M_{aero,b}\right)$

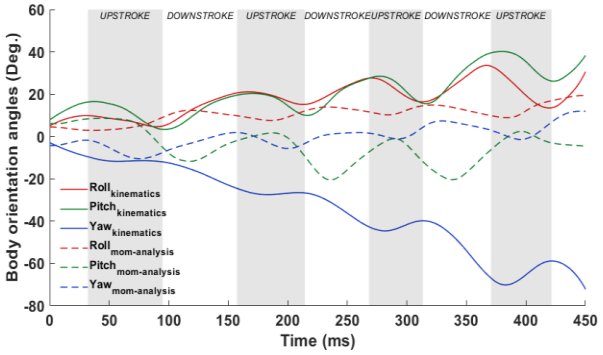

(b) $\boldsymbol{\alpha} = [I]^{-1}(-M_{loc})$

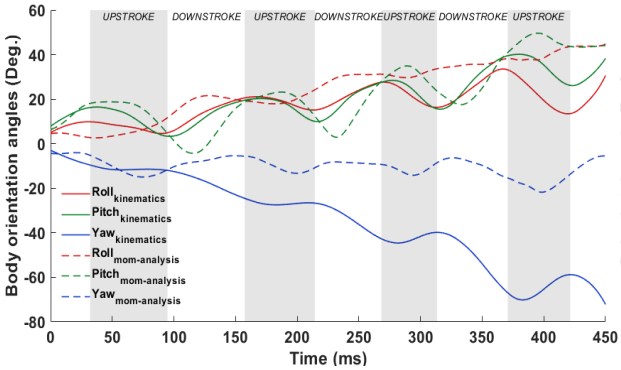

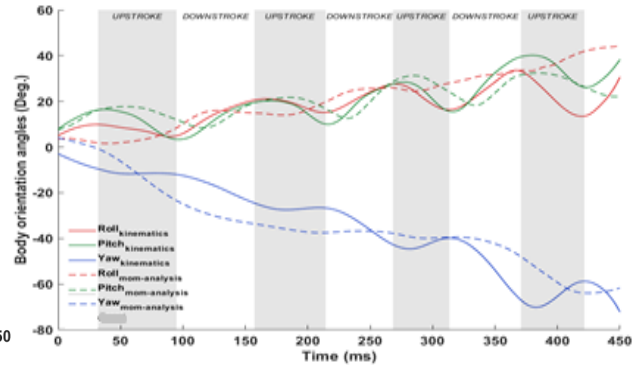

(c) $\boldsymbol{\alpha} = [I]^{-1}\left(M_{aero,b} - M_{loc}\right)$ (d) $\boldsymbol{\alpha} = [I]^{-1}\left(M_{aero,b} - M_{loc} - \left[\dot{I}\right]\boldsymbol{\omega} - \boldsymbol{\omega} \times [I]\boldsymbol{\omega}\right)$

Figure 18: Contribution of different terms in the rotational analysis of the sweeping turn of *H. pratti*. Solid lines depict measered values while dashed lines are predictions. Red, green and blue, respectively, show roll, pitch and yaw angles.

A rotational analysis done for the sweeping turn of the *H. pratti* bat shows the individual effects of the aerodynamic ($M_{aero,b}$) and local (M_{loc}) moments even more clearly. Similar to the straight flight, just using the aerodynamic moments to predict the orientation angles captures the overall trend of the increasing roll moderately well. Although the roll prediction follows the measured data reasonably well, the pitch and yaw are moderately different as shown by Figure 18-a, the pitch being over-predicted and yaw under-predicted. Also, the intra-cycle fluctuations of the orientation angles are not predicted particularly well. In contrast, if just the local moments are used instead of the aerodynamic moments, the intra-cycle fluctuations are captured for all three angles with the variations being most prominently visible in the pitch angles. However, the predicted values fail to follow the overall trend as the pitch and yaw angles show decreasing and increasing trends overall, opposite to the measured trends (Figure 18-b). When combined together, the aerodynamic moments and the local moments provide much better prediction of the body orientation angles, capturing both the overall trends (increasing for roll and pitch, decreasing for yaw) and the intra-cycle fluctuations (Figure 18-c). However, there is a phase difference between the measured and predicted roll and pitch angles, slight over prediction of the roll angles and large under prediction of the yaw angles. Capturing the yaw accurately is essential in order to completely characterize the performed maneuver. This is achieved by including the moments caused by the Coriolis ($\left[\dot{I}\right]\boldsymbol{\omega}$) and centrifugal forces ($\boldsymbol{\omega} \times [I]\boldsymbol{\omega}$) in Eqn. 5. With contributions from all the moment terms, the

yaw angles are much better predicted along with the steep drop during the 3rd down stroke, which is significant for the right turn. The phase difference in the measured and predicted pitch and the over prediction of the roll angles are also mitigated (Figure 18-d).

In the second sweeping turn (by the *H. armiger* bat), the measured values from the kinematic data also show increasing roll and pitch angles and decreasing yaw angles consistent with an ascending right turn. As the maneuver takes place towards the beginning of the recorded flight, the roll angles increase till the 3rd cycle and then flatten out for the rest of the flight as the bat continues the right turn as indicated by the continuous decrease in yaw angles. Similar intra-cycle trends are noted as the other flights with the roll, pitch, and yaw angles increasing (-ve for yaw) during the down stroke and decreasing and/or levelling-off during upstroke.

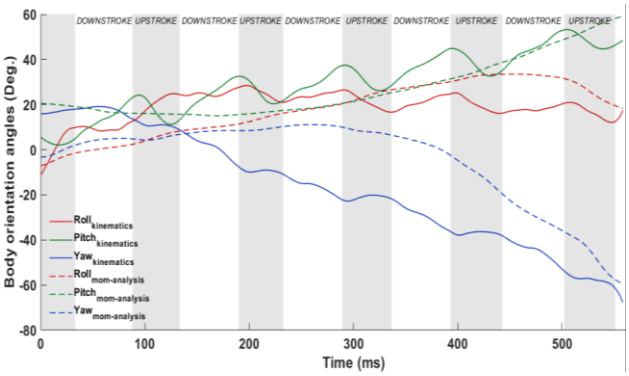

(a) $\boldsymbol{\alpha} = [I]^{-1}\left(M_{aero,b}\right)$

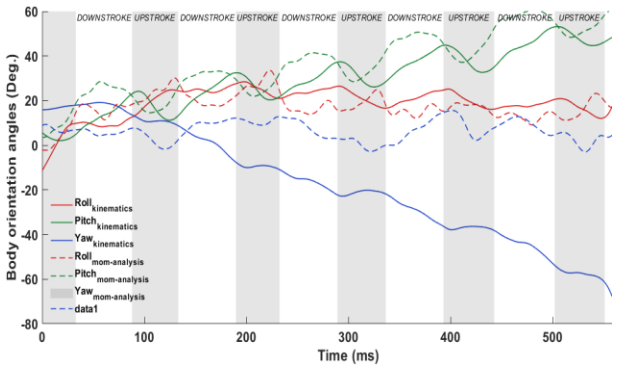

(b) $\boldsymbol{\alpha} = [I]^{-1}(-M_{loc})$,

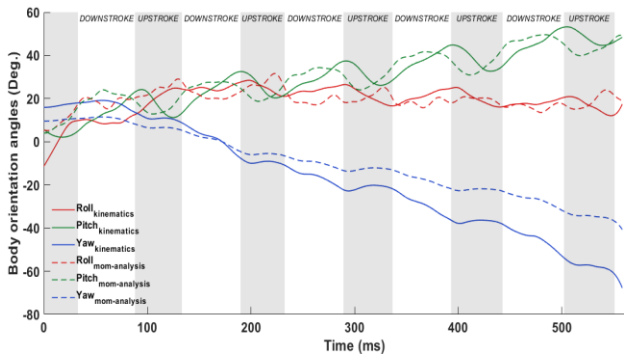

(c) $\boldsymbol{\alpha} = [I]^{-1}\left(M_{aero,b} - M_{loc}\right)$

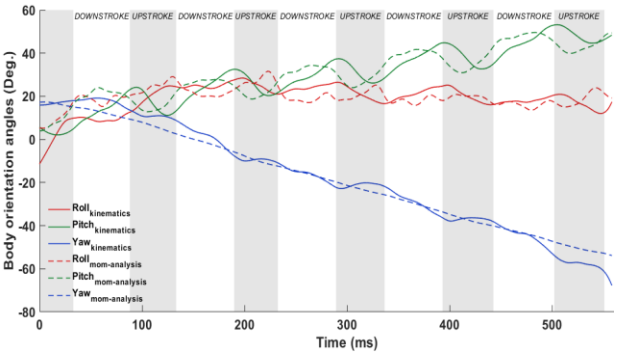

(d) $\boldsymbol{\alpha} = [I]^{-1}\left(M_{aero,b} - M_{loc} - \left[\dot{I}\right]\boldsymbol{\omega} - \boldsymbol{\omega} \times [I]\boldsymbol{\omega}\right)$

Figure 19: Contribution of different terms in the rotational analysis of the sweeping turn of *H. armiger*. Solid lines depict measured values while dashed lines are predictions. Red, green and blue, respectively, show roll, pitch and yaw angles.

The rotational analysis of the *H. armiger* sweeping turn yield findings consistent with those for the *H. pratti*. The aerodynamic moments contribute in capturing the overall trends (Figure 19-a) while the local moments contribute to the intra-cycle trends, again, most prominent in the pitch angles (Figure 19-b). With just the local moments active, the phase difference between the measured and predicted pitch angles persist along with the moderate over prediction of pitch and severe under prediction of yaw. Their combined effect predicts the roll and pitch angles with good agreement but again under predicts the yaw (Figure 19-c), although decreasing the severity of the under-prediction. Finally, with all the components active, good agreement is seen between the predicted and measures angles in all three directions (Figure 19-d). While the inclusion of the Coriolis and centrifugal terms in the moment analysis proved to be paramount in both sweeping turns, their effect was clearly more prominent in the *H. pratti* bat as the *H. armiger* showed somewhat better agreement with the measured kinematics even without them (Figure 19-c as opposed to 18-c). In both these maneuvers, between the Coriolis and the centrifugal terms, the latter seemed to be somewhat dormant as just adding the centrifugal moments along with the aerodynamic and local moments in the rotational analysis did not show any improvement.

Finally, the evolution of rotation angles during a U-turn are investigated. The kinematic values shown in Figure 20 suggest that the bat re-orients its heading by 170° indicated by the change in yaw angle during the U-turn. The rate of change of yaw angle increases during the initiation phase

(cycles 3 and 4) and the roll which is initially constant at approximately 20°-25° increases sharply during the 4th cycle down stroke as the bat approaches the apex of the turn in cycle 5 and then straightens out as it executes the U-turn and egresses out. The pitch angle on the other hand undergoes a steady increase during the approach phase till the 3rd cycle, and starts to decrease as the bat goes into the U-turn readying itself for the descent as it exits out of the turn. The intra-cycle trends are similar as that observed in the above three flights.

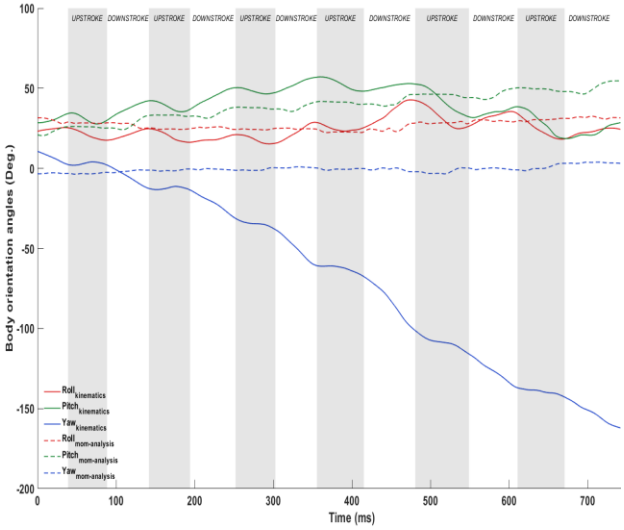

(a) $\boldsymbol{\alpha} = [I]^{-1}(M_{aero,b})$

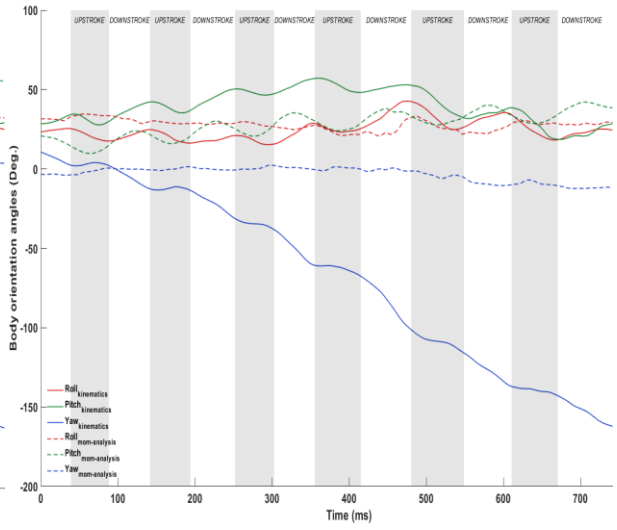

(b) $\boldsymbol{\alpha} = [I]^{-1}(-M_{loc})$

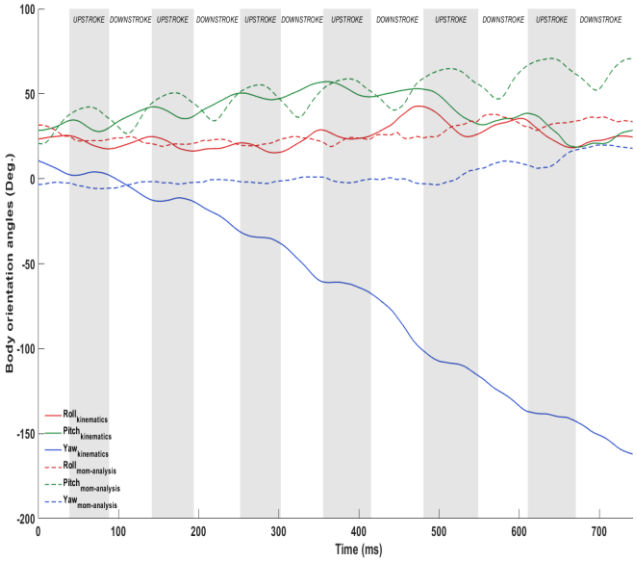

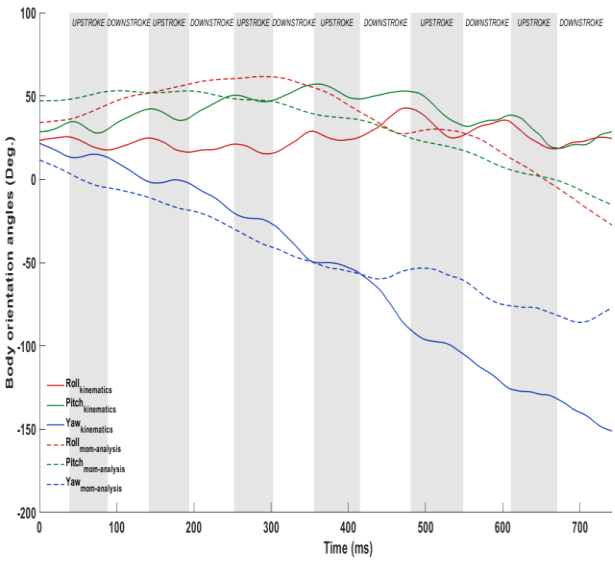

(c) $\boldsymbol{\alpha} = [I]^{-1}\left(M_{aero,b} - M_{loc}\right)$

(d) $\boldsymbol{\alpha} = [I]^{-1}\left(M_{aero,b} - M_{loc} - \left[\dot{I}\right]\boldsymbol{\omega}\right)$

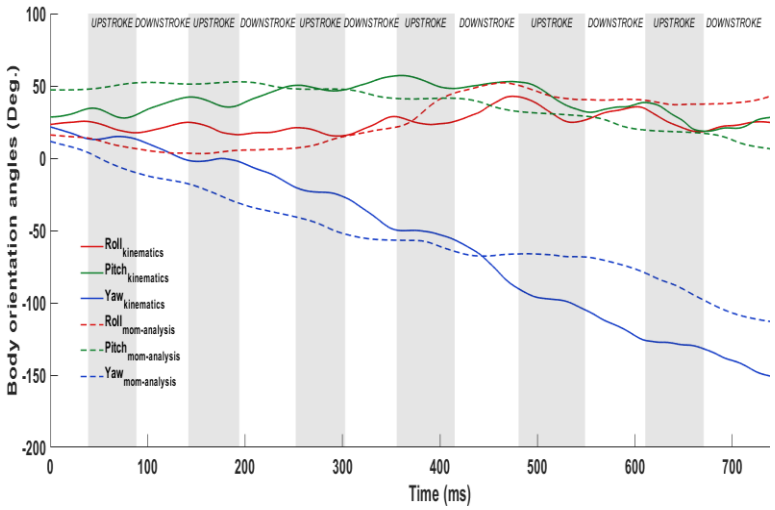

(e) $\boldsymbol{\alpha} = [I]^{-1}\left(M_{aero,b} - M_{loc} - \left[\dot{I}\right]\boldsymbol{\omega} - \boldsymbol{\omega} \times [I]\boldsymbol{\omega}\right)$

Figure 20: Contribution of different terms in the rotational analysis of the U-turn. Solid lines depict measered values while dashed lines are predictions. Red, green and blue, respectively, show roll, pitch, and yaw angles.

Going to the contributions of different terms from Eqn. 5, unlike the sweeping turns, the aerodynamic moments alone do not capture almost any characteristic trend as the predictions in Figure 20-a follow almost a linear constant trend for all three angles. The local moments alone, resolve the intra-cycle fluctuating trend in roll and pitch but fails to do so for yaw angles (Figure 20-b). It is only when these two components are combined, some cyclic behavior is captured in the predicted yaw angles, but the overall trend deviates even more from the measured values

(Figure 20-c). The roll predictions at this point follow the measured values moderately well also displaying some intra-cycle fluctuations. Although the predicted pitch captures the cyclic fluctuations, the overall trend seems to differ from the measured values especially at the apex of the turn and onwards (cycle 5 and 6). It is only after the Coriolis term is added (Figure 20-d), that the yaw prediction starts to resemble the decreasing trend during approach and initiation phases, but again diverges after the apex of the turn is achieved. The roll prediction actually deteriorates but the predicted pitch angles follow the decreasing trend after coming out of the turn. One differentiating feature from the sweeping turns is that, a significant individual effect of the centrifugal term is visible for the first time in the U-turn maneuver. With all the 4 terms of Eqn. x present (Figure 20-e), the roll prediction accurately captures the overall trend during the entirety of the flight, pitch prediction shows good agreement for most of the flight time (accept for the approach phase), and the yaw prediction follows the measured trend even after the apex of the turn (as opposed to 20-d). It is notable difference between the sweeping and U-turn done by the *H. armiger* bat is that in the sweeping turn, just the aerodynamic and local moments were able to capture the measured yaw angles to some degree but completely failed to do so for the U-turn. The fact that these two maneuvers were performed sequentially, strongly indicates that the more acute the maneuver becomes, the Coriolis and centrifugal terms become more significant.

To summarize, the aerodynamic moments mostly account for the overall trend whereas the local inertial moments generate the intra-cycle fluctuations. The moments coming from the local Coriolis and centrifugal forces are essential to achieve the desired yaw which is the most important rotational component in achieving the desired turn. The more acute the maneuver becomes the more importance these two terms seem to carry. Especially, the centrifugal term influences the U-turn the most as no noticeable effects of the centrifugal moments were seen in the case of the

sweeping turns. For all the four flights, just the aerodynamic moments do a fairly good job in predicting the roll, a combined contribution from the aerodynamic and local inertial moments are needed for a reasonable pitch angle prediction and all the four components of Eqn. 5 are needed to accurately predict the yaw angles.

4. CONCLUSIONS

The two unique features that distinguish bat flight from insect flight are i) highly articulated wing bone-muscle structure making the wing to body mass ratio substantial, and ii) a highly stretchable wing membrane that can deform to optimize aerodynamic force generation, allowing them to excel at maneuvers. These two features combined, make the coupled effect of wing inertia in the motion dynamics extremely important. As bat wings make up ~20-30% of the total mass, the acceleration felt by the flapping wings during straight flight and maneuvers is substantial and must be considered for dynamic analysis of translational and rotational motion.

In the current study, we have used the measured wing kinematic data of four flights of two species, *H. armiger* and *H. pratti*, with varying maneuverability to solve for the detailed aerodynamic forces. This is supplemented by using the detailed mass distribution to account for the inertial consequences of wing motion on the complete motion dynamics of flight. The roles played by aerodynamic and inertial forces and moments in effectuating the complete maneuver is identified with separate analyses for the translational and rotational motions.

The inertial forces are found to be of the same order of magnitude as the aerodynamic forces. During translational it was found that the inertial effect of the wing perturbations are consequential in accurately describing the motion dynamics in maneuvering flights. While, the aerodynamic forces alone can estimate the overall trends in flight velocity quite well, the wing inertia plays a

key role in predicting the variations that occur within a wingbeat cycle. The inertial effects are consistently found to be more prominent in the direction of gravity (z_g-direction) for the *H. armiger* bat in accordance with the primary flapping moton. In the sweeping and U-turn climbing maneuvering flights of the *H. armiger* , exclusion of inertial forces underpredicts the velocity and the measured gain in altitude indicating that z_g-directional inertial forces not only contribute to cyclic fluctuations but also to the mean motion. On the other hand, the *H. pratti* bat mostly utilizes aerodynamic forces for gaining altitude.

Finally, the total acceleration and moments experienced by the bat wings has been broken into several components and their individual contributions in effectuating the rotational maneuver has been decoded. Unlike in translational dynamics, wing inertia has a much greater influence on rotational dynamics. While, generally the aerodynamic moments mostly guide the overall body rotation over the flight duration, inertial moments in addition to introducing cyclic fluctuations, also influence the rotational dynamics over the duration of the flight much more so than in translational motion. The moments generated by the local Coriolis and centrifugal forces are found to be essential to achieve the desired yaw angle which is fundamental to the desired turning maneuver. These two terms become crucially important as the turning maneuver becomes more acute as in a 180° U-turn. The effect of the centrifugal term is strongest during the U-turn. For all the four flights, just the aerodynamic moments predict the trend in roll angle reasonably well, a combined contribution from the aerodynamic and local inertial moments are needed for pitch angle prediction and all the four components of inertia are required to accurately predict the yaw angle. This also leads us to conclude that the roll maneuver is primarily driven by aerodynamic asymmetries during flight, whereas the yaw maneuver is primarily driven by imbalances in wing inertial moments experienced by the two wings. The detailed contribution of the separate

aerodynamic, inertial, Coriolis and centrifugal moments in effectuating the translational and rotational aspects of different maneuvers provides guidance for maneuverable MAV designs.

ACKNOWLEDGEMENTS

The authors acknowledge Advanced Research Computing at Virginia Tech for providing computational resources for the numerical simulations (URL: http://www.arc.vt.edu). We wish to thank Dr. Mayuresh Patil for his help with the system dynamic equations. The authors would also like to acknowledge Prof. Rolf Mueller for providing the experimental facilities for the flight measurements, Xiaozhou Fan for the flight measurements on the *H. pratti*, Dr. Peter Windes for the flight measurements on the *H. armiger* and also for developing the foundational software environment used in this work. Peter Windes was supported on NSF CBET Grant No. 1510797.

REFERENCES

[1] H. Shyy, W., Aono, H., Kang, C.-K., and Liu, An Introduction to Flapping Wing Aerodynamics, Cambridge Univ. Press, Cambridge, MA, 2013.

[2] C.J. Pennycuick, Mechanics of flight, Avian Biol. 5 (1975) 1–75.

[3] J. Young, S.M. Walker, R.J. Bomphrey, G.K. Taylor, A.L.R. Thomas, Details of insect wing design and deformation enhance aerodynamic function and flight efficiency., Science. 325 (2009) 1549–52. doi:10.1126/science.1175928.

[4] Cheng, B., "Flying of Insects," Bioinspired Structures and Design, Cambridge Univ. Press, United Kingdom, 2020. doi:https://doi.org/10.1017/9781139058995.012.

[5] A.M. Mountcastle, S.A. Combes, Wing flexibility enhances load-lifting capacity in

bumblebees, Proc. R. Soc. B Biol. Sci. 280 (2013). doi:10.1098/rspb.2013.0531.

[6] L. Zheng, T.L. Hedrick, R. Mittal, Time-Varying Wing-Twist Improves Aerodynamic Efficiency of Forward Flight in Butterflies, PLoS One. 8 (2013) e53060. doi:10.1371/journal.pone.0053060.

[7] M.H. Dickinson, Wing Rotation and the Aerodynamic Basis of Insect Flight, Science (80-.). 284 (1999) 1954–1960. doi:10.1126/science.284.5422.1954.

[8] T. Nakata, H. Liu, A fluid–structure interaction model of insect flight with flexible wings, J. Comput. Phys. 231 (2012) 1822–1847. doi:10.1016/J.JCP.2011.11.005.

[9] C.P. Ellington, C. Van den Berg, A.P. Willmott, Leading-edge vortices in insect flight, Nature. 384 (1990) 626–630.

[10] M. Sun, J. Tang, Unsteady aerodynamic force generation by a model fruit fly wing in flapping motion, J. Exp. Biol. 205 (2002) 55–70. doi:10.1242/jeb.205.1.55.

[11] A.L.R. Thomas, G.K. Taylor, Animal Flight Dynamics I. Stability in Gliding Flight, J. Theor. Biol. 212 (2001) 399–424. doi:10.1006/JTBI.2001.2387.

[12] G.K. Taylor, A.L.R. Thomas, Animal Flight Dynamics II. Longitudinal Stability in Flapping Flight, J. Theor. Biol. 214 (2002) 351–370. doi:10.1006/JTBI.2001.2470.

[13] G.K. Taylor, A.L.R. Thomas, Dynamic flight stability in the desert locust Schistocerca gregaria, J. Exp. Biol. 206 (2003) 2803–2829. doi:10.1242/jeb.00501.

[14] A.P. Willmott, C.P. Ellington, The mechanics of flight in the hawkmoth Manduca sexta I. Kinematics of hovering and forward flight, J. Exp. Biol. 200 (1997) 2705–2722. doi:10.1242/jeb.200.21.2705.

[15] J.K. Sun, M.; Liu, Y. P.; Wang, Dynamic flight stability of a hovering hoverfly, J. Theor. Biol. 348 (2014) 100–112. doi:10.1016/j.jtbi.2014.01.026.

[16] M. Sun, Y. Xiong, Dynamic flight stability of a hovering bumblebee, J. Exp. Biol. 208 (2005) 447–459. doi:10.1242/jeb.01407.

[17] M. Sun, J. Wang, Y. Xiong, Dynamic flight stability of hovering insects, Acta Mech. Sin. Xuebao. 23 (2007) 231–246. doi:10.1007/s10409-007-0068-3.

[18] G.R. Spedding, M. Rosén, A. Hedenström, A family of vortex wakes generated by a thrush nightingale in free flight in a wind tunnel over its entire natural range of flight speeds, J. Exp. Biol. 206 (2003) 2313–2344. doi:10.1242/jeb.00423.

[19] C.J. Pennycuick, Modelling the Flying Bird, Academic Press, New York, 2008.

[20] B. Parslew, W.J. Crowther, Simulating avian wingbeat kinematics, J. Biomech. 43 (2010) 3191–3198. doi:10.1016/J.JBIOMECH.2010.07.024.

[21] B. Parslew, Predicting power-optimal kinematics of avian wings, J. R. Soc. Interface. 12 (2015). doi:10.1098/rsif.2014.0953.

[22] T.L. Hedrick, J.R. Usherwood, A.A. Biewener, Low speed maneuvering flight of the rose-breasted cockatoo (Eolophus roseicapillus). II. Inertial and aerodynamic reorientation, J. Exp. Biol. 210 (2007) 1912–1924. doi:10.1242/jeb.002063.

[23] T.L. Hedrick, A.A. Biewener, Low speed maneuvering flight of the rose-breasted cockatoo (Eolophus roseicapillus). I. Kinematic and neuromuscular control of turning, J. Exp. Biol. 210 (2007) 1897–1911. doi:10.1242/jeb.002055.

[24] J.A. Cheney, N. Konow, K.M. Middleton, K.S. Breuer, T.J. Roberts, E.L. Giblin, S.M.

Swartz, Membrane muscle function in the compliant wings of bats, Bioinspir. Biomim. 9 (2014) 025007. doi:10.1088/1748-3182/9/2/025007.

[25] A. Hedenström, L.C. Johansson, M. Wolf, R. von Busse, Y. Winter, G.R. Spedding, Bat Flight Generates Complex Aerodynamic Tracks, Science (80-.). 316 (2007) 894–897. doi:10.1126/SCIENCE.1142281.

[26] T.Y. Hubel, N.I. Hristov, S.M. Swartz, K.S. Breuer, Wake structure and kinematics in two insectivorous bats, Philos. Trans. R. Soc. B Biol. Sci. 371 (2016). doi:10.1098/rstb.2015.0385.

[27] J.A. Cheney, N. Konow, A. Bearnot, S.M. Swartz, A wrinkle in flight: The role of elastin fibres in the mechanical behaviour of bat wing membranes, J. R. Soc. Interface. 12 (2015). doi:10.1098/rsif.2014.1286.

[28] J.A. Cheney, J.J. Allen, S.M. Swartz, Diversity in the organization of elastin bundles and intramembranous muscles in bat wings, J. Anat. 230 (2017) 510–523. doi:10.1111/joa.12580.

[29] S.M. Swartz, Skin and bones functional, architectural, and mechanical differentiation in the bat wing, Bat Biology and Conservation, 1998. doi:10.1371/journal.pone.0218672.

[30] J.W. Bahlman, R.M. Price-Waldman, H.W. Lippe, K.S. Breuer, S.M. Swartz, Simplifying a wing: diversity and functional consequences of digital joint reduction in bat wings, J. Anat. 229 (2016) 114–127. doi:10.1111/joa.12457.

[31] Y. Winter, O. Von Helversen, The energy cost of flight: Do small bats fly more cheaply than birds?, J. Comp. Physiol. - B Biochem. Syst. Environ. Physiol. 168 (1998) 105–111.

doi:10.1007/s003600050126.

[32] R. Von Busse, R.M. Waldman, S.M. Swartz, C.C. Voigt, K.S. Breuer, The aerodynamic cost of flight in the short-tailed fruit bat (Carollia perspicillata): Comparing theory with measurement, J. R. Soc. Interface. 11 (2014). doi:10.1098/rsif.2014.0147.

[33] F.T. Muijres, G.R. Spedding, Y. Winter, A. Hedenström, Actuator disk model and span efficiency of flapping flight in bats based on time-resolved PIV measurements, Exp. Fluids. 51 (2011) 511–525. doi:10.1007/s00348-011-1067-5.

[34] F.T. Muijres, L.C. Johansson, M.S. Bowlin, Y. Winter, A. Hedenström, Comparing Aerodynamic Efficiency in Birds and Bats Suggests Better Flight Performance in Birds, PLoS One. 7 (2012) e37335. doi:10.1371/journal.pone.0037335.

[35] U.M. Norberg, T.H. Kunz, J.F. Steffensen, Y. Winter, O. von Helversen, The cost of hovering and forward flight in a nectar-feeding bat, Glossophaga soricina, estimated from aerodynamic theory, J. Exp. Biol. 182 (1993). https://jeb.biologists.org/content/182/1/207 (accessed March 16, 2021).

[36] A. Hedenström, L.C. Johansson, G.R. Spedding, Bird or bat: comparing airframe design and flight performance, Bioinspir. Biomim. 4 (2009) 015001. doi:10.1088/1748-3182/4/1/015001.

[37] N. Konow, J.A. Cheney, T.J. Roberts, J. Iriarte-Díaz, K.S. Breuer, J.R.S. Waldman, S.M. Swartz, Speed-dependent modulation of wing muscle recruitment intensity and kinematics in two bat species, J. Exp. Biol. 220 (2017) 1820–1829. doi:10.1242/jeb.144550.

[38] D.K. Riskin, D.J. Willis, J. Iriarte-Díaz, T.L. Hedrick, M. Kostandov, J. Chen, D.H.

Laidlaw, K.S. Breuer, S.M. Swartz, Quantifying the complexity of bat wing kinematics, J. Theor. Biol. 254 (2008) 604–615. doi:10.1016/j.jtbi.2008.06.011.

[39] P. Windes, D.K. Tafti, R. Müller, Determination of spatial fidelity required to accurately mimic the flight dynamics of a bat, Bioinspiration and Biomimetics. 14 (2019). doi:10.1088/1748-3190/ab3e2a.

[40] L.C. Johansson, M. Wolf, A. Hedenström, A quantitative comparison of bird and bat wakes, J. R. Soc. Interface. 7 (2009) 61–66. doi:10.1098/rsif.2008.0541.

[41] M. Wolf, L.C. Johansson, R. Von Busse, Y. Winter, A. Hedenström, Kinematics of flight and the relationship to the vortex wake of a Pallas' long tongued bat (Glossophaga soricina), J. Exp. Biol. 213 (2010) 2142–2153. doi:10.1242/jeb.029777.

[42] P. Windes, X. Fan, M. Bender, D.K. Tafti, R. Müller, A computational investigation of lift generation and power expenditure of Pratt's roundleaf bat (Hipposideros pratti) in forward flight, PLoS One. 13 (2018) 1–26. doi:10.1371/journal.pone.0207613.

[43] F.T. Muijres, L. Christoffer Johansson, Y. Winter, A. Hedenström, Leading edge vortices in lesser long-nosed bats occurring at slow but not fast flight speeds, Bioinspir. Biomim. 9 (2014) 025006. doi:10.1088/1748-3182/9/2/025006.

[44] L.C. Johansson, M. Wolf, R. von Busse, Y. Winter, G.R. Spedding, A. Hedenström, The near and far wake of Pallas' long tongued bat (Glossophaga soricina)., J. Exp. Biol. 211 (2008) 2909–18. doi:10.1242/jeb.018192.

[45] S. Sekhar, P. Windes, X. Fan, D.K. Tafti, Canonical description of wing kinematics and dynamics for a straight flying insectivorous bat (Hipposideros pratti), 2018.

doi:10.1371/journal.pone.0218672.

[46] L.C. Johansson, J. Håkansson, L. Jakobsen, A. Hedenstrom, Ear-body lift and a novel thrust generating mechanism revealed by the complex wake of brown long-eared bats (Plecotus auritus), Sci. Rep. 6 (2016) 1–9. doi:10.1038/srep24886.

[47] C. Schunk, S.M. Swartz, K.S. Breuer, The influence of aspect ratio and stroke pattern on force generation of a bat-inspired membrane wing, Interface Focus. 7 (2017). doi:10.1098/rsfs.2016.0083.

[48] U.M. NORBERG, Some Advanced Flight Manoeuvres of Bats, J. Exp. Biol. 64 (1976). https://jeb.biologists.org/content/64/2/489 (accessed March 16, 2021).

[49] A.J. Bergou, S.M. Swartz, H. Vejdani, D.K. Riskin, L. Reimnitz, G. Taubin, K.S. Breuer, Falling with Style: Bats Perform Complex Aerial Rotations by Adjusting Wing Inertia, PLOS Biol. 13 (2015) e1002297. doi:10.1371/journal.pbio.1002297.

[50] J. Iriarte-Díaz, S.M. Swartz, Kinematics of slow turn maneuvering in the fruit bat Cynopterus brachyotis., J. Exp. Biol. 211 (2008) 3478–89. doi:10.1242/jeb.017590.

[51] P. Henningsson, L. Jakobsen, A. Hedenström, Aerodynamics of manoeuvring flight in brown long-eared bats (Plecotus auritus), J. R. Soc. Interface. 15 (2018). doi:10.1098/rsif.2018.0441.

[52] H.D. Aldridge, Turning flight of bats, J. Exp. Biol. 128 (1987). https://jeb.biologists.org/content/128/1/419 (accessed March 16, 2021).

[53] B.Y.H.D.J.N. Aldridge, Body Accelerations During the Wingbeat in Six Bat Species: The Function of the Upstroke in Thrust Generation, J. Exp. Biol. 130 (1987) 275–293.

[54] J. Iriarte-Díaz, D.K. Riskin, D.J. Willis, K.S. Breuer, S.M. Swartz, Whole-body kinematics of a fruit bat reveal the influence of wing inertia on body accelerations., J. Exp. Biol. 214 (2011) 1546–53. doi:10.1242/jeb.037804.

[55] D.K. Riskin, A. Bergou, K.S. Breuer, S.M. Swartz, Upstroke wing flexion and the inertial cost of bat flight, Proc. R. Soc. B Biol. Sci. 279 (2012) 2945–2950. doi:10.1098/rspb.2012.0346.

[56] D. Yin, Z. Zhang, M. Dai, Effects of inertial power and inertial force on bat wings, Zoolog. Sci. 33 (2016) 239–245. doi:10.2108/zs150182.

[57] D.B. Boerma, K.S. Breuer, T.L. Treskatis, S.M. Swartz, Wings as inertial appendages : how bats recover from aerial stumbles, (2019). doi:10.1242/jeb.204255.

[58] X. Fan, K. Breuer, Low-Order Modeling of Flapping Flight with Highly Articulated, Cambered, Heavy Wings, AIAA J. (2021) 1–10. doi:10.2514/1.j060661.

[59] C.T. Orlowski, A.R. Girard, Modeling and simulation of nonlinear dynamics of flapping wing micro air vehicles, AIAA J. 49 (2011) 969–981. doi:10.2514/1.J050649.

[60] D. Rahman, Aevelina; Windes, Peter; Tafti, Turning-Ascending Flight of a H. pratti Bat, R. Soc. Open Sci. (n.d.). doi:under review.

[61] P. Windes, D.K. Tafti, R. Müller, Kinematic and aerodynamic analysis of a bat performing a turning-ascending maneuver, Bioinspiration and Biomimetics. 16 (2020). doi:10.1088/1748-3190/abb78d.

[62] P. Windes, D.K. Tafti, R. Müller, Analysis of a 180-degree U-turn maneuver executed by a hipposiderid bat, PLoS One. 15 (2020) 1–23. doi:10.1371/journal.pone.0241489.

[63] T.L. Hedrick, J.R. Usherwood, A.A. Biewener, Wing inertia and whole-body acceleration: An analysis of instantaneous aerodynamic force production in cockatiels (Nymphicus hollandicus) flying across a range of speeds, J. Exp. Biol. 207 (2004) 1689–1702. doi:10.1242/jeb.00933.

[64] D. Rahman, Aevelina; Windes, Peter; Tafti, Data used for analyzing a turning-ascending flight of a H. pratti bat, (n.d.). doi:10.5061/dryad.mcvdnck2c.

[65] D.K. Tafti, GenIDLEST - A scalable parallel computational tool for simulating complex turbulent flows, in: ASME-IMECE, 2001: pp. 347–356.

[66] A. Rahman, D. Tafti, The role of vortex–vortex interactions in thrust production for a plunging flat plate, J. Fluids Struct. 96 (2020) 103011. doi:10.1016/J.JFLUIDSTRUCTS.2020.103011.

[67] H. Hosseinzadegan, D.K. Tafti, A Predictive Model of Thrombus Growth in Stenosed Vessels with Dynamic Geometries, J. Med. Biol. Eng. 39 (2019) 605–621. doi:10.1007/s40846-018-0443-5.

[68] H. Elghannay, D. Tafti, K. Yu, Evaluation of physics based hard-sphere model with the soft sphere model for dense fluid-particle flow systems, Int. J. Multiph. Flow. 112 (2019) 100–115. doi:10.1016/J.IJMULTIPHASEFLOW.2018.12.004.

[69] D. Tafti, C. Dowd, X. Tan, High Reynold number LES of a rotating two-pass ribbed duct, Aerospace. 5 (2018). doi:10.3390/aerospace5040124.

[70] K. Yu, H.A. Elghannay, D. Tafti, An impulse based model for spherical particle collisions with sliding and rolling, Powder Technol. 319 (2017) 102–116.

doi:10.1016/J.POWTEC.2017.06.049.

[71] A. Rahman, D. Tafti, Characterization of heat transfer enhancement for an oscillating flatplate-fin, Int. J. Heat Mass Transf. 147 (2020). doi:10.1016.

[72] K. Nagendra, D.K. Tafti, K. Viswanath, A new approach for conjugate heat transfer problems using immersed boundary method for curvilinear grid based solvers, J. Comput. Phys. 267 (2014) 225–246. doi:10.1016/j.jcp.2014.02.045.

[73] Z. Cao, D.K. Tafti, M. Shahnam, Modeling drag force in ellipsoidal particle suspensions with preferential orientation, Powder Technol. 378 (2021) 274–287. doi:10.1016/j.powtec.2020.09.067.

[74] T.K. Oh, D. Tafti, K. Nagendra, LES-conjugate heat transfer analysis of a ribbed cooling passage using the immersed boundary method, Proc. ASME Turbo Expo. 5A-2019 (2019) 1–16. doi:10.1115/GT2019-90397.

[75] K. Viswanath, K. Nagendra, J. Cotter, M. Frauenthal, D.K. Tafti, Straight-line climbing flight aerodynamics of a fruit bat, Phys. Fluids. 26 (2014). doi:10.1063/1.4864297.

APPENDIX A

To derive the expression for the moment of inertia matrix [I], we start from the expressions of the linear and angular momentums, $\boldsymbol{L}$ and $\boldsymbol{P}$

$$\boldsymbol{L} = \sum m_i \boldsymbol{v}_{i,b}$$

$$\boldsymbol{P} = \boldsymbol{r}_{i,b} \times \sum m_i \boldsymbol{v}_{i,b} = \sum m_i \boldsymbol{r}_{i,b} \times \boldsymbol{v}_{i,b} = \sum m_i \boldsymbol{r}_{i,b} \times \left(\boldsymbol{\omega} \times \boldsymbol{r}_{i,b} + \boldsymbol{v}_{o,g}\right)$$

Where, $\boldsymbol{v}_{o,g}$ = velocity of the COM or the body frame origin

$$\boldsymbol{P} = \sum m_i \boldsymbol{r}_{i,b} \times \left(\boldsymbol{\omega} \times \boldsymbol{r}_{i,b}\right) + \sum m_i \boldsymbol{r}_{i,b} \times \boldsymbol{v}_{o,g} = -\sum m_i [\boldsymbol{r}_{i,b} \times \left(\boldsymbol{r}_{i,b} \times \boldsymbol{\omega}\right)] + 0$$

Using the relationship $\boldsymbol{b} \times (\boldsymbol{b} \times \boldsymbol{c}) = \boldsymbol{b}^2 \boldsymbol{c}$ [REF. a]

$$\boldsymbol{P} = [-\sum m_i \boldsymbol{r}_{i,b}^2]\, \boldsymbol{\omega}$$

By definition, angular momentum, $\boldsymbol{P} = [I]\boldsymbol{\omega}$

Thus, $[I] = [-\sum m_i \boldsymbol{r}_{i,b}^2] = \sum \boldsymbol{r}_{i,b} \times m_i \boldsymbol{r}_{i,b}$

and $\left[\dot{I}\right] = \frac{d[I]}{dt} = -\sum 2\, m_i \boldsymbol{r}_{i,b} \frac{d\boldsymbol{r}_{i,b}}{dt} = -\sum 2\, m_i \boldsymbol{r}_{i,b}\, \boldsymbol{v}_{i,b}$

The moment equation in the body frame is given by Eqn. (3) as follows -

$$\sum \boldsymbol{r}_{i,b} \times \boldsymbol{F}_{aero,i,b} = \sum \boldsymbol{r}_{i,b} \times m_i \left(\boldsymbol{a}_{i,b} + \boldsymbol{\alpha} \times \boldsymbol{r}_{i,b} + 2\boldsymbol{\omega} \times \boldsymbol{v}_{i,b} + \boldsymbol{\omega} \times \left(\boldsymbol{\omega} \times \boldsymbol{r}_{i,b}\right)\right) \ldots\ldots (3)$$

Term 1: $\sum \boldsymbol{r}_{i,b} \times m_i \left(\boldsymbol{a}_{i,b}\right) = M_{loc}$

Term 2: $\sum \boldsymbol{r}_{i,b} \times m_i \left(\boldsymbol{\alpha} \times \boldsymbol{r}_{i,b}\right) = \sum m_i \left[\boldsymbol{r}_{i,b} \times \left(\boldsymbol{\alpha} \times \boldsymbol{r}_{i,b}\right)\right] = -\sum m_i [\boldsymbol{r}_{i,b} \times \left(\boldsymbol{r}_{i,b} \times \boldsymbol{\alpha}\right)] = [I]\boldsymbol{\alpha}$

Term 3: $\sum \boldsymbol{r}_{i,b} \times m_i \left(2\boldsymbol{\omega} \times \boldsymbol{v}_{i,b}\right) = \sum m_i\left[\boldsymbol{r}_{i,b} \times \left(2\boldsymbol{\omega} \times \boldsymbol{v}_{i,b}\right)\right] = -\sum 2m_i[\boldsymbol{r}_{i,b} \times \left(\boldsymbol{v}_{i,b} \times \boldsymbol{\omega}\right)]$

$$= [-\sum 2m_i \boldsymbol{r}_{i,b}\boldsymbol{v}_{i,b}]\boldsymbol{\omega} = \left[\dot{I}\right]\boldsymbol{\omega}$$

Term 4: $\sum \boldsymbol{r}_{i,b} \times m_i \left(\boldsymbol{\omega} \times (\boldsymbol{\omega} \times \boldsymbol{r}_{i,b})\right) = -\sum m_i\left[\left(\boldsymbol{\omega} \times (\boldsymbol{\omega} \times \boldsymbol{r}_{i,b}\right) \times \boldsymbol{r}_{i,b}\right]$

$= -\sum m_i \left[\left(\boldsymbol{\omega} \times \boldsymbol{r}_{i,b}\right).\left(\boldsymbol{\omega}.\boldsymbol{r}_{i,b}\right) - \boldsymbol{r}_{i,b}\left(\boldsymbol{\omega}.\left(\boldsymbol{\omega} \times \boldsymbol{r}_{i,b}\right)\right)\right]$, using vector triple product

$= -\sum m_i \left[\left(\boldsymbol{\omega} \times \boldsymbol{r}_{i,b}\right).\left(\boldsymbol{\omega}.\boldsymbol{r}_{i,b}\right) - \boldsymbol{r}_{i,b}\left(\boldsymbol{r}_{i,b}.\left(\boldsymbol{\omega} \times \boldsymbol{\omega}\right)\right)\right]$, using scalar triple product

$= -\sum m_i\left[\left(\boldsymbol{\omega} \times \boldsymbol{r}_{i,b}\right).\left(\boldsymbol{\omega}.\boldsymbol{r}_{i,b}\right)\right]$, using $(\boldsymbol{\omega} \times \boldsymbol{\omega}) = 0$

$= \boldsymbol{\omega} \times \left[\sum -m_i\left[\left(\boldsymbol{r}_{i,b}.\left(\boldsymbol{r}_{i,b}.\boldsymbol{\omega}\right)\right)\right]\right]$, using Jacobi identity [REF. b]

$= \boldsymbol{\omega} \times [I]\boldsymbol{\omega}$

Thus Eqn. 4 is derived from Eqn. 3 to take the following form

$$M_{aero,b} = \sum \boldsymbol{r}_{i,b} \times \boldsymbol{F}_{aero,i,b} = M_{loc} + [I]\boldsymbol{\alpha} + \left[\dot{I}\right]\boldsymbol{\omega} + \boldsymbol{\omega} \times [I]\boldsymbol{\omega} \ldots\ldots\ldots (4)$$

REFERENCE

[a] Yamazaki H, Nakamura Y. Cross Products and Tripple Vector Products in 3-dimensional Euclidian Space. Journal of Formalized Mathematics. 2003;15

[b] Hall, Brian C. Lie Groups, Lie Algebras, and Representations: An Elementary Introduction, Graduate Texts in Mathematics. Springer. 2015; 222 (2nd ed.)

Chapter 6: Concluding Remarks and Scope for Future Work

1. CONCLUDING REMARKS

This chapter summarizes the main findings of the research performed, the ultimate goal of which is to investigate the synergistic effects of kinematics, aerodynamics, and inertia on flapping maneuvers with application to micro-air vehicles. In the first phase, a canonical case of a plunging flat plate was investigated to establish the interdependence of flapping kinematics and the ensuing aerodynamics. As small scale flapping flights are characterized by low Reynolds number, a detailed analysis of the vortex dynamics at $Re = 100$ was conducted over a wide range of reduced frequencies $0.25 \leq k \leq 16$ and plunge amplitudes $0.03125 \leq h \leq 8$ to give plunge velocities ranging from $0.25 \leq kh \leq 4$. It was reported that, instead of increasing monotonically with kh, thrust production maximized at $kh = 1$ and reduced thereafter. The rate at which thrust production dropped was dependent on h – decreasing rapidly at large plunge amplitudes when the reduced frequency was small, so much so that at low k and high kh the force produced reverted back to drag.

It was also shown that LEVs contributed to thrust production by inducing counter flow velocities near the flat plate, whereas TEVs did the opposite. At low $kh < 1$, the LEVs were not strong enough to induce a counter-flow at the plate, rather they convected down the plate to the trailing edge with the TEVs directly shed into the wake. As kh increased, the LEVs increased in size and strength to be able to induce a counter-flow near the plate. Moreover, the induced velocities of both LEVs and TEVs were not high enough for the TEVs to become consequential by convecting upstream and influence the flow at the plate. Thrust production was found to be maximum in this regime. As kh increased further, especially in the cases of higher h, the LEVs and TEVs presented a chaotic

regime in which non-linear vortex-vortex interactions dominated. Three main mechanisms of such interactions were identified, the net effect of which was to decrease the residence time of LEVs near the plate and reduce thrust. In order to estimate the sole effect of LEV strength on thrust coefficient, the TEVs were eliminated by conducting a numerical experimentation in the form of a splitter plate set in the wake of the primary flat plate. With only LEVs present in the flow field, the thrust coefficient (C_T) increased monotonically with *kh* for all the tested frequencies. With this regular trend, a parametrization of thrust coefficient was possible with frequency (k) and amplitude (h) where the observed C_T closely followed the proposed parametric equation with an excellent R^2 value.

The first phase of this research provided detailed demonstration of how the non-linear interactions in the operating kinematic conditions affected the ensuing aerodynamic features. The second phase however, took a more direct approach to link the defining components of a maneuvering motion- the kinematics, the aerodynamics, and the inertial counterparts. Firstly, a turning ascending maneuver of a *H. pratti* bat was investigated with special attention given to the turning mechanics and identification of commonalities with a similar previous maneuver from a *H. armiger* bat. Both bats utilized roll and yaw rotations of the body synergistically to redirect the force vector inward to provide the required centripetal force to control the turn. In order to generate the roll and yaw moments, the bats utilized force as well as moment-arm asymmetries between the two wings. Both flights evidenced the inside wing to be drawn closer to the body to reduce the moment arm and accentuate force asymmetries. Force asymmetries were also created by introducing phase lags between the two wings and redirecting force production to different parts of the wings. The commonalities noted in both flights during the maneuver included marked increase in the flapping frequency, shortening of the upstroke compared to the downstroke and generation of a small thrust

force in the upstroke, all of which were absent in straight flight and thus characterized the maneuver. Secondly, the inertial consequences coming from the acceleration of the bat wings were investigated. As bat wings make up a larger fraction of total mass in comparison to birds or insects, the acceleration felt by the flapping wings during a target maneuver were found to be substantial and thus were included in the motion dynamics. This was done by using the measured wing kinematic data from four different maneuvers and the detailed mass distribution to solve for the detailed aerodynamic forces and the inertial consequences due to the motion of the wing during the maneuvers. The individual roles of the aerodynamic and inertial forces and consecutive moments in effectuating the complete maneuver was identified with separate analyses for the translational and rotational motions. The inertial forces were in the same order of magnitude as the aerodynamic forces. While, the aerodynamic forces alone were enough to estimate the overall translational velocity trends quite well, the wing inertia played a key role in predicting the intricate fluctuations occuring within a wingbeat cycle and also contributing to altitude gain of the *H. armiger*. To characterize the rotational aspect of the analyzed maneuvers, the total acceleration and moments felt by the bat wings were broken into several components. While effectuating a turn, the aerodynamic moments were mostly effective in defining the overall rotational trends whereas the local inertial moments contributed to the intra-cycle fluctuations seen in the angular orientation. The moments coming from the local Coriolis and centrifugal forces were found essential to achieve the desired yaw angle which changed anywhere between 60° to 180°. For all the four flights, just the aerodynamic moments reasonably predicted the roll angle, combined aerodynamic and inertial contributions were needed for pitch angle prediction and all the four inertia components were necessary to accurately predict the yaw angle. Both in translation and

rotation, the inertial effects were more prominent in and about the z-direction which is consistent with the primary flapping moton.

Bat flight is capable of providing a compelling model for bioinspired MAV designs. Thus it is important to understand the interplay between the kinematic, aerodynamic and inertial features used by bats to effectuate a certain maneuver. The current research is unique in that it directly relates the motion kinematics to aerodynamic and inertial force generation which is a critical component for identifying key maneuvering traits used across different bat species and individuals. The detailed contribution of the separate aerodynamic, inertial, Coriolis and centrifugal moments in effectuating the translational and rotational aspects of different maneuvers can provide valuable future guidance for maneuverable and agile MAV designs.

2. SCOPE FOR FUTURE RESEARCH

This research has investigated the intricate details of kinematics, aerodynamics and inertia of four different maneuvers coming from two different bat species, *H. pratti* and *H. armiger* which are morphologically similar. The interesting and impactful findings of the current research holds the possibility of paving the way for future research scopes. Further methodical investigation of other maneuvers such as sharp descent, landing, aerial somersault etc. will add to a more comprehensive understanding of kinematic asymmetries, aerodynamic forces, inertial effects, and their inter-dependence. Another direction to venture into would be to investigate other bat species with different wing morphologies. Preliminary work has been done in this regard with the aim to aid future research. Several flights have been recorded from yet another species (*Rhinolophus ferrumequinum*) which is much smaller in size. A comparison between some basic morphological parameters among the species are shown in Table 1.

Table 1: Comparison among different bat species

Bat name	Species	Mass (g)	Wingspan (cm)	Diet
Pratt's roundleaf bat	*Hipposideros pratti*	50 - 65	50 - 55	Insectivorous
Great roundleaf bat	*Hipposideros armiger*	50 - 65	50 - 55	Insectivorous
Greater horseshoe bat	*Rhinolophus ferrumequinum*	15 – 25	35 - 40	Insectivorous

The kinematic data regarding the Greater Horseshoe bat has already been collected utilizing the 3D motion capture system used in the current research. As these bats are significantly smaller, the number of white marker points on the wings tracked in the captured videos have been reduced as shown in Figure 1.

Figure 1: Marker pattern on small bat wing

The experiments have resulted in multiple flight paths featuring straight flight, lateral turns, ascending maneuvers, U-turns etc. -To provide a starting point for future research, we have chosen a right turn ascending maneuver of the Greater Horseshoe bat and preprocessed the video recording data in pixel frame to kinematic data in physical co-ordinate system. A preliminary aerodynamic simulation has also been run using the in-house incompressible Navier Stokes solver GenIDLEST. Given future resources, analyses of this and other flights from varying species will allow a more comprehensive understanding of bat flight maneuvers.